2810376850

REFERENCE ONLY

# UNIVERSITY OF LONDON THESIS

Degree PhD Year 2008 Name of Author BOHNDIEK, SARAH, ELIZABETH.

**COPYRIGHT**

This is a thesis accepted for a Higher Degree of the University of London. It is an unpublished typescript and the copyright is held by the author. All persons consulting the thesis must read and abide by the Copyright Declaration below.

**COPYRIGHT DECLARATION**

I recognise that the copyright of the above-described thesis rests with the author and that no quotation from it or information derived from it may be published without the prior written consent of the author.

**LOAN**

Theses may not be lent to individuals, but the University Library may lend a copy to approved libraries within the United Kingdom, for consultation solely on the premises of those libraries. Application should be made to: The Theses Section, University of London Library, Senate House, Malet Street, London WC1E 7HU.

**REPRODUCTION**

University of London theses may not be reproduced without explicit written permission from the University of London Library. Enquiries should be addressed to the Theses Section of the Library. Regulations concerning reproduction vary according to the date of acceptance of the thesis and are listed below as guidelines.

A. Before 1962. Permission granted only upon the prior written consent of the author. (The University Library will provide addresses where possible).

B. 1962 - 1974. In many cases the author has agreed to permit copying upon completion of a Copyright Declaration.

C. 1975 - 1988. Most theses may be copied upon completion of a Copyright Declaration.

D. 1989 onwards. Most theses may be copied.

☐ This copy has been deposited in the Library of UCL

☐ This copy has been deposited in the University of London Library, Senate House, Malet Street, London WC1E 7HU.

# Active Pixel Sensors for breast biopsy analysis using X-ray Diffraction

Sarah Elizabeth Bohndiek

A Thesis submitted to the University of London for the degree of Doctor of Philosophy

Department of Medical Physics and Bioengineering

University College London, UCL

2008

UMI Number: U591414

All rights reserved

INFORMATION TO ALL USERS
The quality of this reproduction is dependent upon the quality of the copy submitted.

In the unlikely event that the author did not send a complete manuscript
and there are missing pages, these will be noted. Also, if material had to be removed,
a note will indicate the deletion.


UMI U591414
Published by ProQuest LLC 2013. Copyright in the Dissertation held by the Author.
Microform Edition © ProQuest LLC.
All rights reserved. This work is protected against
unauthorized copying under Title 17, United States Code.


ProQuest LLC
789 East Eisenhower Parkway
P.O. Box 1346
Ann Arbor, MI 48106-1346

I, Sarah Elizabeth Bohndiek, confirm that the work presented in this thesis is my own. Where information has been derived from other sources, I confirm that this is indicated in the thesis.

Signature .

# Abstract

Breast cancer diagnosis currently requires biopsy samples to be analysed by a histopathologist; a time consuming, highly specialised process. X-ray diffraction is a quantitative technique that can distinguish between healthy and diseased breast biopsy samples using the change in proportions of fat and fibrous tissue that occurs when cancer invades. A semi-automated breast biopsy analysis system based on X-ray diffraction could yield a faster patient diagnosis. Recording X-ray diffraction patterns is a challenging task needing low noise, large area, and wide dynamic range detectors. Scientific complementary metal oxide semiconductor (CMOS) Active Pixel Sensors will soon be able to meet all of these demands in a single device.

Characterization of two novel Active Pixel Sensors that advance towards an ideal X-ray diffraction detector is presented. 'Vanilla' exhibits a low read noise of $55e^-$ r.m.s. and high quantum efficiency of up to 70% so was selected for the design and implementation of the first 'Active Pixel X-ray Diffraction' (APXRD) system. Following on from Vanilla, the 'Large Area Sensor' (LAS) covered an area of over $29cm^2$ and had a wide dynamic range of over 95dB.

The first linear systems model of an Active Pixel Flat Panel Imager (scintillator coupled APS) was formulated in the design of the APXRD system, to select filters to narrow the spectral width of the X-ray beam and predict the recorded scatter intensity. Following system implementation, scatter signatures were recorded for numerous breast tissue equivalent samples. A multivariate analysis model calibrated with these was able to predict the percentage fat content of an 'unknown' sample to within 3%; a very promising result. The width of the filtered polychromatic X-ray spectrum had only a minor influence on the APXRD scatter signatures indicating that the system preserves all relevant structural information.

# Contents

# Acknowledgements

I wish to express my gratitude to my supervisors Professor Robert Speller and Dr Gary Royle for their continued support and excellent advice throughout the course of this project.

I also wish to thank the RC-UK MI3 consortium for funding this work and providing an excellent network of experienced researchers with whom I have had many valuable discussions. In particular I would like to thank: Nigel Allinson for driving and inspiring both myself and the consortium; Andrew Blue for providing equipment for sensor characterization and helpful dialogue on different methods; Andy Clark and Jamie Crooks for their invaluable assistance in controlling and characterizing the sensors; Renato Turchetta for answering my numerous questions and supporting many visits to Rutherford Appleton Laboratory.

My appreciation is also extended to the members of the Radiation Physics group, both past and present, from whom I have sought help, support, advice and expertise on many occasions. In particular, thanks go to Emily Cook for her help with the energy dispersive X-ray diffraction experiments; Colin Esbrand for being an excellent desk mate and listener; Alessandro Olivo for challenging and questioning results; and Costas Arvanitis for the long debates that made both our work stronger.

Finally, I would like to thank my family for their ongoing encouragement and pride that make all that I achieve worthwhile.

# List of Journal Publications

## First Author

1. S E Bohndiek, A Blue, A T Clark, M L Prydderch, R Turchetta, G J Royle and R D Speller (2008) Comparison of methods for estimating the conversion gain of CMOS Active Pixel Sensors *IEEE Sensors* **10** 1734–1744.

2. S E Bohndiek, E J Cook, C D Arvanitis, A Olivo, G J Royle, A T Clark, M L Prydderch, R Turchetta and R D Speller (2008) A CMOS Active Pixel Sensor system for laboratory-based X-ray diffraction of biological tissue *Physics in Medicine and Biology* **53** 655–672.

3. S E Bohndiek, C D Arvanitis, G J Royle, A T Clark, J P Crooks, M L Prydderch, R Turchetta, A Blue, V O'Shea and R D Speller (2007) A characterization study of two novel Active Pixel Sensors *Optical Engineering* **46** 124003.

## Other

1. C D Arvanitis, S E Bohndiek, J Blakesley, A Olivo and R D Speller (2008) Signal and noise transfer properties of CMOS based active pixel flat panel imagers coupled to structured CsI:Tl, accepted in *Medical Physics*, September 2008.

2. J P Crooks, S E Bohndiek, H XingLiang, B Ott, J Osmond, G Villani, A Clark, R Halsall, M Key-Charriere, S Martin, M Towrie and R Turchetta (2008) Prototype CMOS sensor with in-pixel intelligent features, accepted in *IEEE Sensors*, June 2008.

3. C D Arvanitis, S E Bohndiek, G J Royle, A Blue, H X Liang, A Clark, M Prydderch, R Turchetta and R D Speller (2007) Empirical electro-optical and X-ray performance evaluation of CMOS Active Pixel Sensors for low dose, high resolution x-ray medical imaging *Medical Physics* **34** 4612–4625.

4. J A Griffiths, G J Royle, A M Hanby, J A Horrocks, S E Bohndiek and R D Speller (2007) Correlation of energy dispersive diffraction signatures and

microCT of small breast tissue samples with pathological analysis *Physics in Medicine and Biology* **52** 6151-6164.

5. A Olivo, C D Arvanitis, S E Bohndiek, A T Clark, M Prydderch, R Turchetta and R D Speller (2007) First evidence of phase-contrast imaging with laboratory sources and active pixel sensors *Nucl Inst Meth A* **581** 776-782.

6. A Blue, R Bates, A Laing, D Maneuski, V O'Shea, A Clark, M Prydderch, R Turchetta, C Arvanitis and S E Bohndiek (2007) Characterisation of Vanilla - A novel active pixel sensor for radiation detection *Nucl Inst Meth A* **581** 287-290.

# List of Figures

# List of Tables

# Chapter 1

# Introduction

## 1.1 Background and Motivation

Breast cancer is now the most common cause of death in women worldwide (Héry *et al.*, 2008). Over 44,000 women are diagnosed with breast cancer each year, following a 50% increase in incidence in the last 20 years (Cancer Research UK, 2008). The NHS UK Breast Screening Programme (UKBSP) was founded in 1988 with the aim of detecting breast cancer at an earlier stage when metastatic disease is less likely and in turn, improving patient prognosis (Wyld and Ingram, 2007). The UKBSP offers 3 yearly X-ray mammography screening to women over 50 and currently examines over 1.5million women each year. From these exams, over 14,000 cases of breast cancer are found annually, representing 8 in 10 of the detected cases of breast cancer in this age group.

The success of the UKBSP is partially determined by the accuracy of detecting tumours in X-ray mammography. The overall sensitivity of X-ray mammography is widely accepted to be 80-90%, while specificity can be up to 95% (Reddy and Given-Wilson, 2004; Banks *et al.*, 2004). Combined data from studies in the last decade indicate that this has been sufficient to account for a median breast cancer mortality reduction of 46% (range 24% to 65%) (Dixon, 2006). Breast screening is therefore accepted as a cost effective (£45.50 per woman screened) means of detecting early stage cancer (7.1 cancers per 1000 women screened) (National Health Service, 2008).

Up to 10% of women screened are recalled because an abnormality is observed on their mammogram. This most commonly manifests as a mass, asymmetry or distortion in the breast tissue, or clustered microcalcifications, indicative of malignant disease (Reddy and Given-Wilson, 2004). When a woman is recalled, they enter the standard, multidisciplinary, 'triple assessment' scheme of diagnosis (British Medical Journal, 2008). This involves

1. Clinical examination - performed by a doctor

2. Radiological assessment - X-ray mammography, sometimes MRI or ultrasound

3. Histopathological evaluation - microscopic examination of breast tissue acquired through biopsy

For women referred from screening, further radiological assessment will only be carried out if necessary. Each stage of the triple assessment is graded by a level of suspicion of disease and the overall combination of these grades decides the outcome. The average waiting time for a result is 7 days. This is a traumatic period for the patient, whose anxiety may persist even if they receive an 'all clear' (Advisory Committee on Breast Cancer Screening, 2006). A significant portion of this delay comes from the histopathological evaluation. This final stage of triple assessment tests tissue excised from the suspicious lesion for signs of cancer. Results from biopsy analysis are divided into five categories: inadequate, benign, atypia, suspicious and malignant. Surgical diagnostic excision biopsy and histological examination of the tissue sections was historically the gold standard of histopathological evaluation (Ellis *et al.*, 2004). The majority of breast cancers are now diagnosed nonoperatively; in 2003/04, 93% of cancers diagnosed by the UKBSP were confirmed in this manner (Lieske *et al.*, 2006).

Two accurate techniques for nonoperative diagnosis are fine needle aspiration cytology (FNAC) and core needle biopsy (CB). A comparison of these methods is made in Table 1.1.

Fine needle aspiration cytology (FNAC) uses a thin needle to extract cells from the suspected lesion, which are then stained and analysed. The process is highly operator dependent but in general, around 3-4 aspirations will obtain the optimum yield of cells (Ellis *et al.*, 2004). Complete sensitivity is given by the number of cases placed in one of the final three categories above, compared to the actual number of cancers. For FNAC, complete sensitivity is 83%, specificity is 87% and the inadequate rate is just over 6% (Britton, 1999). As FNAC requires only a fine needle and syringe, it is often referred to as the 'low cost' biopsy option (Ellis *et al.*, 2004; Wallis *et al.*, 2007), although a recent study by Hukkinen *et al.* (2008) questioned this assumption as they found the overall cost of both procedures to be

Table 1.1: Comparison of the relative advantages of Fine Needle Aspiration Cytology (FNAC) and Core Needle Biopsy (CB) in breast cancer diagnosis

| | Advantages | Disadvantages |
|---|---|---|
| FNAC | Simple equipment | Needs experienced physician |
| | Can do same day analysis | No distinction of *in situ* vs invasive carcinoma available |
| | Less traumatic than CB | No architecture features |
| CB | No specialist expertise | Time consuming analysis |
| | Architectural details available | Needs local anaesthetic |
| | Can identify microcalcifications and benign disease | Potential for tumour cell feeding along needle track |

equivalent when both equipment and expertise were accounted for.

Core needle biopsy (CB or CNB) refers to the excision of long (1-2cm), thin (1-3mm diameter) tissue cores (Houssami *et al.*, 2006). These are easier to obtain than aspiration biopsies as they can be completed with automatic 'guns'; they do, however, require a local anaesthetic to be administered. At least 5 cores are required to yield a 90% correspondence with excisional biopsy and 99% diagnosis rate. Core biopsies are radiographed on a standard clinical X-ray source to check accurate targeting of the lesion (Guinebretière *et al.*, 2005), especially in cases where microcalcifications are present (Liberman *et al.*, 1994). Results of this X-ray can then be used to assist pathologists in choosing tissue samples or sections for evaluation.

Compared to FNAC, CB confers a number of advantages. Firstly, complete sensitivity is 95%, specificity is 98% and the inadequate rate is just over 1% (Britton, 1999), a better overall performance. Secondly, obtaining an actual core of tissue yields architectural information that is not available with a cell sample so a definitive diagnosis of different types of benign disease may be made (Wallis *et al.*, 2007). Further, information on cancer grade and invasion are available instantly if a tumour is found. Finally, CB provides much better sensitivity and specificity than FNAC for lesions containing microcalcifications. As a result, CB has widely replaced FNAC both in the UK (Lieske *et al.*, 2006) and worldwide (Houssami *et al.*, 2006).

Despite the success of nonoperative diagnosis, there is still potential for improvement. In general, reducing the time taken for histopathological analysis, and in turn diagnosis, would dramatically reduce patient anxiety and optimize management. More specifically, standardization of the semi-quantitative histopathological assessment would reduce errors and improve the chances of definitive one-stage surgery (Singh and Wells, 2001).

A landmark study by Raab *et al.* (2005) made the first attempt to assess the frequency and clinical impact of errors in the histopathological diagnosis of cancer. They found that the level and cause of errors was highly variable between institutions; unsurprising given the subjective nature of sample interpretation. Significantly, up to 15% of breast samples had a diagnosis error, attributed either to sampling (inadequate or inappropriate biopsies, 70% of cases) or interpretation (operator dependent). Given these two main causes of error, strategies for improving nonoperative diagnosis can be identified. Immediate analysis of core biopsies to assess sample quality and content would remove sampling errors and increase the speed of diagnosis as further cores could be obtained if a lesion had been missed. It is, however, impractical for a pathologist to study cores as they are obtained. Interpretation errors could be reduced if samples were reviewed by a second pathologist. Most UK pathology departments do not have an extra pathologist available for error checking and interpretation errors can be correlated with excessive workload (Ramsay, 1999), so requiring a second analysis of all samples could be counterproductive.

A simple, quantitative and semi-automated analysis system for core biopsies would be a cost effective method to reduce the number of unnecessary biopsies, improving the accuracy of lesion sampling and reducing the waiting time for diagnosis. Improving the quality of information available to histopathologists would aid their selection of tissue sections and reduce sample preparation errors (Liberman *et al.*, 1994). To be widely accepted, such a system would need to: provide accurate information about the content of a core sample; operate at high throughput; and be easy to install, maintain and calibrate.

Given core biopsies are already radiographed, a simple biopsy analysis system could use X-ray imaging and be based around existing clinical radiographic equipment. Further to standard radiography, it would need to provide material-specific information to accurately identify the tissue composition of a biopsy sample, lesions types, as well as the presence and type of microcalcifications. The ability to distinguish microcalcification types would be a valuable adjunct to histopathology, where the calcium oxalate formations associated with benign lesions - over 20% of microcalcification cases (Ellis *et al.*, 2004) - cannot be seen with histology stains (Shousha, 2003).

X-ray diffraction has historically been used to investigate the structure of matter at the molecular level, in particular, to find the position of atoms in crystals (Hukins, 1981). Similarly, the X-ray diffraction information from semi-crystalline materials and amorphous biological tissues depends on their average intermolecular spacings (Kidane *et al.*, 1999). The differences between healthy and cancer invaded breast tissue on both the structural and molecular levels suggest that X-ray diffraction could be a suitable technique for breast biopsy analysis.

## 1.2 X-ray diffraction as a material-specific modality

### 1.2.1 X-ray interactions in matter

At diagnostic energies (<100keV), the dominant interactions between X-ray photons and matter are photoelectric absorption, coherent (Rayleigh) scattering and incoherent (Compton) scattering. Photoelectric absorption occurs when a photon collides with an atom resulting in the ejection of a bound electron. A traditional X-ray image is formed of X-rays that pass directly through an object without interaction; contrast depends on the differential absorption of X-rays by different tissue types.

Coherent scattering is an elastic scattering process, described in classical terms by the interaction of the electric field of an X-ray beam with the electron charge distribution of a material. The incident photon causes the bound atomic electrons

to oscillate and subsequently emit radiation of the same wavelength as the incident photon. The probability of an unpolarized X-ray photon scattering coherently from a single free electron into solid angle $d\Omega$ is given by the differential Thomson cross section

$$\frac{d\sigma_0}{d\Omega} = \frac{r_0^2}{2}(1 + \cos^2\theta) \quad \mathrm{m^2 sr^{-1}\,per\ e^-} \tag{1.1}$$

where $\theta$ is the scattering angle and $r_0 = 2.82 \times 10^{-15} m$ is the classical electron radius. Coherent scatter from an atom is the superposition of scattered waves from all electrons in the charge distribution, with a linear differential scattering cross section of

$$\frac{d\sigma_{coh}}{d\Omega}(\theta) = \frac{d\sigma_0}{d\Omega} F^2(x, Z) \quad \mathrm{m^2 sr^{-1}\,per\ atom} \tag{1.2}$$

where $F(x, Z)$ is the coherent scatter form factor and Z is the atomic number. $F(x, Z)$ accounts for interference between X-rays scattered from different electrons in a material and is related to the electron charge distribution by Fourier transform (Harding *et al.*, 1987). $x$ is the momentum transferred to the photon, causing it to be scattered by angle $\theta$

$$x = \left(\frac{1}{\lambda}\right) \sin\left(\frac{\theta}{2}\right) \tag{1.3}$$

where $\lambda$ is the photon wavelength. The form factor $F(x, Z)$ is written as a function of $x$ to account for the fact that the structure in scattered intensity due to interference depends on both energy and angle.

Incoherent scattering is the inelastic scattering of an X-ray photon by an atomic electron in which the electron gains kinetic energy. The electrons behave as individual, uncorrelated scattering sites (Speller and Horrocks, 1991) and interactions are considered to occur with outer-shell, essentially free electrons (Boone, 2000). Further to these 'single scattering' events, a uniform background of spatially uncorrelated multiple scatters will also be present.

In practice, it is often difficult to separate scattering contributions from coherent and incoherent sources, thus the total differential linear scattering cross section is often measured (LeClair *et al.*, 2006). At low energies (E$\ll$511keV) this simplifies to

$$\frac{d\sigma_{total}}{d\Omega} = \frac{d\sigma_0}{d\Omega}[F^2(x, Z) + F_{KN} S(x, Z)] \quad \mathrm{m^2\ sr^{-1}} \tag{1.4}$$

where $F_{KN}$ is the Klein-Nishina factor giving the probability of scattering from a free electron and $S(x, Z)$ is the incoherent scattering function. $S(x, Z)$ accounts for the effects of atomic binding on the scattering probability.

Both scattering processes deflect photons from the primary beam, causing degradation of image quality in a standard medical X-ray by adding noise at the imaging receptor. Early studies on the optimization of mammographic systems (Johns and Yaffe, 1983) found that while the coherent scattering cross section is relatively small, it exhibits a highly forward peaked distribution, whereas incoherent and multiple

scatters are approximately uniform. Thus at diagnostic energies and small angles ($< 10°$) from the primary beam, coherent scatter dominates other X-ray interactions despite its smaller cross section. For example, it accounts for 50% of single scatter events at 80keV, rising to 91% at 20keV (Morin and Berroir, 1983).

The structure of coherent scatter intensity was found to be far from uniform (Muntz *et al.*, 1983) due to interference between X-rays that are coherently scattered from electrons in the same atom, molecule, or neighbouring molecules (Johns and Cunningham, 1983). Constructive interference occurs subject to the Bragg condition, $n\lambda = 2d\sin(\theta)$, where $\lambda$ is the photon wavelength, d is the spacing of atomic planes in the material and $\theta$ is the scattering angle. It can be seen by analogy to Equation 1.3 above that the momentum transfer parameter is related to the atomic spacing by $x = 1/2d$ and is therefore a material specific parameter. The pattern of interference peaks in coherently scattered intensity as a function of momentum transfer is referred to as an 'X-ray diffraction profile', or 'scatter signature' and is unique for a given material. The positioning of peaks in this 'signature' reveals the structure of the material, while the peak widths relate to the degree of order of the material; more crystalline substances have narrower peaks (Hukins, 1981).

For a crystalline material with long range order, sharp peaks are visible in the scatter signature over a wide range of momentum transfer values. For amorphous materials and powders, broad concentric circles symmetric about the primary beam are apparent at low angles (Cullity, 2003). For biological tissues, the scatter signature consists of a single, relatively broad peak that occurs at $x < 5nm^{-1}$, followed by a broad, low intensity region that is independent of interference effects and is given by the 'free atom' form factor (Kidane *et al.*, 1999). For a composite material, the scatter signature is a linear superposition of the signatures of its components weighted by their concentrations. X-ray diffraction therefore provides a means to determine both the structure and composition of a material based on the measurement of its scatter signature.

### 1.2.2 Changes to breast tissue caused by cancer invasion and benign abnormalities

A normal adult mammary gland (breast) is composed of stroma (supporting connective tissue), adipose (fatty tissue) and epithelium (glandular tissue) (Moore and Dalley, 1999). The relative proportions of these components depend on numerous factors including age and breast size. The average ratio of adipose to fibroglandular tissue in a nonlactating breast has been estimated anatomically to be 1:1 (Geddes, 2007). The components of the breast are arranged as a series of 10-15 glandular lobules embedded in the adipose and stroma, which are drained by lactiferous (milk) ducts at the nipple. The structure is shown diagrammatically in Figure 1.1.

The majority of diseases of the breast, both malignant and benign, arise in the

Figure 1.1: Illustration of the structure of an adult breast (Larsen, 2002)

glandular epithelium (Millis *et al.*, 1994). Lesions are composed of different proportions of stroma, adipose and epithelium, depending on the type of abnormality. All lesions are characterized by an increase in the proportion of stroma (Fernández *et al.*, 2002) and in turn the volume of collagen, the main structural protein in connective tissue. Any analysis technique capable of evaluating the relative proportion of stroma (or collagen) in a biopsy could thus identify diseased tissue. The potential for distinguishing benign from malignant disease would then relate to other characteristics of the lesion. For example, many breast lesions are also accompanied by microcalcification formation and the composition, size and number of these is highly lesion specific (Tse *et al.*, 2008).

Generally, benign lesions retain some of the normal lobular structure of the breast but are characterized by an increase in the proportion of fibrous and glandular tissue relative to fat. For example, fibroadenoma is a proliferation of stromal and glandular components while fibrocystic change (FCC) is a generalized term relating to fibrosis (a scarring process leading to increased stromal component), adenosis (an increase in the number or size of glandular components) or cyst formation (dilation of ducts by fluid).

Breast carcinoma is an uncontrolled proliferation of epithelial cells that most frequently arises in the terminal ducts of the gland lobules. It does not retain the normal lobular structure of the breast and proliferating epithelial components are randomly arranged (Millis *et al.*, 1994). Two types of breast carcinoma dominate. '*in situ*', which accounts for up to 30% of breast carcinomas, is a proliferation of epithelial cells that have undergone malignant transformation at the site of origin, but are confined by a basement membrane. It has no lymphatics or blood vessels

in the epithelial layer so cannot metastasize. Infiltrating carcinoma takes differing forms, in general displaying varying amounts and compositions of stroma. It may be uniformly distributed, or contain a fibrotic, acellular core with a malignant periphery. Microcalcification formation may occur either around secretory vesicles or in necrotic debris (Tse *et al.*, 2008).

The fact that lesion formation is often accompanied by fibrosis means that while normal breast tissue is predominantly composed of adipose, diseased tissue is predominantly fibroglandular. The relative proportions are generally found to be around 70-80% adipose to 20-30% fibroglandular in normal tissue (Farquharson and Geraki, 2004). The adipose content reduces to around 30% in fibrocystic change, 15-20% in carcinoma and down to almost 0% in fibroadenoma (Haka *et al.*, 2005). This reduction in adipose content can be understood by recognising that some adipocytes (fat cells) can be retained in carcinoma as it infiltrates between them, whereas benign lesions such as fibroadenoma grow by pushing aside the fatty tissue and thus contain almost no adipocytes.

Different length scales can be interrogated using X-ray diffraction techniques. Small angle X-ray scattering (SAXS) is used to study supramolecular length scales of 1-100nm (momentum transfer values of $x$=0.005-0.5nm$^{-1}$) so can be used to investigate changes in collagen type and arrangement (Theodorakou and Farquharson, 2008). It has been shown that differences in the SAXS signatures from normal, benign and malignant tissues can be related to the supramolecular structural order of collagen in the tissues (Fernández *et al.*, 2002). Large angle X-ray scattering (LAXS) studies, accessible with existing clinical radiographic equipment and thus of greatest interest in this study, investigate intermolecular length scales of 0.1-1nm ($x$=0.5-5nm$^{-1}$) and are directly sensitive to changes in the adipose content of tissues. In the following section, a brief summary of the previous studies of biological tissues using X-ray diffraction is made.

### 1.2.3 Previous X-ray diffraction studies of biological tissue

#### Experimental options

As detailed above (Equation 1.3), scatter signatures are usually displayed as a function of momentum transfer to account for their dependence on photon energy and scatter angle. Scatter signatures may be recorded by measuring either

1. The energy dispersion of a polychromatic X-ray source at fixed angle (EDXRD)
   *or*
2. The angular dispersion of a monochromatic source (ADXRD)

Figure 1.2 illustrates how these two techniques can be implemented. For EDXRD, an X-ray source with a broad Bremsstrahlung is coupled with an energy resolving

detector positioned at a fixed angle. For example, a tungsten target X-ray tube may be combined with a photon counting High Purity Germanium (HPGe) detector. The incident X-ray spectrum shown on the left hand side of the figure is collimated to a pencil beam when it arrives at the sample. A further collimator is placed at the energy resolving detector to limit the scattering angle to $\theta_j$. The scatter signature is recorded by the detector as a function of energy.

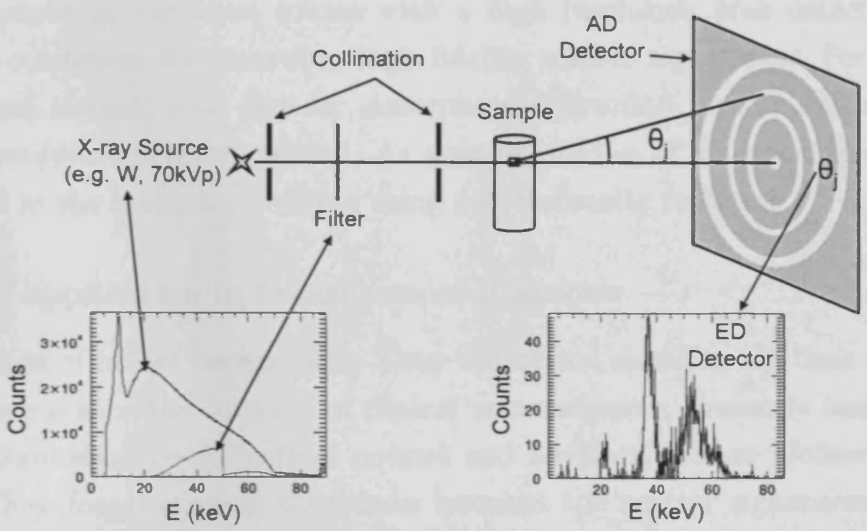


Figure 1.2: Illustration of energy and angle dispersive X-ray diffraction. In the case of EDXRD, the full tungsten spectrum is incident upon the sample and the energy dispersion of scattered X-rays is recorded using an energy resolving detector fixed at $\theta_j$. For ADXRD, the spectral width may be narrowed using filtration or a monochromator, and an area detector is used to record the angular dispersion of scattered photons.

In the case of ADXRD, a monochromatic source of X-rays such as a synchrotron is required. A standard laboratory X-ray tube can be used provided it is filtered to create a quasi-monochromatic beam. For example, in a diffractometer, a photon counting crystal is mounted on a goniometer that rotates about a sample holder and the monochromatic X-ray source is typically formed using a copper target with nickel filtration, leaving only Cu-K$\alpha$ characteristic X-rays. Diffractometers are well established 'gold standard' instruments for structure determination. Another option is to create a 'pink' beam with a somewhat broader spectral width, like the second spectrum shown on the left of Figure 1.2. Although this decreases the angular resolution of the profiles, higher incident intensities are available.

The choice of experimental technique is largely determined by the required momentum transfer resolution, which for coherent scattering at small angles ($< 10°$) is given by (Harding and Schreiber, 1999)

$$\left(\frac{\Delta x}{x}\right)^2 = \left(\frac{\Delta E}{E}\right)^2 + \left(\frac{\Delta \theta}{\theta}\right)^2 \tag{1.5}$$

In the energy dispersive case, $(\Delta E/E)$ is dominated by the detector energy resolution, which for HPGe is <1% at 60keV. $(\Delta\theta/\theta)$ is more limiting as it depends on the design and machining of the collimator arrangement used to select the angle of interest. In the angle dispersive case, $(\Delta E/E)$ is dominated by the X-ray source employed so is minimized by using monochromatic radiation. $(\Delta\theta/\theta)$ depends on the resolution of the area detector and is usually negligible.

A synchrotron radiation source with a high resolution area detector provide the ideal conditions for recording high fidelity scatter signatures. For the study of biological tissues, with broader, amorphous diffraction peaks, high momentum transfer resolution is rarely needed. As a result, studies of biological tissue may be performed in the laboratory setting using polychromatic radiation.

### Potential application in breast cancer diagnosis

Early studies of breast tissues using X-ray diffraction aimed to use their scatter signatures to enhance the contrast of clinical mammograms, presently limited by the similar attenuation coefficients of normal and neoplastic tissue (Johns and Yaffe, 1987). They found striking differences between the scatter signatures of normal breast tissue and carcinoma in terms of peak position, height and full width at half maximum (FWHM) (Evans *et al.*, 1991). A landmark study by Kidane *et al.* (1999) investigated 100 breast tissue samples covering a range of pathologies. They found that adipose tissue exhibits a relatively sharp maximum at $1.1\text{nm}^{-1}$, while fibroglandular and diseased tissues exhibit a broader peak at higher momentum transfer values, with carcinoma peaking at $1.6\text{nm}^{-1}$. There was little distinction between different types of benign and malignant tissue, but diseased and healthy tissues could be distinguished by their fat content. Table 1.2 summarises the previous X-ray diffraction studies of breast tissue and indicates the use of energy and angle dispersive techniques is fairly balanced.

It has also been demonstrated that information obtained with X-ray diffraction correlates well with pathological analysis (Griffiths *et al.*, 2007; Kidane *et al.*, 1999). The effective d-spacings of the main breast tissue types have been evaluated as 0.33nm for carcinoma, 0.36nm for fibrocystic changes, 0.46nm for adipose and 0.4nm for fibroglandular tissue (Changizi *et al.*, 2005), revealing that cancer invasion produces a measurable change in the molecular structure of the tissue. The most recent X-ray diffraction studies of breast tissue have focused on the practicalities of clinical application including producing 'images' based on diffraction information and selecting an appropriate method for quantifying the composition of a sample.

For X-ray diffraction to enhance the contrast in mammography, a 2D image is needed rather than a 1D scatter signature. Planar X-ray diffraction images are obtained by raster scanning a sample slice through a pencil beam. The acquired 3D data set contains the directions of the 2D raster scan in the first two dimensions and

Table 1.2: X-ray diffraction studies of breast tissue listed in chronological order. Key: MWPC=multiwire proportional counter, NaI=sodium iodide proportional counter, CCD=charge coupled device, CZT=cadmium zinc telluride, XRF = X-ray Fluorescence.

| Reference | X-ray Source | Detector | Materials measured | Comments |
|---|---|---|---|---|
| Evans *et al.* (1991) | Cu (60kVp, Cu 0.5mm) | MWPC | Olive oil, PMMA, $H_2O$, blood, breast tissues | Peak position, FWHM and peak height distinguish tissue types |
| Peplow and Verghese (1998) | Synchrotron (20keV) | NaI | Tissue substitute materials and fixed breast tissue | Tabulate coherent scatter form factors ($x$=0.14 to $x$=13nm$^{-1}$) |
| Kidane *et al.* (1999) | W (80kVp, Al, Be 2.5,2mm) | HPGe at 6° | Normal and neoplastic (malignant and benign) breast tissues | Use peak shape and height to classify breast tissues |
| Fernández *et al.* (2004) | Synchrotron (12.5keV) | Frelon CCD | Normal and neoplastic (malignant) breast tissues | Supramolecular collagen structure differs between tumour and healthy tissue |
| Changizi *et al.* (2005) | W (60kVp) | HPGe at 6.5° | Normal and neoplastic (malignant and benign) breast tissues | Show significant ($p< 0.001$) differences between peak positions of breast tissues |
| James (2006) | Synchrotron | Film | Hair from breast cancer patients | Suggest cancer changes collagen structure in hair |
| LeClair *et al.* (2006) | W (50kVp) | CZT at 6-15° | Normal and neoplastic (malignant) breast tissues | Extract coherent scattering cross section from EDXRD using model |
| Ryan and Farquharson (2007) | W (80kVp) | HPGe at 7.5° | Normal and neoplastic (malignant and benign) breast tissues | Perform multivariate analysis (SIMCA) to classify tissues |
| Griffiths *et al.* (2007) | W (70kVp, 1mm Al) | HPGe at 6° | Normal and neoplastic (malignant) breast tissues | Identify potential error of $< 1\%$ for diffraction based biopsy analysis |

momentum transfer in the third. Material specific images are obtained by selecting different momentum transfer 'planes'. Griffiths *et al.* (2003) demonstrated that the image contrast obtained from X-ray diffraction images is approximately double that for a conventional transmission image. Other authors have extended this planar scan to perform computed tomography using both pencil beam (Harding *et al.*, 1987; Westmore *et al.*, 1997) and fan beam (Schlomka *et al.*, 2003) geometries.

Quantification of sample content based solely on information from scatter signatures requires a multivariate approach to include information from multiple momentum transfer values. Multivariate analysis (MVA) is a statistical technique that can be applied to complex systems where many variables influence the measurement of a sample. Exploratory data analysis uses Principle Components Analysis (PCA) to look at relationships within a given set of samples and variables. Round *et al.* (2005) showed that it was possible to correlate breast tissue samples into 'tumour' and 'normal' tissue groups using PCA. Ryan and Farquharson (2007) use a number of classification models to distinguish between multiple tissue types. Their best model showed 54% sensitivity and 100% specificity but results were limited by the poor statistical quality of the recorded scatter signatures used for modelling. Future investigations will be need to establish the number of calibration samples and data corrections required to build a robust multivariate analysis model.

### Other applications

Table 1.3 illustrates that the earliest studies of coherent scatter in medicine focused on characterizing the scatter signatures of biological tissues to identify potential applications. Aside from breast tissue analysis, Elshemey *et al.* (2003) have demonstrated that it is possible to differentiate normal, cirrhotic and cancerous liver from the scatter signatures of lyophilized blood. Other applications include evaluation of bone mineral density (BMD) and identification of kidney stone types.

The composition of normal bone is 43% mineral phase (mostly bone mineral), 32% organic matrix (mostly collagen), and 25% water (Nyman *et al.*, 2005). Bone diseases such as osteoporosis are characterized by reduced bone mass and microarchitectural deterioration of bone tissue leading to bone fragility (Kanis and Glüer, 2000). Bone mineral content is often used to establish bone health as it provides a quantitative estimate of the amount of mineralised bone tissue per unit volume. As trabecular bone mineral content declines, it is replaced by adipose tissue. X-ray scattering measurements of bone can be correlated with the ratio of adipose tissue to bone mineral (Newton *et al.*, 1992). Royle *et al.* (1999) found that the scatter signatures of dry bone from an osteoporosis study and bone from excised femoral heads could accurately estimate bone mineral content using multivariate analysis when compared to 'gold standard' techniques.

For some kidney stones, composition is a key indicator of pathophysiology and

Table 1.3: X-ray diffraction studies for other applications. Key: XRII=X-ray Image Intensifier, GSO=Gadolinium Silicate, PMT=Photomultiplier Tube.

| Application | Reference | X-ray Source | Detector | Materials measured | Comments |
|---|---|---|---|---|---|
| Tissue/plastics characterization | Kosanetzky *et al.* (1987) | Diffractometer (6.9keV) | Scintillation detector | $H_2O$, numerous plastics and tissues | First basis for selecting application areas of X-ray diffraction |
| | Harding *et al.* (1987) | Diffractometer (6.9keV) | Scintillation detector | As Kosanetzky | Image slices of materials and phantoms using X-ray diffraction CT |
| Kidney stone identification | Dawson *et al.* (1996) | W (70kVp) | HPGe at 6° | Intact kidney stones classified by type | Show it is possible to distinguish oxalate from other types using LAXS |
| | Davidson *et al.* (2005) | W (70kV, 0.4mm Gd) | CCD+XRII | Various plastics, KS materials (pure+intact) | Use diffractometer (8keV) to verify results from polychromatic system |
| | Ancharov *et al.* (2007) | Synchrotron (3.7keV) | Image Plate | Intact kidney stones classified by type | Demonstrate possibility of *in vivo* kidney stone studies |
| Assessing bone mineral density | Newton *et al.* (1992) | Diffractometer (8keV) | Kodak film | Bone (cortical, trabecular), adipose tissue | Use adipose:mineral ratio in bone scatter signatures to identify disease |
| | Royle and Speller (1995) | W (70kV, 1mm Al) | HPGe at 6° | Fresh, dried and encased femoral heads | Correlate ratio of bone and marrow peak intensities with bone tissue present; compare to 'gold standard' methods |
| | Westmore; Batchelar 1996;2006 | W (70kV, 0.4mm Gd) | CCD+XRII | Various plastics and bone equivalent materials | Assess data corrections needed for measurements of bone density in $gcm^{-2}$ |
| | Schlomka *et al.* (2003) | W (150kV, 1.8mm Al, 0.5mm Cu) | GSO+PMT | $H_2O$ filled PMMA cylinder; inserts of bone materials | Fan beam X-ray diffraction CT with filtered back-projection |

a determinant of treatment success. The prevalence of kidney stones has doubled in the past two decades and the lifetime risk is around 15% in the developed world (Moe, 2006). In spite of this high incidence rate, techniques for stone composition and structure analysis are limited. The preferred noninvasive treatment modality is shock wave lithotripsy (SWL), but stone fragmentation is limited for calcium oxalate monohydrate, calcium phosphate dihydrate and cystine stones (Madaan and Joyce, 2007). A nondestructive *in vivo* technique capable of evaluating kidney stone composition would therefore prove useful. Davidson *et al.* (2005) have shown that the most common kidney stone components can be characterized through laboratory-based X-ray diffraction studies. They have also shown that the method is able to identify structure and composition in mixed stones, a promising result (Davidson *et al.*, 2006).

### 1.2.4 Instrumentation requirements for a breast biopsy analysis system

X-ray diffraction is a notoriously demanding application for instrumentation. Most experiments using breast tissue have been carried out with synchrotron radiation sources, or with laboratory-based energy dispersive systems. Experiments using synchrotron radiation cannot be employed for widespread for clinical work due to the lack of available sources. Photon counting High Purity Germanium (HPGe) detectors are used most frequently to achieve high energy resolution in energy dispersive systems (Knoll, 2000), but they require cooling to liquid nitrogen temperatures so often require a bulky cryostat making them less suitable for clinical application.

Alternative detector materials for EDXRD include Cadmium Zinc Telluride (CZT) (LeClair *et al.*, 2006) and silicon. CZT does not need cooling, can achieve adequate energy resolution of 5% at 60keV (Malden and Speller, 2000) and has good detection efficiency at up to 150keV. However, it can distort measured spectra due to trapping of holes during charge transport (LeClair *et al.*, 2006) so further technological development is needed before it will be suitable for EDXRD. Controlled drift detectors (CDD) using silicon for X-ray detection have recently been developed for X-ray diffraction studies (Pani *et al.*, 2007) and provide both energy (4% at 13.9keV) and position (180$\mu$m pixels) resolution (Castoldi *et al.*, 2007). However, they are currently limited in area, have high leakage current and exhibit relatively poor detection efficiency for energies greater than 20keV due to the inherent detection efficiency of silicon.

Limitations in EDXRD detectors imply that a breast biopsy analysis system would need to be based around ADXRD with a standard clinical X-ray source. A suitable angle dispersive X-ray diffraction detector must then be sought. The major drivers of detector development for X-ray diffraction are synchrotron radiation sources as they perform a multitude of diffraction studies for users ranging from

Table 1.4: Ability of available X-ray diffraction detectors to meet application requirements (Lewis, 2003; Brügemann and Gerndt, 2004). ✓= device can already meet, □ = device will be able to meet with future developments, ✗ = device cannot meet due to fundamental limitations, - = requirement not relevant. The CCD is assumed to be coupled with an XRII; the APS is assumed to be scintillator coupled.

| Requirements | IP | MWPC | CCD | PAD | APS |
|---|---|---|---|---|---|
| Large area ( 40x40$cm^2$) | ✓ | □ | ✓ | □ | ✓ |
| High spatial resolution (< 250$\mu$m) | ✓ | ✓ | ✓ | □ | ✓ |
| Low noise | ✓ | ✓ | ✓ | □ | ✓ |
| High dynamic range (over 120dB) | ✓ | ✓ | □ | ✓ | ✓ |
| Linearity | ✓ | ✓ | ✓ | ✓ | □ |
| Fast digital readout O($\mu$s) | ✗ | - | ✗ | ✓ | ✓ |
| High frame rate (over $10^5$fps) | ✗ | - | ✗ | - | □ |
| High quantum efficiency | ✓ | ✓ | □ | ✓ | □ |
| Spatial and spectral information | ✗ | ✓ | ✗ | □ | ✗ |

materials science through to molecular biologists.

The 1991 European Workshop on X-ray detectors detailed the ideal specification of a synchrotron X-ray diffraction detector. Large area (> 40x40$cm^2$) would be required to visualise the entire scatter signature and must be combined with small pixel sizes (250x250$\mu m^2$) so that diffraction peaks are sampled with sufficient resolution. Wide dynamic range (>120dB) is needed so that both intense and weak reflections can be recorded simultaneously. A further requirement is good linearity across the dynamic range to ensure that relative peak intensities are not skewed by nonlinearity of the detector response. High frame rates (> $10^5$fps) are required for studies of phenomenon such as phase transitions, where X-ray diffraction allows the onset of the transition to be viewed. Energy sensitivity up to 35keV provides complete knowledge of the X-ray diffraction properties of the material as both energy and angle dispersion are then available. Future requirements identified in a review of diffraction detectors by Brügemann and Gerndt (2004) indicate that many of these specifications have yet to be realised (Lewis, 2003).

For a clinical system, the frame rate requirement can be relaxed, but low cost, along with ease of calibration and maintenance, are important. The similar scatter intensities from different tissues means that the dynamic range requirement could be relaxed, although the ability to simultaneously record the transmitted X-ray beam and the scatter signature from a particular tissue sample enables automatic angular calibration using the beam centre and raises the possibility of combining diffraction and transmission imaging, or using the transmission data to implement an online attenuation correction of the scatter signature. It would therefore be advantageous to achieve at least an 80dB dynamic range to record both of these. The available instrumentation for ADXRD is assessed below. A comparison of the various detector technologies and the demands of X-ray diffraction studies is shown in Table 1.4.

### Current X-ray diffraction detectors

Early diffraction studies were made with analogue imaging receptors such as film and image plates. Film offers a high spatial resolution but has a limited dynamic range of around 40dB and requires digitization for quantitative analysis. Image plates offer large area (>30cmx30cm), wide dynamic range (up to 120dB) and good spatial resolution (Amemiya, 1995) but require a mechanical exchange of plates between images and offline readout (Mezouar *et al.*, 2005). Analogue receptors are thus limited by the need for offline processing.

X-ray diffraction imaging receptors with digital readout fall into two categories: photon counting, and integrating. A photon counting detector registers the charge packet from each incident X-ray photon individually using self-triggering electronics. An integrating detector sums all of the charge that is generated by incident X-ray photons during a set exposure period.

Photon counting detectors include multi-wire proportional counters (MWPCs) and scintillation crystals (read out via photomultiplier tubes or other photon counting detectors). Despite recent developments in MWPCs yielding micron resolution over an area of $100cm^2$ and very high dynamic range (Takeda *et al.*, 2005), they are highly complex, sensitive instruments so their uptake in diffraction applications has been limited (Ortũno Prados *et al.*, 1997; Masson *et al.*, 2005). Sodium iodide is the main scintillation crystal employed in diffractometers but this arrangement has recently been shown to be unsuitable for measuring amorphous samples as it is difficult to correct for all systematic errors and record a clean profile (Johns and Wismayer, 2004). It is estimated that an accuracy of no better than 20% is possible.

The charge coupled device (CCD) is the dominant integrating detector in X-ray diffraction. It is a pixellated silicon detector fabricated on specialised metal oxide semiconductor (MOS) lines. 'Charge coupling' refers to the process of moving optically induced signal charge from one storage site to the next through a series of MOS capacitors (Janesick, 2001). The CCD exhibits low noise and dark current (when peltier cooled) as well as good system gain and linearity (Tate *et al.*, 2005; Ito *et al.*, 2007). Serial readout via a single output node limits the available frame rate and results in sensitivity to radiation damage defects (Gruner, 2002). The device area is limited to $2.5x2.5cm^2$ (Nagarkar *et al.*, 2006) meaning that demagnifying optics, or array tiling are needed to achieve large area.

A standard CCD is only sensitive to optical illumination. Two options exist for X-ray detection with the CCD: it can be coupled to an X-ray converter, e.g. scintillator or X-ray Image Intensifier (XRII), or fabricated using deep depletion technology. An XRII is frequently used to create a large area imaging receptor and provide both signal gain and magnification. The XRII does, however, introduce artifacts such as geometric distortions, temporal lag and shading (Yagi *et al.*, 2004). It is also possible to produce CCDs that utilize deep depletion regions to enable

direct detection of X-ray photons in the silicon. These provide a quantum efficiency of around 30% at 8keV (Livet *et al.*, 2000) and provide position sensitive photon counting. Unfortunately, they cannot detect hard X-rays and are more sensitive to radiation damage than a standard CCD (Gruner, 2002).

### Recent developments

CCDs are widely accepted as the 'gold standard' solid state imaging sensor in many applications. Their limitations have come to the fore in the past few years, as demand for high frame rate, large area devices has risen. A number of new solid state detectors have recently emerged as competitors to the CCD, particularly in X-ray diffraction studies where they are beginning to bridge the gap between application requirements and actual performance. The Pixel Array Detector (PAD) and the CMOS Active Pixel Sensor (APS) both have the potential to challenge the supremacy of the CCD in the near future.

The pixel array detector (PAD) is a pixellated semiconductor layer that directly converts X-rays into charge carriers, coupled to a pixellated electronics layer, which processes the generated carriers. The charge carriers drift from the sensor to the electronics via bump bonds. This design provides good noise performance and time resolution, along with good dynamic range and on-chip frame storage (Rossi *et al.*, 1999). It also offers flexibility as materials other than silicon can be exploited as the semiconductor layer (Sellin *et al.*, 2001).

A number of issues still need to be resolved before the PAD can be utilized on a large scale. Firstly, packaging and device yield issues must be overcome for the device to be fabricated in large area; it is currently limited to 1.4x1.4cm$^2$ (de Vries *et al.*, 2007) and tiling is used to reach larger areas. Secondly, careful calibration of the electronics is required (Ponchut and Zontone, 2003). Radiation damage has been shown to occur in both the short and long term in the electronics and semiconductor layers respectively. Finally, and perhaps most severely limiting, is the charge diffusion that occurs in the sensor when small pixel sizes are fabricated (Medipix, 2006). Early PADs had very large pixel sizes, of the order of 100s$\mu$m (Boudet *et al.*, 2003). Only recently have they managed to obtain pixels of the order of 10s$\mu$m (de Vries *et al.*, 2007). Prototypes are now being developed that use thresholding and charge summing to overcome the charge diffusion issue (Ballabriga *et al.*, 2007).

The CMOS Active Pixel Sensor (APS), is a relatively old technology compared with the PAD. It was originally conceived by Noble (1968), who implemented the first silicon array with an active buffer transistor per pixel. As its name suggests, the APS is a detector with 'active' buffering and/or amplification in each pixel. The first modern APS was produced by Yadid-Pecht *et al.* (1991).

As Active Pixel Sensors are made on standard Complementary MOS (CMOS) fabrication lines, analogue and digital electronics can easily be included on-chip. It

also confers the advantages of low voltage operation, leading to low power consumption, and low cost of manufacture. The per-pixel charge detection and amplification enable direct signal buffering and random access readout. Electronics can also be integrated for timing and control, or for more advanced applications such as on-pixel analogue-to-digital conversion (ADC). This high level of integration makes CMOS APS the preferred technology for 'camera-on-a-chip' imaging applications (Fossum, 1997).

Including extra transistors in each pixel inevitably added noise and reduced quantum efficiency, limiting the early application of the APS. As CMOS technology has advanced, however, the performance of the APS has improved vastly and it now dominates unit sales in the consumer imaging market according to the 2007 In-Stat review of image sensors. APS designs can now reach noise levels of less than $50e^-$ r.m.s. (Pain *et al.*, 2003), have quantum efficiency similar to the CCD, dynamic range of over 100dB (Yadid-Pecht, 1999) and can be produced in areas up to CMOS wafer scale (currently over 12cm x 12cm) (Scheffer, 2007). Although these advances have yet to be combined in a single device, further design developments and the scaling of CMOS technology means that they are likely to be available in the very near future.

Commercial APS have been demonstrated in SAXS synchrotron experiments in the last few years. Ponchut (2001) made the first demonstration using a small area APS coupled to an XRII but this device suffered from high fixed pattern noise and dark current. Yagi *et al.* (2004) used large area (up to 11.2cm x11.8cm) scintillator-coupled APSs from Hamamatsu and RadIcon for powder diffraction, but these lack flexibility for scientific imaging and have a high read noise. A better solution lies in exploiting on-chip and in-pixel electronics to create a high specification device to satisfy all of the requirements of X-ray diffraction imaging.

### Summary of available detectors and requirements for a clinical system

To summarise, the requirements for an X-ray diffraction detector that could be included in a clinical breast biopsy analysis system are:

- Large area: at least $16\text{cm}^2$ with $50\mu$m pixels
- Low readout noise: at most $50e^-$ r.m.s.
- Good conversion gain: at most $50e^-$ per digital number output from the sensor ADC (i.e. $50e^-$/DN)
- High dynamic range: at least 80dB to simultaneously measure primary and scattered photons simultaneously
- Linearity: within 5% across dynamic range

- Quantum efficiency as high as possible
- Low cost and ease of maintenance

Given the current status of the technology, the CCD and APS would provide similar performance for breast biopsy analysis with X-ray diffraction. However, the CCD is a mature technology close to its fundamental limits, while the APS is still developing at a rapid pace and has the potential to outperform the CCD in the near future. For this reason, the APS will be investigated further and a detailed review of the current status of the technology is presented in the next section.

## 1.3 CMOS Active Pixel Sensors for X-ray Diffraction

### 1.3.1 What are Active Pixel Sensors?

The most simple CMOS Active Pixel Sensor (hereon referred to as Active Pixel Sensor, or 'APS') contains a photodiode, usually of n-well/p-substrate type, and three transistors ('3-T') per pixel as shown in Figure 1.3 (a). The reset transistor clears the pixel of integrated charge. The source follower transistor is the input transistor of a source follower; a simple amplifier. The sense node capacitance converts electrons from the photodiode into a voltage that is isolated from the large column bus capacitance and buffered by the source follower (El Gamal and Eltoukhy, 2005). The row select transistor 'activates' the pixel for readout and presents its voltage to the column bus. Each pixel responds as an individual detector element, the operation of which can be separated into three phases: reset, integration and readout.

#### Reset

Reset refers to the operation of clearing the APS photodiode of integrated charge and recharging it to a fixed reference level. Two reset types are available as standard in an APS: soft and hard. The reset is termed 'soft' when the gate-to-drain voltage of the NMOS reset transistor is less than the threshold voltage of the transistor. In this mode, the reset transistor never reaches thermal equilibrium, and the reset level is determined by the initial voltage on the diode and the reset time. Soft reset is therefore susceptible to image lag, where the reset is incomplete and some portion of the signal charge from the previous integration period remains. The reset is termed 'hard' if the gate-to-drain voltage on the reset transistor exceeds its threshold voltage, yielding steady state operation. In this case, image lag is insignificant and greater linearity is achieved, but the noise associated with the reset operation is increased by a factor of $\sqrt{2}$.

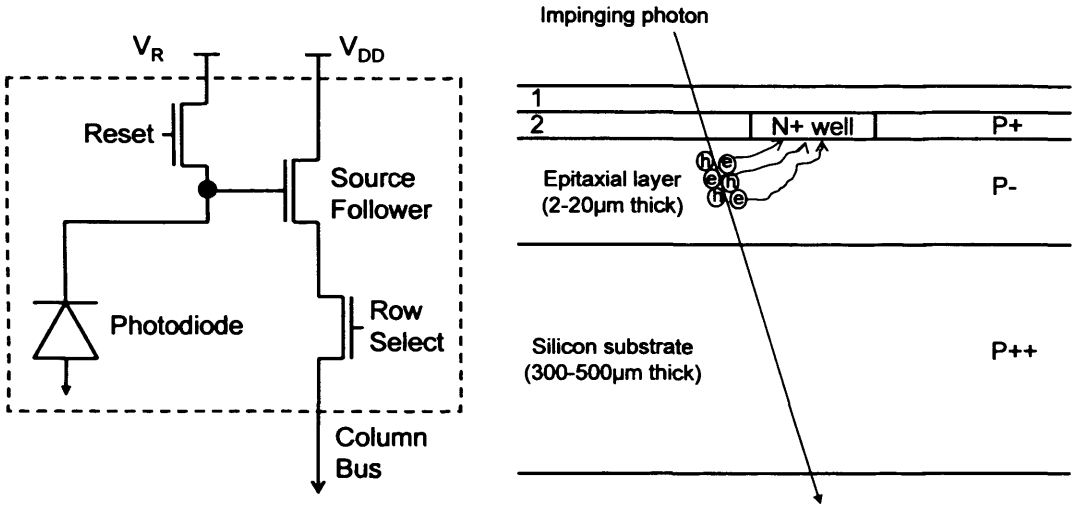


(a) APS pixel layout

(b) Cross section

Figure 1.3: Active Pixel Sensor '3-T' pixel (a) illustrates the arrangement of the reset, source follower and row select transistors in the pixel, while (b) shows a cross-sectional view of the CMOS process layers. Layer 1 is a passivation layer for insulation, usually composed of a series of silicon nitrides and dioxides. Layer 2 is a further silicon dioxide layer containing electronics and metal interconnects. The epitaxial layer is the sensitive volume, while the substrate provides mechanical support.

### Integration

In the next phase of operation, the reset switch is opened and charge is integrated over the photodiode capacitance until the end of a set integration period. Photons incident upon the sensor may interact in the thin epitaxial layer as shown in Figure 1.3 (b), which is lightly doped compared to the substrate. The detecting element, the photodiode, is the p-n junction between the n-well and the p-epilayer. The potential difference across the epilayer acts as a shallow potential well for electrons, which diffuse until they experience the electric field of the n-well/p-epi photodiode and are collected (Turchetta *et al.*, 2003). As the photodiode is reverse biased by the reset operation, the accumulation of charge on the photodiode results in a reduction of the voltage across it.

The 'quantum efficiency' (QE) of the APS is limited by charge generation and collection. Charge generation refers to the ability of the image sensor to detect incoming photons. Photons that reach the epitaxial layer must pass through the 'stack' of metal and polysilicon layers that exist above the sensor (see Figure 1.3 (b)). Reflection losses arise at the boundaries between these layers of dielectric materials. In addition, metal bus lines and interconnects are optically opaque and reduce the sensitive area of the pixel. The resulting 'fill factor' of the pixel is less than 100%. Finally, transmission losses occur when incident photons penetrate the epitaxial layer without interaction.

Charge collection depends on the diffusion of electrons through the epitaxial layer

and the maximum number of charges that can be accumulated in the n-well (the full well capacity). In APS arrays, it is limited by 'crosstalk': the thermal diffusion of signal electrons from the site of generation to neighbouring pixels. Standard CMOS technology uses low resistivity wafers, making the APS more susceptible to crosstalk than the CCD (Janesick and Putnam, 2003). The full well capacity depends on the photodiode capacitance so can be tailored; it is typically around $10^5 e^-$.

#### Readout

The row select transistor activates the in-pixel amplifier to present the signal voltage to the column bus. As APS pixels are directly addressable, signal charge is collected and read from the same region so there is no charge transfer signal loss. A typical APS is read through a 'rolling shutter' mechanism, whereby rows are sequentially read, then reset. In this manner, the integration period is defined by turning the reset switch off for a given number of lines before the readout operation is due. From the column bus, the signal is passed through column parallel amplifiers and analogue-to-digital converters before the digital output is passed off chip (Fossum, 1997). The readout path contains several active devices which may add noise to the final image. This will be discussed further in Chapter 2.

### 1.3.2 Drivers of development

The development of new APS designs has been driven largely by commercial and industrial demands in the last two decades. One of the current challenges for APS designers is to maintain performance as CMOS technology scales. CMOS processes downsize by 0.7 of the minimum feature size every three years (Wong, 1996), driven by the microelectronics industry. Fabrication of image sensors in standard CMOS processes will only continue to be possible provided that downsizing does not affect their performance.

The most common CMOS process for image sensor production is currently $0.35\mu$m, with $0.25\mu$m and $0.18\mu$m increasing in frequency. While smaller pixel sizes, or higher fill factors, are available with smaller processes, a loss of spectral sensitivity, reduced analogue voltage swing, increased leakage currents and decreased dynamic range are also apparent (Lulé, 2000; Wong, 1996). Increased absorption and reflection losses also occur due to the use of silicides in processes below $0.35\mu$m and the increased number of routing levels used. As a result, it will become increasingly necessary to use specialised processes below $0.25\mu$m to maintain performance, or produce new sensor architectures to overcome limitations.

As scientific applications of CMOS APS become more frequent, further demands will be placed on APS performance, leading to bespoke designs for different users. While sensor designers naturally strive for 'smaller, faster, cheaper', the key areas of

development in recent years have been dynamic range extension, intelligent imaging, high speed readout and increased sensor area.

### Dynamic Range

Dynamic range is the ratio of the sensor full well capacity (FW) to the read noise floor ($\sigma_R$) and describes the range of illumination intensities that can be represented in a single image. It is usually given in decibels as

$$DR = 20\log\left(\frac{FW}{\sigma_R}\right) \tag{1.6}$$

The dynamic range of Active Pixel Sensors is typically in the range of 65-75dB (Yadid-Pecht, 1999), while the dynamic range of a typical natural scene is 120dB (Acosta-Serafini *et al.*, 2004). Many methods of increasing APS DR have been tested; the most successful use logarithmic pixels, individual pixel reset, multiple sampling, or 'time-to-first-spike' asynchronous readout.

Logarithmic pixels use the exponential sub-threshold characteristics of a MOS transistor connected to the photodiode (Fossum, 1997) to achieve up to 170dB of DR (Burghartz *et al.*, 2006). Such sensors are popular in industrial and commercial applications, including factory automation and automotive cameras. Large fixed pattern noise and poor signal-to-noise ratio compared to linear integrating sensors prevents their application in scientific work.

'Individual pixel reset' (IPR) architectures (Yadid-Pecht *et al.*, 1997) compare the voltage in each pixel to a saturation threshold at various time increments during the integration phase. If the saturation level is passed, the pixel is reset; the number of resets performed and the final signal level are stored in each pixel. DR of 13 bits (78dB) has been achieved, compared to 11 bits (66dB) in standard operation (Yadid-Pecht and Belenky, 2003). Such designs can only be used in static imaging applications, as their automatic adjustments will fail in a changing scene.

Multiple sampling uses a combination of exposures to synthesise a wide DR image. Long exposures capture the darker areas of a scene, while shorter exposures capture brighter areas without saturating. Liu and El Gamal (2003) sample the pixel signal multiple times within a single exposure, using photocurrent estimation and saturation detection algorithms to enhance DR by 30dB at the high end and 8dB at the low end of the 47dB single capture DR. A sensor with 132dB DR was presented by Stoppa *et al.* (2002), where the sensor adapts its overall integration time to the local illumination conditions during three 8-bit linear ramps. The bandwidth needed to readout multiple frames per scene and the extra in-pixel electronics needed to implement multiple sampling circuits mean further developments in data acquisition and CMOS technology are needed to make multiple sampling devices viable.

'Time-to-first-spike' imaging sensors create one pulse event per pixel per frame

representing the incident illuminance when the photodiode voltage drops below a global threshold, rather than integrating the signal. A digital counter records the time when the pulse is created, and the pixel address is output. The dynamic range is simply given by the ratio of the longest and shortest firing times, limited only by dark current at the high end, and start of the reference voltage ramp at the low end. By varying the threshold voltage, 104dB dynamic range has been achieved (Guo *et al.*, 2007).

A multitude of wide dynamic range CMOS sensors have been produced in the last 5 years. The best method for achieving wide dynamic range depends on the demands of the application e.g. static vs video rate imaging, noise restrictions and bandwidth availability.

### Intelligent processing

The advent of sensors with a 'digital pixel' architecture (DPS) in the late 1990s led to a flood of CMOS pixels with advanced processing and electronics in-pixel. A DPS performs analogue-to-digital conversion (ADC) at the pixel level, providing a fully digital interface. The main advantages conferred by the DPS architecture are low power consumption, high conversion speeds (DuBois *et al.*, 2008) and very high readout rates (Kleinfelder *et al.*, 2001).

A popular use of digital pixel technology is to detect temporal changes in a scene. A spatio-temporal image of a moving object can be acquired using a digital pixel sensor that contains in-pixel memory as it can record both position and 'time-to-threshold' information. Chi *et al.* (2007) present a novel circuit for deriving object velocity. They compare the photocurrent integrated in two consecutive frames to a 'rejection band': a change above this flags a '1' in a 1-bit pixel memory; a change below flags a '0'. This design enables both the speed and direction of the motion to be evaluated using the frame rate and post-processing of the binary image. Another method for achieving this is to implement an array of self-resetting, asynchronous pixels that provide adaptive timing and spatial resolution (Bermak and Yung, 2006). In addition to standard imaging capabilities, 'time-to-threshold' information is triggered when the photodiode voltage crosses an external threshold and this time stamp stored in-pixel using an 8-bit memory.

As CMOS feature sizes down scale, it may be possible to balance the increasing demand for in-pixel processing with the loss of fill factor from the extra in-pixel transistors (El Gamal and Eltoukhy, 2005). As an alternative, DuBois *et al.* (2008) show that it is possible to exploit analogue in-pixel processing elements at high frame rates by redesigning the standard APS layout. They centre an analogue processing element between a group of four adjacent octagonal pixels, which in 0.35$\mu$m technology reaches a fill factor of 25%. Each processing element can be reprogrammed depending on the desired task, and a 93% correspondence was demonstrated be-

tween in-pixel and off-chip implementations of Sobel and Laplacian operators for edge detection.

### High speed readout

Digital pixel sensor technology already provides access to readout rates of up to $10^5$fps. The main limitation to high speed readout is not the sensors themselves, but the data transfer and storage issues that arise from such high frame rates. For example, a 1Mpixel sensor with 12-bit quantization produces a 2Mb frame. If it were read at $10^5$fps, this equates to 200Gb/s data transfer rate, far exceeding the maximum available using the Camera Link standard of 0.3Gb/s (CameraLink, 2004). Until readout options with larger bandwidth and data transfer rates are available, other alternatives for achieving high frames rates must be sought.

Two of the fastest megapixel sensors on the market include random-access memory on-chip to store frames and use the inherent random access readout to implement windowing (June 2008). Photron's Ultima APX-RS can read 3000fps in full frame mode, or a 128x16 pixel region of interest (ROI) at $2.5\text{x}10^5$fps (Photron, 2008). The Phantom v12 from Vision Research has 32Gb of on-board RAM so can run at over $6\text{x}10^3$fps in full frame mode, or up to $10^6$fps for a 128x8 ROI (Vision Research, 2008). Such commercial designs frequently suffer high read noise and lack customizable options making them unsuitable for scientific applications.

Adaptive multi-resolution circuits that locate and track objects using regions of interest 'on-the-fly' could become a popular high speed solution for scientific applications. A dynamically reconfigurable vision sensor (DRVS) was proposed by Pain *et al.* (2002) to image multiple regions of interest with variable resolution. Up to three partially overlapping regions of interest can be used for object tracking. Sugiyama *et al.* (2005) uses on-chip profile acquiring circuits combined with 3 photodiodes per pixel arranged in an 'L' shape to detect a moving object and follow it using an adaptive region of interest. Further, Choi *et al.* (2007) uses adaptive imaging to suppress motion blur by reading the sensor in reduced resolution mode at over 960fps when motion is detected. These implementations of windowing are limited by a variety of factors including large window size, high read noise, low sensitivity and low full frame rate. The field of high speed readout is thus still an area of development, awaiting vast increases in data transfer speeds.

### Large area

The traditional demands on APS area are for down- rather than upscaling; mobile phone camera applications require small, low power, low cost devices. The advent of 'stitching' technology brought the ability to seamlessly scale CMOS sensors up to full wafer size ($12\text{x}12\text{cm}^2$). This generated interest from radiologists whose conventional large area solid state detectors have large pixels, high noise and low frame rates.

Hamamatsu and Rad-icon Imaging Corp. were quick to acknowledge this interest, working on large area Active Pixel Sensor flat panel imagers (APFPI, referring to scintillator coupled devices) as early as 1997. Their sensors have been successfully demonstrated in digital radiography and industrial nondestructive testing, where the relative portability of the systems was a priority (Cho *et al.*, 2005; Brunetti and Cesareo, 2007). Recent offerings from both companies strive to reduce the readout noise, improve conversion gain and increase area still further. The Hamamatsu C9732DK measures 120mm by 120mm with 50$\mu$m pixels for high resolution imaging and has 75dB dynamic range despite 1250$e^-$ read noise (Hamamatsu, 2008). The RadIcon RadEye 100 (Rad-icon Imaging Corp, 2008) has dimensions of 98mm by 49mm with 96$\mu$m pixels and has been designed to be '3-sides' buttable so can reach much greater areas when tiled. This design has a much lower read noise of 250$e^-$ but suffers poor conversion gain of 0.2$\mu$V/$e^-$.

Literature reports of the development and characterization of large area APSs are scarce, despite demand for such devices from numerous scientific applications, X-ray diffraction being just one. It is therefore difficult for users to judge the actual performance of commercial devices as manufacturer specification sheets are often the only available source of information. Scheffer (2007), from Cypress Semiconductor, present a wafer scale (8.4Mpixel) APS with standard '3-T' layout, designed for X-ray radiology applications. They achieve a much lower read noise than current commercial options of just 91$e^-$ and show that it is possible to scale standard APS technology without loss of performance. Other implementations of large area devices have been presented by Ay and Fossum (2006) (76mm x 77mm) and earlier still, Meynants *et al.* (2003) (35mm x 24mm).

### 1.3.3 Potential for a bespoke X-ray diffraction detector

It is clear that the development of high dynamic range, high speed CMOS Active Pixel Sensors has been vast in the last decade. Large area sensors, currently commercially available, are just beginning to emerge with noise and dynamic range specifications that are suited to X-ray diffraction applications.

While quantum efficiency will suffer if devices are produced in standard processes with small feature sizes, many foundries now offer specialized CMOS image sensor processes combined with stitching technology to achieve areas up to 12cm by 12cm without loss of performance. Even higher areas are possible if sensors are designed for tiling. Read noise levels are now less than 50$e^-$ and falling through the use of advanced pixel and readout circuit designs.

The real challenge is now combining 20 years of development into a single device: a large area, low noise, high dynamic range sensor that can meet the demands of readout speed and quantum efficiency set by X-ray diffraction. This vision could become a reality in the near future and if it does, the APS will be the ideal detec-

tor for a breast biopsy analysis system using X-ray diffraction. It is thus necessary fully understand the performance of Active Pixel Sensors so that quantitative measurements may be made and their potential as angle dispersive X-ray diffraction detectors can be evaluated.

## 1.4 Hypothesis of this work

To investigate the potential application of novel CMOS Active Pixel Sensor technology in X-ray diffraction studies of breast biopsy samples with the aim of improving the speed and accuracy of breast cancer diagnosis.

## 1.5 Structure of the rest of this thesis

In this chapter, the motivation for this work was explored and an evaluation of the existing instrumentation for X-ray diffraction measurements was made. A detailed review of CMOS Active Pixel Sensor operation and performance followed. The structure of the rest of the thesis is as follows:

- Chapter 2 describes the roadmap to an ideal X-ray diffraction detector and introduces the evaluation methods used to determine the performance of APSs.
- Chapter 3 presents the performance of two Active Pixel Sensors and critically evaluates their potential as X-ray diffraction detectors
- Chapter 4 describes the development of an angle dispersive 'Active Pixel X-ray Diffraction' (APXRD) system for breast biopsy analysis
- Chapter 5 presents the results obtained with the APXRD setup including: measured X-ray diffraction signatures; phantom imaging for resolution verification and contrast evaluation; and multivariate analysis for predicting sample composition
- Chapter 6 summarises the system development completed so far and the future tests required prior to clinical implementation

# Chapter 2

# Active Pixel Sensors: Design Specifications and Characterization Methods

## 2.1 Overview of chapter

This chapter introduces the specifications and pixel architectures of two Active Pixel Sensors whose potential as X-ray diffraction detectors is explored in this work. The methods available for performance evaluation of the sensors are reviewed and a summary of the parameters that may be derived for a sensor is given.

### 2.1.1 Roadmap to the ideal X-ray diffraction detector

As described in the last chapter, key properties of an X-ray diffraction detector include large area, low noise, high dynamic range, good linearity, fast readout, high frame rate and high quantum efficiency. The current status of APS technology shows promising advances in each of these areas. To reach the ultimate in X-ray diffraction performance requires a series of intermediate designs to test how well the above features can be combined. Both Active Pixel Sensors investigated here were produced by the RC-UK M-I$^3$ consortium, which aspires to break the constraints of current scientific imaging by exploiting state-of-the-art APS technology (Multidimensional Integrated Intelligent Imaging - M-I$^3$, 2008). Vanilla is a versatile, low noise APS with high speed region-of-interest (ROI) readout and analogue or digital output options. It combines increased speed and functionality with low noise operation. The Large Area Sensor, or 'LAS' was designed specifically for X-ray diffraction measurements and attempts to combine low noise, high speed readout and wide dynamic range in a large area device.

### 2.1.2 Challenges of evaluating APS performance

As Active Pixel Sensors have only recently emerged as a viable option for scientific imaging, their behaviour is not yet fully understood. It will be shown in Section 2.3.1 that APSs suffer an inherent nonlinearity that arises both from the source follower and the variation of sense node capacitance with signal charge level. These nonlinearities can be controlled and compensated for provided they are well characterized. Early evaluation of Active Pixel Sensor performance simply used CCD characterization methodology as the nonlinearity of the APS had not been recognised. However, the 'gold standard' methods for evaluating semiconductor detector performance assume linear sensor response in their derivation, so are not directly applicable for APS characterization. Recently, authors have sought to develop new methods that account for APS nonlinearity. The literature lacks a rigorous study of the four available characterization methods, so a brief derivation of these will be given below and a comparison of their accuracy and reliability made in Chapter 3.

## 2.2 Design specifications of 2 Active Pixel Sensors for scientific imaging

The characteristics of both sensors to be tested are presented below: the sensors share an identical readout system, illustrated in Figure 2.1; pixel layouts can be seen in Figure 2.2. They are controlled from a PC via a National Instruments Labview 7.1 interface or compiled C executable. Sensor reset, integration and readout are determined by stimulus vector playback in the Xilinx FPGA Development board. Data may be saved on a standard MS Windows host PC or laptop via a Gbit fibre optic link or network cable respectively. The laptop system has the added benefit of portability, while the PC system can also be used to control GPIB devices.

### 2.2.1 Vanilla

A key feature of Active Pixel Sensors is their random access readout. 'Vanilla' is a versatile APS designed to enable a large number of scientific users to test APS technology in their fields. Position location and tracking are a primary focus of this design, which provides up to six dynamically reconfigurable regions of interest (ROIs) down to 6x6 pixels in size. Including both analogue and digital circuits on-chip allows Vanilla to achieve a high full frame rate of over 100fps, and also attain a high ROI frame rate of over 20,000fps. The fill factor has been maximised to ensure the highest possible sensitivity is achieved.

Vanilla is a 520x520 array of pixels on a 25$\mu$m pitch operating in rolling shutter mode, whose pixel layout is shown in Figure 2.2 (a). In order to optimize the signal-to-noise ratio obtained for scientific imaging, a 'flushed' reset circuit (Pain *et al.*,

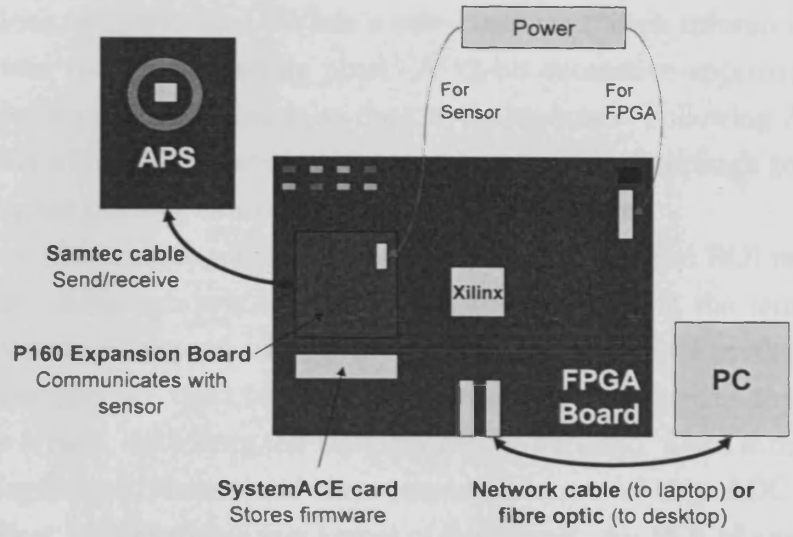


Figure 2.1: Illustration of the data acquisition system used to control and readout the sensors. The sensor is connected to the Xilinx FPGA development board via a high performance 120 way Samtec cable. For each APS, the P160 expansion card is unique and the SystemACE module contains a separate set of firmware.

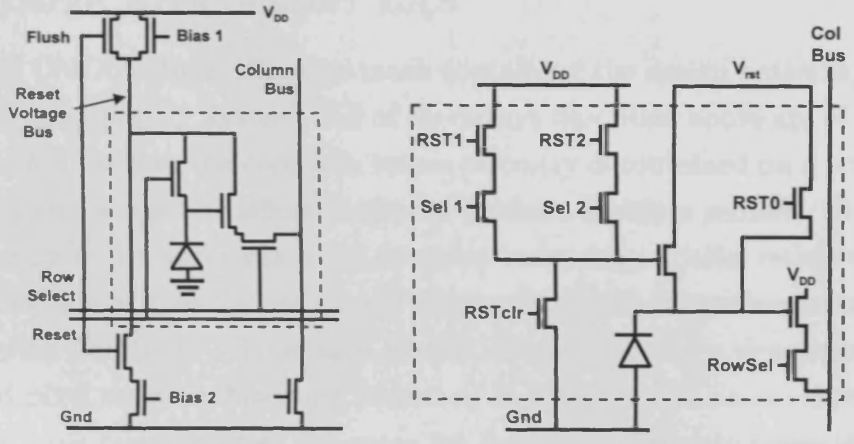


(a) Vanilla (b) Large Area Sensor

Figure 2.2: Layouts of the CMOS pixels for the M-I$^3$ sensors evaluated in this work. In (b), RST0, RST1 and RST2 refer to the three reset levels that may be applied to each pixel.

2003) was included to achieve low reset noise. A flush reset circuit enables a hard reset and a soft reset to be applied consecutively. The hard reset acts as the 'flush' as it completely erases the pixel, while the soft reset yields the reduced mean square noise voltage of $\frac{k_B T}{2C_{ph}}$ where $k_B$ is Boltzmann's constant, T is temperature and $C_{ph}$ is the capacitance of the photodiode (Tian *et al.*, 2001). The circuit is included off-pixel to maintain a high fill factor of 75%.

Two 10-bit address decoders provide random access to the Vanilla array enabling two modes of operation. In full frame mode, addresses for all rows are supplied in sequence as a digital input to the decoders and for each row address, read and

reset operations are performed. When a row is selected, each column read line will show data from the corresponding pixel. A 12-bit successive approximation ADC is available for every four columns so data is multiplexed. Following ADC, data is parallel loaded into a 12-bit wide shift register and shifted through to the output. Full frame digital readout can reach speeds of up to 140fps.

In ROI mode, analogue random access facilitates high speed ROI readout at 10-bits resolution. Although row addressing and reset operate in the same way as for full frame readout, the speed of operation is increased. In ROI mode, two column sampling capacitors are used to pipeline the readout. This means that while data from one row is read, data from the next row can be accessed. Data is output serially via two analogue multiplexors and then converted by an off-chip ADC.

The smallest ROI available is a kernel of 6x6 pixels. An ROI of any rectangular size up to, but not including, the full array dimensions, can be selected by the user before imaging begins. A single 6x6 pixel ROI can achieve a frame rate of over 20kfps and up to six different ROIs may be specified in any imaging acquisition.

### 2.2.2 Large Area Sensor: LAS

A standard CMOS reticle, the glass mask containing the design patterns, is limited in size to approximately 2x2cm$^2$. All of the arrays described above are of small area (<1.3x1.3cm$^2$) because the complete sensor circuitry is contained on a single reticle that is stepped across the silicon wafer to produce multiple sensors. To scale the sensor area up to full wafer size using stitching technology, special reticle designs are needed. The 'Large Area Sensor' (LAS) attempts to scale the performance advances achieved with Vanilla to a large area device. It also contains a development of the 'individual pixel reset' architecture described in Chapter 1 to create three different integration time regions across the array for dynamic range enhancement.

LAS is a 1350x1350 array of pixels on a 40$\mu$m pitch, each containing 9 transistors. The sensor has been designed for full wafer scale production in future, but the first production has an area of 5.4x5.4cm$^2$. The reticle used to produce the stitched sensor is shown in Figure 2.3. The reticle is subdivided into 4 parts that are stepped repeatedly across the wafer. With reference to the left of Figure 2.3, each sensor stitch block (B) contains 270 rows and columns, so a 5 by 5 arrangement of stitch blocks compose the full array. Each top stitch block contains the reset circuitry, while each bottom stitch block contains the readout shift registers and ADCs. There is a dedicated differential analogue output for every section of 135 columns, which connects to a 14-bit pipelined ADC (Analog Devices AD9252). Side stitch blocks contain row logic. A sensor is created by combining a set of stitch blocks, an example of which is shown on the right of Figure 2.3.

The pixel layout can be seen in Figure 2.2 (b). Each pixel has a fill factor of 64%. As for Vanilla, flush reset circuitry and address decoders for ROI readout

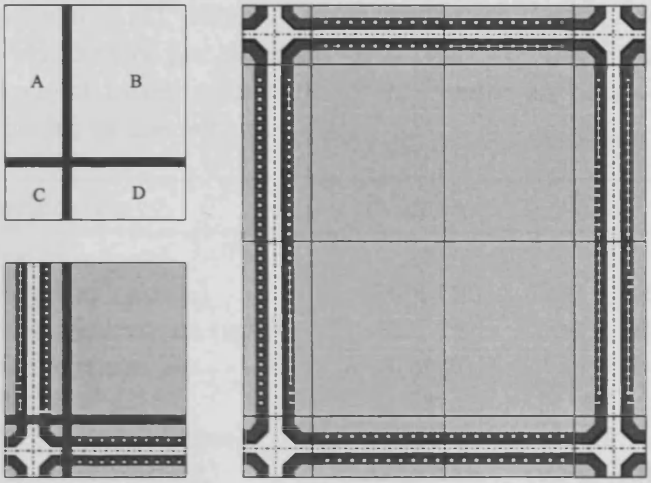


Figure 2.3: Illustration of how a CMOS reticle may be subdivided into side (A), sensor (B), corner (C) and top or bottom (D) then tiled to create a seamlessly stitched array.

are included on-chip. The maximum frame rate achievable with parallel analogue readout is 20fps.

To achieve the wide dynamic range required for X-ray diffraction, 6 extra transistors (in addition to a '3-T' layout) are included per LAS pixel to define 'regions of reset' (RORs) with different integration times. This implementation is appropriate for X-ray diffraction studies as the scene being imaged is generally static. By default, all pixels in a row are reset to the same level, RST0, when the rolling shutter first passes. If Sel 1 or Sel 2 are enabled (see Figure 2.2 (b)) that pixel will later be reset to level RST1 or RST2 to reduce the integration time. The longest integration time, used to record the low intensity signals, is 2.3s. The minimum ROR integration time that can be used in combination with this is 37$\mu$s and this records the most intense regions of the image. These extrema define a minimum dynamic range of 96dB. For the purpose of application in X-ray diffraction, this effectively allows the transmitted beam and/or intense reflections to be visualised in the same frame as low intensity scatter peaks.

### 2.2.3 Summary of design specifications

Table 2.1 lists the design specifications of both sensors i.e. the performance they are expected to achieve based on their design. The actual performance of any sensor inevitably depends on the conditions under which it is operated (Hopkinson *et al.*, 2004) and the data acquisition system used to retrieve data from it. A full characterization of each sensor is therefore required to assess their suitability for angle dispersive X-ray diffraction.

Table 2.1: Specifications of MI[3] sensors. LAS stands for 'Large Area Sensor'. Frame rates are given in FPS (frames per second). 'Ltd. by FW' means there is no firmware limitation on the longest integration time of the sensor and it is effectively limited by the full well capacity of the sensor

| Specification | Vanilla | LAS |
|---|---|---|
| Pixel Size ($\mu$m) | 25 | 40 |
| Array Size (pixels) | 520 x 520 | 1350 x 1350 |
| Array Dimensions (mm) | 13 x 13 | 54 x 54 |
| Epi Thickness $\mu$m | 14 or 20 | 5 or 15 |
| Fill Factor (%) | 75 | 64 |
| FPS (max full frame) | 140 | 20 |
| FPS (ROI readout) | up to 24K | up to 13K |
| Noise Floor ($e^-$) | 25 | 27 |
| Full Well Capacity ($e^-$) | $10^5$ | $10^5$ |
| Min. Integration Time | 0.2s | 10$\mu$s |
| Max. Integration Time | Ltd by FW | 2.3s |
| Int time variable on array? | No | Yes |
| Release date | Sept 2006 | May 2008 |

## 2.3 Active Pixel Sensor performance evaluation

### 2.3.1 Active Pixel Sensor noise sources

Noise sources in an APS can be classified into three main types: read noise, shot noise and fixed pattern noise. An expression for the total noise of an APS may be written as

$$\sigma^2_{total} = \sigma^2_{shot} + \sigma^2_{read} + \sigma^2_{fpn} \tag{2.1}$$

Detailed analysis of APS noise has been published by, for example, Tian *et al.* (2001) and Janesick (2007). The dominant noise source in an APS depends on the phase of operation. Noise from the reset transistor dominates during the reset phase. Shot noise is dominant during integration, while in the readout phase noise is limited by transistors in the readout chain both on- and off-pixel. A brief summary of the main noise sources is detailed below.

#### Read Noise

Any noise source that is not a function of signal is classified as read noise. For Active Pixel Sensors, read noise encompasses a wide variety of transistor and amplifier noise sources and can be subdivided as

$$\sigma^2_{read} = \sigma^2_{sf} + \sigma^2_{reset} + \sigma^2_{d,shot} + \sigma^2_{adc} + \sigma^2_{col} + \sigma^2_{sys} \tag{2.2}$$

These components are:

- $\sigma^2_{sf}$: white, flicker and RTS noise of the source follower transistor ultimately

limits the sensor noise

- $\sigma^2_{reset}$: thermally generated noise due to the reset operation, given by $k_B T C_{SN}/q$ for hard reset, where $k_B$ is Boltzmann's constant, T is the temperature and $C_{SN}$ is the sense node capacitance
- $\sigma^2_{d,shot}$: shot noise due to thermally generated dark current, unwanted charge generated by the sensor in the absence of illumination
- $\sigma^2_{adc}$: ADC quantization noise given by the r.m.s. error about a perfect ramp, $\frac{1}{12}$DN for an ideal ADC
- $\sigma^2_{col}$: represents the thermal and flicker noise contributed by the column amplifier
- $\sigma^2_{sys}$: represents all of the system noise sources such as preamplifier noise, transient noise, power supply noise and electromagnetic interference

Read noise dominates all other noise sources at low illumination levels so limits the low light level performance of an APS. Some read noise sources can be eliminated using 'correlated double sampling' (CDS). This requires two time-correlated non-destructive samples of the pixel signal to be made; one just after reset, the other post integration. Subtracting these yields the signal voltage alone, removing reset noise and suppressing flicker noise. CDS requires a 'transfer' transistor to be included in the APS pixel so a non-destructive sample of the reset level can be made. Most Active Pixel Sensors cannot be sampled non-destructively meaning CDS is not frequently employed. Instead, an approximate 'digital CDS' is performed by subtracting an average dark field from any data frames.

### Shot Noise

The fundamental limit on image sensor performance is shot noise, which arises from the Poisson variation in the rate of photon arrival at the sensor. It is given by the standard deviation of the number of interactions per pixel, a random phenomenon which is distributed both spatially and temporally. Signal shot noise is dominant while the sensor is in its integration phase and is given by $\sigma_{shot} = \sqrt{S}$.

### Fixed Pattern Noise

The presence of transistors in each pixel makes APSs highly susceptible to fixed pattern noise (FPN). FPN produces the same spatial variation in each frame so is said to be 'fixed' in time. It arises from a number of sources and may be decomposed in separate effects due to pixels and columns (El Gamal *et al.*, 1998). Pixel-to-pixel pattern noise (PP-FPN) occurs due to differences in the offset and gain of transistors in each pixel, as well as differences in charge collection efficiency

(Janesick, 2007). Column-to-column pattern noise (CC-FPN) is due to differences in the column amplifiers and manifests as vertical streaks in an image.

Offset FPN is independent of signal and can be attributed to device mismatches between pixels. Dark current FPN, or dark signal nonuniformity (DSNU), is generated by artifacts resulting from CMOS fabrication that produce signal charge in the absence of illumination. It can be removed using correlated double sampling (CDS), or dark field subtraction. Gain FPN, also known as photo response nonuniformity (PRNU), is signal dependent and can be significant as the image sensor nears saturation. It occurs because different pixels in an array respond to light with different gains so produce different photocurrents. It is particularly significant at high light intensity, where the greatest difference in photocurrents is produced. A gain calibration and offset map for the sensor can be calculated in order to suppress these noise sources.

The overall FPN of an APS can be represented as (Janesick, 2007)

$$\sigma_{fpn} = P_N S \tag{2.3}$$

where S is the signal and $P_N = \sigma/\overline{S}$ is the 'FPN quality factor'. If the mean of each pixel signal over N frames is $\overline{S_{i,j}}$, where $i$ and $j$ index rows and columns, FPN can be further decomposed as $F_{i,j} = Y_i + X_{i,j}$, where $Y_j$ represents the column FPN component and $X_{i,j}$ the pixel FPN component. $F_{i,j}$ is calculated using the following:

$$F_{i,j} = \overline{S_{i,j}}(DN) - \overline{S}(DN) \tag{2.4}$$

From this derivation of $F_{i,j}$, we can then calculate the column and pixel components and their variances according to:

$$\overline{Y_j} = \frac{1}{N}\sum_{i=1}^{L} F_{i,j} \quad ; \quad \overline{X_{i,j}} = F_{i,j} - \overline{Y_j} \tag{2.5}$$

$$\overline{\sigma_Y}^2 = \frac{1}{M-1}\sum_{j=1}^{M} \overline{Y_j}^2 \; ; \; \overline{\sigma_X}^2 = \frac{1}{M(N-1)}\sum_{i=1}^{N}\sum_{j=1}^{M} \overline{X_{i,j}}^2 \tag{2.6}$$

### Other noise sources

It should be noted that the sources of noise described above are by no means the only noise sources present in Active Pixel Sensors. For example, Fano noise is the variance in the number of electron-hole pairs produced in the silicon but only becomes appreciable in the soft X-ray regime. Further, when part of the image is subject to high illumination levels, signal charge generated in one pixel can diffuse far enough that it is collected in another (Shcherback *et al.*, 2004). This is known as crosstalk and may cause reduced spatial resolution. It can be minimised by design

and decreases with photodiode area.

That the understanding of CMOS technology is still in its infancy presents a barrier to full characterization of Active Pixel Sensors. As the technology scales, the noise sources that dominate APS performance change and suddenly a new factor needs to be considered that was not a problem previously. In addition, the advanced pixel designs created to solve, for example, fixed pattern noise problems, will simply bring other noise sources to dominance. In general, it should be considered that the noise sources described above are present in all APSs; a search for further sources of noise will be needed if a device does not perform as expected during performance evaluation.

#### Nonlinearity

The inherent nonlinearity of the APS arises from two key sources (Janesick, 2007). Gain 'V/V' nonlinearity arises from the nonlinearity of the source follower in pixel, as well as from any other amplifiers in the amplification chain; it can generally be well controlled by design. Sensitivity '$V/e^-$' nonlinearity arises because the APS photodiode is an element of the sense node so the sense node capacitance $C_{SN}$ varies with charge level according to

$$C_{SN}(V_{SN}) = q\frac{dS(e^-)}{dV_{SN}} \tag{2.7}$$

where q is the unit of electronic charge, $S(e^-)$ is the signal in electrons and $V_{SN}$ is the sense node voltage. As a result, the charge to voltage relationship is nonlinear causing a reduction in signal and noise at high signal levels as compared to the case of constant capacitance (Tian *et al.*, 2001). While this yields a slightly higher signal-to-noise ratio for general imaging applications, it can yield serious systematic errors in scientific imaging applications and the severity of the issue will worsen as CMOS technology downscales (Janesick *et al.*, 2006). For the purpose of performance evaluation, the presence of nonlinearity means we require new testing methodology.

### 2.3.2 Camera conversion gain

To compare the performance of different sensors, their properties should be expressed in physical terms ($e^-$), rather than the relative digital number (DN) output from analogue-to-digital conversion of the signal charge. Sensor conversion gain is defined as the number of electrons represented by each digital number, denoted by $K(e^-/DN)$ or $G(DN/e^-) = K^{-1}$ depending on the conversion required. This encompasses two fundamental gain stages in an APS; the charge-to-voltage conversion ($V/e^-$) and analogue-to-digital conversion ($DN/V$).

Camera characterization has traditionally been performed with 'gold standard' Mean-Variance (Holdsworth *et al.*, 1990) and/or Photon Transfer (Janesick, 2001) techniques. These analyses break down when the sensor response is nonlinear. As a result, performance parameters may be incorrectly estimated, leading to inappropriate sensor choices for scientific applications. APS nonlinearity has been overcome thus far by evaluating the sensor performance only in its low illumination 'linear region', where the effect of a changing sense node capacitance is assumed to be negligible. This prevents accurate evaluation of parameters such as full well capacity and quantum efficiency. To fully understand the performance of Active Pixel Sensors, it is necessary to extend the scope of the characterization studies to include nonlinear techniques.

Recently, authors have begun to seek alternative methods of characterizing nonlinear CMOS APS. Janesick (2007) has proposed that the conversion gain be separated into signal and noise gains. This method will be referred to as 'nonlinear compensation' (NLC) for the rest of the thesis. Pain and Hancock (2003) redefine the conversion gain as a function of illumination rather than as a constant and their method is known as 'nonlinear estimation'. These studies are timely given the recent increase in the number of scientific users who wish to obtain quantitative information from APSs employed in their imaging systems.

The following sections present brief derivations of both linear and nonlinear analysis methods. The APS performance evaluations made in Chapter 3 will employ one or more of these methods and an intercomparison of the methods will be made on the Vanilla sensor results. The comparison of these methods may be found in its complete form in Bohndiek *et al.* (2008a). All data analysis was completed independently for this work (SB); other authors designed the sensor (AC, MP, RT) and collaborated in experimental design and data acquisition (AB) (see Chapter 3).

### 2.3.3 Conversion gain derivation for linear camera response

#### Mean-Variance Analysis

Mean-variance analysis is the 'gold standard' for derivation of the conversion gain parameter for charge-coupled devices (CCDs) (Stark *et al.*, 1992; Beecken and Fossum, 1996). The full derivation using statistical analysis of the observed signal has been published by, for example, Holdsworth *et al.* (1990).

For a linear sensor with constant conversion gain, an input of $P_I$ interacting optical photons produce a signal

$$S(DN) = G(DN/e^-)P_I = \frac{P_I}{K(e^-/DN)} \tag{2.8}$$

For wavelengths greater than 400nm, a single photon produces one electron-hole

pair in silicon devices. The mean output signal $\overline{S}$ is thus

$$\overline{S}(DN) = \overline{G}(DN/e^-)\overline{N} \tag{2.9}$$

where $\overline{N}$ is the mean number of signal electrons. Using the Burgess variance theorem, assuming a Poisson distribution of incident photons and negligible gain variance we arrive at

$$\sigma_S^2 = \overline{G}\,\overline{S} + \sigma_R^2 \tag{2.10}$$

where $\sigma_R^2$ is added in quadrature to represent fluctuations in the illumination independent term (read related noise) that are present in reality. Plotting $\sigma_S^2$ vs. S(DN) yields a mean-variance graph (see Figure 2.4). The slope of this graph provides $G(DN/e^-)$; the intercept, $\sigma_R^2$.

The data for the mean-variance graph should be determined from N frames measured at a number of illumination levels between dark and saturation, and calculated from (Pain and Hancock, 2003):

$$\overline{S_{i,j}} = \frac{\sum_k S_{i,j,k}}{N} \quad ; \quad \overline{S} = \frac{\sum_{i,j} \overline{S_{i,j}}}{LM} \tag{2.11}$$

$$\sigma_{i,j}^2 = \frac{\sum_k S_{i,j,k}^2}{N} - [\overline{S_{i,j}}]^2 \quad ; \quad \sigma_S^2 = \frac{\sum_{i,j} \sigma_{i,j}^2}{LM} \tag{2.12}$$

where S represents the signal and $\sigma$ represents the root-mean-square (r.m.s.) noise. The dark offset level, $S_D$, should be calculated by applying Equation 2.11 to a set of N frames recorded without illumination. Figure 2.5 illustrates the notation used in these equations. The temporal average (over N) accounts for pixel variations in time, while the spatial average (over L, M) accounts for variations across the array.

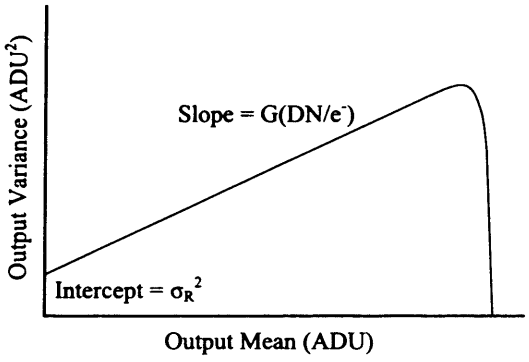


Figure 2.4: Mean-variance graph showing the linear increase in sensor noise with signal up to the saturation point. The gradient of the linear region is the conversion gain $G(e^-/DN)$ and the intercept is the sensor read noise $\sigma_R^2$.

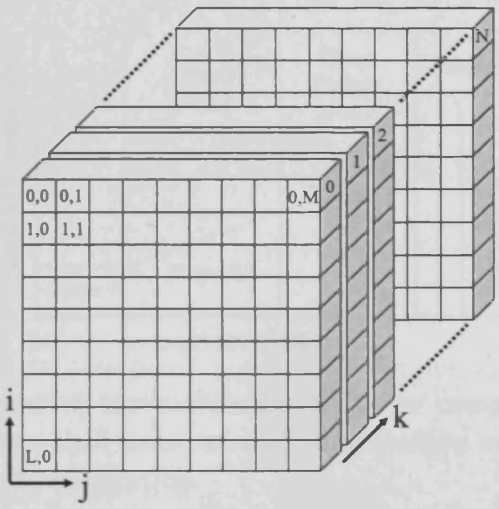


Figure 2.5: Illustration of frame indexing for mean variance analysis with Equations 2.11 and 2.12, where i refers to rows, j to columns and k to frames

### Photon transfer - Noise decomposition

The photon transfer technique (Janesick, 2001) may also be used to calculate the conversion gain. Assuming the sensor noise sources are uncorrelated, the standard formula for propagation of errors may be applied to Equation 2.8 and read noise added in quadrature to obtain

$$\sigma_S^2(DN) = \left[\frac{\partial S}{\partial P_I}\right]^2 \sigma_{P_I}^2 + \left[\frac{\partial S}{\partial K}\right]^2 \sigma_K^2 + \sigma_R^2 \tag{2.13}$$

Substituting from Equation 2.8 and again assuming a Poisson distribution of incident photons ($\sigma_{P_I}^2 = \overline{P_I}$) and negligible gain variance, we can simplify Equation 2.13 to

$$K(e^-/DN) = \frac{S(DN)}{\sigma_S^2(DN) - \sigma_R^2(DN)} \tag{2.14}$$

where $\sigma_R^2$ is the illumination-independent sensor noise (read noise) and $\sigma_S^2$ is the illumination-dependent noise of an image at signal level S(DN). $\sigma_S^2 - \sigma_R^2$ is the signal shot noise $\sigma_{shot}^2$. We plot logarithmically the r.m.s. noise of the sensor $\sigma_S$ against the average sensor signal $\overline{S(DN)}$ to produce the 'photon transfer curve' (PTC).

$$\log[K] = \log[S(DN)] - \log[\sigma_S^2(DN) - \sigma_R^2(DN)] \tag{2.15}$$

Provided that the sensor parameters are set such that $K(e^-/DN) \leq \sigma_R$, ADC quantization noise can assumed to be negligible (Janesick, 2001).

Given the noise sources dominant in an APS (see Section 2.3.1), we expect the PTC to exhibit three limiting regimes. Read related noise is independent of illumination so will exhibit a gradient of zero. This is dominant at low signal levels but as illumination increases, the photon shot noise should become dominant. From

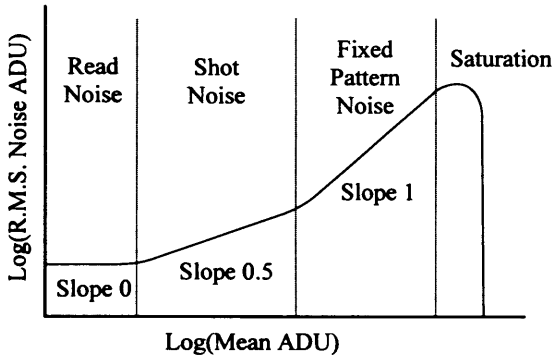


Figure 2.6: Photon transfer curve showing all noise components, limited by read noise at low illumination, shot noise at mid illumination and fixed pattern noise at high illumination prior to saturation.

Poisson statistics, we expect a gradient of $\frac{1}{2}$ as $\overline{S} = \sigma^2_{shot}$. At high signal levels, fixed pattern noise from transistors and amplifiers present both in pixel, and per column, dominates. At this level, we observe a gradient of 1 as FPN increases with proportion to the signal. The ideal photon transfer curve of these noise components is illustrated in Figure 2.6.

To determine the conversion gain from the photon transfer curve, we need to remove all noise sources apart from the signal shot noise. Subtracting two consecutive images at a single illumination level will remove the fixed pattern noise. For any pair of frames (denoted by A and B), we calculate the frame mean $\overline{S_k}$ for k=A and k=B, the corrected mean $\overline{S}$ with k=Dark and the temporal noise $\sigma^2_S$ using:

$$\overline{S_k} = \frac{1}{LM}\sum_{i,j} S^k_{i,j} \tag{2.16}$$

$$\overline{S} = \frac{1}{2}[\overline{S_A} + \overline{S_B}] - \overline{S_D} \tag{2.17}$$

$$\sigma^2_S = \frac{1}{2(N-1)}\sum_{i,j}[(S^A_{i,j} - \overline{S_A}) - (S^B_{i,j} - \overline{S_B})]^2 \tag{2.18}$$

where $\overline{S_D}$ is the dark offset level. The additional factor of two in Equation 2.18 is present to account for variances adding when two images are subtracted. The uncertainty in deriving the variance is given by $\sqrt{2/N}$ where N is the number of pixels in the region of interest used for analysis. A 100x100 ROI thus defines an error of 1.4%. Results can then be averaged over different areas of a single frame, or over many pairs of frames to improve accuracy further.

Subtracting the variance of the differenced dark field from the variance at each illumination level will remove the read noise from the photon transfer curve. If the linear fit to the shot noise region is given by $y = mx + c$ then $K(e^-/DN) = 10^{\frac{c}{m}}$. The PTC can thus be plotted with FPN removed and the shot noise component isolated in a plot of $(\sqrt{\sigma^2_S - \sigma^2_D})$ vs. S(DN).

#### Limitations of these methods

Linear methods can only be applied provided the following assumptions hold:

1. The sensor output signal is linear with illumination
2. Fluctuations in the number of incident photons are described by a Poisson distribution
3. Incident photons are converted to signal electrons in the pixel with quantum efficiency $\eta$
4. The variance in the conversion gain $\sigma_G^2$ is small

In addition to the above, the application of the photon transfer method requires that noise sources in the sensor are uncorrelated.

While the above assumptions often hold in other imaging sensors, the linearity assumption cannot hold for the APS. The conversion gain derived by mean-variance or photon transfer methods can therefore be in severe error, deviating by up to 200% in some cases (Janesick *et al.*, 2006).

### 2.3.4 Conversion gain derivation for nonlinear camera response

#### Nonlinear compensation

For a nonlinear sensor, the slope of the shot noise limited region of a PTC will deviate from $\frac{1}{2}$. If the nonlinearity is due to V/V (gain) nonlinearity, the conversion gain changes with signal level but standard photon transfer methods can be applied to 'linearized' data. This can be justified because the nonlinearity arises from gains in the readout chain. $V/e^-$ (sensitivity) nonlinearity means that the conversion between signal electrons and pixel voltage varies due to the changing sense node capacitance. The use of a single, constant, conversion gain parameter $K(e^-/DN)$ is thus inappropriate. $K(e^-/DN)$ gives false estimates of the number of signal electrons in the pixel and in turn, false estimates of the sensor performance parameters.

Instead, Janesick (2007) decomposes $K(e^-/DN)$ into a signal gain, $S(e^-/DN)$, used to calculate the signal in $e^-$ and full well capacity, and noise gain, $N(e^-/DN)$, used to calculate the read noise. Rearranging Equation 2.7 shows that

$$S(e^-) = \frac{1}{q}\int_{V_R}^{V_{SN}} C_{SN}(V_{SN})dV_{SN} \tag{2.19}$$

At low illumination levels, nonlinearity is not significant so we can assume that $K(e^-/DN) = S(e^-/DN) = N(e^-/DN)$ and thus determine the signal conversion

gain at low illumination. The signal level at the first illumination level can then be calculated in absolute units, $S_1(e^-)$. Provided we have accurate knowledge of the illumination input at higher signal levels (e.g. light intensity or exposure time), $S_n(e^-)$ can be calculated in proportion to $S_1(e^-)$. $S_n(e^-)$ is an accurate estimate of the number of signal electrons in the pixel at illumination level 'n'. Dividing this by the sensor output $S_n(DN)$ at that level determines the signal gain $S(e^-/DN)$ as a function of illumination. Non-linearity is thus accounted for using the number of signal electrons at low illumination levels where the response is linear and scaling to the illumination level for frame 'n'. The noise conversion gain may be found as a function of illumination using $N(e^-/DN) = \sqrt{S(e^-)}/\sigma_{shot}$.

NLC can be used to separate the effects of the two different sources of nonlinearity if both are present. The slope of the shot noise curve will always deviate from $\frac{1}{2}$ if any nonlinearity exists. If the signal and noise gains are the same but both decreasing at low signal levels, V/V nonlinearity exists. If the signal and noise gains increase and diverge at higher signal levels, $V/e^-$ nonlinearity exists (Janesick, 2007). This divergence in signal and noise gains arises because the changing sense node capacitance has a greater effect on signal gain than noise gain at high intensities.

### Non-Linear Estimation

An alternative method for coping with the change of sense node capacitance with signal is to change the way that we define the conversion gain.

In the linear mean-variance method (Section 2.3.3), the transfer function f[ ] relating the mean number of electrons in a pixel, N, to the sensor output, S(DN) yields S(DN)=f[N], so the conversion gain is the slope of the Mean-Variance graph $G(DN/e^-) = \frac{d\sigma_S^2}{dS} = f'[N]$. If the sensor is nonlinear, this conversion gain will vary significantly with signal, leading to severe inaccuracies in the calculation of, for example, quantum efficiency.

To avoid this error, Pain and Hancock (2003) relate the slope of the transfer function between mean signal and incident photon flux to the conversion gain. This is similar to the signal gain of the NLC method, which is related to the low illumination signal as a function of the known illumination intensity. The derivation of the two methods is, however, somewhat different. The NLE conversion gain is also a function that varies with illumination, rather than a constant. Performing a Taylor expansion of f(n) about N, the mean number of electrons in a pixel, we can estimate the mean output ignoring terms of second order or higher with

$$S'(P) = \frac{dS}{dP} = \frac{dN}{dP}\frac{dS}{dN} = \eta\frac{dS}{dN} \approx \eta f'[N] \tag{2.20}$$

where S is the sensor output signal.

As the reset noise originates from inside the pixel, it is also affected by the

variation of the conversion gain. The conversion gain $G(DN/e^-)$ falls as the charge in the pixel increases (i.e. with increasing signal) meaning the contribution of reset noise to the overall noise falls. The output-referred noise is composed of signal shot noise and sensor read noise

$$\sigma_S^2 = \sigma_{ds}^2 + f'[N]^2(\sigma_N^2 + \sigma_{rst}^2) \tag{2.21}$$

where $\sigma_{ds}^2$ represents the downstream noise, $\sigma_N^2$ is the noise of the input signal electrons and $\sigma_{rst}^2$ is the reset noise. This expression can be rewritten in terms of measurable quantities using Poisson statistics and rearrangement of Equation 2.20 to yield (Pain and Hancock, 2003)

$$\sigma_S^2 = \sigma_{ds}^2 + \frac{1}{\eta}\left(\frac{dS(P)}{dP}\right)^2 P + \left(\frac{1}{\eta}.\frac{dS(P)}{dP}\right)^2 \sigma_{rst}^2 \tag{2.22}$$

where $dS/dP$ is the slope of the transfer function between the incident photon flux and signal output. A multivariate fit to the variables $S'(P)^2.P$ and $S'(P)^2$ can then be performed,

$$\sigma_S^2 = a + b[S'(P)]^2 P + c[S'(P)]^2 \tag{2.23}$$

where $a = \sigma_{ds}^2$, $\frac{1}{b} = \eta$ and $b.a^2 = \sigma_{RST}^2$. S and $\sigma_S^2$ should be calculated using Equations 2.11 and 2.12. The quantum efficiency as a function of signal level is given by

$$\eta \approx \frac{P[S'(P)]^2}{(\sigma_S^2 - \sigma_{ds}^2)} \tag{2.24}$$

The conversion gain is then estimated as the ratio of the derivative of the signal to the quantum efficiency as a function of illumination (Kuschak, 2007).

Given a sufficiently large data set, nonlinear estimation (NLE) can reliably estimate APS quantum efficiency. As the multivariate fit is very sensitive to variations in the input parameters, values for downstream noise and reset noise should be calculated from the conversion gain. The read noise of the sensor is given in the usual way from the variance of the difference of two dark frames. This method offers an alternative approach to that derived by Janesick (2007), enabling results obtained for nonlinear sensors to be cross referenced.

### 2.3.5 Performance parameters available from optical characterization

Each analysis method described requires a data set consisting of the sensor response under uniform illumination across a range of intensities. The following parameters may be derived from this data set once the conversion gain has been calculated. Quantities listed in Table 2.2 are best illustrated graphically, while those listed below

may be tabulated to provide a complete performance specification of an image sensor. These parameters form a complete description of the performance of any imaging device and therefore allow its suitability for different applications to be evaluated. They also enable corrections to be made for imperfections such as nonlinearity.

1. **Integral Non-Linearity** is the difference between the data points and the linear regression fit to the linearity graph computed as

$$INL = \frac{S_{max} - S_{min}}{ADCrange} \times 100 \tag{2.25}$$

2. **Linear range** should cover 80% of the sensor output range for standard mean-variance analysis to apply. In this case, the range is taken up to the point where the INL begins to deviate from its low illumination value.

3. **Dark Current** is the slope of the graph of output signal in $e^-$ vs integration time, normally written as current per unit area

4. **Read Noise** is product of the r.m.s. dark noise and the conversion gain $\sigma_R(e^-) = K(e^-/DN)\sigma_D(DN)$

5. **Full well capacity** is the product of the signal level at which the maximum variance occurs and the conversion gain $FW(e^-) = K(e^-/DN)S_{max}$. With linear methods the standard conversion gain, evaluated at low illumination ($K_{low}$), will significantly underestimate the full well capacity. To compensate for this, when using linear methods, the conversion gain should also be evaluated close full well ($K_{high}$).

6. **Dynamic range** DR $= 20\log\left(\frac{FW(e^-)}{\sigma_R(e^-)}\right)$

7. **Spectral responsivity** is calculated as the ratio of sensor response (in photocurrent per area, $Am^{-2}$) to the irradiance of the field ($Wm^{-2}$) and is given in $AW^{-1}$

8. **Quantum efficiency** $\eta$ is calculated for the illumination wavelength with Equation 2.24 using NLE, or from the spectral response as $QE = \frac{hc}{\lambda q}SR$, or may be determined as the slope of the transfer function between signal output given in electrons and input in photons

9. **Fixed pattern noise** may be separated into column and pixel components then represented as a % of the mean signal level at which it is measured. The method used for FPN calculation was detailed in Section 2.3.1.

Table 2.2: List of quantities to be represented graphically.

| Abscissa | Ordinate | Performance parameters derived from graph |
|---|---|---|
| P (# photons) | $S(e^-) - S_D(e^-)$ | Illustrates sensor linearity, slope gives quantum efficiency |
| $t_{int}$ | $S_D(e^-)$ | Slope used to derive dark current |
| S(DN) | $\sigma_S^2$ | Slope used to derive conversion gain in M-V analysis |
| $\log(S - S_D(DN))$ | $\log(\sigma_S^2 - \sigma_D^2)$ | Identify shot noise limited region for conversion gain calculation in Janesick method for linear sensor response |
| $S(e^-)_{true}$ | $S(e^-)_{false}$ | Illustrates the operating region over which $K(e^-/DN)$ nonlinearity is evident |
| $S(e^-)$ | $K, S, N(e^-/DN)$, | Illustrate nonlinearity in conversion gain using Janesick method for nonlinear sensor response |
| P (# photons) | $\eta$ | Illustrates effect of using NLE on settling QE |
| P (# photons) | $G(DN/e^-)$ | Shows the variation of the conversion gain with illumination |

## 2.4 Summary

In this chapter, the specification and operation of two Active Pixel Sensors designed for scientific imaging has been described. A complete framework for Active Pixel Sensor performance evaluation was established in order that accurate characterization of each device can be performed. Results presented in the next chapter will enable an appropriate selection of analysis methods for future Active Pixel Sensors. Following characterization, the suitability of each device for application in X-ray diffraction can be reviewed.

# Chapter 3

# Empirical evaluation of Active Pixel Sensor Performance

## 3.1 Overview of chapter

The measured performance of the APSs in terms of linearity, quantum efficiency, temporal and fixed pattern noise, and dynamic range will be presented in this chapter. Demonstration of their functionality is also made. Results from both sensors are reviewed in terms of the current state of the art available in the literature. They are then compared and an assessment of their suitability for X-ray diffraction studies is made based on these results.

## 3.2 Vanilla

### 3.2.1 Initial characterization

Preliminary tests with Vanilla indicated that, as expected, nonlinearity was present for both hard and flush reset types. Particularly severe deviations were observed for flush reset, with integral nonlinearity values of over 20% close to full well (Arvanitis, 2007). In an attempt to minimise the impact of nonlinearity, sensor parameters including reset times, ADC range and centre were optimized to finely quantize the linear range for initial noise measurements and device demonstrations. When operating in hard reset under these conditions, the ADC saturates before sensor saturation is observed so the full well capacity and linear range of the sensor cannot be directly evaluated. While these settings are adequate for use in low illumination conditions (below the onset of nonlinearity), the full range of the sensor must be interrogated for complete characterization of the device to be performed. This requires the application of nonlinear techniques. A comparison of results using Vanilla to compare the available characterization methods is presented below.

### 3.2.2 Comparison of characterization methods

#### Experimental setup

A standard measurement protocol was employed to record the data set for testing conversion gain derivation methods. A protocol for achieving 'flat field illumination' conditions is published in Standard 1288 of the European Machine Vision Association (2005). The protocol for setup of the light source states that if d is the distance between the light source and sensor, and D is the diameter of the light disk, the f number $f = \frac{d}{D}$ of the setup must equal 8 (Figure 3.1).

The light disk was provided by a narrowband LED (LumiLED) at 520nm (measured FWHM 35nm) coupled with three white diffusion sheets (Lee Filters, white 129), each with 87% attenuation. The distance to the sensor was set accordingly. Light intensity was varied by changing the voltage across the terminals of the LED. The LED was found to be stable over hours of operation and the power output was repeatable if the same voltage was applied again. The illumination uniformity was measured using an independent calibrated photodiode (Hamamatsu S1336-5BQ) to be within 1% across the array. The irradiance of the field, defined as the radiant flux incident upon a unit area of a surface in $Wm^{-2}$, was recorded for each illumination level to enable application of the nonlinear methods. This was again measured using the photodiode, placed at the position of the sensor prior to the data acquisition and read out via a Keithley 237 High Voltage Source-Measure Unit (SMU). This experimental arrangement was developed jointly with Dr C D Arvanitis (Arvanitis, 2007) and Dr A Blue (University of Glasgow). Experimental measurements were made at the University of Glasgow.

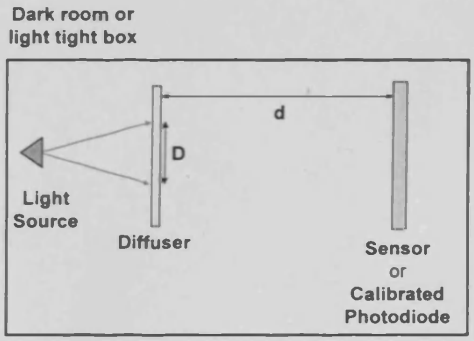


Figure 3.1: Experimental setup to create the uniform illumination field needed to perform optical characterization measurements

Vanilla was operated in analogue readout mode at 4fps under hard reset for characterization. Hard reset was chosen for the measurements as it demonstrates a greater linearity than flush reset, so gives a good compromise between performance of the linear analysis methods and testing of the nonlinear methods. Further, the 'superlinearity' of flush reset means it is unsuitable for X-ray diffraction measurements, so the sensor is unlikely to be employed using this mode of operation. In

Table 3.1: ADC parameters used under 'default' conditions and for finer quantization of the linear range. The external ADC voltage range may be as low as 500mV but operates reliably at 700mV. The common mode voltage can be adjusted between 0 and 3300mV.

| Parameter set | ADC voltage range (mV) | Common Mode Voltage (Centre) (mV) |
|---|---|---|
| Default | 1300 | 1925 |
| Fine | 700 | 2000 |

the initial measurements, around 4% of the Vanilla pixels were observed to 'spike' randomly to low digital number values. The mechanism behind this phenomenon is assumed to be readout related (Konstantinidis, 2008). An algorithm was written to identify and remove any pixels that exhibit this behaviour and they were excluded from the analysis.

The ADC voltage range and centre position were set to the 'default' options so that the full range of the sensor from dark to saturation could be measured. Table 3.1 compares these values to those used in initial measurements that provide a finer quantization of the linear range of the sensor. It should be noted that these values are sensor specific; the common mode voltage must be fine tuned for different sensors in order to completely visualise the dark field of the sensor.

For the linear mean-variance analysis (and NLE), 100 frames were recorded at each illumination level and 90 frames were analysed. The first 10 frames to be retrieved from the FPGA were discarded to ensure that no artifacts from the start of the readout stream or settling effects were included in calculations. According to the model of Beecken and Fossum (1996), analysis of 100 frames will reduce the deviation of the sample variance from the population variance to less than 1%. A central region of 400x400 pixels was analysed to avoid introducing errors due to edge effects. Far fewer frames are required to determine the conversion gain via the PTC method as $\sigma_K$ scales with $1/\sqrt{N_{pix}}$. The assumption that the gain variance is small can therefore hold with analysis of a 100x100 region in just 2 consecutive frames. 10 frame pairs were used to allow for averaging of results. In both linear analysis methods, the conversion gain was derived within the linear range of the sensor.

The graphs listed in Table 2.2 can be seen below and the resulting performance parameters from each method are summarised in Table 3.2.

### Linear analysis results

The mean-variance and photon transfer techniques described in Chapter 2 were first applied to the data set in order to derive the performance parameters that are obtained using linear analysis methods on a nonlinear sensor. Figure 3.2 (a) shows the mean-variance graph for the Vanilla sensor data set and shows that the response

of the sensor is nonlinear as the typical mean-variance pattern (see Figure 2.4) is not followed. The linear range of the curve was determined using the deviation of the mean-variance graph from the initial, low illumination gradient. This method was chosen due to the relative lack of sensitivity of the INL threshold to nonlinearity effects in the PTC noted above. Using the integral slope (the slope including all values up to and including the chosen value) of the linear region of the curve (30% dynamic range) we obtain a conversion gain of $G(DN/e^-) = 0.0497 \pm 0.0002$, or equivalently $K(e^-/DN) = 19.9 \pm 0.1$. Using the intercept of this fit, the read noise is derived as $51.8 \pm 0.3 e^-$. Figure 3.2 (b) shows the result of using this conversion gain to calculate the number of signal electrons as a function of the number of incident photons. The slope of this graph yields a quantum efficiency of 60%.

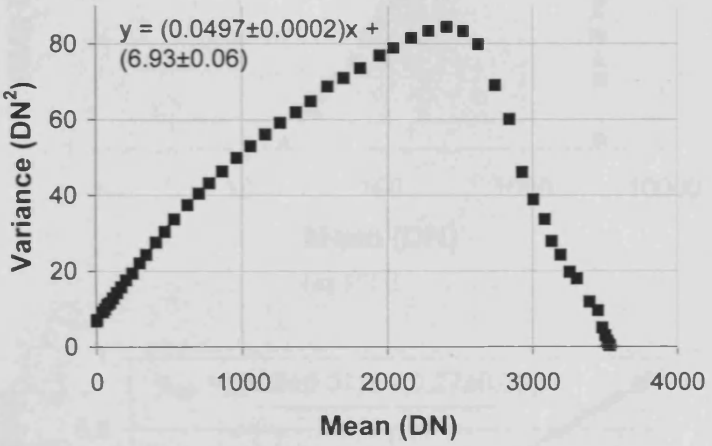


(a) Mean-Variance graph

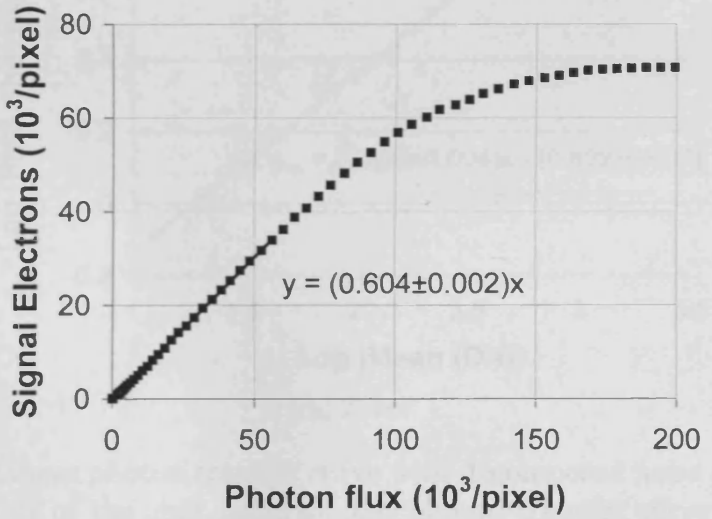


(b) Response Linearity

Figure 3.2: (a) Mean-Variance result, showing a linear rise in sensor noise up to $\approx$ 500DN. (b) The number of electrons produced in a pixel, calculated using the conversion gain derived from (a), for a given incident photon flux

The photon transfer curves of 'read and shot noise' and 'shot noise' are shown in Figure 3.3 (a). Figure 3.3 (b) zooms in on the shot noise curve below full well between 0 and 2300DN (65% dynamic range). A linear fit to the whole zoomed

portion exhibits a slope of 0.46, indicating some deviation from linearity. The low and high illumination regions were then examined separately to study the onset of nonlinearity and this is shown in the figure. It can be observed that the slope of the shot noise limited graph is $\frac{1}{2}$ at low illumination (between 0 and 480) and reduces to 0.36 between 480 and 2300, indicating significant deviation from linearity beyond 480DN ($10^4 e^-$).

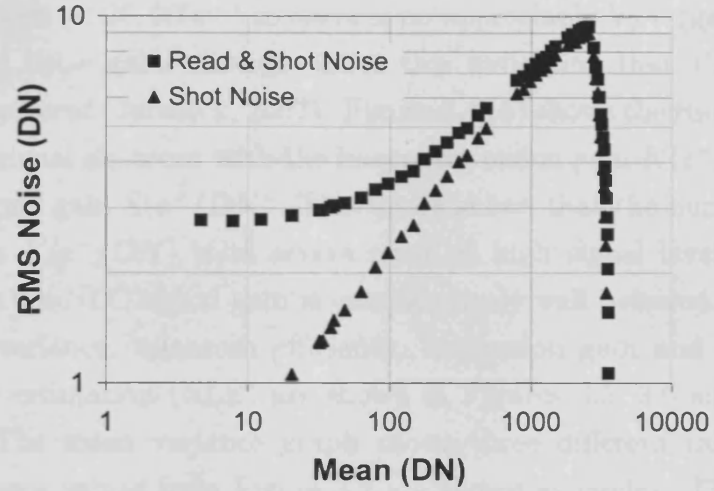


(a) PTC

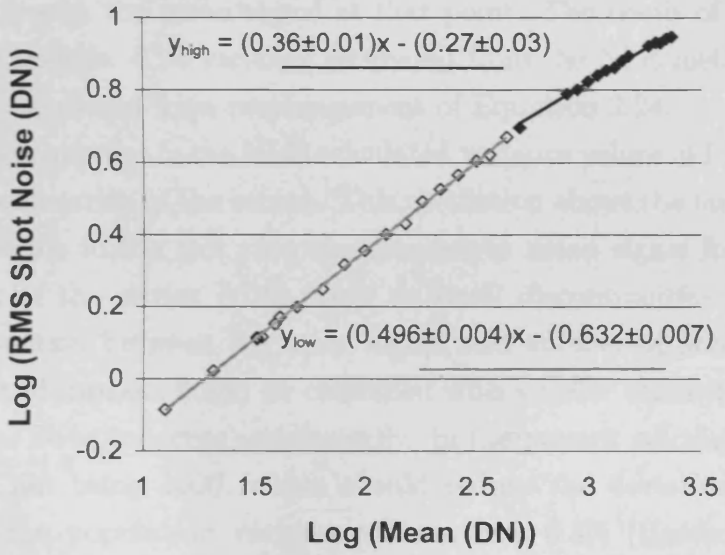


(b) Zoom

Figure 3.3: (a) Linear photon transfer curve with decomposed noise components (b) A selected portion of the shot noise limited photon transfer curve between 0 and 2300DN is shown on the right. The slope of the shot noise graph deviates from $\frac{1}{2}$ with increasing signal indicating that the sensor response is nonlinear

The 'linear' graphs show that the nonlinearity of Vanilla results in deviation from the expected behaviour for the mean-variance and photon-transfer results. We can extract sensor performance parameters only by restricting our analysis to the linear region of the sensor. This restriction does not account for the nonlinearity, it simply avoids it. It will therefore result in a less accurate estimation of the sensor

performance parameters both due to the reduced number of points used in the linear fits and the inaccurate estimation of the conversion gain.

### Nonlinear analysis results

First, nonlinear compensation (NLC) was applied to the linear photon transfer data. Figure 3.4 (a) shows that $K(e^-/DN)$, $S(e^-/DN)$ and $N(e^-/DN)$ track each other at low signal levels ($< 25,000e^-$) so there is no appreciable V/V (gain) nonlinearity. The signal and noise gains diverge above this indicating that $V/e^-$ (sensitivity) nonlinearity is present (Janesick, 2007). Figure 3.4 (b) shows the result of calculating the number of signal electrons with the linear conversion gain $K(e^-/DN)$ compared to the NLC signal gain $S(e^-/DN)$. This figure shows that the number of electrons estimated with $K(e^-/DN)$ is in severe error at high signal levels, whereas that estimated with the NLC signal gain is comparatively well behaved.

The mean-variance, quantum efficiency, conversion gain and linearity results from nonlinear estimation (NLE) are shown in Figures 3.5, 3.6 and 3.7 (a and b) respectively. The mean variance graph shows three different calculations. The measured variance values from Figure 3.2 are shown as circles. The integral slope was calculated for each of the measured values and the resulting variance found by multiplying this with the mean signal at that point. The result of this calculation is plotted as diamonds. The variance estimated from the NLE method is shown as squares and is calculated from rearrangement of Equation 2.24.

An oscillation appears in the NLE calculated variance values in Figure 3.5 around the onset of nonlinearity in the sensor. This oscillation about the measured variance values is likely due to the fact that the increase in mean signal for each intensity step was $\approx$2% of the sensor ADC range so small discontinuities are observed in the transfer function between the mean signal and number of photons. Ideally, a greater number of frames should be combined with smaller intensity steps to allow the multivariate fit to converge satisfactorily. In the present calculations, 90 frames were analysed but using 1000 frames should reduce the deviation of the sample variance from the population variance to less than 0.3% (Beecken and Fossum, 1996). Given the file size (0.5Mb) and acquisition time for 1000 frames (5 minutes), however, it would be impractical to implement this with our existing experimental arrangement. Full automation of the acquisition process would be needed to obtain such a large data set. The temperature and time stability of the sensor output would also need to be thoroughly evaluated. It should be noted that this oscillation does not impact the accuracy of the performance parameter calculations made in NLE as these are evaluated directly from the mean-variance data.

Oscillations about a central quantum efficiency value of 65% can be seen in Figure 3.6 (a). Averaging this data up to $10^5$ photons/pixel yields a value of quantum efficiency with a lower standard error across the dynamic range ($\eta$=0.65, standard

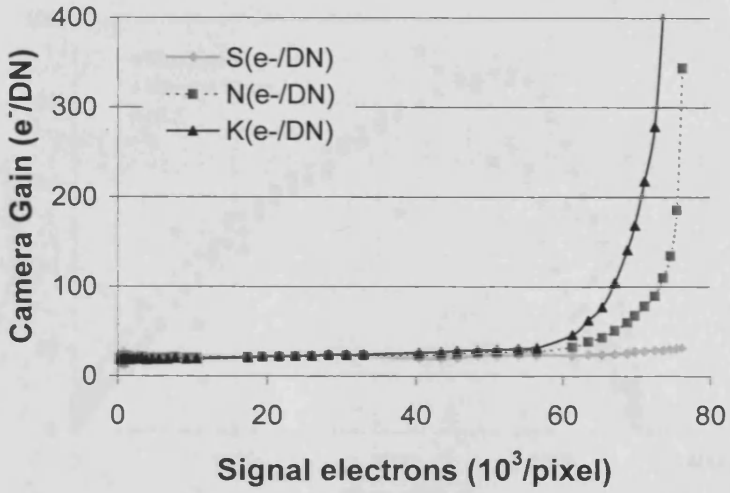


(a) NLC Conversion Gains

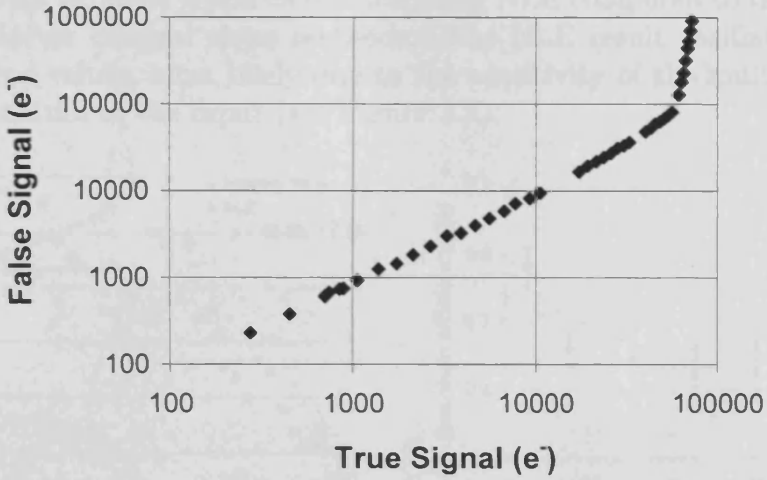


(b) False vs true signal

Figure 3.4: (a) Comparison of the 'linear' conversion gain and the 'nonlinear compensation' signal and noise gains (b) Shows how the number of signal electrons in the pixel is overestimated when $K(e^-/DN)$ is used to calculate the number of electrons ('false') as compared to $S(e^-/DN)$ ('true')

error 0.02) than that obtained using the integral slope data ($\eta$=0.68, standard error 0.07). This is because the quantum efficiency calculated from the integral slope data diverges from 30% to over 100% with increasing illumination. The initial estimate of the quantum efficiency of the sensor (Bohndiek *et al.*, 2007) gave a value of $57 \pm 6\%$ at 520nm. This measurement used a low illumination level and the linear conversion gain to calculate the sensor photocurrent therefore the value agrees with the above results within the bounds of error.

The effect of the number of frames used for analysis on the estimate of the quantum efficiency is shown in Figure 3.6 (b). Each point in the NLE series of Figure 3.6 (b) is the result of averaging the first half of the points (45) in Figure 3.6 (a), reproduced for mean-variance values calculated using between 5 and 90 frames. The error bars display the standard error in the average. This increases with number of frames because the actual number of points averaged is constant (45), but the

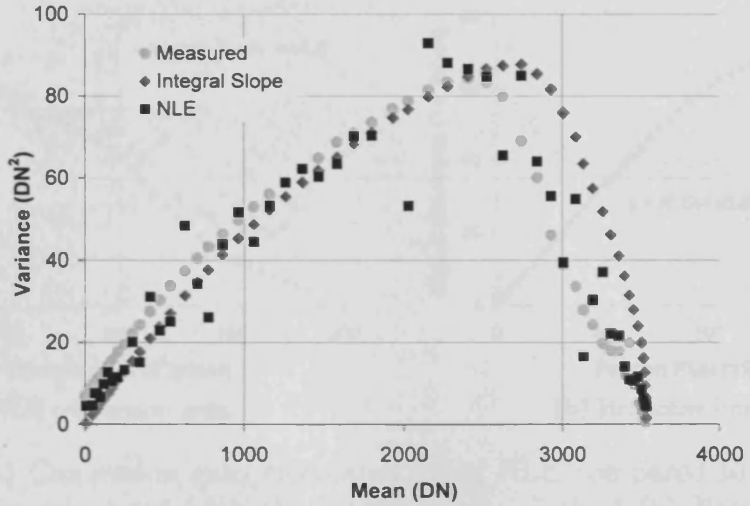


Figure 3.5: Mean variance graph calculated using NLE compared to that calculated with differential or integral slope methods. The NLE result oscillates about the actual measured values, most likely due to the sensitivity of the multivariate fit to small discontinuities in the input (see Figure 3.2).

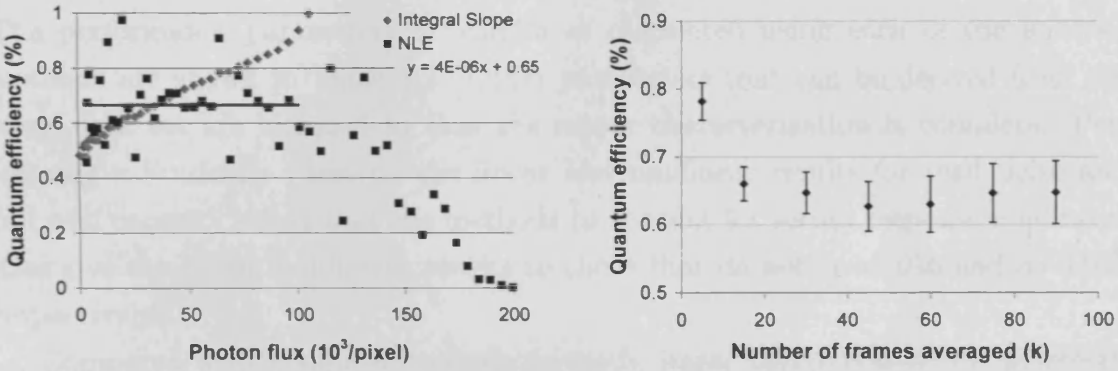


(a) NLE QE

(b) Effect of number of analysis frames

Figure 3.6: (a) Quantum efficiency (QE) calculated using the conversion gain from NLE compared to the integral slope method (b) Shows the convergence of the QE estimate with increasing numbers of frames; each QE value is the average of the first 45 points in (a), reproduced for variance values calculated using between 5 and 90 frames.

standard deviation of these points increases as using more frames to calculate the mean and variance reveals the true structure in the input data.

For the conversion gain, the oscillation settles about a value of $0.047e^{-}/DN$. Using this NLE value of the conversion gain, the number of signal electrons was calculated and then plotted as a function of the number of photons in Figure 3.7 (b). The slope of this linearity curve is consistent with the quantum efficiency found in Figure 3.6.

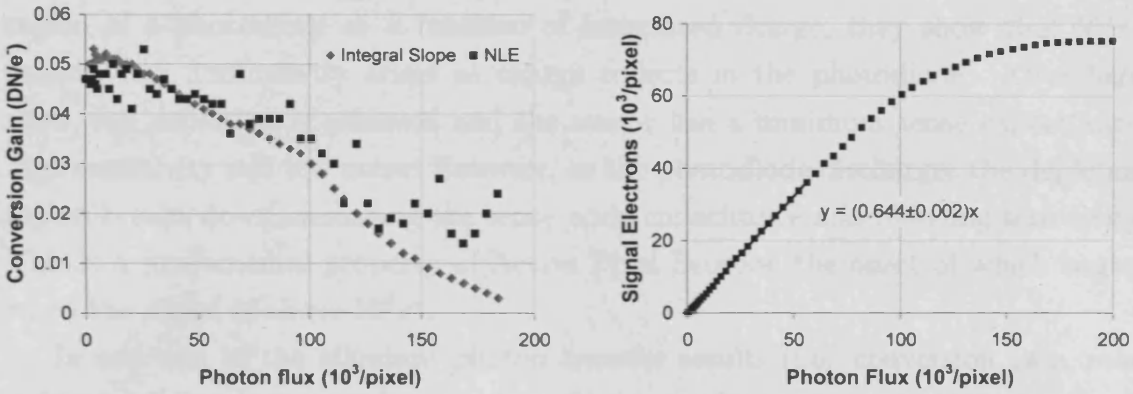


(a) NLE conversion gain

(b) Response linearity

Figure 3.7: (a) Conversion gain calculated using NLE compared to that given by conversion gain calculated with the integral slope method (b) Response linearity illustrating the number of electrons produced in the pixel (calculated using the conversion gain in (a)) for a given incident photon flux

### Discussion

The performance parameters of Vanilla as calculated using each of the analysis methods are shown in Table 3.2. Other parameters that can be derived from the same data set are included so that the sensor characterization is complete. Performing a Student's t-test on the linear and nonlinear results for read noise and full well capacity shows that the methods to account for sensor response nonlinearities give significantly different results to those that do not (p=0.016 and p=0.003 respectively).

Compared with nonlinear analysis methods, linear methods severely underestimate the full well capacity of the sensor when using the standard conversion gain K, and severely overestimate it using the 'full well' conversion gain, $K_{high}$. The reason for this is clear from the NLC result. The standard conversion gain from the mean-variance and photon transfer methods is lower than the signal gain of S=$24.1 \pm 0.1 e^-/DN$ found using NLC and so yields an underestimation of the full well capacity. Figure 3.4 shows that the standard 'linear' conversion gain K diverges significantly a high illumination so using the high illumination conversion gain $K_{high}$ to determine the full well capacity leads to an overestimation.

Linear methods give a good estimation of the read noise for this APS, but still slightly underestimate the result. The reason for this can again be seen from the NLC results where the noise gain used to determine the sensor read noise is N=$19 \pm 0.1 e^-/DN$, while the linear photon transfer method estimates the conversion gain at $K = 18.9 \pm 0.3 e^-/DN$, a similar value. This would not necessarily be true in all cases and more generally, the linear methods may seriously underestimate the sensor read noise.

The onset of nonlinearity at around $2\text{x}10^4 e^-$ is in agreement with the theory presented by Janesick *et al.* (2006). Using PISCES simulations of the depletion

region of a photodiode as a function of integrated charge, they show that $V/e^-$ (sensitivity) nonlinearity arises as charge collects in the photodiode. After hard reset, full depletion is achieved and the sensor has a minimum sense capacitance, high sensitivity and low noise. However, as the photodiode discharges the depletion region breaks down increasing the sense node capacitance and reducing sensitivity. This is a fundamental property of Active Pixel Sensors, the onset of which begins when the signal is above $10^4 e^-$.

In addition to the standard photon transfer results (i.e. conversion gain, read noise and full well capacity), a number of other performance parameters were evaluated. The linear range of the sensor was found through evaluating the integral nonlinearity to be 30% of the dynamic range, far lower than the ideal prerequisite of 80% for application of linear analysis methods. Fixed pattern noise was shown to be less than 2% at half saturation.

The results obtained using the two nonlinear analysis methods are consistent indicating that NLE could be used as a cross check of the NLC performance parameter calculation, or *vice versa*. Both analyses give useful insights into the behaviour of the sensor, with NLC providing a means to distinguish V/V and $V/e^-$ nonlinearities as well as decomposing signal and noise gains. NLE provides the quantum efficiency of the sensor as an integral part of the analysis.

Given the sensitivity of NLE to small fluctuations in the transfer curve between mean signal and photon flux, NLC should be regarded as the more stable method for small ($<$ 100 frame) data sets. It is advantageous to perform both nonlinear analysis methods if a large number of frames can be acquired since the measurement time far exceeds the data processing time. It is clear that some nonlinear analysis should always be performed for APSs, even when the sensor response appears linear from the characteristic curve, as this linearity may not extend to the mean-variance result. The results of this comparison of linear and nonlinear methods will enable an appropriate choice of analysis to be made for future Active Pixel Sensors.

### Summary of Vanilla performance

From the nonlinear characterization, Vanilla was found to have a read noise of $55e^-$, twice that of the design specification and a full well capacity of $73\text{x}10^3 e^-$, lower than the $10^5$ of the specification. Investigation of the dark exposure variation with integration time showed that the range 0.001s to 1s can be used without loss of dynamic range due to dark current. The peak spectral output occurs between 600nm and 800nm, a range similar to other CMOS imagers (Bohndiek *et al.*, 2007). Despite the use of a standard CMOS process, a high quantum efficiency of $65 \pm 2\%$ is observed at 520nm due to the small number of layers in the stack resulting in a smaller reflection loss compared to other devices. Vanilla thus exhibits favourable characteristics of a high quantum efficiency, along with low noise, dark current and

Table 3.2: Results from four analysis methods. $C_g$ makes general reference to a conversion gain. $K$ is the conversion gain evaluated at low illumination levels where the shot noise limited slope is $\frac{1}{2}$. $K_h$ is the conversion gain evaluated close to full well. FWC refers to full well capacity, DR to dynamic range, QE to quantum efficiency and SR to spectral response. FPN was evaluated at half-saturation.

| Parameters | Mean Variance | Photon Transfer | NLC | NLE |
|---|---|---|---|---|
| $C_g$ | 19.9 ± 0.1 (K) | 18.9 ± 0.3 (K) | 19 ± 0.1 (N) | 21.3 ± 0.1 |
| ($e^-/DN$) | 33.2 ± 0.3 ($K_h$) | 30.5 ± 0.3 ($K_h$) | 24.1 ± 0.1 (S) | |
| Read noise ($e^-$) | 51.8 ± 0.3 | 52.3 ± 0.7 | 54.8 ± 0.3 | 55.4 ± 0.2 |
| FWC ($e^-$) (using K) | (56.2 ± 0.3)x$10^3$ | (56.4 ± 0.7)x$10^3$ | (95 ± 6)x$10^3$ | (72.6 ± 0.3)x$10^3$ |
| FWC ($e^-$) (using $K_h$) | (94.1 ± 1.4)x$10^3$ | (91.2 ± 1.4)x$10^3$ | (72.0 ± 0.3)x$10^3$ | n/a |
| DR (dB) | 60.7 ± 0.8 (K) | 60 ± 1 (K) | 62.4 ± 0.4 | 62.3 ± 0.2 |
| QE $\eta$ | 0.60 ± 0.02 | 0.61 ± 0.02 | n/a | 0.65 ± 0.02 |
| SR ($mAW^{-1}$) | 255 ± 8 | 268 ± 8 | n/a | 278 ± 9 |
| Linear range | | 30% | | |
| $I_{dark}$ | | 40pA$cm^{-2}$ | | |
| FPN C-C | | 0.8% | | |
| FPN P-P | | 1.6% | | |

fixed pattern noise.

### 3.2.3 Demonstration of functionality

In addition to its standard full frame imaging capability, Vanilla can also perform region of interest readout in analogue mode. To test the increase in frame rate that is achieved in this mode, a blade rotating at approximately 3.5Hz was placed in front of the sensor, illuminated by an LED. Figure 3.8 shows a series of images of the blade acquired using different regions of interest. For each frame size, a sequence of 200 images was recorded. Full frame readout in analogue mode at 4fps cannot track the motion of the blade (Figure 3.8 a). If a smaller region is chosen, the readout rate increases proportionally (see Table 3.3) and the ability to resolve the edge of the blade improves. Visually, increased clarity of the passing edge with more frequent samples indicates an increasing frame rate. Using knowledge of the frame rates, the rotation frequency was verified by the number of frames needed to envisage a whole revolution. The signal profile across the blade for the different frame rates is shown in Figure 3.9.

A 6x6 pixel kernel can be accessed at almost 25Kfps in Vanilla using random pixel addressing. Vanilla can also provide access to up to 6 regions of interest concurrently. This compares favourably with previous implementations of ROI readout.

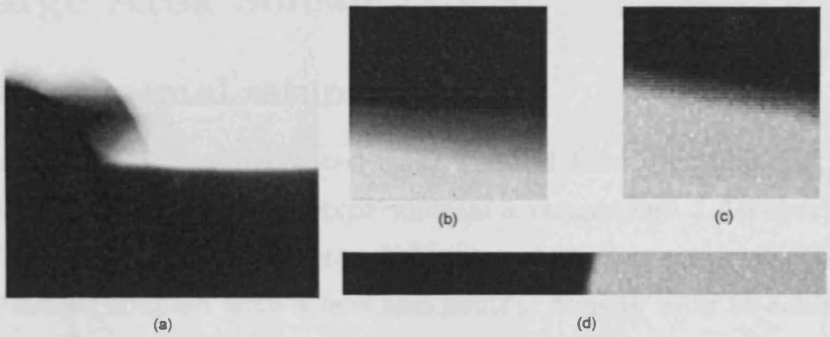


Figure 3.8: Demonstration of region of interest (ROI) readout in Vanilla using optical illumination. A blade rotating at approximately 3.5Hz was used to obscure the sensor from a light source. Full frame readout at 4fps shown in (a) is too slow to visualise the edge of the blade. Smaller regions of interest read out at higher rates so the clarity of the blade edge improves. A 100x100 region is shown in (b), a 50x50 region in (c) and a 10x200 region in (d).

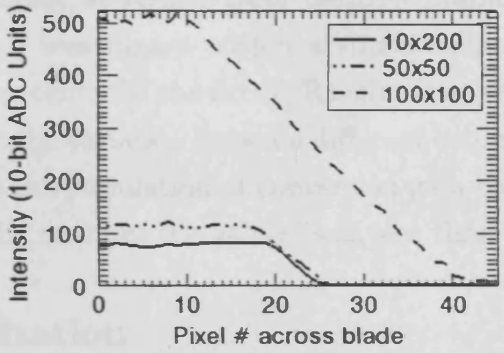


Figure 3.9: Profiles across the blade edge (in pixels) illustrates the increase in the sampling frequency with decreasing ROI size. The width of the edge is 33 pixels in Figure 10 (b) and only 7 in (d).

Table 3.3: Frame rates for region of interest readout in the current data acquisition system; see Figure 3.8 for illustration

| Region of interest size | Frame rate (fps) |
|---|---|
| Full frame (520x520) | 4 |
| 100x100 | 110 |
| 50x50 | 432 |
| 10x200 | 554 |
| 6x6 (minimum size) | 24,395 |

For example, Schrey *et al.* (2002) could obtain 850fps for a single 128x128 ROI, but used skip logic so the minimum kernel was limited to 32x32 pixels. Commercially, Photron's Ultima APX-RS can read a single 128x16 pixel kernel at 250Kfps (Photron, 2008), reaching a higher frame rate than Vanilla but again with a larger minimum kernel size.

## 3.3 Large Area Sensor (LAS)

### 3.3.1 Experimental setup

The Large Area Sensor was evaluated using the flat field illumination protocol described above, but with a different experimental arrangement. LAS characterization was performed at Rutherford Appleton Laboratory using an array of LEDs at 546nm (bandwidth 30nm) coupled with a lens and neutral density filter to achieve uniform illumination. Given the large size of the array and the precision of the ADC, it was impractical in terms of data storage to acquire data in small illumination steps across the dynamic range, making mean-variance and NLE analysis unsuitable. As a result, photon transfer and NLC methods were applied to the data acquired from LAS.

LAS was operated in hard reset mode and 10 frames were recorded at each intensity level for averaging of results from multiple frame pairs. The region of interest used for analysis was placed within a single column ADC output of one sub-stitched region in the centre of the array. Results from this region are presented below. It was found that the variation between different column outputs and stitched regions, calculated from the population of conversion gain results as the ratio of the standard deviation to the mean of the values, was less than 4%.

### 3.3.2 Characterization

The response of the Large Area Sensor to an incident photon flux and the related integral nonlinearity are shown in Figures 3.10 (a) and (b) respectively. It is clear from the calculation of INL that the onset of $V/e^-$ nonlinearity occurs at around $2x10^4e^-$ as expected from the discussion in Section 3.2.2. A surprising result is the low quantum efficiency of just 19% estimated from the photoresponse graph. Discussions with the foundry indicate that LAS has a particularly complex 10 layer stack meaning that pronounced oscillations are observed in the quantum efficiency between 500 and 600nm. The quantum efficiency values vary between 30% and 70% assuming 100% fill factor, therefore for LAS would vary between 19% and 44%.

The standard linear photon transfer result for LAS is shown in Figure 3.11. The onset of nonlinearity is again marked by a change in the slope of the shot noise limited curve from 0.5 to 0.3, observed at around 3000DN. The signal and noise gains are decomposed in Figure 3.12 (a) and the behaviour of the 'false vs true' signal is shown in (b). This figure shows that some V/V (gain) nonlinearity is present in LAS as initially, a decrease in all gains can be observed (Janesick, 2007). The gain values separate dramatically after around $10^4e^-$ have been accumulated due to $V/e^-$ nonlinearity. Using the signal gain, the number of electrons accumulated under dark conditions with increasing integration time was evaluated and the dark current of the sensor was found to be $11pAcm^{-2}$.

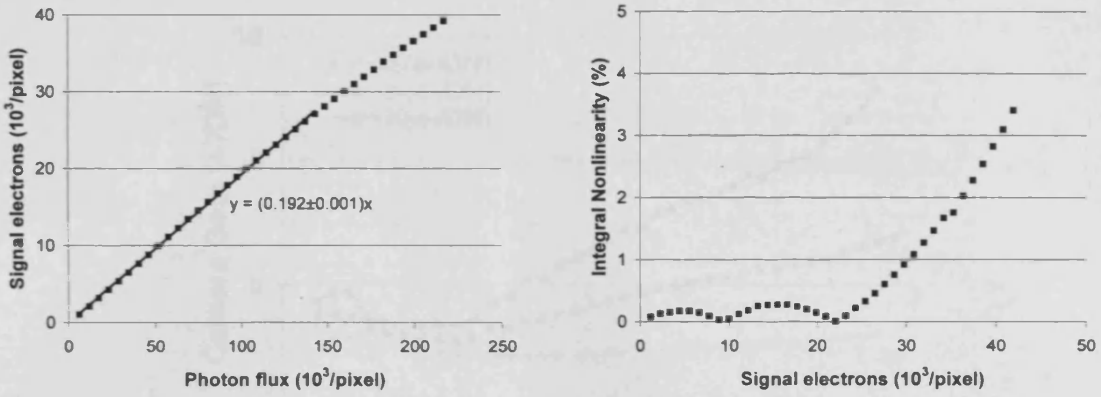


(a) Linearity (b) INL

Figure 3.10: Response of LAS to a given input photon flux when the number of signal electrons is calculated using the NLC signal gain

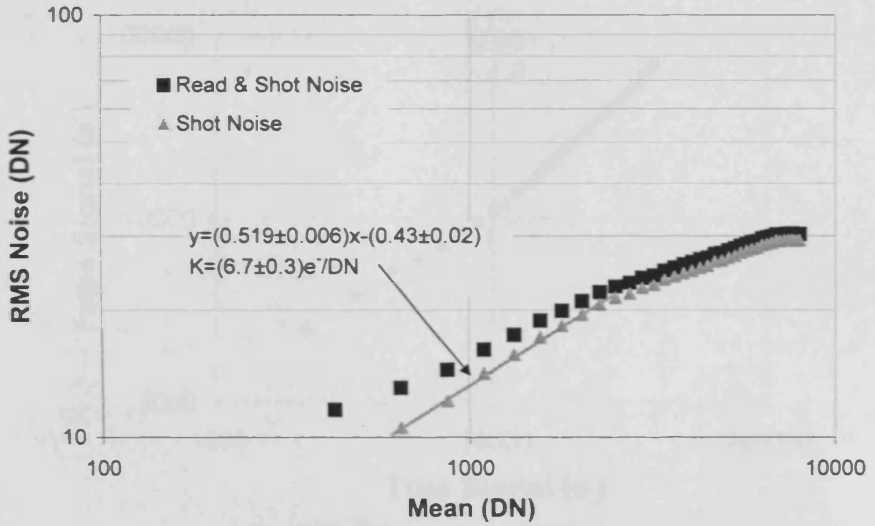


Figure 3.11: Read and Shot noise photon transfer curve, together with the decomposed shot noise component, is shown.

An example of how the sensor can be linearized is shown in Figure 3.13. The noise gain is used to convert the r.m.s. noise in DN to $e^-$, while the signal gain is used to convert the mean. The result accounts for the nonlinearities in both signal and noise gains and provides a linear shot noise limited photon transfer curve. This illustrates how the knowledge gained during characterization can be used to correct the inherent nonlinearity of the device for general imaging scenarios, by deriving the signal and noise gains on a per pixel basis.

While it was noted above that the conversion gain differs by less than 4% between the different column outputs and sub-stitches of the array, it was observed that images obtained from the sensor exhibited fixed pattern noise due to both. Examples of images from the sensor can be seen in the next section. Referring to Table 3.4, an attempt was made to find the effect of each of these sources of fixed pattern noise on the overall array. Using an average of 50 frames at half-saturation, the fixed pattern noise of the whole array was found to be 1.5% due to column FPN and 6%

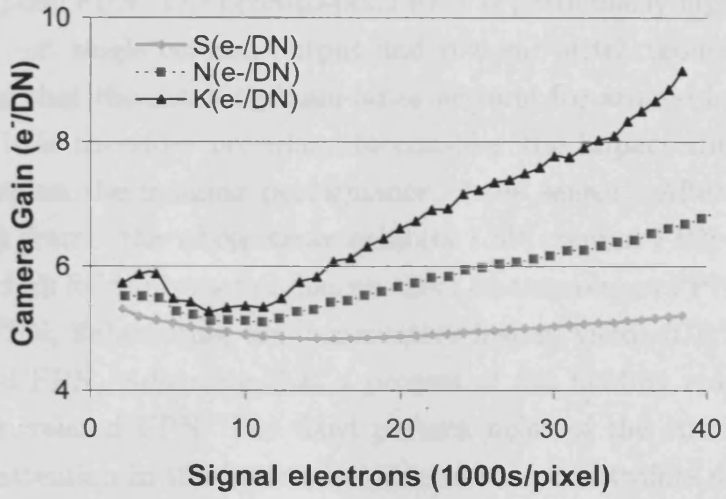


(a) NLC gains

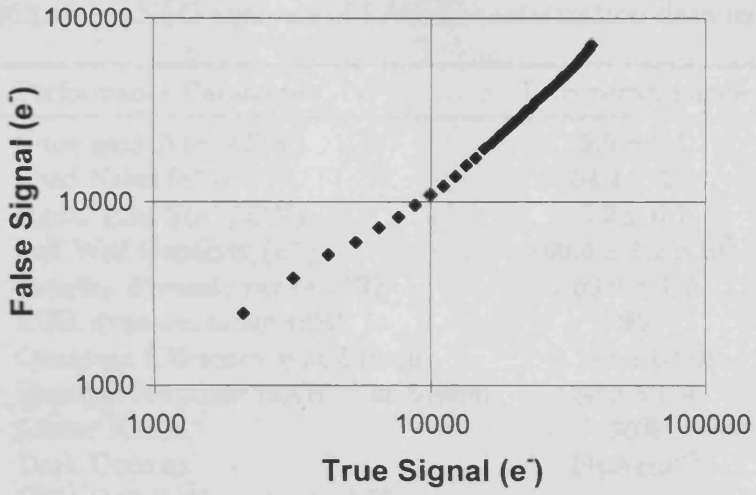


(b) False vs true signal

Figure 3.12: (a) Comparison of the 'linear' conversion gain with the signal and noise gains (b) The initial decrease in conversion gains at low signal levels indicates gain nonlinearity is present, while the later increase in conversion gains can be attributed to $V/e^-$ nonlinearity.

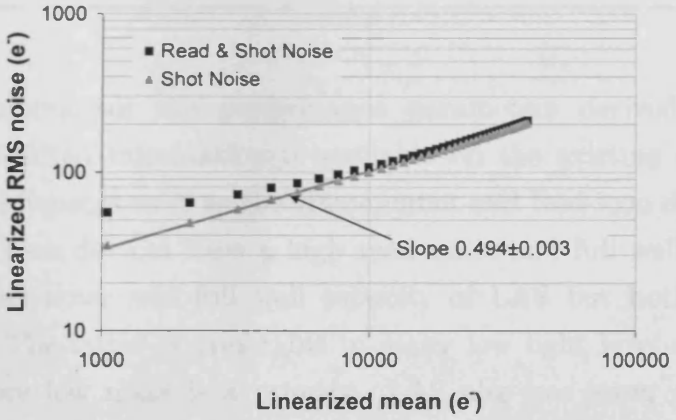


Figure 3.13: The photon transfer curve may be linearized by converting the data to signal electrons using the signal and noise gains.

due to pixel-to-pixel FPN. The pixel-to-pixel FPN is particularly high, but confining calculations to just single column output and row sub-stitch reduces this value to 2.9%, indicating that the stitching boundaries account for around half of the pixel-to-pixel FPN. It is therefore necessary to consider the impact this fixed pattern noise could have on the imaging performance of the sensor. After subtraction of an average dark frame, the whole array exhibits 1.5% column FPN and 4.0% pixel FPN therefore dark field subtraction has no effect on the column FPN but somewhat reduces pixel FPN. Subtracting two consecutive frames yields 0.01% column FPN and 0.22% pixel FPN, indicating that a process of flat fielding may be needed to correct the gain related FPN. The fixed pattern noise of the stitched boundaries merits further attention in the future, but due to time constraints no further study will be presented in this work.

Table 3.4: Results from NLC analysis of LAS characterization data using hard reset.

| Performance Parameter | LAS performance |
|---|---|
| Noise gain $N(e^-/DN)$ | $5.5 \pm 0.1$ |
| Read Noise ($e^-$) | $54.4 \pm 1.0$ |
| Signal gain $S(e^-/DN)$ | $5.2 \pm 0.1$ |
| Full Well Capacity ($e^-$) | $(60.4 \pm 1.2)$x$10^3$ |
| Imaging dynamic range (dB) | $60.9 \pm 1.7$ |
| ROR dynamic range (dB) | 95 |
| Quantum Efficiency $\eta$ at 546nm | $0.192 \pm 0.001$ |
| Spectral Response $mAW^{-1}$ at 546nm | $80.3 \pm 0.4$ |
| Linear Range | 30% |
| Dark Current | $11pAcm^{-2}$ |
| FPN C-C (half-saturation) % | |
| Whole array | 1.5 |
| Single column output | 0.8 |
| Single row sub-stitch | 0.6 |
| FPN P-P (half-saturation) % | |
| Whole array | 6.0 |
| Single column output | 3.2 |
| Single row sub-stitch | 2.9 |

Table 3.4 summarises the performance parameters derived from the NLC analysis. Only limited information is available on the existing commercial large area Active Pixel Sensors such as the Hamamatsu and Rad-icon devices mentioned in Chapter 1. These devices have a high read noise and full well capacity, rather than the low read noise and full well capacity of LAS but both achieve similar dynamic range. The latter is preferable in many low light level scientific imaging applications where low noise is a priority. LAS also has lower dark current and superior conversion gain compared to these sensors. Compared to Scheffer (2007), the only publication containing detailed characterization of a large area device, LAS has around half the quantum efficiency relative to fill factor. LAS does, however,

exhibit far lower dark current and half the read noise, but a factor of 10 less full well capacity leads to a dynamic range of just 61dB compared to their 76dB if operated without the regions of reset. With regions of reset enabled, a minimum of 95dB can be achieved (see Chapter 2). The Large Area Sensor can therefore compete with existing large area Active Pixel Sensors in terms of dark current, read noise and conversion gain, but the complex stack above the active layer of the pixel means it suffers from a relatively poor quantum efficiency. This could be overcome in future generations of the device by choosing a different foundry, or using a modified CMOS process.

### 3.3.3 Demonstration of functionality

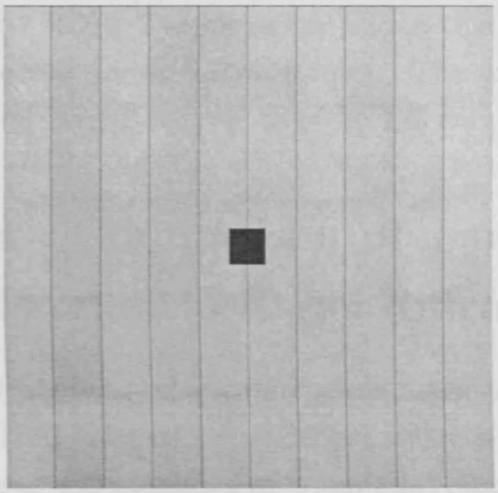

(a) Central ROR

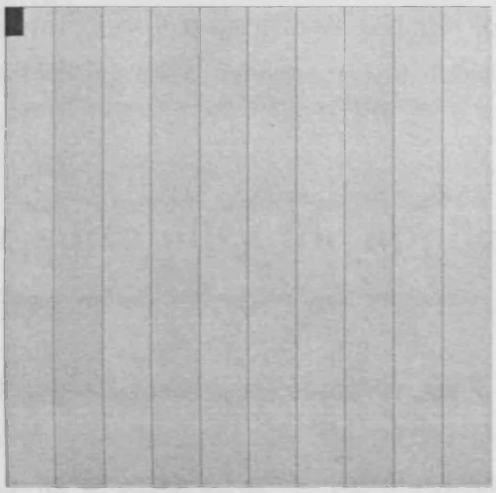

(b) Corner ROR

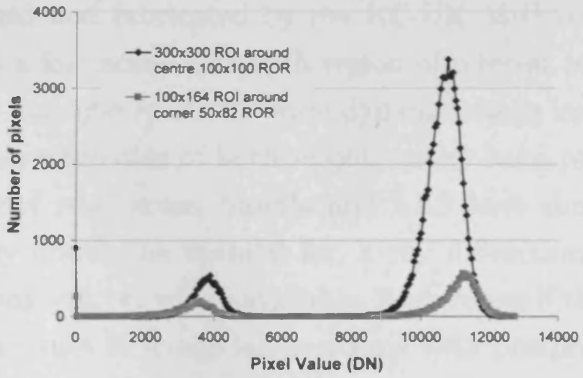


(c) Histogram of values

Figure 3.14: Demonstration of a region of reset (ROR) with 181$\mu$s integration time in a surrounding area of 2.3s. (a) ROR of 100x100 pixels at (625,625) (b) ROR of 50x82 pixels placed at (0,0) (c) Histograms of pixel values taken around the RORs illustrating that while the normal region is saturated, the ROR is not. The five evenly spaced horizontal stripes observed in the images are due to fixed pattern noise at the stitching boundaries; dark columns are due to the defective columns.

The flexible region of reset capability included in each LAS pixel can be used to enhance the dynamic range of the device under static imaging conditions. Two

different regions of reset (RORs) can be defined on the sensor in addition to the global reset, provided they are nested so that the central region has a shorter integration time than the outer region. The nesting is required because the regions of reset are created using a second and third rolling shutter phase. The integration time is defined by setting a number of rows to wait before these rolling shutters are performed. The integration time of a given pixel therefore depends on which rolling shutter was the last to be applied to it. In Figure 3.14 (a), a 100x100 ROR has been placed at (625,625) and the sensor illuminated uniformly. The integration time of the outer region is the maximum available (2.3s), while the ROR has an integration time of 181$\mu$s yielding a dynamic range of 86dB. An ROR of 50x82 pixels is placed at (0,0) in Figure 3.14 (b). Figure 3.14 (c) presents the histogram of values in a 300x300 region centred on the 100x100 ROR and a 100x164 region centred on the 50x82 ROR. The histogram shows that the outer array is saturated and the ROR is barely above the dark level. The pixels yielding zero values are the defective columns that occur once every 135 columns.

## 3.4 Comparison of sensor suitability for application in X-ray diffraction

In Chapter 1, the requirements for an ideal angle dispersive detector for an X-ray diffraction-based breast biopsy analysis system were laid out and the Active Pixel Sensor was identified as a potential candidate for meeting all of the requirements in a single device in the near future. In this chapter, the characteristics of two Active Pixel Sensors designed and fabricated by the RC-UK M-I$^3$ consortium have been presented. Vanilla is a low noise APS with region of interest readout and LAS is a large area APS with multiple resets for wide dynamic range imaging.

The measured characteristics of both sensors under hard reset are compared in Table 3.5. In terms of read noise, Vanilla and LAS have similar performance at around 55$e^-$, slightly above the optimal for X-ray diffraction. Lower read noise could be achieved using soft or, where available, flush resets if the linear range could be sacrificed and the issues of image lag overcome with postprocessing. The linear range of both sensors is only around 30%, but using the signal and noise gains derived from the NLC characterization, the entire dynamic range can be linearized by converting the recorded signal and noise from digital numbers to electrons.

For the X-ray diffraction application, Vanilla has superior performance in terms of quantum efficiency and is let down only by its small area and relatively narrow dynamic range. Requirements could be relaxed if only scattered X-rays were to be recorded, rather than a combination of transmitted and scattered X-rays, in which case neither of these limitations would apply. The dynamic range required to measure both is at least 80dB making LAS, with its programmable regions of reset,

Table 3.5: Comparison of M-I$^3$ sensors to existing CCD X-ray diffraction detectors. X-ray converters are an X-ray Image Intensifier (XRII), fibre optic taper (FOT) with scintillator and scintillator with fibre optic plate (FOS). - indicates quantity is unknown for this device. 'XRD performance' rates the overall suitability of each device for use in an X-ray diffraction based breast biopsy analysis system out of 8 by counting the number of criteria between 'Sensor area' and 'Readout time' where the sensor matches the system requirements

| | Yagi *et al.* (2004) | Tate *et al.* (2005) | Ito *et al.* (2007) | Vanilla | LAS |
|---|---|---|---|---|---|
| X-ray imaging area (cm$^2$) | 14x11 | 4.9x4.9 | 24x24 | 1.3x1.3 | 5.4x5.4 |
| Equivalent pixel size ($\mu$m) | 220 | 48 | 240 | - | - |
| Sensor area (cm$^2$) | 0.7x0.5 | 2.5x2.5 | 2.5x2.5 | 1.3x1.3 | 5.4x5.4 |
| Sensor pixel size ($\mu$m) | 9.9 | 24 | 24 | 25 | 40 |
| Conversion gain ($e^-$/DN) | 20 | 4 | 4 | 20 | 5 |
| Noise ($e^-$rms) | 17 | 12 (−35°C) | 12 (−30°C) | 55$e^-$ | 54$e^-$ |
| Dynamic range (dB) | 62 | 88 | 86dB | 62dB | from 95dB |
| QE (optical, %) | up to 40 | 80% at 545nm | up to 40% FI | up to 70% | 20% at 520nm |
| Frame rate (fps) | 290 | 0.05 | 0.5 | up to 24x10$^3$ | up to 13x10$^3$ |
| Readout time | 10ms | 21s | 1.9s | 10$\mu$s | - |
| X-ray converter | XRII | Lens coupled phosphor | FOT coupled phosphor | FOS | FOS |
| XRD performance | 4 | 5 | 4 | 4 | 6 |

the only sensor to satisfy this requirement.

In terms of the functionality demonstrated for each sensor, LAS provides tailored characteristics for X-ray diffraction studies. The regions of reset yield a simple and effective mechanism to visualize the scattered and transmitted X-ray beams simultaneously using multiple exposure times on the array. This would enable correction to be made for self attenuation of X-ray photons within the sample, but also yields the possibility of performing both X-ray transmission and diffraction imaging simultaneously.

Based on the results of these characterization studies, both sensors have the potential to perform well in an X-ray diffraction system. In Table 3.5, the characterization results of Vanilla and LAS are compared to results from recent characterization studies three charge coupled device (CCD)-based X-ray diffraction systems. Each of the CCD systems has a form of demagnification via either an X-ray image intensifier, fibre optic taper or lens based system. These introduce artifacts and losses into the imaging system as described in Chapter 1 so it has been assumed that a wafer scale APS-based system would directly couple to a scintillator via a small fibre optic stud. There is, however, no reason why the current APSs could not be coupled with demagnifying optics to achieve competitive area if required.

Overall, it can be seen that Vanilla and LAS compare favourably with the CCD systems in terms of pixel size, conversion gain, dynamic range and readout time. Vanilla also exhibits very competitive quantum efficiency, while LAS has the highest dynamic range. The APSs have higher read noise than the CCDs, but the two CCDs with best overall performance (Tate *et al.*, 2005; Ito *et al.*, 2007) require peltier cooling to achieve their noise figure. This table illustrates that Vanilla and LAS are not only competitive with other CMOS Active Pixel Sensors, but also compare favourably with the current 'gold standard' X-ray diffraction detector, the CCD. Given the potential for future developments in APS technology, it is therefore prudent to implement a prototype breast biopsy analysis system that takes advantage of the benefits of Vanilla and LAS to test the potential of such a system. In the following chapters, such a system will be designed, implemented and tested and conclusions drawn as to its future potential.

# Chapter 4

# Development of an X-ray diffraction system using Active Pixel Sensors

## 4.1 Overview

This chapter describes the development of an experimental system for angle dispersive X-ray diffraction studies of breast biopsy samples. The system employs a polychromatic X-ray beam, which is filtered to create a quasi-monochromatic 'pink' beam. An Active Pixel Sensor is employed as the angle dispersive detector. It will be referred to as the 'Active Pixel X-ray Diffraction', or APXRD, system. A series of pure, tissue-equivalent, samples are used to test the system covering a range of compositions relevant to breast biopsy analysis, as well as bone mineral density evaluation and kidney stone identification.

The design of the X-ray diffraction system was achieved using a linear systems model of the scintillator-coupled APS, or 'Active Pixel Flat Panel Imager' (APFPI). While both Vanilla and LAS could be used as the angle dispersive detector, LAS was not released until May 2008 so the system development and characterization in this chapter was performed with Vanilla. A feasibility study using the Large Area Sensor is presented in Chapter 5.

Two validations of the linear systems model were made. To verify the energy dependent sections, the 'pink' spectrum was combined with monoenergetic diffraction data in a linear superposition integral. The diffractometer (monoenergetic 8keV copper K$\alpha$ X-rays) data catalogued in the International Centre for Diffraction Data (ICDD) Powder Diffraction File was used. To verify the predicted output intensity, the conversion function of the APFPI between incident X-ray photons and signal electrons ($e^-$/X-ray) was measured and compared to the final value produced by the model.

The implementation of the APXRD system involved optimization of both the

physical parameters of the setup including the collimator angular acceptance, as well as operational parameters of Vanilla including reset, ADC range, integration time and conversion gain. An abbreviated presentation of the experimental design and implementation was made in Bohndiek *et al.* (2008b). All model development was completed independently for this work (SB); other authors (initials given) helped with the energy dispersive measurements (EC) and advised on APXRD experimental design (AO, GR, RS) or Vanilla implementation (CA, AC, MP, RT). Three plastic phantoms, designed to evaluate the angular acceptance and contrast potential of the APXRD system, are also presented.

## 4.2 Tissue-equivalent samples

A number of biological tissue equivalent materials were used to test the feasibility of using Active Pixel Sensors in X-ray diffraction. Samples interrogated cover the three main application areas of X-ray diffraction in medicine: breast biopsy analysis (the focus of this work), bone mineral density evaluation and kidney stone identification. The two other application areas were considered for two reasons. Firstly, the ICDD catalogue details the relative intensity of reflections as a function of d-spacing but this is not available for amorphous materials meaning bone mineral and kidney stone materials are listed, while breast tissue is not. Secondly, with the development of the APXRD system aimed at ease of implementation, these other application areas may also benefit from such a system should the scatter signatures measured provide sufficient sensitivity to sample composition.

Tissue equivalent substances were contained in 6mm diameter thin-walled plastic cylinders. Samples containing more than one material were also prepared by measuring content by mass and mixing by hand. They were housed in identical containers to those used for pure samples. The details of all biological equivalent materials, along with abbreviations that will be commonly used in the rest of this work, can be found in Table 4.1.

A description of the composition of human breast tissue was provided in Chapter 1. As human breast tissue was not available for these measurements, a number of substitute materials were sought. The scatter signature of adipose tissue is well matched by both lard and pork fat (Cook, 2008a). Water and chicken breast meat have a similar scatter signature to glandular (fibrous) tissue and cancerous tissue can be simulated using pork muscle (Kidane *et al.*, 1999; Peplow and Verghese, 1998). A selection of mixed samples were also prepared to test the capability of the system to identify different components in 'biopsy equivalent' samples. These will be described in Chapter 5.

As the decline of trabecular bone mineral content in diseased bone is accompanied by an increase in adipose tissue content, X-ray scattering measurements of

Table 4.1: Sample materials used for X-ray diffraction studies. Breast tissue composition was taken from Kidane *et al.* (1999), kidney stone prevalence from Moe (2006) and bone composition from Nyman *et al.* (2005).

| Sample material | Abbrev. | % of composition and/or occurrence |
|---|---|---|
| *Breast Tissue Substitutes* | | |
| Lard | None | Adipose tissue equivalent scatterer |
| Pork Fat | Fat | As above |
| Water (distilled) | None | Glandular tissue equivalent scatterer |
| Pork Muscle | None | Tumour equivalent scatterer |
| Chicken meat | None | Fibrous tissue |
| *Kidney Stone Substitutes* | | |
| Calcium oxalate monohydrate | COM | 40-60% of detected stones |
| Calcium phosphate | CP | 20-60% of detected stones |
| Calcium phosphate dihydrate | CPD | 2-4% of detected stones |
| Magnesium ammonium phosphate | MAP | 5-15% of detected stones |
| Uric acid | UA | 5-10% of detected stones |
| *Bone Substitutes* | | |
| Bone - Mineral phase | HAP | 43% by volume |
| Bone - Organic matrix | Collagen | 32% by volume |
| Water | None | 25% by volume |

bone can be correlated with the ratio of adipose tissue to bone mineral (Newton *et al.*, 1992). Pure samples composed of hydroxyapatite (HAP) and compacted collagen from bovine achilles tendon (both from Sigma Aldrich Co.) were used as 'bone equivalent' samples. Lard was used as the adipose tissue equivalent. A mixed sample of HAP and lard was also prepared in proportions of 50:50 by mass.

For kidney stone investigations, chemically pure samples for each stone group (oxalate, phosphate and urate) were obtained from Sigma Aldrich Co. (Davidson *et al.*, 2005). These were available for all samples except calcium oxalate dihydrate (COD). The prevalence of the different kidney stone types has been described by Moe (2006) and is detailed in Table 4.1. Cystine was omitted due to its particularly low prevalence. Kidney stones are rarely found in a pure form. The definition of a 'pure' stone is one containing 70% or more of one constituent. Prevalent mixtures include oxalate-apatite stones (35-40% of all detected stones) and oxalate-uric acid stones (5% of all detected stones) (Moe, 2006). Mixed samples of calcium oxalate and apatite as well as calcium oxalate and uric acid were thus prepared according to the proportions given by Pak *et al.* (2003) (COM:HAP 70:30) and Parks *et al.* (1997) (COM:UA 30:70, 50:50, 70:30).

Plastics are commonly used as tissue equivalent materials for testing transmission imaging systems (Kosanetzky *et al.*, 1987). Similarly, it is possible to select plastics to test X-ray diffraction systems, although different criteria are applied i.e. diffraction peak position is considered as well as the linear mass-attenuation

coefficient. The plastics selected as well known calibration samples are listed in Table 4.2. In this work, six plastics whose primary diffraction peaks lie in the range $0.8 < x < 1.4nm^{-1}$ were selected. They are: acrylic, polyethylene (PE), polypropylene (PP), polytetrafluoroethylene (PTFE), polyvinylchloride (PVC) and polyoxymethylene (Acetal). X-ray diffraction and linear attenuation data for these six materials is listed in Table 4.2, acquired from the ICDD Powder Diffraction File and Boone and Chavez (1996) respectively.

Table 4.2: Data used to design phantoms. Chemical formula, attenuation coefficient ($\frac{\mu}{\rho}$) at 42keV and density ($\rho$) obtained from NIST XCOM tables for all materials except Acetal. 'x' is the momentum transfer parameter; primary refers to the X-ray diffraction peak with dominant intensity. Diffraction data is from the International Centre for Diffraction Data (ICDD). *N.B.* MD=medium density

| Plastic | Formula | Primary x ($nm^{-1}$) | $\frac{\mu}{\rho}$ ($cm^2g^{-1}$) | $\rho$ ($gcm^{-3}$) | $\mu$ ($cm^{-1}$) |
|---|---|---|---|---|---|
| Acetal | $[OCH_2]_n$ | 1.40 | 0.23 | 1.43 | 0.33 |
| Acrylic | $[C_5O_2H_8]_n$ | 0.82 | 0.23 | 1.19 | 0.27 |
| PE | $[C_2H_4]_n$ | 1.22 | 0.23 | 0.93 (MD) | 0.21 |
| PP | $[C_3H_6]_n$ | 0.69 | 0.22 | 0.91 | 0.20 |
| PTFE | $[C_2F_4]_n$ | 1.00 | 0.25 | 2.2 | 0.55 |
| PVC | $[C_2H_3Cl]_n$ | 1.08 | 0.73 | 1.4 | 1.02 |

## 4.3 Energy and Angle Dispersive X-ray Diffraction System

X-ray diffraction peaks are catalogued in terms of their momentum transfer argument (Equation 1.3), which means that the combined energy and angle dispersion of scattered polyenergetic X-rays contains all available X-ray diffraction information. Knowledge of the X-ray diffraction properties of all of the samples under 'ideal' conditions yields an opportunity to model the performance of the APXRD system. This will be described in Section 4.5.2. Further, as all of the materials tested are 'equivalents' rather than actual tissue samples, their chemical properties may deviate from those expected in theory. A complete diffraction data set enables the scatter peaks of all sample materials that are accessible in the energy and angle range of interest to be catalogued in a measurement that is independent of the Active Pixel Sensor system. The X-ray scatter signatures acquired with the APXRD system can therefore be verified to ensure that they truly represent scatter from the material and are not simply experimental artifacts.

A planar High Purity Germanium (HPGe) Ortec EG&G photon detector was mounted on a rotating arm as shown in Figure 4.1 (Bohndiek *et al.*, 2008b; Cook, 2008a). The first aperture, composed of a layer of lead and a layer of aluminium, is of 5mm diameter and blocks radiation scattered from the X-ray tube casing and

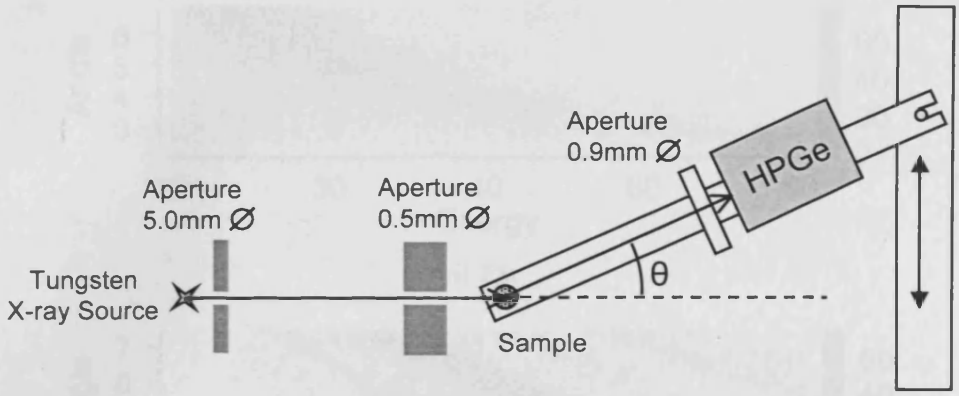


Figure 4.1: Instrumentation for energy and angle dispersive X-ray diffraction experiments (not to scale). HPGe detector mounted on a rotating arm to enable both energy and angle dispersion of scattered photons from the sample to be recorded. Data was taken between 2.5° and 10°. ∅ indicates diameter

window. The second aperture is a pinhole insert of 20mm depth and 0.5mm diameter. The collimation system restricted the angular acceptance at the detector to less than 0.1°. The translation stage used to rotate the arm could reach 12° and moved in $(0.1 \pm 0.05)°$ steps. Using Equation 1.5 with an energy resolution of 1% at 60keV, the limiting momentum transfer resolution of the system at 2.5° and 70keV is $0.05\text{nm}^{-1}$ (5%).

Angular positions were calibrated using a material with a single, well-defined diffraction peak (caffeine). An AGO Installations Philips Tungsten target industrial X-ray source with 0.8mm Be inherent filtration and nominal focal spot size of 3mmx3mm was operated at 70kVp and 15mA. For each sample, the detector was rotated between 2.5 and 10° and at each position, an energy spectrum was acquired with 600s live time. A background data acquisition was made with an empty sample holder in place so scatter from the experimental setup could be subtracted, leaving only X-ray scatter from the sample itself. The tungsten spectrum was recorded using a 30$\mu$m pinhole at 0° for filtration modelling (Section 4.5.3). Breast tissue equivalent samples were recorded at coarser angular increments due to time constraints. Data acquired from this system is henceforth referred to as the 'complete data set'.

Examples of the resulting diffraction data for fat and hydroxyapatite are shown in Figure 4.2. Energy dispersion is displayed on the x axis, angle dispersion on the y axis and number of X-ray counts on the z axis (white=0 counts). The fat sample was used in the optimization of the APXRD experimental setup, while hydroxyapatite was used to validate results from the linear systems model.

## 4.4 The Active Pixel Sensor as an X-ray detector

To create an X-ray imaging system using an Active Pixel Sensor, incident X-rays must be converted into visible light. For Vanilla, the peak sensitivity range is 540-

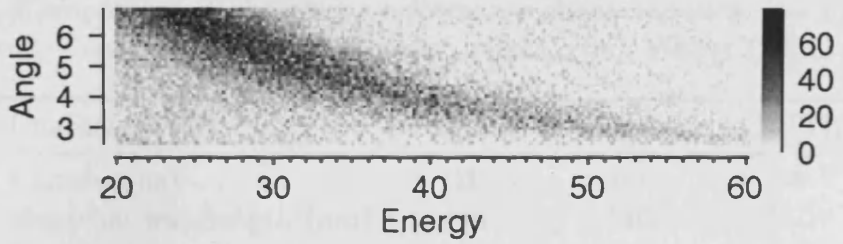


(a) Fat

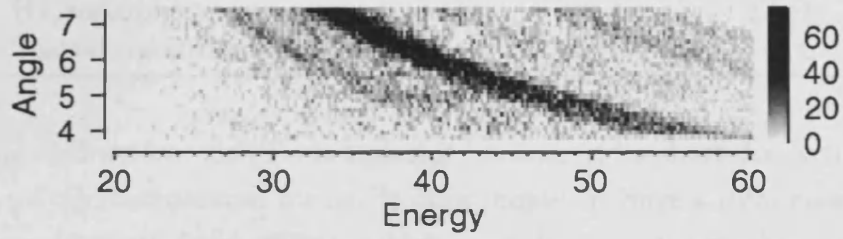


(b) Hydroxyapatite

Figure 4.2: Energy-angle diagrams: x axis shows the photon energy in keV; y axis shows the angle in degrees; z axis shows number of counts recorded. Hydroxyapatite shows a major peak at $1.8\text{nm}^{-1}$, while fat shows a single broad peak about $1.1\text{nm}^{-1}$.

620nm (Bohndiek *et al.*, 2007). An ideal scintillator material should (Knoll, 2000):

1. Convert the energy of incident X-ray photons into visible light via prompt fluorescence with high efficiency and linearity
2. Be transparent to its own emission wavelength
3. Have a short decay time for light emission
4. Be scalable to a large area

Materials with potential to satisfy these requirements fall into the categories of 'organic' or 'inorganic'. 'Organic' scintillators include plastics and glasses but with peak emission wavelengths less than 450nm, are not well matched with the peak response of silicon. The scintillation mechanism for 'inorganic' scintillators is governed by the properties of dopants, or 'activators', so it is possible to tailor the wavelength of emission based on the activator used.

Table 4.3 presents the characteristics of three different scintillators, two of which meet the requirements for coupling to a silicon sensor. NaI(Tl) is included as a standard reference material as it is perhaps the best understood scintillation material. Terbium doped gadolinium oxysulfide ($Gd_2O_2S$:Tb) has competitive properties in terms of emission wavelength and efficiency, but is not produced in a structured form so has a lower spatial resolution. It also has a slow decay time, meaning that afterglow from a previous exposure may degrade the next image. Thallium doped caesium iodide, CsI(Tl), is an alkali halide material with high intensity emission peaked around 550nm. It can be grown in a structured form with columns of $6\mu m$ diameter using a patterned substrate to reduce lateral spreading of fluorescence light.

Table 4.3: Comparison of phosphor performance characteristics. U=unstructured, S=structured, C=single crystal, P=powder. Nikl (2006); Weber (2002)

| Characteristic | NaI(Tl) | $Gd_2O_2S$:Tb | CsI(Tl) |
|---|---|---|---|
| Photons/keV | 41 | 60 | 66 |
| Emission wavelength (nm) | 410 | 540 | 550 |
| Density ($gcm^{-3}$) | 3.67 | 7.3 | 4.51 |
| Decay time ($\mu s$) | 0.23 | 600 | 0.8 |
| Hygroscopicity | Yes | No | Slight |
| Spatial resolution (U/S/P) | U, C | U, P | S, C |

For X-ray diffraction, CsI(Tl) is superior because of its short decay time and the availability of microstructured forms. It does, however, have a dual caesium/iodine K edge around 33keV (Nikl, 2006), which must be considered when selecting the X-ray spectrum to use with the APXRD system as it will affect APFPI sensitivity. Structured CsI(Tl) was obtained from Hamamatsu Photonics in two different areas: 1.8x1.8$cm^2$ for coupling to Vanilla, and 5.4x5.4$cm^2$ for the Large Area Sensor. Each scintillator is 150$\mu m$ thick and is grown on a 3mm thick etched fibre optic plate (FOP). The combined scintillator and fibre optic plate are referred to as a 'fibre optic scintillator' (FOS).

The FOP, in addition to improving spatial resolution, also helps to reduce the probability of direct X-ray detection by the sensor as only 1% of incident X-rays are transmitted by a 3mm plate, thus reducing potential for radiation damage. The properties of the FOP are determined largely by the fibre size and the core-to-cladding ratio (packing fraction). For the Hamamatsu scintillators, the packing fraction is 75% meaning that over the surface area of the sensor, 75% is coupled with fibre core but 25% is covered by fibre cladding. One serious problem with FOPs can be crosstalk between the columns. To prevent this, extramural absorber (EMA) is placed between the columns to absorb any light leakage from the core glass.

Finally, the FOS must be coupled to the sensor to form an APFPI. This was achieved using a silicone coupling gel (Gruner, 2002) to match the refractive indices of the FOP and the sensor passivation material preventing losses that would occur at an air gap. The thickness of this coupling layer is crucial: too thin and air bubbles will exist; too thick and optical spreading between adjacent pixels will be high (Arvanitis *et al.*, 2007). A syringe was used to apply Visilox V-711 silicone grease to the sensor surface in a pattern optimized to ensure even coverage.

## 4.5 Linear systems model of the Active Pixel X-ray Diffraction (APXRD) System

To design the APXRD system, a model of the APFPI was developed and the complete data set passed through it to predict the scatter signature that would be recorded for each sample. Two features of the recorded scatter signatures were investigated: the effect of spectral shape on the scatter peaks and the intensity of scattered radiation. The APS can record only the angle dispersion of the X-ray diffraction data thus the choice of spectral shaping filter for the 'pink' beam is crucial. Using the complete data set, it is possible to model relevant materials that could be used as filters, which would be prohibitively expensive to compare experimentally. With an appropriate filter chosen, the intensity of integrated counts (signal electrons) can be estimated by modelling the signal transfer properties of the scintillator-coupled Active Pixel Sensor. This is important as the intensity of coherently scattered radiation from biological materials could fall below the detection limits (i.e. noise) of the APS.

Two independent steps were taken to validate the model. First, calculations using ICDD data were used to check the energy dependent signal transfer, i.e. the spectral shaping. Next, the measured conversion function of the APFPI was used to check the predicted intensity of the scatter signatures, i.e. the modelled detection capability of the APS. In this section, the theoretical background of the model will be briefly introduced and the model stages identified. The methods of validation will then be detailed and the selection of spectral shaping filters and calculation of the expected scatter intensity will be made.

### 4.5.1 Theoretical background to linear systems modelling

Linear systems theory decomposes an imaging system into a series of amplification and scattering stages. A digital X-ray imaging system is regarded as 'linear' for all object inputs $f_1(x,y)$ and $f_2(x,y)$ and all constants $a$ and $b$ if

$$S[af_1(x,y) + bf_2(x,y)] = aS[f_1(x,y)] + bS[f_2(x,y)] \tag{4.1}$$

For APXRD, the operating range of the APS can be confined to the linear, shot noise-limited region as the intensity of scattered radiation is relatively small, meaning 'small-signal linearity' may be assumed (Cunningham and Shaw, 1999).

Between the input and output of an amplification stage, there is a change in the mean number of quanta that compose the image. The transfer properties of an amplification stage are characterized by a mean gain $\overline{g_i}$ and variance in that gain $\sigma^2_{g_i}$. The gain tells us the number of quanta that exit the stage for a given number of input quanta. A scattering, or 'spreading', stage does not change the number of

quanta but instead changes their spatial distribution.

The output of a given stage in a linear systems model depends on both the input, and the signal and noise transfer characteristics of the stage. The transfer relationships for amplification and spreading processes were derived by Rabbani *et al.* (1987) and summarized by Siewerdsen *et al.* (1997). The purpose of this model was to test the variables in the experimental setup of the APXRD system, rather than to provide rigorous characterization of the detector. Further, at low illumination levels, readout noise dominates in an APS. For these reasons, signal transfer alone was included in the model.

An amplification stage changes the number of quanta in an input distribution $q(x, y)$ according to

$$\overline{q_i} = \overline{g_i q_{i-1}} \tag{4.2}$$

This equation can be easily cascaded when a stage represents a binomial selection process. In such a stage, a photon may or may not be transferred, according to binomial selection. The overall gain of consecutive binomial selection stages is simply the product of their individual gains $\overline{g_i} = \Pi(\overline{g_1}, \overline{g_2}, ..., \overline{g_{i-1}}, \overline{g_i})$ while the variance is given by binomial statistics as $\sigma^2_{g_i} = \overline{g_i}(1 - \overline{g_i})$. These two relationships allow for great simplification in linear systems models, which provide a simple approach to describing the signal transfer in an imaging system.

### 4.5.2 Model of the APXRD system

In order to form a linear systems model, the APXRD system must be broken down into its constituent signal transfer stages. The experimental apparatus for the modelled APXRD system is shown in Figure 4.3. The X-ray source is the same as that used for the energy and angle dispersive system (see Section 4.3). It was assumed that the Vanilla APS would be scanned along a horizontal line perpendicular to the X-ray beam to achieve up to 15° angular dispersion.

The system was then broken down into 'energy dependent' and 'energy independent' sections. The 'energy dependent' parts of the model include the spectral

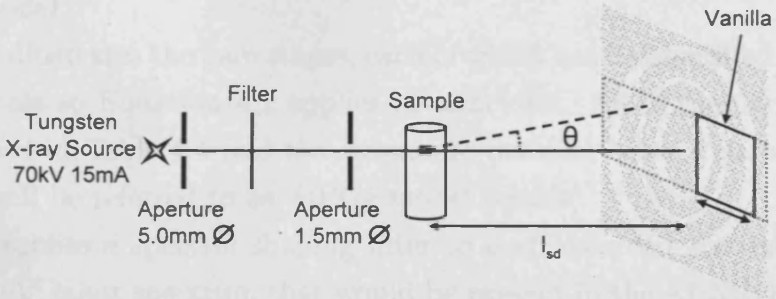


Figure 4.3: Instrumentation for angle dispersive X-ray diffraction (not to scale). The Vanilla APS was translated across the scatter signature to record data between 2.5° and 15°. ⌀ indicates diameter.

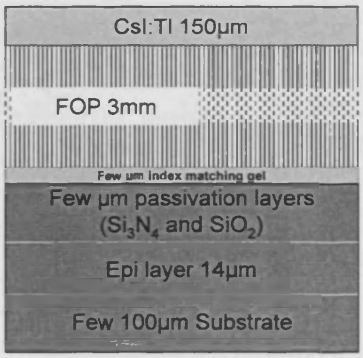


Figure 4.4: Cross section of the Active Pixel Flat Panel Imager

shaping filter and the detection of X-ray photons in the scintillator. The spectral shaping filter is applied to the complete data set prior to its propagation through the model. The quantum detection efficiency of the scintillator is applied when the X-rays arrive at the APFPI. Prior to this, adjustments were made to the complete data set to account for differences in the exposure time of the two systems (600s for the HPGe system, up to 12s for the APXRD system) and collimation. The integration time taken for the APS was 6.1s as an intermediate value in the available range. Further, correction for the differences in the solid angle subtended by the detectors at the sample were made:

$$\Omega_{pinhole} = \frac{\pi r^2_{pinhole}}{d^2_{HPGe}} \quad ; \quad \Omega_{pixel} = \frac{A_{pixel}\cos^3\theta}{d^2_{pixel}} \tag{4.3}$$

where $d^2_{HPGe}$ is the distance between the HPGe detector aperture and the sample and $d^2_{pixel}$ is the equivalent for the APS pixel. The model is therefore considered to begin when these photons arrive at the scintillator surface.

The 'energy independent' part of the model is the transfer of the generated optical photons through the scintillator, FOP and APS passivation layers to the photodiode in the APS pixel. The cross section of the layers in the APFPI can be seen in Figure 4.4. Regions in dark grey are part of the sensor, while light grey represents the FOS. These layers form the gain stages of the 'energy independent' part of the model.

Figure 4.5 illustrates the gain stages, each of which can be identified as a binomial selection process so Equation 4.2 applies in each case. All of the parameters used are summarised in Table 4.4 and the stages are detailed below. Data output from these stages will be referred to as 'HPGe model results'.

*Stage 0*: applies a spectral shaping filter to each recorded scatter signature to mimic the 'pink' input spectrum that would be present in the APXRD system. The attenuation coefficients of the filter materials were obtained from Boone and Chavez (1996).

*Stage 1*: is the start of the linear systems model. The energy dependent, quan-

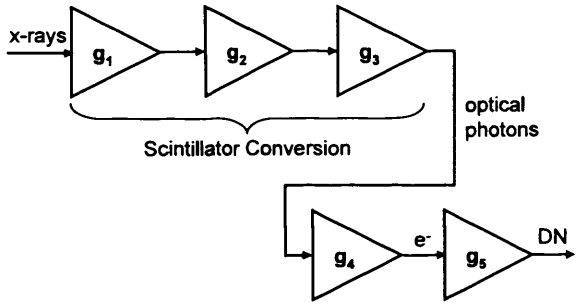


| Stage | Description |
|---|---|
| 0 | Input X-rays |
| 1 | Quantum detection efficiency of CsI:Tl |
| 2 | Generation/emission of optical quanta |
| 3 | Optical losses in FOP |
| 4 | APS quantum efficiency |
| 5 | APS conversion gain (DN/e$^-$) |

Figure 4.5: Stochastic amplification stages obeying binomial statistics used to evaluate the expected APS scatter signature.

tum detection efficiency (QDE) of the scintillator is

$$g_1(E) = 1 - e^{-[\frac{\mu}{\rho}(E)\rho_s]c_{sI}} \tag{4.4}$$

where $\frac{\mu}{\rho}(E)$ is the energy-dependent mass attenuation coefficient of caesium iodide in $\mathrm{cm^2g^{-1}}$. This was obtained from Boone and Chavez (1996) assuming negligible contribution from thallium doping. $\rho_s$ is the surface density of the scintillator given by the product of the density of caesium iodide ($4.51\mathrm{gcm^{-3}}$), adjusted for the scintillator packing density $p_f$ (Hamamatsu, 2007) and the nominal thickness of the scintillator ($150\mu$m).

When evaluating the system conversion function, the mean gain $\overline{g_1}$ of stage 1 is needed. This is found by integrating the product of the QDE, $g_1(E)$, and the normalized incident 'pink beam' spectrum $q_{rel}(E)$ over all input energies.

$$\overline{g_1} = \int_E q_{rel}(E) g_1(E) dE \tag{4.5}$$

The complete data set for hydroxyapatite after stage 1 is shown in Figure 4.6 (b).

*Stage 2*: The gain of stage 2 is the scintillation light yield. It depends on both the energy of the incident X-ray photons and the depth at which they are absorbed by the scintillator. Generation and emission of optical quanta is dependent on absorption of the X-ray photon and the probability that the resulting optical photons can pass through the remaining caesium iodide layer. The depth dependent absorption process was implemented using the work of Vedantham *et al.* (2004a) and is illustrated in Figure 4.7.

When an incident X-ray is absorbed by the scintillator, a K fluorescent X-ray may be produced if the incident energy is greater than the K edge of the scintillator. Three paths to optical emission thus exist: local emission without K fluorescence, local emission with K fluorescence or remote emission due to absorption of K fluorescence. A parallel cascade would thus be needed in the linear systems model to represent all three paths (Vedantham *et al.*, 2004a). Monte carlo studies of energy

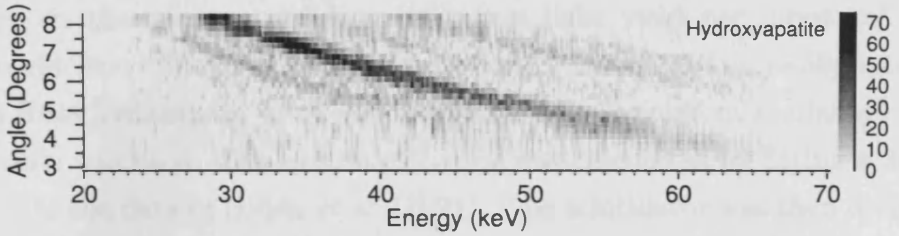


(a) Energy-angle diagram, z axis shows number of counts recorded

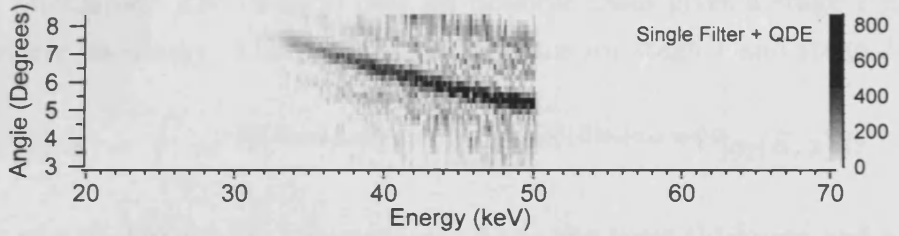


(b) Energy dependent changes due to filter and QDE, z axis shows counts adjusted by model

Figure 4.6: (a) shows the complete data set input for HAP, as seen in Figure 4.2. (b) shows the effect of a spectral shaping filter (Gadolinium) and the quantum detection efficiency of the scintillator upon the complete data set i.e. the output of Stage 1.

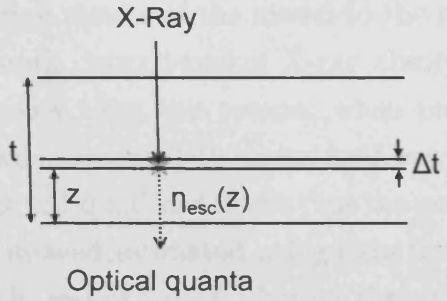


Figure 4.7: Diagram of propagation for depth dependent absorption. Includes attenuation of X-rays through distance t-z, absorption of X-rays in layer of thickness $\Delta$t then escape of optical photons through thickness z governed by the escape efficiency $\eta_{esc}(z)$

deposition in 200$\mu$m of CsI indicate that only around 15% of the total energy deposition at 35keV is reabsorbed K fluorescence (Boone, 2000). This falls off further to 10% at 50keV and 5% at 60keV. In a structured scintillator, reabsorption should occur within the primary column or adjacent columns. The contribution of K fluorescence to the total energy deposition is thus small, so the effect was neglected and a simple serial cascade added to the linear systems model. This simplification has been made by other authors (Siewerdsen *et al.*, 2004) in linear systems models where rigorous characterization of the detector is not required, as is the case here.

Neglecting K fluorescence, the number of photons escaping the scintillator is

$$g_2(E,z) = W_{CsI}(E)\eta_{esc}(z)E \tag{4.6}$$

where $W_{CsI}$ is the caesium iodide scintillation light yield per input keV, $\eta_{esc}$ is the escape efficiency and $E$ is the energy in keV. A value of $W_{CsI}$=58photons/keV was taken from Vedantham *et al.* (2004b), where an average of available literature measurements was used. The escape efficiency was calculated by fitting a 3rd-order polynomial to the data of Hillen *et al.* (1991). The scintillator was then divided into 1$\mu$m layers using the method of Suryanarayanan *et al.* (2006) and for each layer, the attenuation before, probability of absorption in, and probability of escape from the layer was calculated. The integral over all possible cases gives a stage 2 gain that depends solely on energy. The product of the gains for stage 1 and stage 2 is

$$g_1(E)g_2(E) = \int_{z=t}^{0} e^{-[\frac{\mu}{\rho}(E)\rho_s]_{CsI:Tl}(t-z)}[1 - e^{-[\frac{\mu}{\rho}(E)\rho_s]_{CsI:Tl}\Delta t}]g_2(E,z)dz \tag{4.7}$$

where t is the thickness of the scintillator, $\Delta$t is the layer thickness and z indexes the layer depth as shown in Figure 4.7. The mean gain for stage 2 may then be calculated for conversion function evaluation as

$$\overline{g_2} = \frac{\int_E q_{rel}(E)g_1(E)g_2(E)dE}{\overline{g_1}} \tag{4.8}$$

It was noted when comparing results of the model to the measured APS conversion gain that including the depth dependence of X-ray absorption had little influence on the outcome of the model. For this reason, when predicting APXRD scatter signatures, interactions were assumed to occur half way through the scintillator removing the z dependence of Equation 4.6 and thus the need to perform the integral in Equation 4.7. $\eta_{esc}$ was instead estimated using data from Lubinsky *et al.* (2006).

*Stage 3*: accounts for the loss of optical photons through the fibre optic plate and coupling fluid that attach the scintillator to the APS. The efficiency of transmission of the fibre optic plate is given by (Hejazi and Trauernicht, 1997)

$$\eta_{FO} = NA^2 T_F (1 - L_R) F_C \tag{4.9}$$

where $NA^2$ is the square of the numerical aperture of the plate, $T_F = e^{-\mu l}$ is the transmission of the fibre core, $(1 - L_R)$ accounts for the losses due to Fresnel reflections and $F_C$ is the core fill factor. $T_F$ and $F_C$ were obtained from the manufacturer (Hamamatsu, 2007). The mean gain of stage 4 is therefore

$$\overline{g_4} = T_{coating}\eta_{FO} \tag{4.10}$$

where $T_{coating}$ is included to account for any losses due to coatings on the scintillator.

*Stage 4*: is included to account for losses in the passivation and metal layers above the active layer in the APS. Passivation layers are required to insulate the active layer and protect it from damage. Metal layers provide the interconnects

Table 4.4: Values of parameters used in linear systems model.

| Parameter | Value |
|---|---|
| Scintillator type | CsI:Tl |
| Scintillator thickness | 150$\mu$m |
| Caesium Iodide packing density $p_f$ | 74% |
| Caesium Iodide scintillation light yield | 58photons/keV |
| Escape efficiency $\eta_{esc}$ | 0.5 |
| Peak light output | 550nm |
| Fibre optic plate (FOP) thickness and fibre pitch | 3mm, 6$\mu$m pitch |
| Fibre optic plate transmission at 520nm | 63% |
| All FOP effects (including transmission), $g_3$ | 38% |
| CMOS APS Pixel Pitch | 25$\mu$m |
| CMOS APS Fill Factor | 75% |
| Sensor quantum efficiency, $g_4$ | 65% |
| CMOS APS Camera gain constant, $1/g_5$ | $10e^-$/DN |
| Exposure time | 6.1s |
| Sample-detector distance | 10cm |

between the pixel and the control electronics. It also accounts for the sensor fill factor and photodiode quantum efficiency. The value for $g_4$ is the sensor quantum efficiency at 520nm, found to be 65% in Section 3.1.

*Stage 5*: is the gain of the off chip analogue-to-digital converter (ADC) in DN/e$^-$. For Vanilla, this can be tailored by adjusting the ADC range. The full ADC range was used for characterization yielded $21e^-$/DN (0.05DN/$e^-$). For X-ray diffraction, a smaller conversion gain would be preferable. The ADC range can be reduced at the upper end to finely quantize the linear sensor region with a gain of $10e^-$/DN (0.1DN/$e^-$). Stage 5 therefore allows us to predict the X-ray scatter signatures in terms of the ADC output from the APS.

### 4.5.3 Modelling filtration options

#### Validating the scatter signature shape with the 'pink beam' spectrum and ICDD data

Verification of the scatter signatures predicted using the linear systems model was made with data from the ICDD using the method of Westmore *et al.* (1996) to derive the polychromatic X-ray scatter signature as a linear superposition integral of the monochromatic signature with a spectral shape kernel:

$$\frac{\mathrm{d}\sigma_P}{\mathrm{d}\theta}(\theta) = \int_{-\infty}^{+\infty} s_1(\theta')s_2(\theta,\theta')\mathrm{d}\theta \tag{4.11}$$

where $\mathrm{d}\sigma_P/\mathrm{d}\theta$ is the scatter intensity per unit angle for a polychromatic beam. $\theta$ refers to the scattering angle for the polychromatic case, while $\theta'$ is the scattering

angle for the monochromatic case. $s_1(\theta)$ is the probability of coherent scatter given by the Thomson cross section combined with the relevant form factor $F(x, Z)$ and is weighted by a trigonometric factor. This is the raw data from the ICDD, listed as a function of angle through $\theta = 2sin^{-1}(hc/2d\overline{E})$ where d is the atomic spacing and $\overline{E}$ is the mean energy of the spectrum. $s_2(\theta, \theta')$ is the normalized incident polychromatic spectrum inversely weighted by the above trigonometric factor. Results from this analysis will be referred to as 'ICDD model' results.

An example of the ICDD data is shown for hydroxyapatite in Figure 4.8. Figure 4.8 (a) shows the spectrum kernel as a function of wavelength formed by applying a gadolinium filter to the raw tungsten spectrum and accounting for scintillator QDE. The linear superposition integral of this with the raw ICDD data for hydroxyapatite is shown in Figure 4.8 (b). The result from the HPGe model is also shown, normalized to 100 in order to compare the spectral shapes. The bars represent the peak positions taken from the ICDD.

Figure 4.8 (b) illustrates that the two results agree in terms of their peak position (5.4±0.1° for HPGe, compared to 5.5° for ICDD) and overall shape ($1.87 \pm 0.14°$ full width at half maximum, FWHM, for HPGe and 1.98° for ICDD) but differ in magnitude by up to 20% between 5° and 7°. The equivalent result using balanced filters shows a difference of up to 10% in the same region, but again agrees in terms of peak position (6.2±0.1° for HPGe, compared to 6.3° for ICDD) and shape ($3.05 \pm 0.14°$ FWHM for HPGe and 2.94° for ICDD). Given the number of different preparations of hydroxyapatite that are available, one reason for the disparity could be that a slight structural difference has lead to a reflection in the ICDD data not being present, or sufficiently intense, in this hydroxyapatite sample.

This calculation was repeated for all kidney stone equivalent materials. The scatter signatures produced by the HPGe and ICDD models are in agreement overall in terms of both peak position and full width at half maximum. Disparities in magnitude are observed for some materials at certain angles, providing further vindication of the use of the HPGe model to specifically characterize the samples for this experiment, rather than refer to the properties of their general preparations. Given the X-ray diffraction and spectral data used as the input to each model is independent, and the peak position and FWHM were in agreement within the bounds of error for all materials, the HPGe model was taken to yield a valid representation of the expected scatter signature from the APXRD system.

### Optimal X-ray spectrum characteristics

Following validation of the spectral shape, the APXRD linear systems model was used to identify an appropriate filter for spectral shaping. The X-ray spectrum incident upon the sample directly influences the position (angular dependence on mean energy), height (scattered intensity) and width (spectral shape) of peaks in

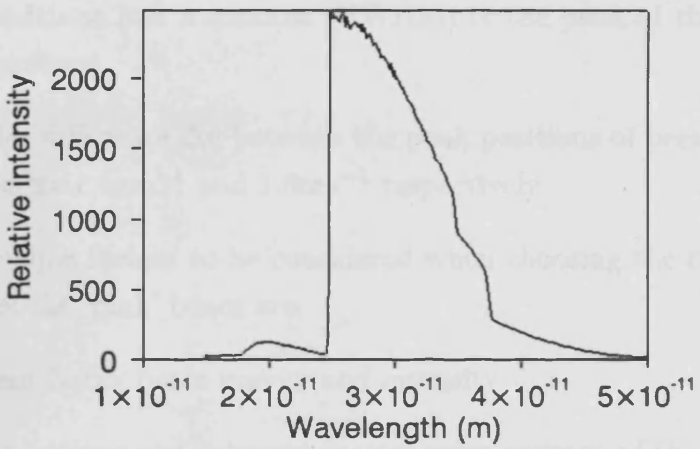


(a) Spectrum kernel

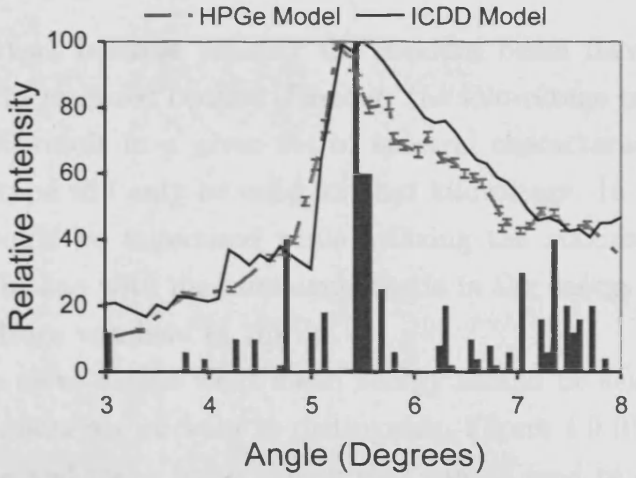


(b) Predicted scatter signature

Figure 4.8: (a) shows the spectrum kernel obtained by filtering the incident X-ray spectrum with gadolinium and accounting for the quantum detection efficiency of the scintillator. (b) shows the scatter signatures predicted using the HPGe and ICDD models showing independent verification of the HPGe model

the scatter signature.

A number of beam filters were tested by attenuating the raw tungsten X-ray spectrum by a given thickness of the material. Various properties of the spectrum were calculated. Further, the scatter signature for lard was predicted for each filter tested. This sample was selected because of its single, relatively narrow peak and the fact that it produces a scatter intensity representative of what would be encountered in a breast biopsy system. The utility of each filter was evaluated in terms of:

- Relative r.m.s. spectral width $\Delta\lambda = \frac{\sqrt{\langle\lambda^2\rangle - \langle\lambda\rangle^2}}{\langle\lambda\rangle}$ (Westmore *et al.*, 1996), calculated from the attenuated raw X-ray spectrum
- The fraction of incident intensity transmitted through the filter $\Delta$I
- Mean energy of the spectrum $\overline{E}$

- The full width at half maximum (FWHM) of the peak of the predicted lard scatter signature
- The angular difference $\Delta\theta$ between the peak positions of breast fat and carcinoma given x=1.1nm$^{-1}$ and 1.6nm$^{-1}$ respectively

The two principle factors to be considered when choosing the mean energy and spectral width of the 'pink' beam are:

1. The incident X-ray beam energy and intensity
2. The peak positions and coherent scatter cross sections of the materials under test

Item (1) is important because filtering the incident beam inevitably results in a drastic reduction in recorded counts. Further, the kilovoltage used to produce the incident beam will result in a given set of spectral characteristics thus the optimization of filter type will only be valid for that kilovoltage. In the ideal situation, spectral width should be minimised while utilizing the maximum possible transmitted intensity. In line with measurements made in the energy dispersive system, X-ray tube kilovoltage was held at 70kVp.

Item (2) helps us to decide what mean energy should be selected based on the properties of the materials we want to distinguish. Figure 4.9 illustrates the region of scattering angle and mean beam energy that can be used to distinguish adipose tissue (x=1.1nm$^{-1}$) and breast carcinoma (x=1.6nm$^{-1}$). The contours on this figure represent constant momentum transfer values between 0.5 and 3nm$^{-1}$. The figure indicates that the largest distinction between the two peaks is available using low mean energies (<50keV).

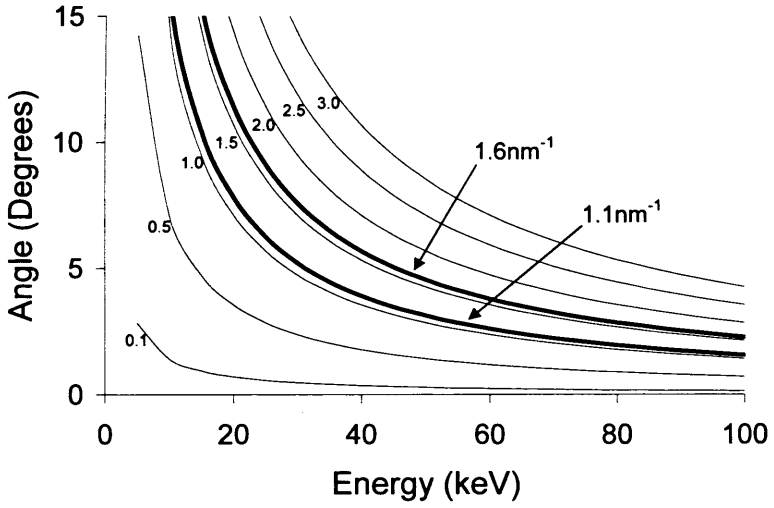


Figure 4.9: Contours of constant momentum transfer with energy and angle illustrate that the largest available distinction between adipose tissue (x=1.1nm$^{-1}$) and breast carcinoma (x=1.6nm$^{-1}$) is available at energies below 50keV.

Combining these two arguments, the energy for interrogating breast tissue samples should be <50keV. The optimum filter choice will be a compromise between high transmitted intensity, narrow spectral width and wide angular distinction of the adipose and carcinoma peaks in breast tissue.

### Filtration methods

Two different methods of beam filtration can be used for spectral shaping. Most simply, single filtration can be applied. This uses the position of the K absorption edge of a material to define a 'passband' of wavelengths. An appropriate thickness of the material has to be chosen so that the incident X-ray beam is sufficiently attenuated.

'Balanced' filtration (Kirkpatrick, 1939) may also be used. Balanced filtration involves two exposures, one with a filter with a high energy K absorption edge, the other with a low K edge filter. By selecting appropriate thicknesses of each filter material in the balance, a subtraction of the two exposures leaves a narrow spectral width. Such balanced filtration techniques have the disadvantage that two different exposures are required, however, they often provide higher count rates and narrower spectral widths than are available with single filtration. In particular, 'K line' filtration uses the characteristic emission lines of the X-ray tube target, selectively attenuating the Bremsstrahlung background on either side of these using materials with K edges slightly above and slightly below the characteristic emission energies. Balanced filtration has been used previously in a variety of applications including baggage scanning (Beevor *et al.*, 1995) and X-ray computed tomography (Saito, 2004).

Difficulties in selecting appropriate filter materials arise from a number of sources. Firstly, and perhaps most significantly, choice is limited by safety (including toxicity and flammability). Next, the materials need to be available in thin foil preparations in order to be easily included into a general X-ray diffraction system. Finally, they must be widely available at reasonable cost. Considering safety, availability and cost, a number of materials between Z=41 and Z=73 were selected as potential filters. Substances with K absorption edges below Silver were neglected as these do not provide sufficient shaping of the X-ray beam, while those above Tantalum were neglected as defining too high a mean energy for these studies.

**K edge filtration** Table 4.5 shows the results from the selection of filters. Figure 4.10 shows the spectra obtained when the raw spectrum is theoretically attenuated by a given filter of the thickness listed in Table 4.5.

The best compromise between optimizing $\Delta\lambda$, $\Delta$I, peak FWHM and $\Delta\theta$ as described above is found with the Samarium filter, with Gadolinium a close second. As Gadolinium has been employed by previous authors (Davidson *et al.*, 2005; Batchelar

and Cunningham, 2002; Westmore *et al.*, 1996), this was selected as the K edge filter as it provides an opportunity to cross reference data from the APXRD system with literature results. For the remainder of this work, 'single filter' refers to the placement of 0.28gcm$^{-2}$ gadolinium (Goodfellow, Gd foil, 99.9% purity) in front of the X-ray source.

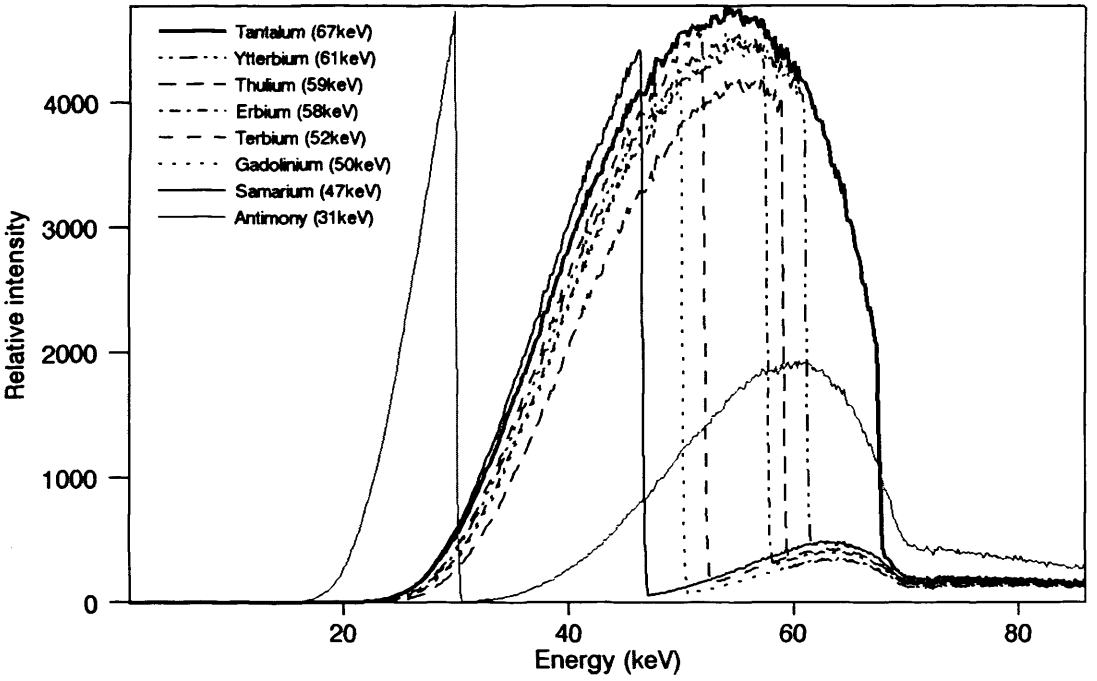


Figure 4.10: Illustration of the spectra defined by a single K edge filtration with some of the available filter materials.

**Balanced filtration** has not been tested previously for X-ray diffraction applications. Table 4.6 shows the results of applying balanced filtration to the lard data set. Tin provides a cost effective option for the lower energy filter. Considering again the

Table 4.5: Spectral characteristics of different K edge filters. t is the filter thickness in mm, $\Delta\lambda$ is the spectral width, $\Delta$I is the fraction of the incident intensity transmitted through the filter and $\overline{E}$ is the mean energy of the spectrum. Fat FWHM is the full width half maximum of the peak of the lard sample. $\Delta\theta$ is the difference of the peak positions of breast fat and carcinoma (x=1.1nm$^{-1}$ and 1.6nm$^{-1}$ respectively).

| Filter | Z | K edge (keV) | t (mm) | $\Delta\lambda$ (%) | $\Delta$I (%) | $\overline{E}$ (keV) | Fat FWHM(°) | $\Delta\theta$ |
|---|---|---|---|---|---|---|---|---|
| Sb | 51 | 30.5 | 0.30 | 42 | 7 | 41 | 5.1 | 1.7 |
| **Sm** | **62** | **46.8** | **0.35** | **21** | **5** | **42** | **1.6** | **1.7** |
| **Gd** | **64** | **50.2** | **0.35** | **19** | **5** | **44** | **1.6** | **1.6** |
| Tb | 65 | 52.0 | 0.30 | 19 | 7 | 44 | 1.8 | 1.6 |
| Er | 68 | 57.5 | 0.25 | 19 | 9 | 47 | 2.1 | 1.5 |
| Tm | 69 | 59.4 | 0.25 | 19 | 8 | 48 | 2.1 | 1.5 |
| Yb | 70 | 61.3 | 0.30 | 20 | 10 | 48 | 2.2 | 1.5 |
| Ta | 73 | 67.4 | 0.10 | 22 | 13 | 50 | 2.3 | 1.4 |

trade off of parameters, it was seen that Samarium balanced with Tin gave the best spectral characteristics. In the remainder of the work, 'balanced filters' refers to a scatter signature measured with two exposures, one with $0.07 gcm^{-2}$ of Samarium (Goodfellow, Sm foil, 99.9% purity), another with $0.15 gcm^{-2}$ of Tin (Goodfellow, Sn foil, 98.8% purity).

Table 4.6: Spectral characteristics of different balanced filters using 70kVp tube setting. Column headings as for Table 4.5 with F1 referring to filter 1 (higher energy K edge) and F2 referring to filter 2.

| F1 | F1 t (mm) | F2 | F2 t (mm) | $\Delta\lambda$ (%) | $\Delta$I (%) | $\overline{E}$ | Fat FWHM(°) | $\Delta\theta$ |
|---|---|---|---|---|---|---|---|---|
| **Sm** | **0.1** | **Sn** | **0.2** | **16** | **11** | **38** | **2.2** | **1.9** |
| Sm | 0.1 | Cd | 0.2 | 20 | 12 | 37 | 2.3 | 1.9 |
| Sm | 0.1 | Ag | 0.2 | 23 | 14 | 37 | 2.3 | 1.9 |
| Gd | 0.09 | Sn | 0.2 | 15 | 12 | 40 | 2.3 | 1.8 |
| Er | 0.1 | Sn | 0.3 | 17 | 11 | 42 | 2.3 | 1.7 |
| Tm | 0.05 | Sn | 0.15 | 10 | 13 | 42 | 2.7 | 1.7 |
| Yb | 0.05 | Sn | 0.12 | 24 | 14 | 40 | 2.6 | 1.8 |
| Ta | 0.05 | Sn | 0.35 | 20 | 12 | 44 | 2.5 | 1.6 |

Finally, 'K line' balanced filtration was tested. As the energy dispersive data set was acquired with the X-ray tube set at 70kV, the effect of selecting the tungsten K lines could not be directly investigated. Instead, the spectral characteristics were evaluated using simulated spectra (SRS78) of up to 140kV. Balanced filtration of Ytterbium and Erbium was applied to these simulated spectra and the results are show in Table 4.7. Results indicate that K line filtration gives a lower overall number of counts than the balanced filtration tested above, but a higher number of counts than the single filtration. However, the higher mean energy defined using this filtration method means the difference between the peak angles of breast adipose and carcinoma is smaller than in the prior two options. As a result, this method of filtration was not investigated further here. It could, however, be of use if the system were to be extended to application in the analysis of more crystalline materials. Materials with multiple narrow peaks in their scatter signature will be more affected by the polychromaticity, so they may benefit from this approach.

Table 4.7: Spectral characteristics of Ytterbium and Erbium balanced filters using various tube settings. Column headings as for Table 4.5

| Kilovoltage | $\Delta\lambda$ (%) | $\Delta$I (%) | $\overline{E}$ | $\Delta\theta$ |
|---|---|---|---|---|
| 80kV | 27 | 1 | 53 | 1.3 |
| 100kV | 22 | 3 | 56 | 1.3 |
| 120kV | 19 | 5 | 58 | 1.2 |
| 140kV | 17 | 6 | 58 | 1.2 |

### Measured Spectra

The X-ray spectra produced using the chosen filters were measured with the HPGe detector in the EDXRD system mounted at $\theta = 0°$ as described previously. The spectra are shown in Figure 4.11. The mean energy of the raw tungsten spectrum was 23keV and the r.m.s. spectral width was 69%, unacceptable for the measurement of angle dispersive scatter signatures. The mean energy of the single filtered spectrum was 42keV, while that of the balanced filter spectrum was 36keV. The spectral widths were 19% and 15% respectively, in line with the values expected.

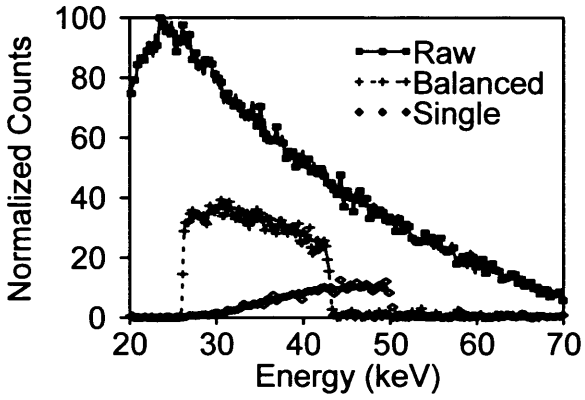


Figure 4.11: Comparison of raw and filtered X-ray spectra recorded using the HPGe detector. Tungsten spectrum is shown in raw form, then with balanced and single filtration applied in turn. Energy shown between 20 and 70keV to aid clarity and avoid the high intensity of L-level emission lines dominating the scale.

## 4.5.4 Predicted scatter signature intensity

**Validation of the predicted scatter intensity using the APS X-ray conversion function**

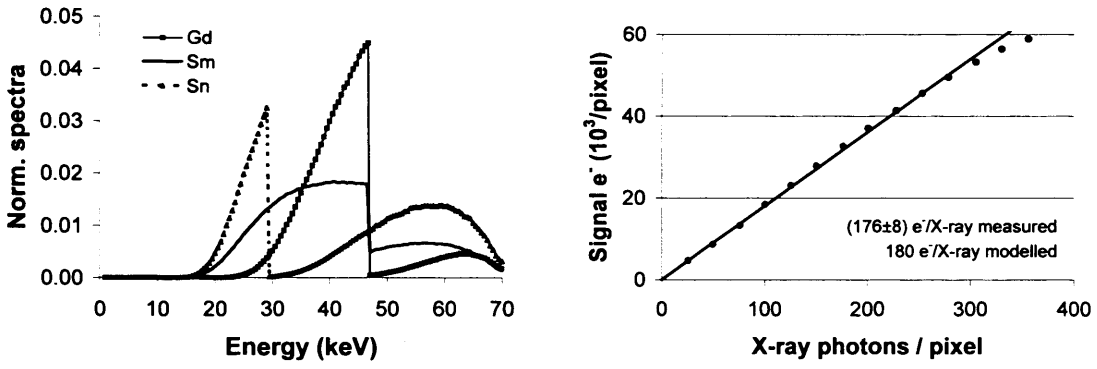


(a) Input spectrum

(b) Measured conversion function

Figure 4.12: (a) Input spectra for the conversion function measurement (b) Resulting conversion function (measured and modelled). Detector input dose range 2-22$\mu$Gy

The X-ray conversion function is used to find the number of signal electrons generated in the APFPI for each incident X-ray photon. Vanilla was placed at a

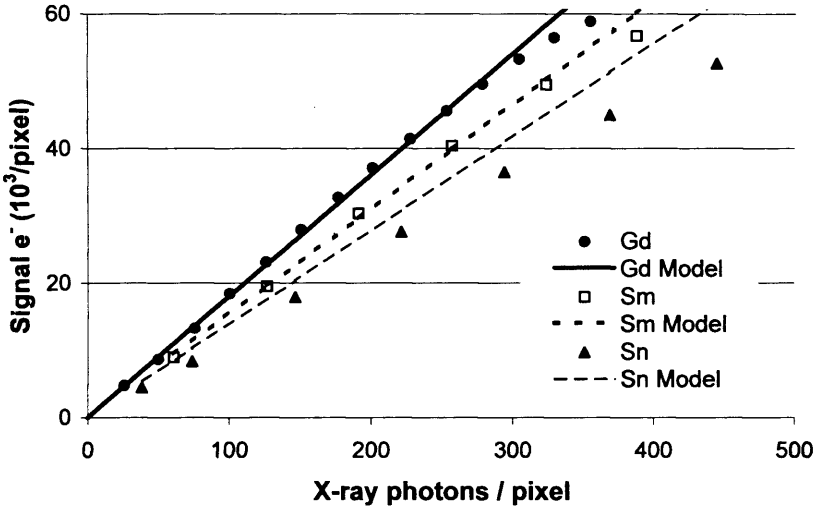


Figure 4.13: Conversion function measured for Vanilla with all filtration options. Modelled results yield $180e^-$/X-ray for Gd, $155e^-$/X-ray for Sm and $139e^-$/X-ray for Sn compared to measured values of $176\pm8e^-$/X-ray for Gd, $155\pm1e^-$/X-ray for Sm and $122\pm6e^-$/X-ray for Sn. Maximum detector input dose was $22\mu$Gy for Gd, $30\mu$Gy for Sm and $37\mu$Gy for Sn.

distance of $107\pm1$cm from the X-ray source operating at 70kV with each of the filters described above. The sensor output was recorded while increasing the tube current. The Vanilla output was converted to signal electrons using the conversion gain. The exposure was measured by replacing Vanilla with a calibrated ionisation chamber (Keithley 35050A Electrometer with 15cc ion chamber). The chamber output was converted from exposure to X-rays per pixel using the fluence per exposure (Boone, 2000) and the pixel area. The raw X-ray spectrum used was that measured using the HPGe system, shown in Figure 4.11 (a). This spectrum was then attenuated by the relevant filter and passed through the linear systems model of the APFPI. The number of signal electrons per incident X-ray photon was thus predicted. The normalized spectra can be seen in Figure 4.12 (a).

The measured conversion function for the Gadolinium filter is shown in Figure 4.12 (b). The nonlinearity at high exposure values is due to the inherent nonlinearity of the APS. The small signal linear fit to this data yields $176\pm8e^-$/X-ray, compared to $180e^-$/X-ray predicted by the model. The quoted error for this value reflects the standard error in the linear fit. The agreement of these two results indicates that the parameters selected in Table 4.4 provide a good representation of the signal transfer in the Vanilla APFPI.

Results for all filters are displayed in Figure 4.13. For Samarium, the measured conversion is $155\pm1e^-$/X-ray compared to $155e^-$/X-ray from the model. For Tin, $122\pm6e^-$/X-ray was measured compared to the model value of $139e^-$/X-ray. Gadolinium has the best response because the spectrum shows the best overlap with the quantum detection efficiency of the scintillator. Both gadolinium and samarium show excellent agreement with the model. For tin, there is a discrepancy that is be-

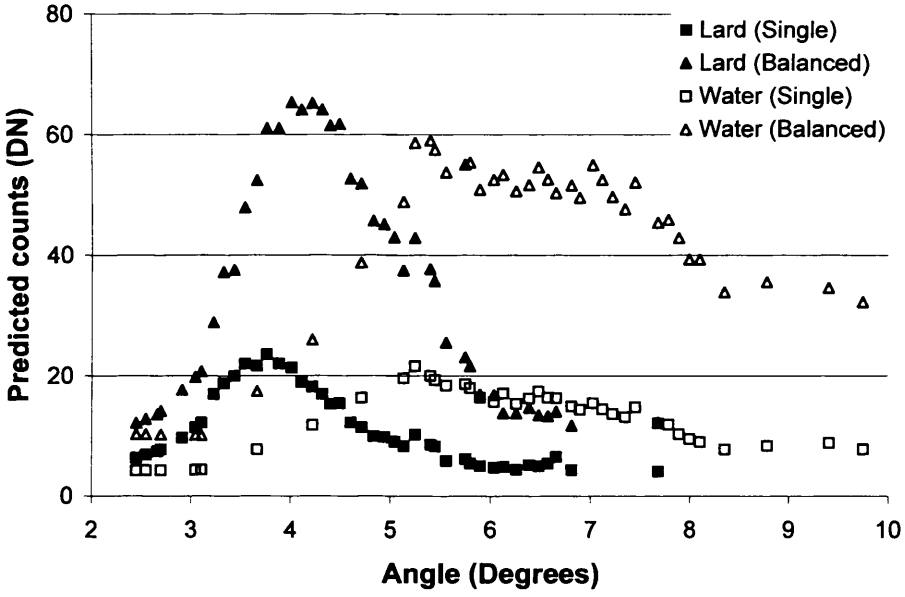


Figure 4.14: Predicted scatter signatures for lard and water using each filtration option given in terms of the sensor output in digital numbers

yond the bounds of error indicating that fewer X-rays are detected than the model predicts. One reason for this may be the lower purity of the tin filters used, as compared to the 100% purity assumed in calculating the attenuation coefficient of tin. Further, there is a 10% tolerance on the thicknesses of the filter. It is possible that the tin filter is up to 0.02mm thicker than expected, whereas the other materials are of the expected thickness. The overall agreement between these measurements and the model indicate that the assumptions made in the model derivation have not had a major impact on the output. For all filter types, greater than 150 X-rays/pixel sees the signal level in electrons reach the onset of nonlinearity so operating with intensities greater than this requires the sensor data to be linearized.

### Scatter signature predictions for breast tissue equivalent materials

Following verification of the number of electrons generated per X-ray, the linear systems model (using the parameters described previously) was used to predict the intensity of the scatter signature that would be recorded by the Vanilla APFPI, in digital numbers. Predictions were made using both filtration options for lard and water and the model outputs are shown in Figure 4.14.

The scattered intensity from the breast equivalent samples is far below the onset of APS nonlinearity so this will not affect the measurements. For the lard sample, peak height is defined as the ratio of the peak intensity to the intensity between 6.2° and 7.8°. For water, the peak height is taken as the ratio between the peak intensity and the intensity below 2.7° as interference effects can still be observed at the upper end of the angular range. From Figure 4.14, peak heights obtained with single filtration are 4.7 and 4.3 for lard and water respectively. For balanced

filtration, these are 4.9 and 5.8 respectively. The full width at half maximum of the fat peaks are 1.6° and 2.2° for single and balanced filtration respectively. Balanced filtration would thus provide a larger peak height and in turn signal-to-noise ratio, but single filtration would give a narrower full width at half maximum and thus better distinction between the fat and fibrous tissue peaks. Both options should therefore be investigated experimentally as they confer different advantages.

### 4.5.5 Summary

This section has described the implementation of a linear systems model to predict scatter signatures recorded by the APXRD system shown in Figure 4.3. Two methods for cross-checking the model were provided. The first used the ICDD catalogue of diffraction data combined with the incident spectral shape to predict the expected scatter signature using a linear superposition integral. The second used the measured conversion function for the APFPI to verify the overall system gain in terms of electrons per X-ray. Together, these verify the propagation of both signal intensity through, and the effect of spectral shape on, the APXRD system.

The model was used to evaluate the optimum choice of spectral shaping filter to narrow the width of the raw tungsten spectrum to a 'pink' beam. A single filter of $0.28 gcm^{-2}$ gadolinium was chosen as the K edge filter, while $0.07 gcm^{-2}$ of Samarium and $0.15 gcm^{-2}$ of Tin were selected as balanced filters. Predicting the scatter signatures that these filters should define for lard and water showed that while single filtration provides a smaller full width at half maximum, balanced filtration confers a larger peak height. Both filtration options should thus be tested in the experimental APXRD system.

## 4.6 Setup, optimization and techniques for evaluation of the APXRD system

This section details the implementation of the APXRD system with Vanilla, including optimization of various experimental parameters, scatter signature calculation and the phantoms used to verify the collimator angular acceptance and evaluate the potential contrast available.

### 4.6.1 Experimental arrangement and parameter optimization

The experimental setup for the APXRD system is shown in Figure 4.15. This was installed at different times on two separate tungsten X-ray sources: one for interrogating single samples and another for scanning phantoms (see below). Optimization

was completed using the fat sample with a single filter on the first system. Both single and balanced filtration options were tested with $l_{sd}$=10cm. Data from Vanilla was recorded at two horizontal positions in the plane of the scatter signature to visualize the scattered intensity between 2.5° and 15°. The setup of the Large Area Sensor will be discussed in Chapter 5. Physically, the most important parameter is the angular acceptance of the collimator as this determines the count rate at the sensor. With Vanilla, relevant setup parameters such as reset type, conversion gain and integration time influence both the quality and intensity of the signal.

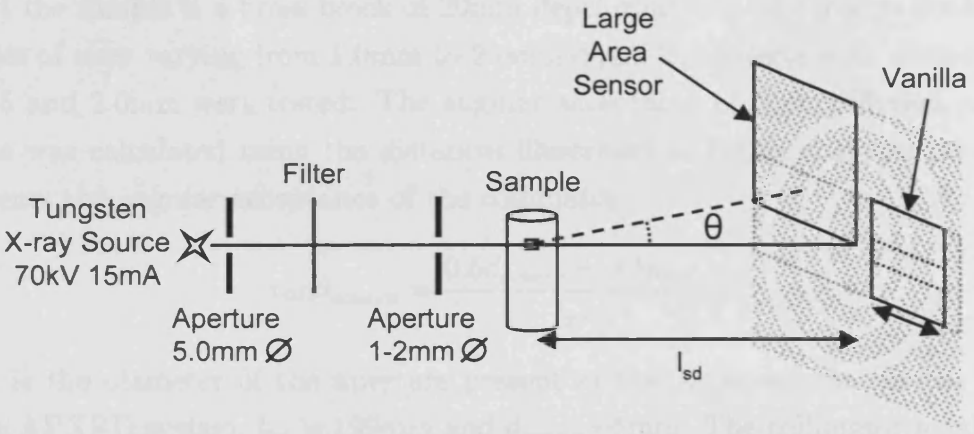


Figure 4.15: APXRD system setup. The area enclosed by the dotted line outside of the Vanilla sensor is the region over which the sensor is scanned. The area marked by the dotted line inside of the sensor indicates the region in which the scatter signature was calculated.

### Scatter signature calculation

For each data set recorded for a given sample, a corresponding background acquisition was recorded with an empty sample holder in place. This was subtracted from the data acquisition to ensure that no scatter from the experimental equipment contaminated the recorded patterns. As described in Chapter 1, incoherent and multiple scattering produce a broad background without interference effects. Corrections for these contributions were neglected for two reasons: firstly, the small sample size (6mm) and the beam energy employed means their contribution will be negligible compared to coherent scatter (Griffiths *et al.*, 2007); secondly, the aim was to keep the APXRD system as simple as possible so only necessary data corrections were performed.

The scatter signature measured by Vanilla was derived by averaging intensity over regions of interest 10 pixels wide (parallel to the scanning direction) and 100 pixels high. The area across which this ROI was scanned is shown as a dotted line in the sensor in Figure 4.15. The region width used corresponds to a scattering angle width of 0.15°. A function relating the geometrical position of the region of interest to the scatter angle was calculated using measurements of the distance of the sensor

from the sample and the offset from the beam centre. The results from each of the translations of the sensor were stitched together to produce the full scatter signature.

### Physical setup

Ideally the irradiation area at the sample should be as small as possible to ensure uniformity of material within the scatter volume and to aid in the definition of the scattering angle. This need must be balanced against the need for a good peak height (i.e. count rate). The aperture used to define the size of the irradiation area at the sample is a brass block of 20mm depth that can take inserts containing pinholes of sizes varying from 1.0mm to 2.0mm diameter. Inserts with diameters of 1.0, 1.5 and 2.0mm were tested. The angular acceptance of these different pinhole options was calculated using the distances illustrated in Figure 4.16, where $\theta_{source}$ represents the angular acceptance of the collimator:

$$\tan\theta_{source} = \frac{0.5d_{source} + 0.5d_{coll}}{l_{xc}} \tag{4.12}$$

$d_{source}$ is the diameter of the aperture present at the X-ray source. In the single sample APXRD system, $l_{xc} = 199mm$ and $d_{source}$=5mm. The collimator resulted in angular acceptances (to within $\pm 0.01°$) of 0.86, 0.93 and 1.01°. The diameter of the beam falling on the sample can be calculated from

$$d_s = 2l_{cs}\tan(\theta_{source}) + d_{coll} \tag{4.13}$$

which for $l_{cs} = 60mm$ yields $h_s$=2.9, 3.6 and 4.2mm for each pinhole respectively. As the typical width of a biopsy sample is up to 3mm in diameter, the 1.5mm diameter pinhole would ensure complete coverage of a real sample. Figure 4.17 (a)

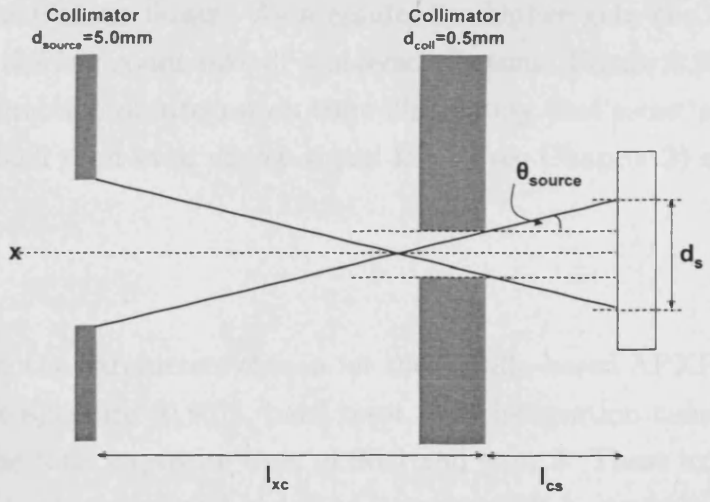


Figure 4.16: Schematic for calculating angular acceptance

shows the effect of changing the angular acceptance between 0.86°, 0.93° and 1.01°

on the scatter signature of pork fat while keeping other setup parameters constant (hard reset, single filter, 12.1s integration time and gain 2). Defining the peak height as the ratio of the maximum value in the peak to the average of the pattern tail between 12° and 15°, the peak heights produced by each collimator were 4.8, 7.3 and 15.3 respectively. The peak FWHM was found to be 2.4° for the two smaller collimation options, rising to 2.7° for the largest option. For integration times less than 6.1s, no discernable peak was visible with the 1.0mm (0.86°) aperture. It was therefore concluded that an angular acceptance of 0.93°, corresponding to the 1.5mm diameter aperture, would be used for the pure sample measurements.

### APS control parameters

Two different gain settings were tested for linearity: $21e^-$/DN (referred to as gain 1) and $10e^-$/DN (gain 2). Integration times of 1.2, 2.4, 6.1 and 12.1s were chosen for testing based upon the predictions of scatter signature intensity given by the linear systems model using 6.1s. A total exposure time of 96s was used and multiple frames were acquired for averaging. Both hard and flush reset types were tested.

Scatter signatures were recorded for pork fat and with single filtration using all available combinations of integration time (1.2, 2.4, 6.1 and 12.1s), ADC gain ($21e^-$/DN and $10e^-$/DN) and reset type (hard and flush) and results can be seen in Figure 4.17 (b) - (d). Peak characteristics and response linearity were calculated for each parameter set.

Peak height was found to increase linearly with increasing integration time. 6.1s allowed sufficient frames to be acquired to reduce the standard error in the mean of each region of interest used for analysis to less than 1%. Equally, a higher tube current could have been used if this had been available. The ratio of the peak heights measured using gain 1 and gain 2 was found to be 2, indicating the relationship between these settings is linear. As a result, the higher gain (i.e. $10e^-$/DN) was selected due to the low count rate of scattered photons. Figure 4.17 (d) plots peak maximum as a function of integration time illustrating that some 'superlinearity' is observed with flush reset even at low signal levels (see Chapter 3) so this setting is unsuitable.

### Summary

From these tests, the parameters chosen for the Vanilla-based APXRD system were: 1.5mm diameter aperture (0.93°), hard reset, 6.1s integration time (16 frames acquired within the total exposure time of 96s) and gain 2. These experimental conditions aimed to achieve a good signal-to-noise ratio (i.e. peak height), as only a horizontal slice through the scatter signature was acquired with Vanilla so radial integration was not performed.

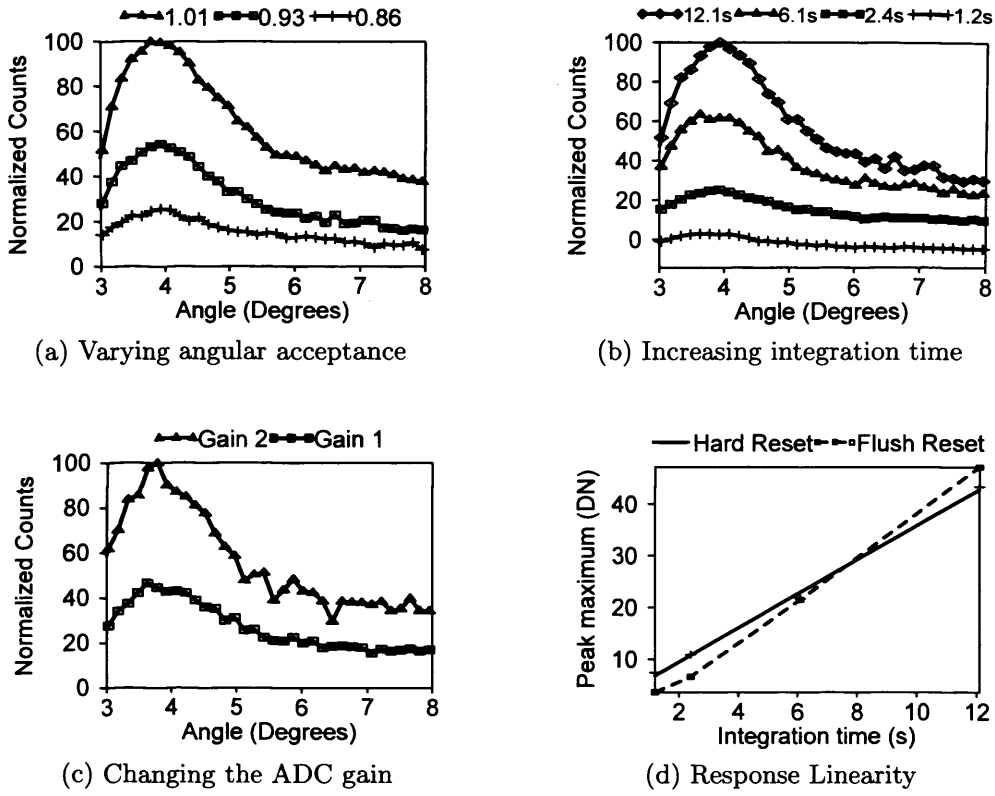


(a) Varying angular acceptance

(b) Increasing integration time

(c) Changing the ADC gain

(d) Response Linearity

Figure 4.17: Experimental and Vanilla parameters tested during system optimization with a sample of pork fat (a) Angular acceptances of 1.01° (triangle), 0.93° (square) and 0.86° (+) (b) Integration times of 12.1s (diamond), 6.1s (triangle), 2.4s (square) and 1.2s(+) (c) Gains 1 (square) and 2 (triangle) (d) Hard (solid line) and flush (dashed line) resets compared in terms of peak maximum measured in the sensor ADC output unit, digital numbers (DN)

### 4.6.2 Influences on angular resolution

A primary concern when evaluating scatter signatures is the angular resolution of the system in question. While geometrically, the accuracy in calculating the scattering angle of a particular peak is good, angular broadening occurs because of a number of different effects in the APXRD system and these must be taken into account. Each of these effects is detailed separately below and a summary is made in Table 4.9. To combine the different influences on the resolution, the general rule for adding independent errors in variable Z, a function of A, B, ..., was used (Squires, 1997)

$$(\Delta Z)^2 = \left(\frac{\partial Z}{\partial A}\Delta A\right)^2 + \left(\frac{\partial Z}{\partial B}\Delta B\right)^2 + \ldots \tag{4.14}$$

#### Sample size and position

Referring to Figure 4.18, the scatter angle is given by

$$\tan\theta = \frac{r}{l_{sd}} \tag{4.15}$$

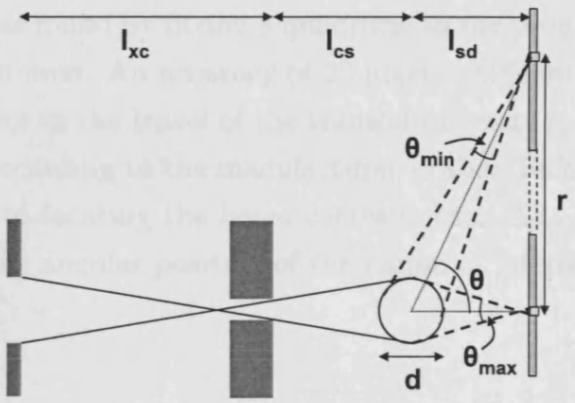


Figure 4.18: Schematic for calculating angular resolution

Using Equation 4.14, the relative uncertainty in the scatter angle due to the measurement of $l_{sd}$ is

$$\frac{\Delta\theta_l}{\theta} = \frac{r\cos^2(\theta)\Delta l_{sd}}{\tan^{-1}(r/l_{sd})l_{sd}^2} \tag{4.16}$$

At small angles, this simplifies to $\Delta\theta_{l_{sd}}/\theta = \Delta l_{sd}/l_{sd}$. At most, $\Delta\theta_{l_{sd}}/\theta = 1.5\%$. Further, the effect of the finite diameter of the sample located at distance $l_{sd}$ from the detector is calculated using the root-mean-square (r.m.s.) uncertainty $\Delta l_{rms}$ given by Westmore *et al.* (1996) as

$$\Delta l_{sd,rms} = \sqrt{\langle(\Delta l_{sd})^2\rangle - \langle(\Delta l_{sd})\rangle^2} = \frac{d}{\sqrt{12}} \tag{4.17}$$

As a result, the relative uncertainty in the scatter angle due to the sample size is

$$\frac{\Delta\theta_{l_{rms}}}{\theta} = \frac{\Delta l_{rms}}{l_{rms}} \tag{4.18}$$

which for a sample holder diameter of 6mm (assuming complete filling) yields 1.8%. In total, the relative uncertainty due to sample size and position is

$$\left(\frac{\Delta\theta_l}{\theta}\right)^2 = \left(\frac{\Delta\theta_{l_{sd}}}{\theta}\right)^2 + \left(\frac{\Delta\theta_{l_{rms}}}{\theta}\right)^2 = 2.3\% \tag{4.19}$$

### Angular position of region of interest

The angle corresponding to each region of interest is calculated using the distance of the sensor from the sample and the distance of the region of interest from the beam centre. The error in measuring the distance of the sensor from the sample is 3%. The error in finding the beam centre from which to calculate the scatter signature arises from the incident X-ray beam width is given by $\Delta\theta_r/\theta = \Delta r/r$. Location of the beam centre for the Vanilla APXRD system was achieved by translating Vanilla by 3mm into the primary beam. An image of the beam was taken at 1mA with a 1.0mm collimator in place and using a short integration time to prevent saturation. The

centre of the beam was found by fitting a quadratic to the profile of the beam image and locating the maximum. An accuracy of 20 pixels (0.05mm) was available using this method. The error in the travel of the translation stage including backlash is a maximum of $16\mu m$ according to the manufacturer (Zaber Technologies, 2008). The maximum error due to locating the beam centre is thus $\Delta\theta_r = 1.8\%$. The overall error in calculating the angular position of the region of interest is $\frac{\Delta\theta_p}{\theta} = 3.4\%$.

### Spectral width

Performing angle dispersive X-ray diffraction with a polychromatic beam leads to severe broadening of the measured scatter signatures. The angular uncertainty caused by the spectral width can be derived from the expression for momentum transfer rearranged to $\lambda x = \sin(\theta/2)$. Applying Equation 4.14 we find that

$$\frac{\Delta\theta_\lambda}{\theta} = \frac{2x\Delta\lambda}{2\sin^{-1}(\lambda x)\cos(\theta/2)} \tag{4.20}$$

where $\Delta\lambda$ is the r.m.s. spectral width $\Delta\lambda_{rms} = \sqrt{\langle\lambda^2\rangle - \langle\lambda\rangle^2}$. At small angles, the r.m.s. uncertainty in the scatter angle due to the spectral width is thus

$$\frac{\Delta\theta_{\lambda rms}}{\theta} = \frac{\sqrt{\langle\lambda^2\rangle - \langle\lambda\rangle^2}}{\lambda} \tag{4.21}$$

As measured in Section 4.5.3, the spectral widths of single and balanced filters were 19% and 15% respectively, giving a substantial reduction in uncertainty as compared to the raw spectrum (69%).

### Self attenuation by the sample

X-ray attenuation prior to scattering causes beam hardening in the incident spectrum and may shift the scattered peak position. Attenuation of the scattered X-rays will also affect the intensity of the scatter signature. Attenuation corrections may be performed using Monte Carlo simulations (Poletti *et al.*, 2002) or by normalizing the signature to the transmitted beam intensity (Batchelar and Cunningham, 2002).

The attenuation of scattered photons depends on the path length through which they travel after interaction. With a sample holder of diameter 6mm, there is only a 1.5% difference in path length for interactions that occur at the start and end of the sample resulting in a negligible (<0.6%) change in intensity. A greater effect is produced by beam hardening prior to the interaction, evaluated using the energy-dependent linear attenuation coefficient of each material (Boone and Chavez, 1996) (see Table 4.8) and the incident beam spectrum employed with single filtration. The angular shift caused by this change in beam energy is given by

$$\Delta\theta_a = \left(2\sin^{-1}\left[x\frac{\mathrm{hc}}{E_1}\right]\right) - \left(2\sin^{-1}\left[x\frac{\mathrm{hc}}{E_2}\right]\right) \tag{4.22}$$

where $E_1$ is the mean energy of the spectrum before encountering the sample and $E_2$ is the mean energy of the spectrum after it has passed through the whole sample (as this is the maximum possible path length before interaction). For hydroxyapatite, the most attenuating sample, this angular shift $\Delta\theta_a/\theta$=3.3% for $\theta = 7.5°$ in the centre of the measured range. For fat, the least attenuating material, $\Delta\theta_a/\theta$=0.3%. As these effects are small relative to the spectral width, no attenuation correction was performed with the Vanilla APXRD system.

Table 4.8: Attenuation coefficients of sample materials from Boone and Chavez (1996)

### Overall uncertainty

The total scatter angle uncertainty due to the above influences is therefore

$$\left(\frac{\Delta\theta}{\theta}\right)^2 = \left(\frac{\Delta\theta_r}{\theta}\right)^2 + \left(\frac{\Delta\theta_l}{\theta}\right)^2 + \left(\frac{\Delta\theta_s}{\theta}\right)^2 + \left(\frac{\Delta\theta_a}{\theta}\right)^2 \tag{4.23}$$

Considering the magnitude of the individual terms shown in Table 4.9, the spectral width is clearly the limiting factor even with beam filtration in place.

Table 4.9: Uncertainty in the scattering angle resolution, i.e. the scatter peak width, defined by the APXRD system

| Source | Symbol | Magnitude (%) |
|---|---|---|
| Sample size and position | $\frac{\Delta\theta_l}{\theta}$ | 2.3% |
| Angular position of region of interest | $\frac{\Delta\theta_p}{\theta}$ | 3.4% |
| Spectral width | $\frac{\Delta\theta_s}{\theta}$ | 19% Gd, 15% Sm-Sn |
| Self attenuation by the sample | $\frac{\Delta\theta_a}{\theta}$ | 3.3% max |

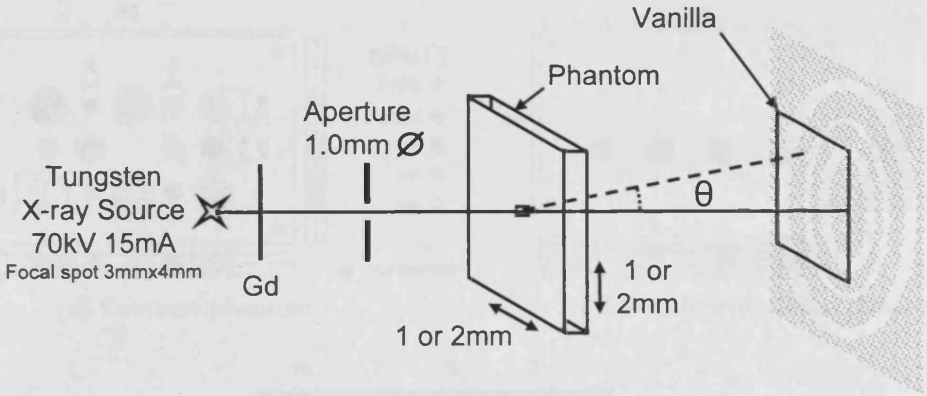


Figure 4.19: Experimental arrangement for phantom imaging

### 4.6.3 Phantoms for spatial resolution and contrast assessment

The experimental setup in Figure 4.15 interrogates only a single position within a sample, set by the incident pencil beam and the position of the sensor. Other authors have investigated the application of X-ray diffraction for contrast enhancement in traditional mammography (Griffiths *et al.*, 2003). The system in Figure 4.15 is not capable of producing X-ray diffraction 'images', as would be needed for this application. It is therefore not possible to evaluate whether the APXRD system could in future be extended to mammography with this setup. In terms of biopsy analysis, this arrangement also requires any suspicious lesions in a sample to lie within the irradiation area so potentially leaves the system open to missing abnormalities.

To overcome these limitations, planar X-ray diffraction imaging could be employed. Planar imaging of a biopsy sample in the APXRD system would involve vertical translation of the entire core biopsy through the pencil X-ray beam. If a sensor with high dynamic range such as the Large Area Sensor were employed in the system, this planar imaging arrangement would also allow the transmission image of the biopsy to be reconstructed.

Figure 4.19 illustrates how the planar imaging capability of the system was tested. This system was installed on a Tungsten AGO 160 X-ray tube with 0.8mm Be inherent filtration and a focal spot size of 2.1x3.8mm (Cook, 2008b). The source was not shielded and no aperture was in place at the tube exit window. A 3mm layer of lead was placed around the tube and between Vanilla and the phantom to prevent radiation leaking from the tube and scattering into the detector. Given Equation 4.12 and $l_{xc} = 168mm$ and $d_{source}$=3.8mm (focal spot size maximum), the angular acceptance defined by a 1.0mm collimator is 0.82° and the height irradiated at the sample is 2mm. A translation stage capable of moving in both the horizontal and vertical directions was used to scan a series of phantoms through the incident X-ray beam. A smaller collimator was chosen as compared to the single sample system to restrict the irradiated area of the sample to within a translation step of

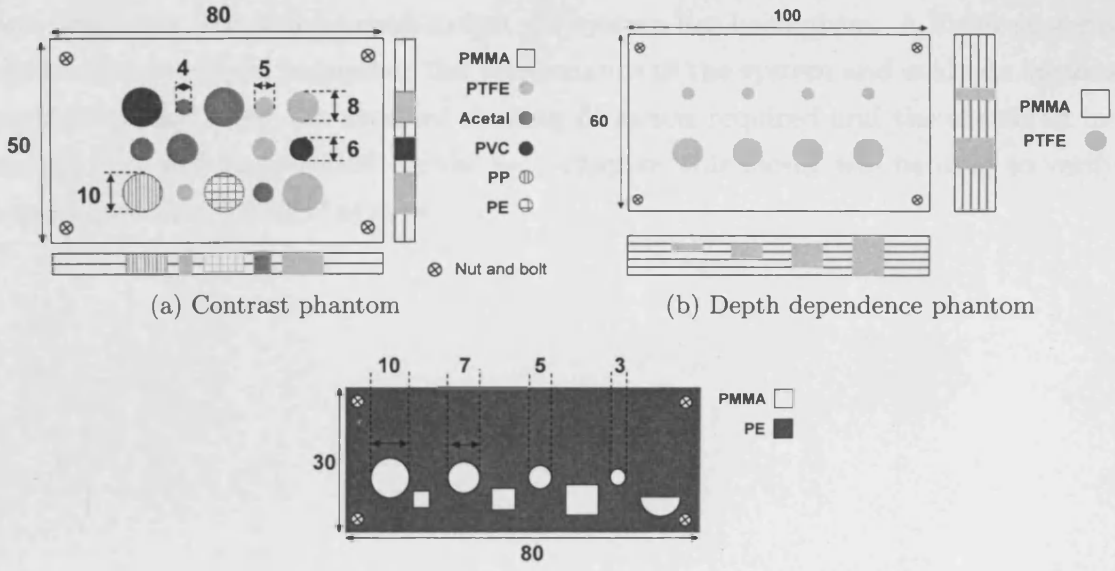


(a) Contrast phantom

(b) Depth dependence phantom

(c) Spatial resolution phantom

Figure 4.20: Three phantoms designed to test the contrast and spatial resolution of the ADXRD system. Side views of (a) and (b) illustrate the penetration of the different inserts within the phantoms.

1mm. Vanilla was fixed in position to record scatter signatures between 2° and 9° to increase the speed of acquisition. At each position, a set of data frames were acquired. At the end of each row, a background acquisition was made.

Three bespoke phantom designs are shown in Figure 4.20. A spatial resolution phantom was produced to test the accuracy of the angular acceptance calculation, along with the ability of the APXRD system to distinguish different shapes. This phantom provides a means to determine the feature sizes that can be resolved by the system. PE is used as the background material with acrylic features because acrylic is widely available in a variety of shapes. These materials were chosen because there is a significant ($0.3\text{nm}^{-1}$) difference between their diffraction peak positions (as documented by the ICDD). A depth dependence phantom was produced to assess the ability of the system to discern a diffraction signal (from PTFE) that had been attenuated by a large amount of tissue equivalent plastic (acrylic). A contrast phantom was designed with inserts of all five plastics with acrylic as the background material. This was used to analyse the contrast obtained with an X-ray diffraction image and in turn assess if any contrast improvement is available using the APXRD system as compared to transmission imaging. The methods for analysing data from the phantom scans will be described in Chapter 5.

## 4.7 Summary

The design, implementation and optimization of an X-ray diffraction system using Active Pixel Sensors has been described in this chapter. A description of the samples

and phantoms that will be used to test the system has been given. A linear systems model was developed to predict the performance of the system and evaluate various parameters including the spectral shaping filtration required and the scattered intensity that will be provided. In the next chapter, this model will be used to verify results from the APXRD system.

# Chapter 5

# Testing of the APXRD system and potential for breast biopsy analysis

## 5.1 Overview

A series of results from the Vanilla-based APXRD system will be presented in this chapter. The scatter signatures recorded for the samples described in Chapter 4 are compared to the output from both models, as well as data found in the literature. Using these results, an assessment of the system performance in X-ray diffraction studies of biological tissue is made. A full system characterization using the resolution, depth dependence and contrast phantoms is then presented, allowing the collimator geometry to be verified and a comparison of the contrast obtained with X-ray diffraction and traditional transmission images is made. The potential of the system to perform quantitative analysis of breast biopsy samples is simulated using the mixed 'breast equivalent' samples. Multivariate analysis is employed to build a regression model that enables the composition of 'unknown' samples to be predicted, hence providing the result that would be needed for a clinical implementation of the system. Finally, the results of a feasibility study using the Large Area Sensor in the APXRD system are presented.

## 5.2 Scatter signatures from plastic reference materials and tissue equivalent samples

### 5.2.1 Data validation

The HPGe and ICDD models were used to verify all APXRD scatter signatures. Hydroxyapatite was used in Chapter 4 to compare the HPGe model results to the ICDD data. The predicted intensities of scatter from the linear systems 'HPGe model' is shown in Figure 5.1 for both filter types compared to the measured result. Given the margin of error due to counting statistics (7% for single filtration, 4%

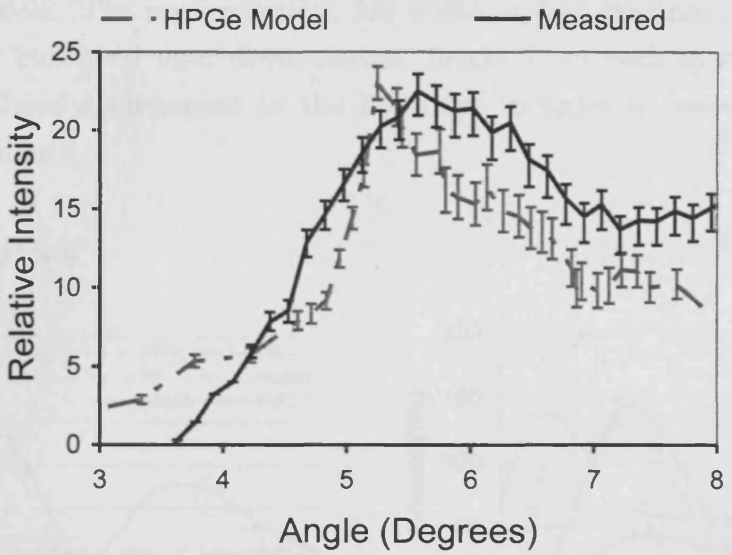


(a) Single filter (actual counts)

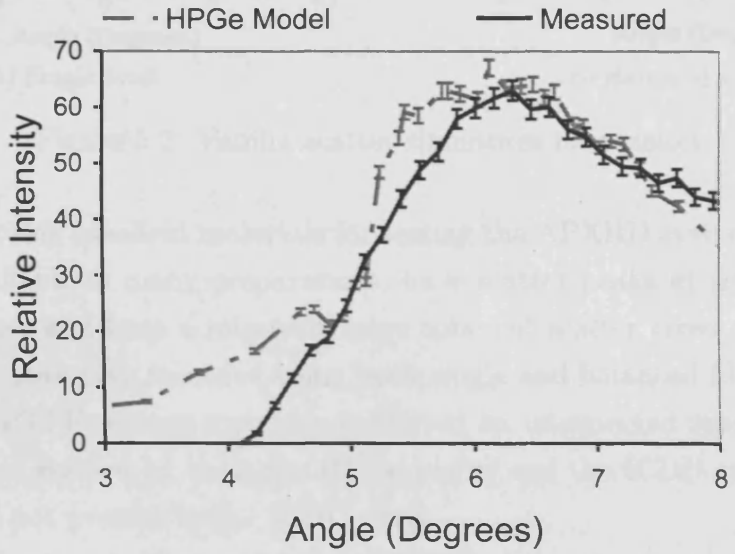


(b) Balanced filter (actual counts)

Figure 5.1: Verification of measured pattern using ICDD and HPGe models. Solid line displays profile measured with prototype Active Pixel Sensor and the dash-dotted line is the result of the HPGe model.

for balanced), the predicted and measured peak intensities can be seen to be in good agreement. The measured peak positions are 5.7±0.2° and 6.4 ± 0.2° for single and balanced filters, compared to predictions of 5.4±0.1° and 6.2±0.1° in the model. It should be noted that the measured result using a single filter is somewhat broader than the HPGe model as compared to balanced filters. This indicates that subtraction of two separate exposures removes an unwanted signal component that the background correction alone does not. It was found that adding an extra filter of 0.027gcm$^{-2}$ of aluminium just after the collimator removed this, thus the added signal is likely to have been fluorescence production from the brass collimator.

For all materials measured, scatter signatures were compared to both the HPGe

and ICDD models. The peak position, full width at half maximum (FWHM) and in the case of biological equivalent tissues, height from each material were also compared to those documented in the literature in order to assess the APXRD system performance.

### 5.2.2 Plastics

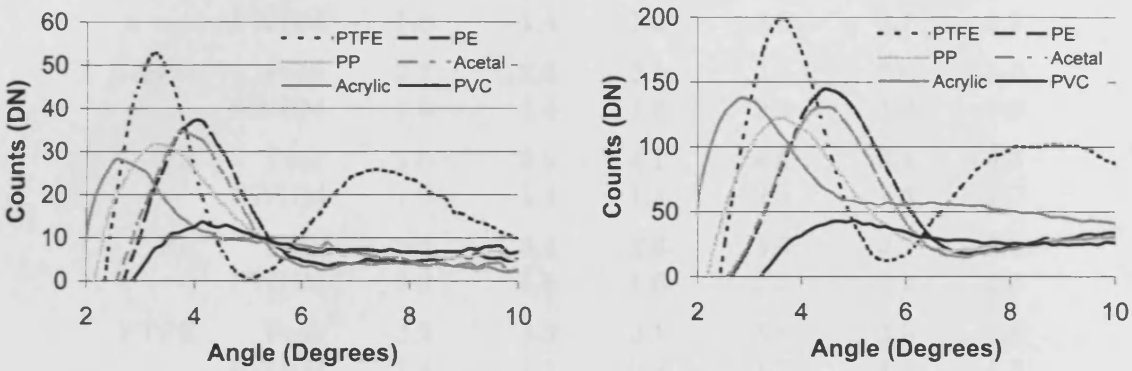


(a) Single filter

(b) Balanced filter

Figure 5.2: Vanilla scatter signatures for plastics

Plastics provide excellent materials for testing the APXRD system because they are widely available in many preparations, have scatter peaks at similar angles to biological tissues and have a relatively large coherent scatter cross section. Figure 5.2 shows the signatures recorded using both single and balanced filtration. It was seen that the PTFE scatter signature exhibited an unexpected second peak. The initial peak was verified by both the HPGe model and the ICDD result, while the second peak is not present in the ICDD result.

Table 5.1 documents the position and FWHM of the plastics scatter peaks from both the APXRD system data, the HPGe model and the ICDD model. It can be seen that the peak positions of all three models are largely in agreement within the errors. The exception to this arises in the ICDD data for PP and PVC, which suggests that the chemical properties of the PP and PVC samples used in this work deviate from the samples that were documented.

The FWHM of the data from the APXRD system is larger than that predicted by both models for both filtration options. This is likely to be due to radiation scattered from the X-ray tube casing and window, or penetrating the detector shielding. The extra contribution is present because the phantom imaging system was used to measure data for pure plastics and no source aperture was present.

Most plastic scatter signatures documented in the literature are from acrylic (also under the trade names of PMMA or lucite) and nylon. Nylon was not used in this work because it is available in many different forms that will have different scatter signatures so it is difficult to predict the results that will be obtained. The measured peak position and FWHM of acrylic agree well with measurements carried out on a

Table 5.1: Characteristics of plastics peaks. The angular errors on the APXRD results for peak position and FHWM are 0.2° and 0.3° respectively, while for the HPGe data they are 0.1° and 0.14° respectively. For the ICDD data, the error is negligible.

| Material | | Single filtration | | | Balanced filtration | | |
|---|---|---|---|---|---|---|---|
| | | APXRD | HPGe | ICDD | APXRD | HPGe | ICDD |
| Acetal | Peak | 3.9 | 3.9 | 3.7 | 4.4 | 4.5 | 4.6 |
| | FWHM | 1.8 | 1.4 | 1.3 | 2.2 | 1.7 | 1.6 |
| Acrylic | Peak | 2.7 | 2.8 | 2.5 | 2.9 | 3.0 | 3.0 |
| | FWHM | 1.8 | 1.4 | 1.8 | 2.4 | 1.9 | 2.9 |
| PE | Peak | 4.0 | 3.9 | 4.1 | 4.5 | 4.4 | 4.3 |
| | FWHM | 1.8 | 1.4 | 1.4 | 2.3 | 1.8 | 1.7 |
| PP | Peak | 3.4 | 3.4 | 2.6 | 3.6 | 3.7 | 2.9 |
| | FWHM | 2.2 | 1.8 | 1.6 | 2.5 | 2.2 | 2.3 |
| PTFE | Peak | 3.2 | 3.3 | 3.1 | 3.6 | 3.6 | 3.8 |
| | FWHM | 1.4 | 1.1 | 0.9 | 1.7 | 1.4 | 1.3 |
| PVC | Peak | 4.2 | n/a | 3.2 | 4.9 | n/a | 3.7 |
| | FWHM | 3.0 | n/a | 1.4 | n/a | n/a | 5.1 |

similar system (Westmore *et al.*, 1996). A separate measurement by Poletti *et al.* (2002) using monoenergetic Mo K$\alpha$ characteristic lines at 17.44keV found the peak at $x = 0.78nm^{-1}$ with FWHM of $0.55nm^{-1}$. For the mean energy of 42keV defined with single filtration, their results are equivalent to a peak of 2.6° and FWHM of 1.9°, in good agreement with those measured here. This shows that for materials with broad scatter peaks, the effect of spectral width on the measured profile is minimal. This result is promising for the chosen application of this system.

### 5.2.3 Breast tissue equivalent samples

Figure 5.3 illustrates the results obtained for the breast tissue equivalent materials of lard (adipose tissue), pork fat (adipose tissue), water (glandular tissue) and pork muscle (carcinoma). The scatter signature of chicken breast meat is not shown to improve the clarity of the figure as it closely overlays the water peak. These results show that balanced filtration gives a much larger peak intensity than single filtration, as expected, but the intensity of scatter using single filtration is still more than sufficient to visualise the different scatter peaks. As ICDD data is not available for the breast tissue materials, results were compared to the HPGe model and found to be in agreement.

A comparison of the measured signatures for the adipose and carcinoma equivalent materials to the data measured by Kidane *et al.* (1999) can be seen in Figure 5.4. The close alignment of the expected peak positions indicates that an acceptable choice of equivalent material has been made in both cases. Both lard and pork fat

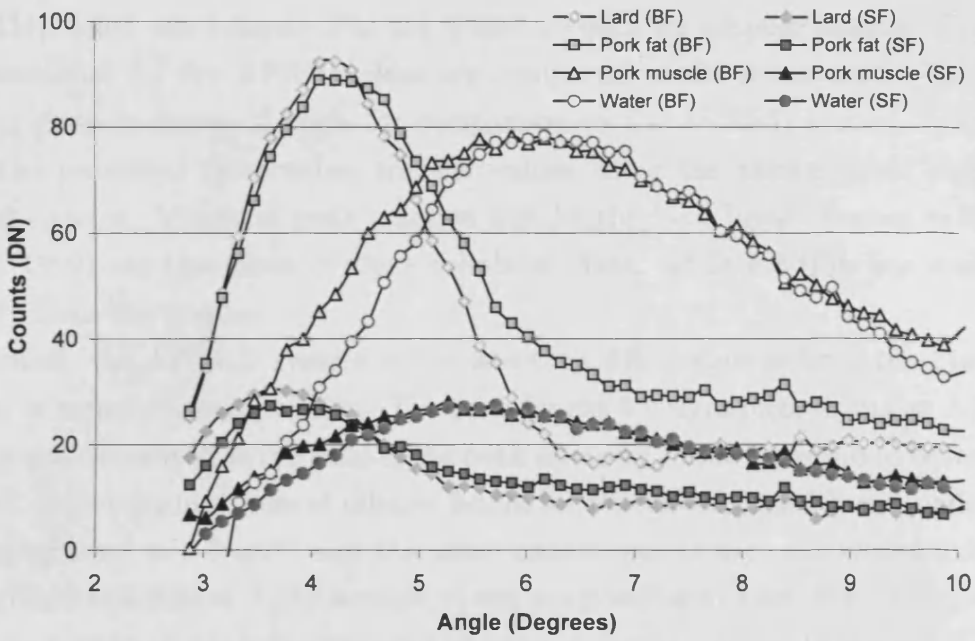


Figure 5.3: Scatter signatures of breast tissue equivalent materials. SF refers to single filtration, BF to balanced filtration. See Table 5.2 for peak characteristics. Chicken breast meat overlays water closely so this was omitted from this figure for clarity.

have a larger full width at half maximum than adipose tissue so in future experiments, other alternatives could be sought. The lard measurement is slightly closer to adipose tissue than pork fat indicating that this provides a better substitute material.

Figure 5.4: Comparison of the scatter signatures from breast equivalent materials measured using single filtration to real tissue signatures from Kidane *et al.* (1999)

Literature measurements are available for pork fat, water and pork muscle and are documented in terms of peak position, height and full width at half maximum

(FWHM). Lard was compared to the literature data for adipose tissues. The peak characteristics for the APXRD data are compared to the literature in Table 5.2. Data is given in terms of angle for comparison to the APXRD system, calculated from the published momentum transfer values using the known mean energy of filtered spectra. Values of peak position and height from breast tissues in Kidane *et al.* (1999) are the mode of their tabulated data, while FWHM was evaluated directly from the graphs.

Overall, the APXRD system shows less than 5% deviation from the literature results in terms of peak position. The peak height for signatures from the APXRD system was calculated as the ratio of the peak intensity to the background between 12 and 15°. The measurements of relative height for Poletti *et al.* (2002) are made using the background at 7-8$nm^{-1}$ and the other measurements were calculated using the background at 3-3.5$nm^{-1}$. As a result, it was not possible to draw direct comparisons between measured peak heights and literature results. Considering the FWHM of APXRD results for pork fat, water and pork muscle compared to Peplow and Verghese (1998), deviations of less than 3%, 8% and 6% are observed respectively. This indicates that as breast tissues have a low degree of order, the broad nature of the amorphous peak largely dominates the effect of spectral width. Using the raw tungsten spectrum at 70kVp to record the scatter signature of lard, a FWHM of 4.8° was measured, twice that given in the literature. The filtration chosen for the APXRD is therefore sufficient to reduce the spectral width so its relative contribution to the peak width is almost negligible.

To construct a system for breast biopsy analysis, we need to identify materials present in an unknown sample given prior knowledge of the scatter signatures of possible components. In Chapter 1 it was suggested that the fat content of a breast biopsy sample could be used to distinguish healthy and diseased tissue, while other features of the samples, such as microcalcifications can identify the category of the disease i.e. benign disease or malignancy. Mixed samples of fibrous (chicken) and adipose (lard) tissue equivalents were prepared using a blender at City University (Farquharson, 2008). Proportions ranging from 0% fat, 100% fibrous, through to 100% fat, 0% fibrous in 10% increments were made, along with samples of 25, 35 and 45% fat content. Scatter signatures were recorded from each of these while the sample was rotated through 360° to ensure all regions of the sample were equally presented to the X-ray beam in case of any nonuniformity in mixing. Data from a selection of these samples is shown in Figure 5.5, along with a predicted signature calculated using a simple weighted superposition of data from the pure samples:

$$Prediction = w_A R_A + w_B R_B \tag{5.1}$$

where A and B refer to the fat and fibrous constituents, $w$ represents the fraction of each material and $R$ denotes the pure scatter signature of that material.

Table 5.2: Values of parameters used to characterize scatter signatures for biological tissues: peak position, relative peak height and full width at half maximum (FWHM). Readers are referred to the individual papers for errors on the data, they are not included here for brevity

| Material | Peak Position | Relative Height | FWHM |
|---|---|---|---|
| *Lard* | | | |
| Single filtration | $3.7 \pm 0.1$ | $3.8 \pm 0.5$ | $2.3 \pm 0.2$ |
| Balanced filtration | $4.2 \pm 0.1$ | $11.8 \pm 0.5$ | $2.3 \pm 0.2$ |
| Kidane *et al.* (1999) Adipose | 3.8 (SF), 4.4 (BF) | 3.2 | 1.5 |
| Poletti *et al.* (2002) Adipose | 3.8 (SF), 4.4 (BF) | 15.3 | 1.4 |
| *Pork Fat* | | | |
| Single filtration | $3.8 \pm 0.1$ | $3.9 \pm 0.5$ | $2.7 \pm 0.2$ |
| Balanced filtration | $4.3 \pm 0.1$ | $6.9 \pm 0.5$ | $2.6 \pm 0.2$ |
| Peplow and Verghese (1998) | 3.9 (SF), 4.5 (BF) | 4.8 | 2.7 |
| *Water* | | | |
| Single filtration | $5.6 \pm 0.1$ | $4.1 \pm 0.5$ | $5.4 \pm 0.2$ |
| Balanced filtration | 6.2 | $4.5 \pm 0.5$ | $5.1 \pm 0.2$ |
| Peplow and Verghese (1998) | 5.5 (SF), 6.5 (BF) | 3.6 | 5.5 |
| Poletti *et al.* (2002) | 5.4 (SF), 6.3 (BF) | 8.4 | 4.0 |
| *Pork Muscle* | | | |
| Single filtration | $5.6 \pm 0.1$ | $4.1 \pm 0.5$ | $5.4 \pm 0.2$ |
| Balanced filtration | $6.1 \pm 0.1$ | $2.5 \pm 0.5$ | $5.8 \pm 0.2$ |
| Peplow and Verghese (1998) | 5.5 (SF), 6.5 (BF) | 3.6 | 5.5 |
| Kidane *et al.* (1999) Carcinoma | 5.3 (SF), 6.2 (BF) | 2.0 | 6.4 |

The changing shape of the material profiles with increasing fibrous content is clearly visible with both filter options, although the distinction of the 20% and 40% fat samples is clearer using the single filter. The accuracy with which the simple superposition (denoted by triangles) predicts the expected profile is sensitive to even relatively small changes in the weighting values. The real test of the system, however, is to predict the content of an unknown sample using its scatter signature, rather than to predict the scatter signature from the sample content. The ability of the APXRD system to do this is tested in Section 5.4 using a multivariate analysis model based upon the mixed sample scatter signatures.

### 5.2.4 Kidney stone and bone equivalent materials

Samples of kidney stone and bone equivalent materials were also interrogated with the APXRD system. Kidney stone equivalents include COM, CP, CPD, UA, MAP and HAP, while bone equivalents include HAP, collagen, water and lard. Collagen produced a broad, low intensity peak at 3.8° and the signatures of water and lard have already been presented so Figure 5.6 shows only the scatter signatures for the powdered samples investigated.

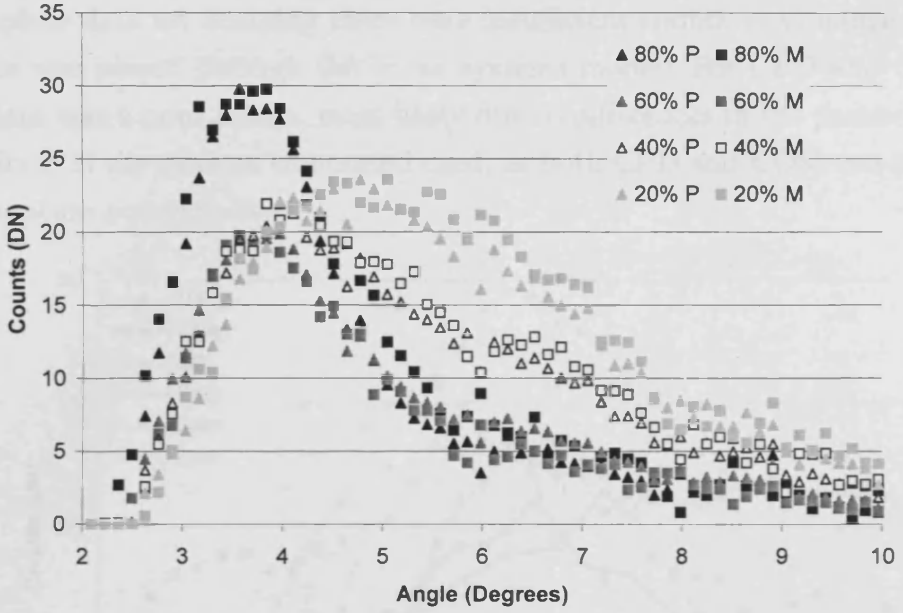


(a) Single filter

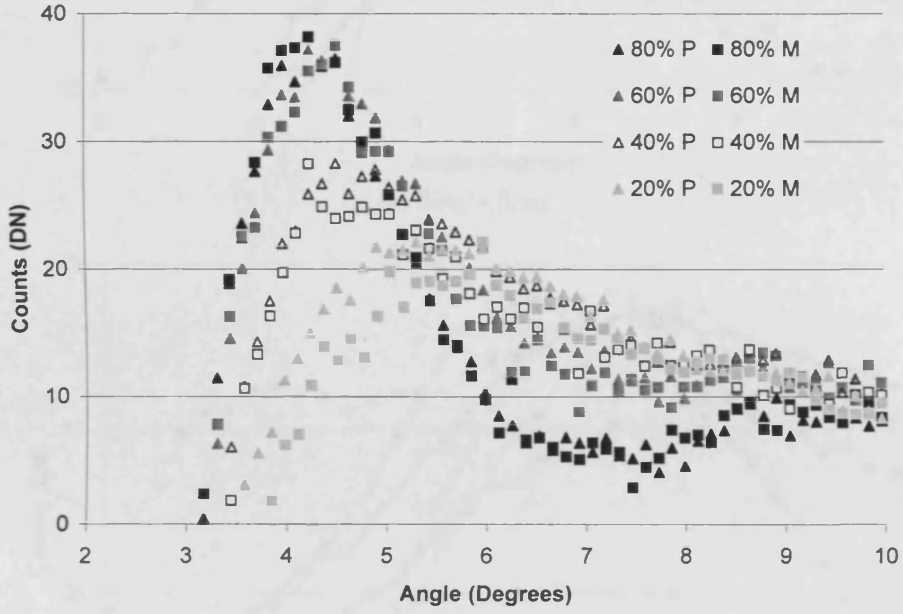


(b) Balanced filter

Figure 5.5: Weighted linear combination of pure sample scatter signatures for fat and fibrous tissue equivalent mixes are shown as triangles (series labelled P). Measured (series labelled M) scatter signatures are shown as squares. Percentages refer to the amount of fat in a given sample. (a) shows the results for the single filter, (b) for the balanced filter.

Validation of the APXRD result was achieved for most of the kidney stone and bone equivalent materials. In general, the material distinction is better with single rather than balanced filtration. Discrepancies arose for MAP, COM and CPD. For MAP, the peak positions are verified but their height is not well matched. The peak seen at 3.5° in the single filtration result should be much more intense, indicating that there was an under-representation of this crystallite orientation in the sample. For COM, a particularly low scatter intensity was recorded by the HPGe detector in

the complete data set meaning there were insufficient counts to visualize a pattern once this was passed through the linear systems model. For CPD and COM, the ICDD data was a poor match, most likely due to differences in the precise chemical composition of the calcium compound used, as both CPD and COM can be verified with literature comparisons.

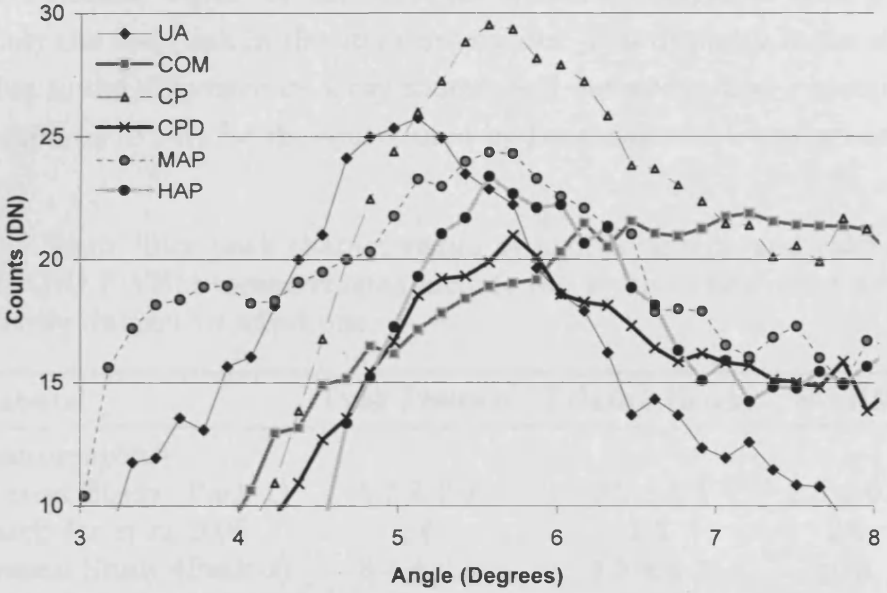


(a) Single filter

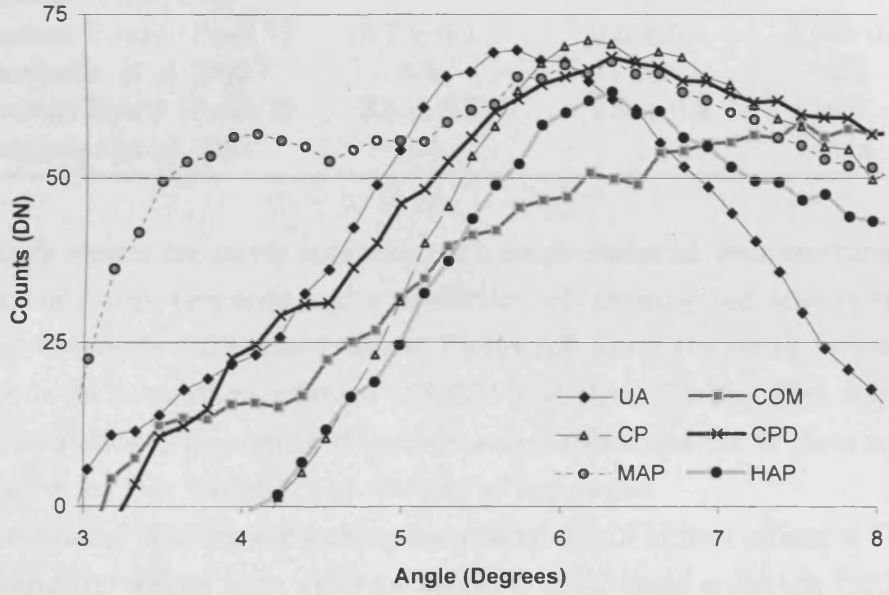


(b) Balanced filter

Figure 5.6: Scatter signatures for kidney stone and bone materials

Signatures were compared to results published by Batchelar *et al.* (2006) for bone and Batchelar and Cunningham (2002) for kidney stones, as their system is most closely aligned to the APXRD arrangement. Comparing to monoenergetic results for these materials is inappropriate as the effect of spectral broadening is severe. As an example, a comparison between the present study and their results

for hydroxyapatite and calcium phosphate using the single beam filter is made in Table 5.3. The peak position and height agree well for the first peak in the scatter signature. However, both materials exhibit a second peak, which can be discerned using the APXRD system but is not sufficiently intense to allow a separate full width at half maximum to be calculated. As a result, there is a disparity between the FWHM results, which for the APXRD system encompasses both peaks but includes only the first peak in the literature results. This disparity in the signatures is likely due to the difference in X-ray source used our source had a spectral width of 19% compared to 14% for the source used by Batchelar and Cunningham (2002).

Table 5.3: Single filter peak characteristics of hydroxyapatite and calcium phosphate. APXRD FWHM measurements include the width of two peaks as they are not sufficiently distinct to select one

| Material | Peak Position | Relative Height | FWHM |
|---|---|---|---|
| *Hydroxyapatite* | | | |
| Present Study (Peak 1) | $5.7 \pm 0.2$ | $2.2 \pm 0.4$ | $2.5 \pm 0.3$ |
| Batchelar *et al* 2006 | 5.6 | 2.5 | 2.0 |
| Present Study (Peak 2) | $8.4 \pm 0.3$ | $1.5 \pm 0.3$ | n/a |
| Batchelar *et al* 2006 | 8.3 | 1.5 | n/a |
| *Calcium Phosphate* | | | |
| Present Study (Peak 1) | $5.7 \pm 0.2$ | $2.6 \pm 0.3$ | $6.0 \pm 0.4$ |
| Batchelar *et al* 2002 | 5.5 | 3.1 | 2.2 |
| Present Study (Peak 2) | $8.5 \pm 0.3$ | $1.8 \pm 0.3$ | n/a |
| Batchelar *et al* 2002 | 8.4 | 1.8 | n/a |

As kidney stones are rarely composed of a single material, four mixtures of powdered materials were prepared and a prediction of the expected scatter signatures made using the method described above. Figure 5.7 shows the result for both filtration methods for a common mixture of COM and HAP (70:30), that accounts for up to 40% of stones. The predicted and measured signatures are in good agreement at wide angles for this mixture, but deviate at low angles.

A less common mixture accounting for around 5% of kidney stones is COM and Uric Acid and the results from different proportions of these materials (30:70, 50:50 and 70:30) are shown for the single filter option in Figure 5.8. The predicted and measured signatures are generally in good agreement, apart from a discrepancy at low angles in the 30:70 result. For balanced filtration there was a marked discrepancy for the 70:30 sample but the other results agreed well.

Discrepancies could arise from a number of sources. Incomplete sample mixing would lead to higher concentrations of one or other of the materials in certain regions. Removing and replacing the sample would then result in different regions and hence compositions being interrogated. Further, the preparation of samples by mass is

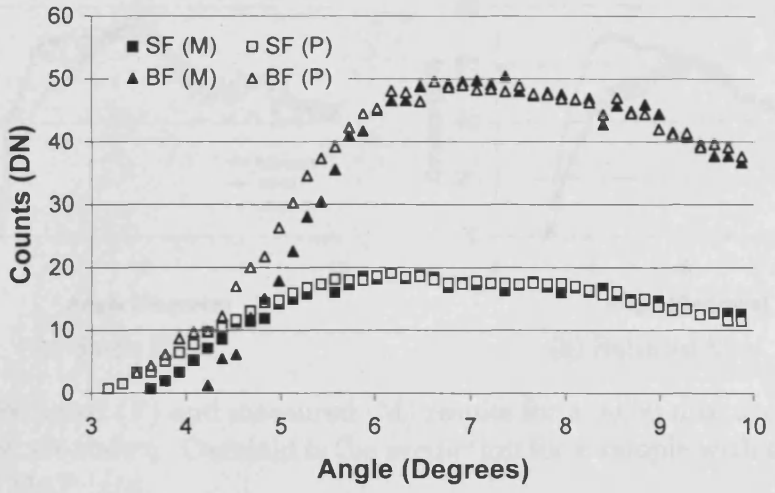


Figure 5.7: Predicted (P) and measured (M) scatter signatures for a mixture of calcium oxalate monohydrate (COM) and hydroxyapatite (HAP), representing the prevalent mixture of calcium oxalate and apatite in kidney stones (70:30)

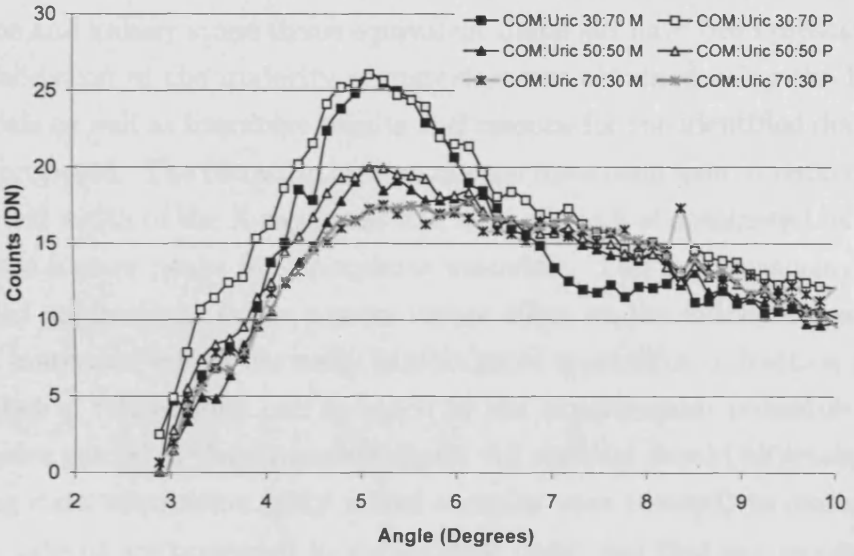


Figure 5.8: Predicted (P) and measured (M) scatter signatures for three mixed samples of calcium oxalate monohydrate (COM) and uric acid (UA) are shown.

only valid if the material densities are equal and this may not be the case for the powdered substances. The fact that 2 of 3 measurements agree for both filtrations indicate that the latter reason is unlikely in this case and the former would provide a better explanation for the discrepancies.

Finally, a 50:50 mixed sample of hydroxyapatite and lard was interrogated to test the ability of the APXRD system to distinguish these components using their scatter signatures (Newton *et al.*, 1992). Figure 5.9 shows that incomplete mixing had an impact on the measurement as a 50:50 superposition of the pure scatter signatures predicts the result for the single filtration measurement, but using balanced filtration the prediction is in severe error and a 62:38 superposition yields close agreement with the measured result.

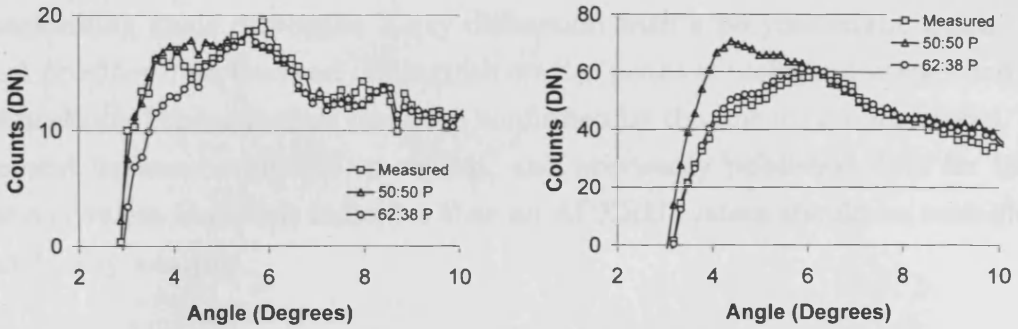


(a) Single filter (b) Balanced filter

Figure 5.9: Predicted (P) and measured (M) results for a 50:50 mixture of hydroxyapatite and lard are shown. Overlaid is the prediction for a sample with a composition ratio of 62:38 HAP:lard.

### 5.2.5 Conclusions

Scatter signatures recorded with the APXRD system for phantom plastics, as well as breast, bone and kidney stone tissue equivalent materials have been presented in this section. Validation of the majority of materials was obtained using the HPGe and ICDD models as well as literature results and reasons for the identified discrepancies have been proposed. The filtration options chosen have been seen to reduce the effect of the spectral width of the X-ray beam to a level where it is dominated by the broad nature of the scatter peaks for amorphous materials. This is a promising result for the intended application. It has a more severe effect on the kidney stone and bone equivalent materials, which normally exhibit more crystalline diffraction peaks.

A number of refinements can be made to the experimental procedure based on the experience gained in these measurements. All samples should be rotated through 360° during data acquisition (only mixed samples were rotated) to ensure all crystallite orientations are presented to the incident beam and that any inhomogeneities or air bubbles within amorphous samples are averaged out. Further, the slightly broader peaks measured with the single filtration option can be prevented if an extra filter of $0.027 gcm^{-2}$ of aluminium is added after the brass collimator to remove fluorescence production from the brass collimator. The output from Vanilla was also observed to drift as a function of room temperature. Data and background measurements therefore either need to be acquired in immediate succession, or normalized to a given value, for example, a dark field measurement or the scatter signature value at wide angles.

For future measurements with the APXRD system, it would be sufficient to employ just one of the filtration options; both yield satisfactory results. Given the convenience of making only one exposure, single filtration might be preferred in general. However, if a smaller collimator were to be used and in turn the count rate reduced, the higher intensity of balanced filtration may be preferable.

Data collected with Vanilla has thus shown that the APS is a suitable device

for performing angle dispersive X-ray diffraction with a polychromatic beam. The system provides data that can distinguish scatter peaks of biological tissues and true identification of the materials has been confirmed by the linear systems model. The agreement between measured, modelled, and previously published data for breast tissue equivalent materials indicates that an APXRD system should be suitable for breast biopsy analysis.

## 5.3 Phantom imaging: system characterization and contrast potential

Following the conclusion that the APXRD system offers a valid option for breast biopsy analysis, a full evaluation of the system performance was needed. To achieve this, a 2D scan of each of the three test phantoms described in Chapter 4 was completed. At each (x,y) location in the scan, a scatter signature was recorded so a 3D array resulted, with the x and y dimensions being the dimensions of the phantom, and the z dimension being a function of angle. For system characterization with the spatial resolution and depth dependence phantoms, 2D scans were used only for feature localization and 1D line scans were used in calculations. In the contrast phantom, over six materials are present so a single material specific image is derived from the scatter signatures to discern each material. The contrast of the resulting image can then be directly compared to a transmission image.

### 5.3.1 System characterization

#### Verifying angular acceptance

As described in Section 4.6.1, the angular acceptance of the experimental phantom scanning system was chosen based on simple geometrical arguments. Using Vanilla to measure the beam dimensions found that the beam height and width in the detector plane were 6.3mm and 4.3mm respectively. The full width at half maximum of these near-Gaussian profiles was 2.9mm and 1.9mm respectively. Using geometry to calculate the beam size in the sample plane yielded 2.6mm height and 1.8mm width with FWHM of 1.2mm and 0.8mm respectively. The beam width for the selected collimator with angular acceptance of 0.83° was expected to be 2mm given the calculation made in Chapter 4. Thus a phantom scan completed with 1mm steps should isolate the scatter signatures from different materials and corresponds to the maximum available resolution. A 'coarser' scan of 2mm steps will subsample the image.

The resolution phantom containing inserts of between 3 and 10mm diameter in both circles and squares was scanned to test this. A 2mm scan was made initially to localise the inserts (see Figure 5.10). A 1mm line scan was then made across

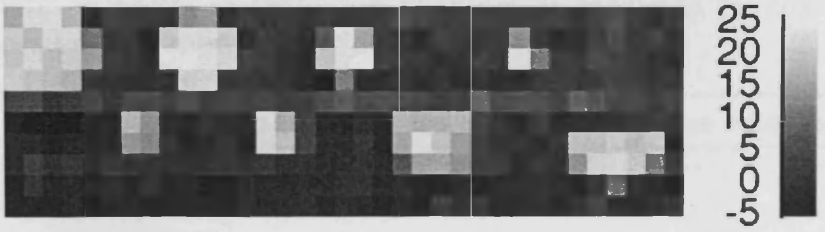


Figure 5.10: Image of resolution phantom acquired in coarse steps of 2mm to localise insert positions. Angle of interest is 3°, the angle of maximum contrast between acrylic and polyethylene. Inserts of circles, squares and a single semicircle can be seen.

the centre of the two lines of inserts. Considering the signatures shown in Figure 5.2, 3° was selected as a suitable angle to highlight the acrylic inserts relative to the background. The two sets of line scan values at 3° are illustrated in Figure 5.11. Thresholding at 6DN (just above the noise level) enables the inserts to be distinguished and Table 5.4 shows the insert sizes evaluated using both the original coarse scan data and the fine line scan data. This table shows that the coarse scan is subsampling the data as expected because it is unable to distinguish the odd sized inserts. All inserts can clearly be delineated by the 1mm scan, indicating that the beam size is as predicted.

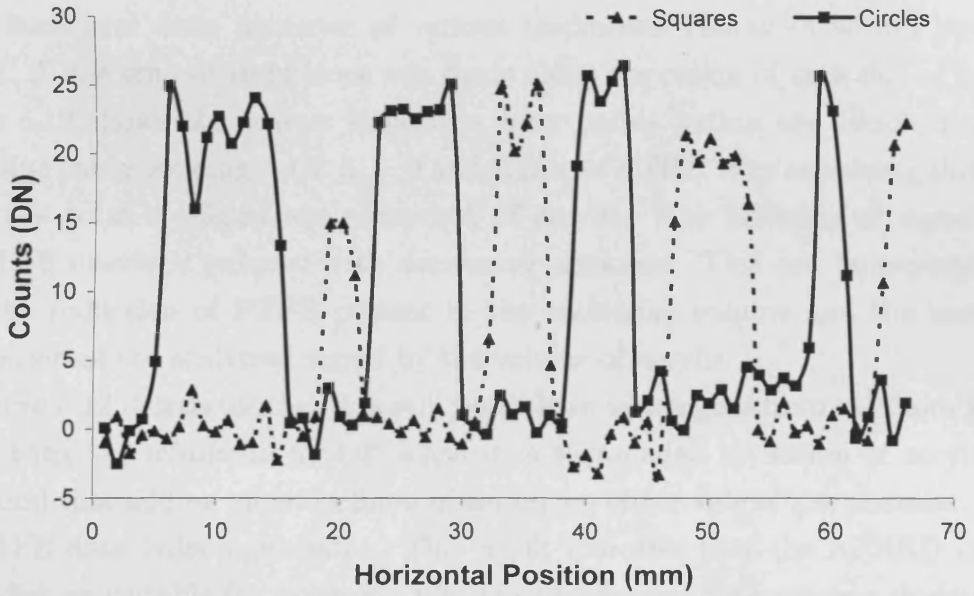


Figure 5.11: Profiles across the 1mm line scan of circular and square inserts. Clear delineation of the inserts from the background is possible, and the insert sizes predicted from thresholding at 6DN (just above the noise level) are listed in Table 5.4.

Table 5.4: Size of inserts in resolution phantom as predicted by coarse and fine scans, compared to the known insert dimension.

| Feature type | Dimension (mm) | Coarse scan size (mm) | Fine scan size (mm) |
|---|---|---|---|
| Circle | 10 | 10 | 10 |
| | 7 | 8 | 7 |
| | 5 | 6 | 5 |
| | 3 | 4 | 3 |
| Square | 7 | 8 | 7 |
| | 5 | 4 | 5 |
| | 3 | 4 | 3 |

### Effect of sample size

Considering the depth dependence of the X-ray diffraction signal in the APXRD system has two benefits. Firstly, it enables the influence of contaminating signal on the scatter signature, such as the paraffin wax that would contain a breast biopsy sample, to be assessed. Secondly, it allows us to establish if the APXRD system could be applied in a 'diffraction enhanced breast imaging' scenario (Griffiths *et al.*, 2003).

The depth dependence phantom described in Chapter 4 contains PTFE inserts with 10mm and 4mm diameter of various thicknesses contained within layers of acrylic. A line scan of 1mm steps was made along the centre of each line of inserts. Figure 5.12 shows the scatter signatures from points within the 10mm diameter insert line corresponding, to 0, 3, 6, 9 and 15mm of PTFE. Any remaining thickness up to the total of 15mm was composed of acrylic. The intensity of signal from the PTFE inserts is reduced with decreasing thickness. This can be explained by both the reduction of PTFE present in the scattering volume and the increased attenuation of the scattered signal by the volume of acrylic.

Figure 5.12 illustrates that it is still possible to view signal from the 3mm PTFE insert using the minimum at 4.6° when it is surrounded by 12mm of acrylic. It was found that adding an extra 3mm of acrylic on either side of the phantom made the PTFE data indistinguishable. This result indicates that the APXRD system would not be suitable for extension into mammography. The average thickness of the compressed breast is around 4cm and the scattered intensity from breast tissue is much lower than that of plastics so it is likely that the signal would be completely attenuated.

Figure 5.13 plots the line scan profiles highlighting both acrylic (a) and PTFE (b) angles of interest. It is clear from the profiles at the PTFE angles of interest that it is not possible to discern the 3mm insert. However, as Table 5.5 shows, the 3mm thick PTFE insert can be identified correctly with 4.5° as the angle of interest. Results from these investigations indicate that over 4 times as much contaminating

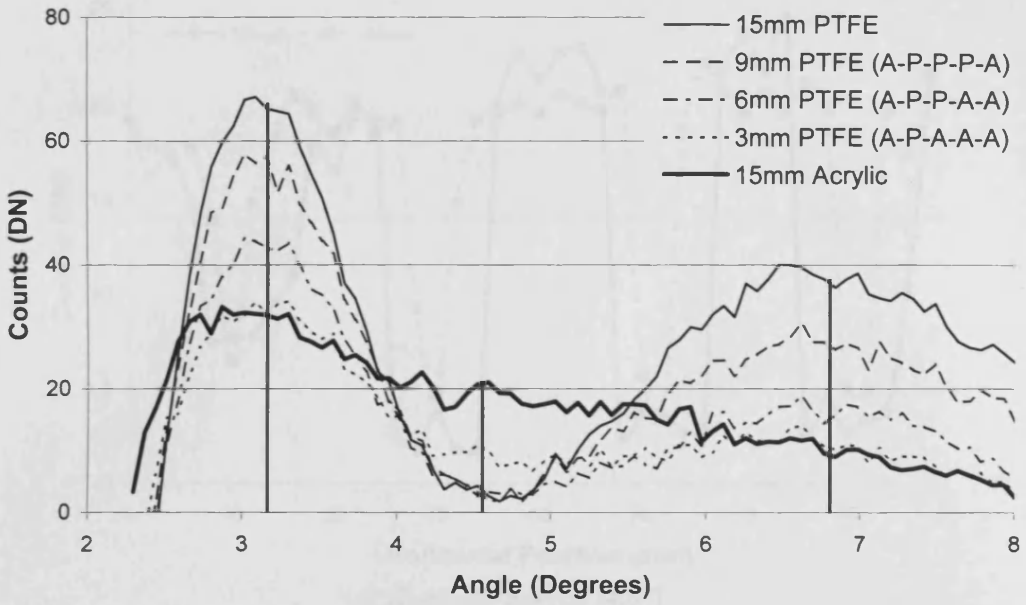


Figure 5.12: Scatter signatures recorded for layers of PTFE, surrounded by increasing thicknesses of Acrylic. The thin solid line illustrates the profile recorded from a 15mm thickness of PTFE centred on scattering volume. Dashed lines show the effect of reducing the thickness of PTFE present (down to 3mm) and replacing it with layers of acrylic. The sequences of letters show the order of materials present, with each representing a 3mm layer. Vertical lines at 3.2, 4.5 and 6.8° highlight relevant angles of interest for discerning acrylic and PTFE data.

Table 5.5: Size of PTFE thicknesses surrounded by acrylic layers. Thresholds were applied to the profiles illustrated in Figure 5.13 of >35, <14 and >12DN for 3.2, 4.5 and 6.8° respectively and the number of horizontal positions above or below the threshold was used to estimate the diameter of the PTFE insert.

| Layers | 10mm diameter | | | 4mm diameter | | |
|---|---|---|---|---|---|---|
| | 3.2° | 4.5° | 6.8° | 3.2° | 4.5° | 6.8° |
| A-P-A-A-A | 2 | 10 | 0 | 0 | 4 | 0 |
| A-P-P-A-A | 10 | 10 | 10 | 4 | 4 | 4 |
| A-P-P-P-A | 10 | 10 | 10 | 4 | 4 | 4 |
| P-P-P-P-P | 10 | 12 | 10 | 4 | 4 | 4 |

material as sample is needed to obscure the interesting signal and careful selection of angles of interest can be used to 'find' signal among this contamination.

### 5.3.2 Contrast potential

#### Angles of maximum contrast and signal-to-noise ratio

When imaging the phantom designed to assess the contrast potential of the system, the most relevant angles to examine are those that correspond to the maximum insert contrast. For each angular plane of information, the contrast of each insert

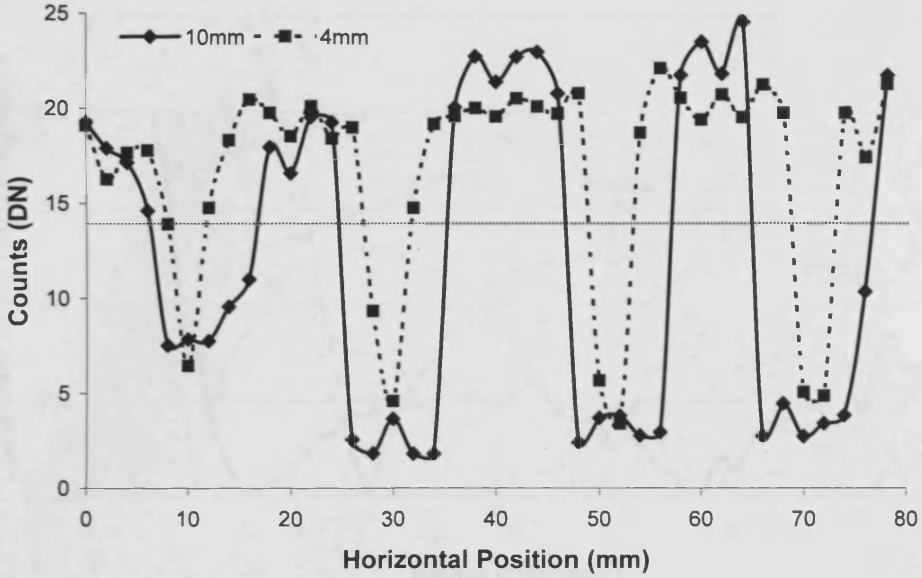


(a) Highlight Acrylic (4.5°)

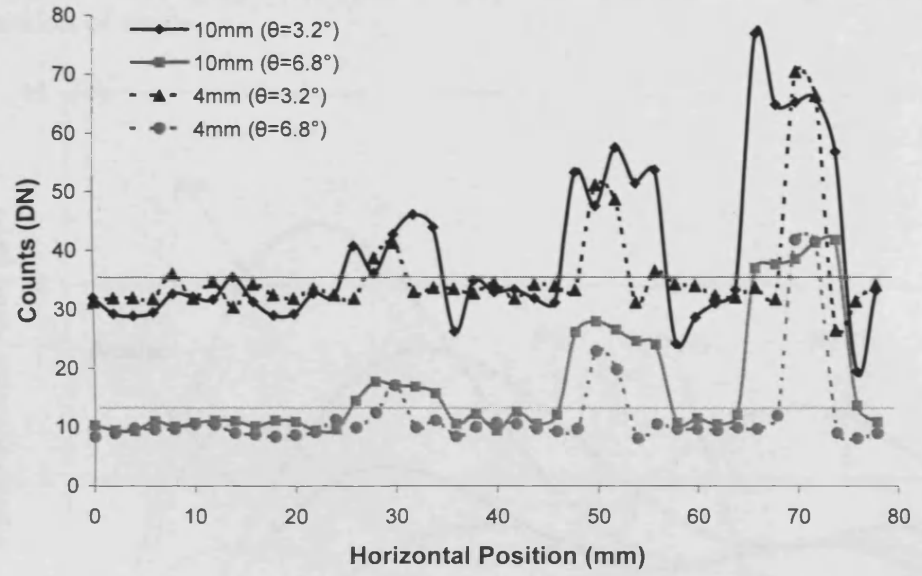


(b) Highlight PTFE (3.2 and 6.8°)

Figure 5.13: The PTFE inserts were centred on horizontal positions of 12, 30, 52 and 70mm. Selecting 3.2°, 4.5° and 6.8° as the angles of interest from Figure 5.12, the profiles above were formed for PTFE diameters of 4 and 10mm, and the predicted dimension of the inserts evaluated.

relative to the acrylic background was calculated using

$$C = \frac{|\mu_1 - \mu_2|}{\mu_1 + \mu_2} \tag{5.2}$$

where the associated error on the contrast $\sigma_C$ is calculated through (Griffiths *et al.*, 2008)

$$\sigma_C^2 = \left(\frac{2\mu_2}{(\mu_1+\mu_2)^2}\right)^2 \sigma_{\mu_1}^2 + \left(\frac{2\mu_1}{(\mu_1+\mu_2)^2}\right)^2 \sigma_{\mu_2}^2 \tag{5.3}$$

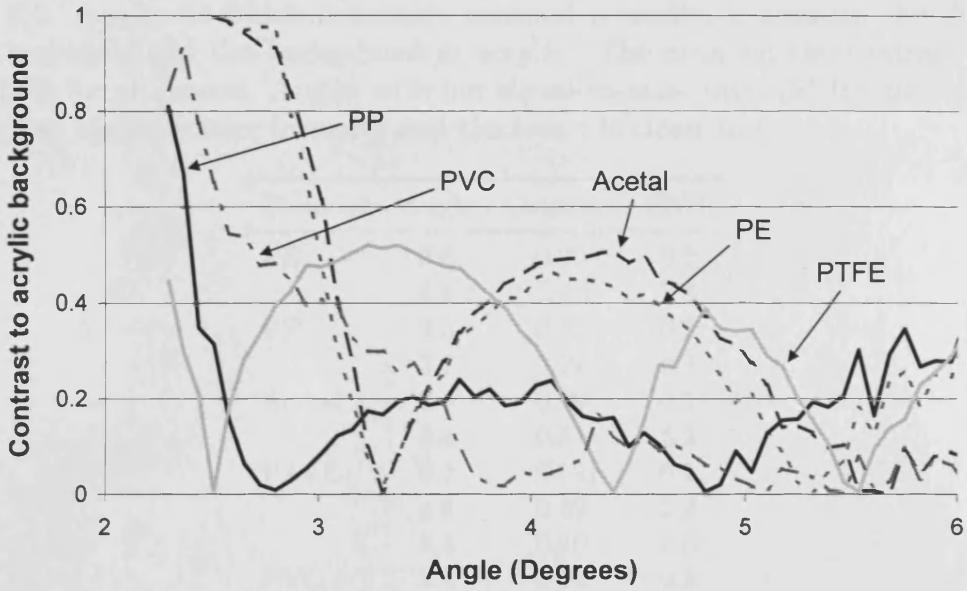


Figure 5.14: Contrast between each insert material and the background of acrylic as a function of angle

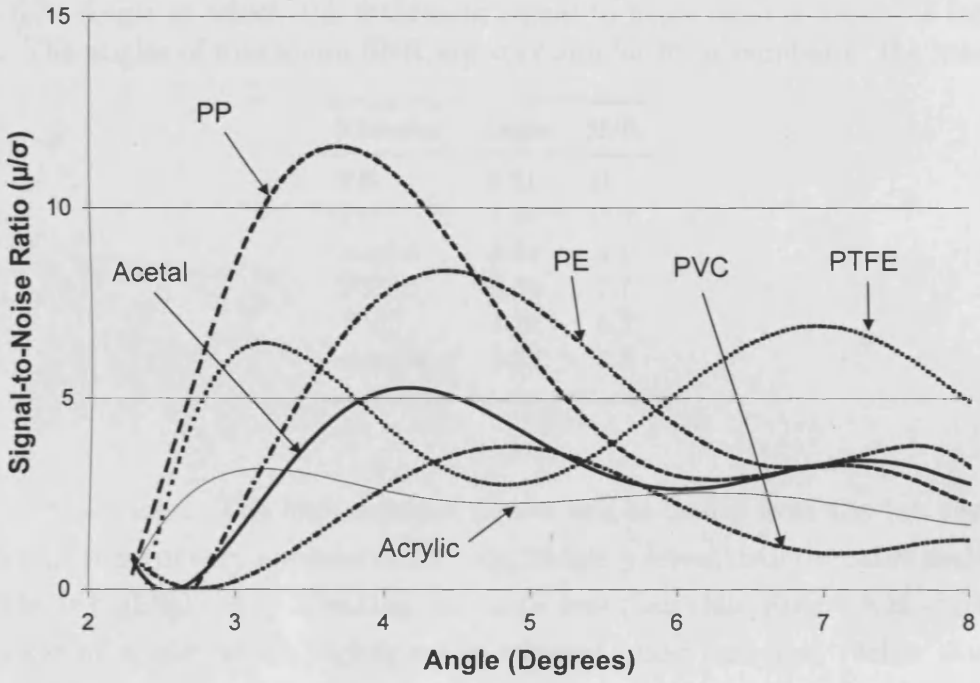


Figure 5.15: Signal-to-noise ratio of each insert as a function of angle

In the case where multiple inserts of the same material are present, data from all inserts were averaged. In addition, the signal-to-noise ratio of each insert is calculated as $SNR = \mu/\sigma$, where $\mu$ is the mean of the insert region and $\sigma$ is the standard deviation. The contrast and signal-to-noise ratio as a function of angle are shown in Figures 5.14 and 5.15 respectively. For most materials, angles that correspond to a high contrast and also provide a good signal-to-noise ratio.

Table 5.6 lists the angles at which the highest contrast can be obtained between a given insert and the acrylic background, along with the signal-to-noise ratio of the

Table 5.6: Angles at which maximum contrast is available between the different insert materials and the background of acrylic. The error on the contrast is less than 0.5% for all inserts. Angles with low signal-to-noise ratio (SNR) indicate that acrylic has higher scatter intensity and the insert is closer to 0.

| Material | Angle | Contrast | SNR |
|---|---|---|---|
| PE | 2.6 | 0.99 | 0.2 |
| | 4.1 | 0.47 | 7.8 |
| PP | 2.3 | 0.81 | 0.2 |
| | 3.7 | 0.24 | 9.7 |
| Acetal | 2.5 | 0.99 | 0.1 |
| | 4.4 | 0.51 | 5.2 |
| PTFE | 3.2 | 0.52 | 6.1 |
| | 4.8 | 0.39 | 1.9 |
| | 8.4 | 0.70 | 3.3 |
| PVC | 2.4 | 0.94 | 0.3 |
| | 4.3 | 0.18 | 3.4 |

Table 5.7: Angle at which the maximum signal-to-noise ratio is available for each insert. The angles of maximum SNR are very similar for a number of the inserts.

| Material | Angle | SNR |
|---|---|---|
| PE | 4.31 | 11.0 |
| PP | 4.38 | 15.8 |
| Acetal | 4.24 | 5.7 |
| PTFE | 6.34 | 7.7 |
| PVC | 4.24 | 5.2 |
| Acrylic | 5.82 | 3.6 |

insert at that point. The high contrast at low angles comes from the fact that the scatter signature of acrylic peaks at 2.7°, significantly lower than the other materials, so acrylic is highlighted by selecting any angle less than this. Figure 5.16 shows the 2D images at angles which highlight the relevant insert material, rather than the background. Images were obtained by averaging data from $\pm 0.2°$ on either side of the identified angle of interest. While PTFE and Acetal can be easily distinguished in this way, the angles of 'maximum contrast' of the other materials do not sufficiently highlight the relevant insert.

Supplementary to the investigation of maximal contrast is that of maximum signal-to-noise ratio. Table 5.7 lists the angles where maximum SNR can be obtained. For PE, PP, Acetal and PVC, $(4.3 \pm 0.1)°$ provides the best SNR whereas for PTFE, this is found at 6.3°. Images at these angles are shown in Figure 5.17.

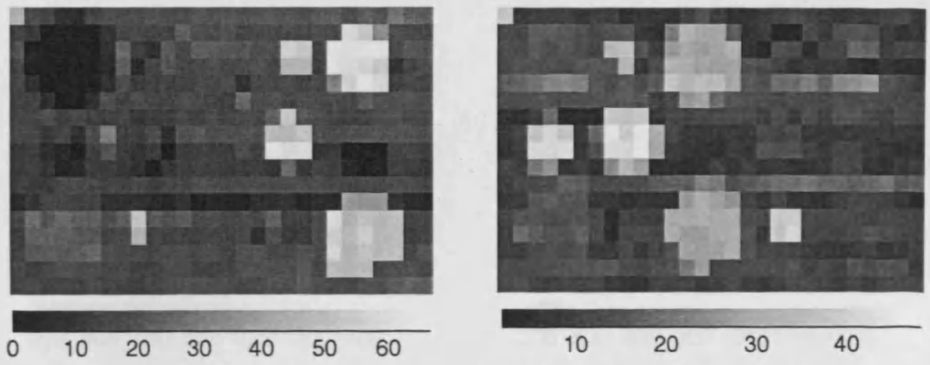


(a) PTFE




(b) PVC (top left)

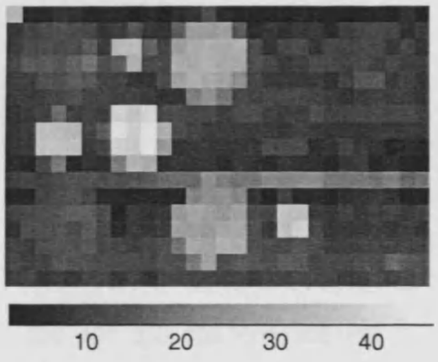


(c) PE (bottom centre) and Acetal (rest)

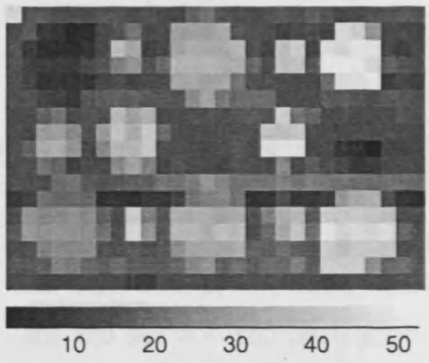


(d) PP (bottom left)

Figure 5.16: Contrast phantom images created by selecting different angles to highlight the maximum contrast of different inserts relative to the acrylic background (see Table 5.6)

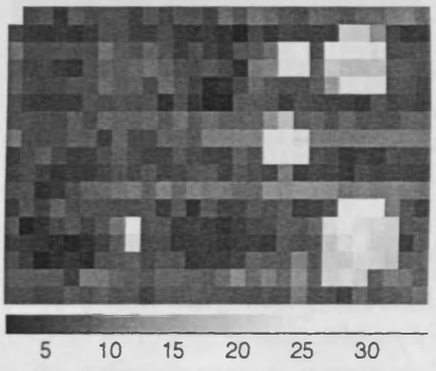


(a) PTFE

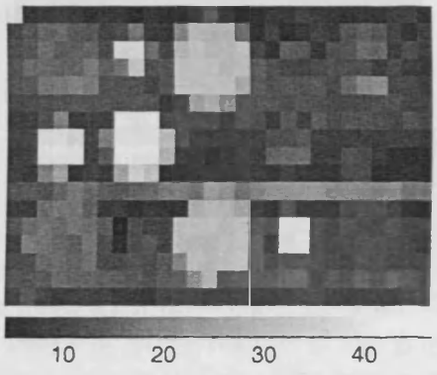


(b) Others

Figure 5.17: Contrast phantom images created by selecting different angles to highlight the maximum signal-to-noise ratio of different inserts (see Table 5.7)

### Producing a material specific image

While the images produced from a single angle individually highlight different materials, a more valuable result for comparing diffraction and transmission data is to combine the diffraction data into a single image that allows all materials to be distinguished. The angles and types of combination to test will depend on the mate-

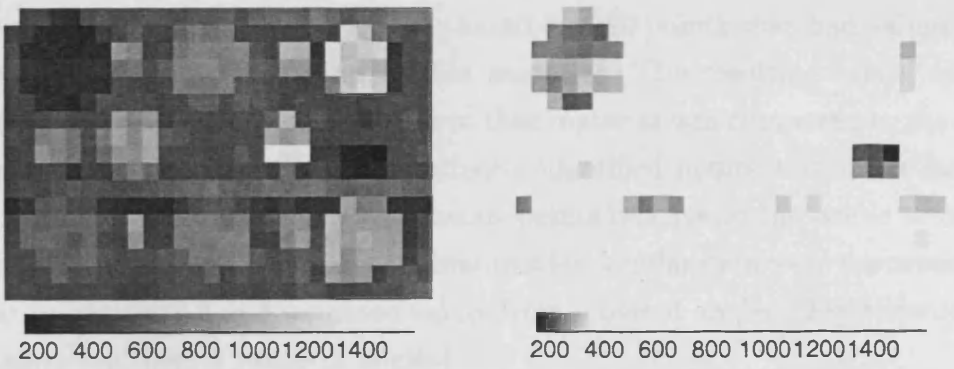


(a) Total




(b) PVC

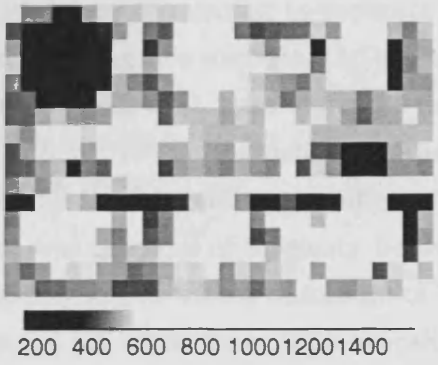


(c) Acrylic

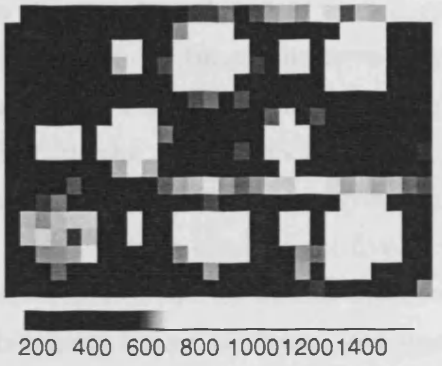


(d) PP

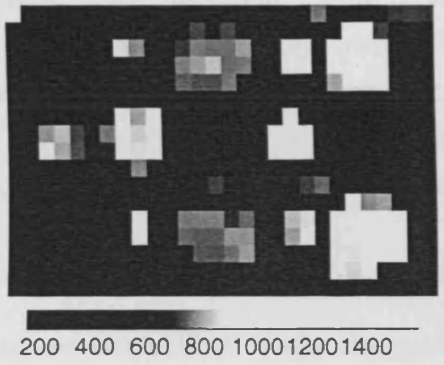


(e) PE and Acetal

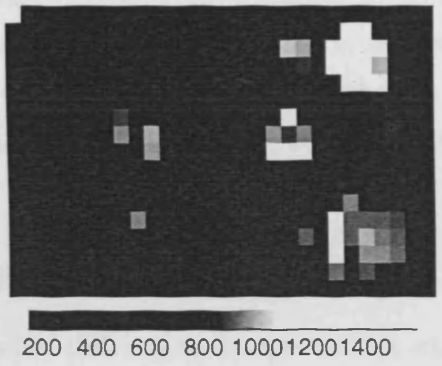


(f) PTFE

Figure 5.18: Contrast phantom images created by summing intensity data between 2 and 5° to enable each material to be identified by a different grey level. Figure (a) shows the complete image, while (b)-(e) select different regions of the grey level to highlight different materials making different inserts visible. The summation of counts was shown to have an accuracy of at least 70% in identifying each material, while maintaining a low error rate of less than 6% of the array.

rials that should be distinguished. Looking at the scatter signatures of the plastics, it is clear that most of the diffraction information exists between 2 and 6°, with higher angles than this relating to the background signal (except for PTFE). This is therefore the most relevant angular range to consider when combining scattered intensity for these materials.

To compare different combination images, a testing methodology was developed. For each plastic insert that could be distinguished in a given combination image,

the range of grey levels it displayed was found and all points that had values in this range were counted as belonging to that material. The resulting 'mask' showing which points in the image corresponded to that material was compared to the known insert positions. The percentages of correctly identified points within the insert(s), missed points in the insert(s) and erroneous points relative to the whole array were calculated. The range of relevant combinations for angular data were narrowed down to linear (addition of 2 or 3 weighted values from different angles), logarithmic, ratio and summation (over a range of angles).

It was clear from testing relevant combinations that the scatter signatures of PE and Acetal were too similar to separate so the PE and Acetal inserts were considered together, leaving five materials to distinguish. Linear combinations were commonly able to distinguish at most three of the plastics. Using logarithmic combinations, it was difficult to distinguish acetal and PE from the acrylic background. Ratios weighted by the relevant angle suffered the same problem. The most promising combination was the sum of intensity between 2 and 5° which enabled all five materials to be distinguished with a minimum of 70% detection of counts within the insert and less than a 6% error rate. The overall combination image is shown in Figure 5.18 (a). Thresholding the relevant grey scale for each material shows that it is possible to distinguish all materials. Some of the images show contamination in horizontal lines 1 and 11 from half way across. These measurement had to be delayed half way through so some temperature drift is present. Data in both lines should belong to the acrylic background so any signal detected when looking at the inserts was ignored and did not contribute to the error count.

### Comparison of diffraction and transmission information

To compare the utility of the material-specific diffraction image with a standard transmission image, the contrast available in each should be compared. A second scan of the contrast phantom was made with Vanilla aligned with the primary beam to record the transmission data in the same steps as the diffraction data. A transmission image acquired in standard imaging geometry would have a much higher spatial resolution than the coarse stepped diffraction scan, so a comparison between the two would not have been appropriate. Further, this arrangement mimics the data that would have been available from the Large Area Sensor had this been used in the phantom scanning system.

Figure 5.19 illustrates the contrast and contrast-to-noise ratio (CNR) available for the different materials in the transmission and diffraction images. The 'Corrected' data refers to dividing the diffraction and transmission images, a common procedure to account for sample self attenuation in X-ray diffraction data. The contrast available from material-specific diffraction image is clearly far higher than that possible using transmission data. The exception is the case of PVC, which from

Table 4.2 has a significantly higher attenuation coefficient than the other plastics so has reasonable contrast in the transmission image. Applying the 'attenuation correction' to the diffraction image only significantly improves the contrast of PTFE, while reducing the PVC contrast to below the transmission level and making a moderate difference to the rest. This is to be expected as PTFE and PVC have the most significantly different attenuation coefficients compared to the rest of the materials (see Chapter 4).

The contrast-to-noise ratio is another relevant measure as it allows us to account for the difference in counting statistics of transmission and diffraction images. It is given by

$$CNR = \frac{|\mu_1 - \mu_2|}{\sigma_1} \tag{5.4}$$

The CNR is superior in the transmission image for 4 out of the 5 materials for this reason. Performing the attenuation corrections adds the noise of the two images in quadrature so the change in CNR after correction is less significant than the change in contrast. For example PTFE contrast increased by 21% with correction whereas CNR increased by only 5%.

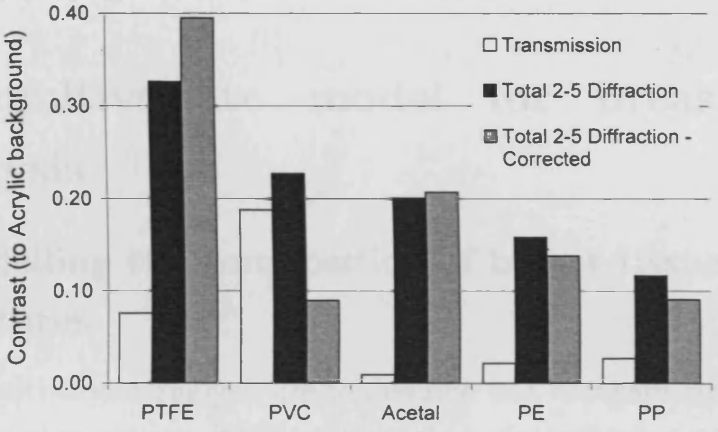


(a) Contrast

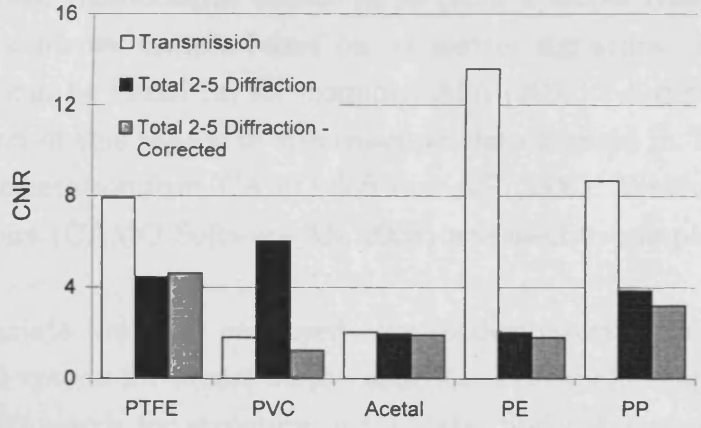


(b) Contrast-to-noise ratio (CNR)

Figure 5.19: Comparison of the contrast available from the transmission image, compared to that of the material-specific X-ray diffraction image. Also included are the results from the 'transmission corrected' material-specific image.

### 5.3.3 Summary of phantom results

2D phantom imaging was completed to characterize the angular acceptance and data depth dependence of the APXRD system. The maximum resolution available with the current system arrangement was found to be 1mm. Better resolution could be obtained by reducing the collimator size, trading scattered intensity for required resolution. By carefully selecting the angle at which to analyse data from the depth dependence phantom scan, it was possible to retrieve signals from PTFE that had been obscured within 12mm of acrylic. However, this signal was entirely lost with the addition of 18mm of acrylic indicating that the APXRD system would not be suitable for application in conventional mammography. Data from the contrast phantom was used to produce a single material-specific diffraction image based on a summation of counts between 2 and 5°. If a planar imaging arrangement were to be employed in a biopsy analysis system to avoid missing lesions in different parts of a sample, a different combination image may be required as different angles of interest exist in this case. Comparing results from the material-specific image to equivalent transmission data, it is clear that superior image contrast is available using the material-specific X-ray diffraction image.

## 5.4 A multivariate model for breast biopsy analysis

### 5.4.1 Modelling the composition of breast tissue equivalent mixtures

The goals of multivariate analysis are to describe and correlate structures in data containing many observations of different variables, for multiple samples of interest. In this work, these relationships enable us to build a model that can predict the composition of a biopsy sample based on its scatter signature. Full multivariate analysis theory can be found in, for example, Afifi (2003). A detailed description of the application of this theory to spectroscopic data is given in The Unscrambler 'Methods' documentation from CAMO Software AS (2006). Version 9.6 of The Unscrambler software (CAMO Software AS, 2008) was used to complete the following analysis.

Two multivariate tools are employed here to demonstrate the potential of using the APXRD system for breast biopsy analysis. Principal Components Analysis (PCA) is used to search for structure in the data, find out how different samples are related to each other and determine how each angle in the scatter signature contributes to this relationship. 'Principal components' (PCs) are orthogonal directions in variable space that sequentially minimise the variance in the data set. The

'residual variance' after each PC has been found is the amount of variation in the data that remains to be explained. This will be minimal when the optimum number of PCs has been found.

Partial Least Squares (PLS) regression looks for relationships between the many variables and samples and produces a predictive model of these relationships with no prior knowledge of the statistics of the data set. PLS is an iterative process of calibration using 'known' samples and validation using 'unknown' samples. The first step of validation is to identify and omit outliers. The second step is to test the performance of the model when new data is introduced. This is frequently achieved using 'full cross validation', where a model is built iteratively by leaving out one calibration sample each time and calculating a sub-model of the remaining samples to predict its value. Finally, the composition of new samples can be predicted. The 'root mean square error' (RMSE) of the model tells us the accuracy with which predictions can be made.

Scatter signatures from four measurements of all fat/fibrous mix samples described in Section 5.2.3 were imported into The Unscrambler (CAMO Software AS, 2008). The average profiles from these measurements are shown in Figure 5.20. Samples with 0%, 20%, 40%, 50%, 60%, 80% and 100% fat were used for calibration, while 25%, 35% and 45% fat samples were used for the final validation stage i.e. prediction. The known fat and fibrous contents of each sample were input as variables for the calibration samples. The sampled angular range of 3-10° associated with the spectra was input and a separate model was built for each filter option.

### 5.4.2 Implementing and testing the model

#### Preprocessing

Data preprocessing may be necessary if the input scatter signatures are of poor statistical quality, or suffer from additive or multiplicative offsets due to data acquisition parameters. Without preprocessing, attempts to form a model of these data sets may only produce a model of the noise and will have reduced predictive capability. The need for preprocessing can be assessed through the RMSE of models produced with different processing applied. A 'predicted vs. measured' graph plots the composition values predicted by the model against those input by the user and should ideally exhibit a slope of 1 and root mean square error in prediction (RMSEP) of 0. Preprocessing should be used only if it yields results that are closer to the ideal than obtained with the raw data.

The Unscrambler software (CAMO Software AS, 2008) includes a number of preprocessing functions relevant to spectral analysis. Mean and/or area normalization rescale the data so that the area under the spectrum is the same for all samples. Savitzky-Golay smoothing removes sharp discontinuities that may appear

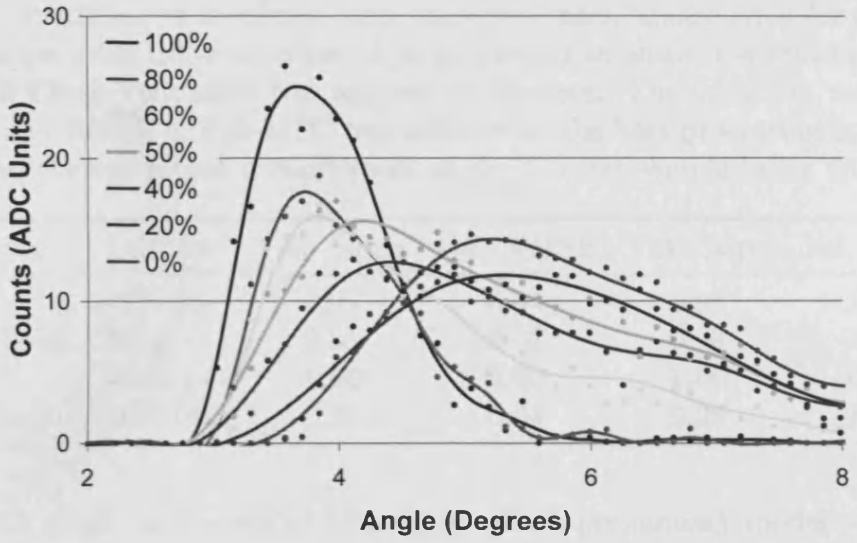


(a) Single filter

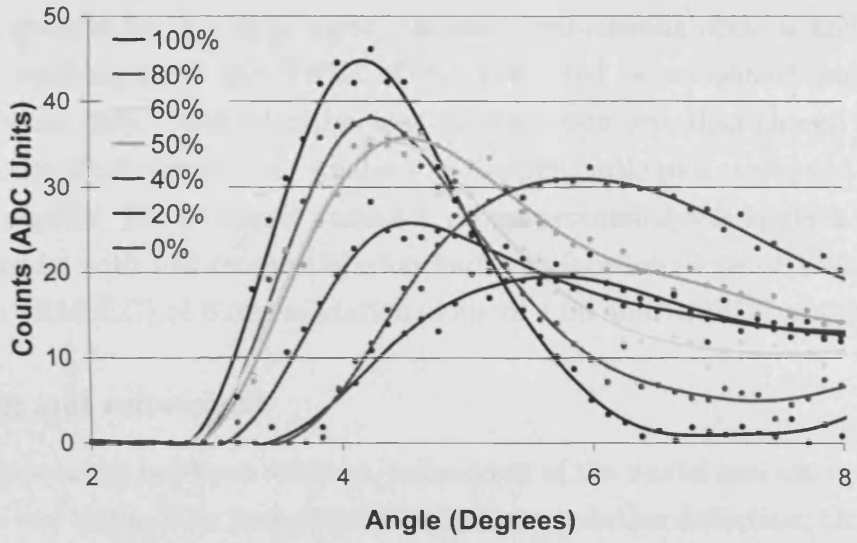


(b) Balanced filter

Figure 5.20: Profiles acquired for fat/fibrous mixtures, labelled by percentage fat content. Savitzky-Golay smoothed data is shown as a line plot with the raw data as points to illustrate the progression between 100% and 0% fat (or 0% to 100% fibrous)

in diffraction spectra due to noise. Centering is the process of subtracting the average from each variable and ensures all results are interpreted in terms of variation around the mean. Centering is enabled as the 'default' for PLS models and should always be performed on spectroscopic data (CAMO Software AS, 2006). Multiplicative scatter correction (MSC) can be used to remove multiplicative (amplification) and additive (offset) effects from a spectrum. The decision to apply MSC can be taken by looking at a 'percentile plot', which shows the variation in data values for each wavelength. The percentile plot highlights the wavelengths that have the largest variation; these are probably the most informative wavelengths. When a baseline shift has occurred, the percentile plot will show a similar spread for all wavelengths, even those whose values are close to zero. In this case, MSC is needed.

Table 5.8: Predicted vs Measured slope and root mean square error for calibration and validation using different types of preprocessing to assess the optimum type to apply. Full Cross Validation was applied in all cases. The optimum results are a slope of 1 and RMSE of 0 so MSC was selected as the best processing option. 40% (4) refers to the 4th repeat measurement of the 40% fat sample being an outlier

| Processing | Outliers | Cal. Slope | Cal. RMSE | Val. Slope | Val. RMSE |
|---|---|---|---|---|---|
| None | 40% (4) | 0.99 | 0.04 | 0.98 | 0.05 |
| Mean Norm. | None | 0.95 | 0.07 | 0.93 | 0.09 |
| **MSC** | **40% (4)** | **1.00** | **0.02** | **1.00** | **0.02** |
| Smoothing | 40% (4) | 0.99 | 0.04 | 0.98 | 0.05 |

For both single and balanced filter data sets, a preliminary model was formed using the minimum in the residual variance to select the optimum number of PCs. This was repeated for the three most relevant preprocessing options and Table 5.8 shows the resulting slope and RMSE of the 'predicted vs. measured graph' for the single filtration data. Multiplicative scatter correction was thus chosen as preprocessing for the single filter data. Analysis of the percentile plot confirmed that MSC should be applied. For balanced filtration, no preprocessing was applied as the preliminary model with full cross validation had a calibration slope of 1.00, RMSE of calibration (RMSEC) of 0.02, validation slope of 1.00 and RMSEP of 0.02.

### Modelling and refinement

Once preprocessing has been selected, refinement of the model and interpretation of the results can begin. The first stage of refinement is outlier detection; three outliers were identified overall. For the single filter data, the 25% data set was of very poor statistical quality, possibly due to the presence of an air bubble in the sample holder although care had been taken to prevent these. The 4th repeat measurement of the 40% sample was also an outlier. For the balanced filters, the 3rd repeat for the 45% sample was an outlier. Where necessary, outliers were omitted from model calibration. The optimum number of principal components for single and balanced filters are 3 and 2 (99.9% explained variance) respectively. The number needed for predictions are 2 and 1 respectively.

### Interpretation

With preprocessing applied, the optimum number of PCs chosen and outliers removed, the data is ready for interpretation. First, a principal components analysis is run using the optimum number of components to look at the structure of the data. Then, the PLS model is calibrated and tested with the validation samples.

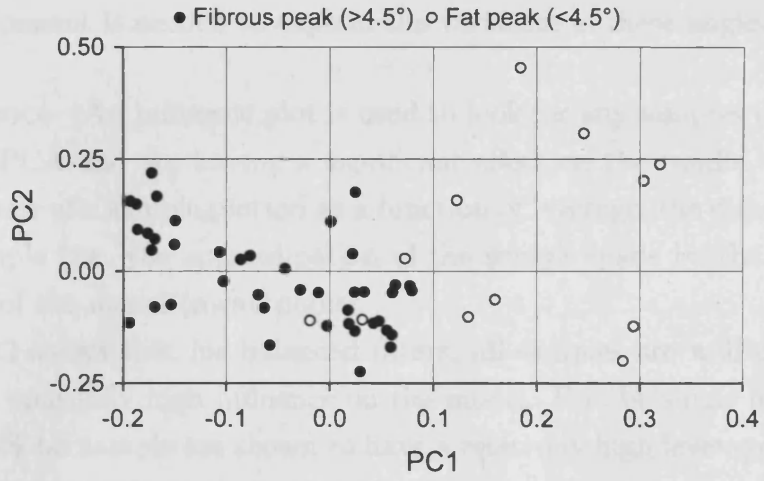


(a) Single filter

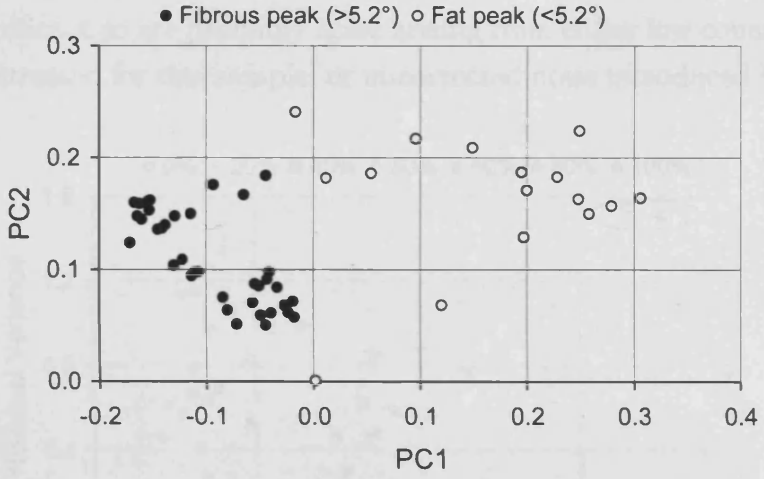


(b) Balanced filter

Figure 5.21: Loadings plots along PC2 and PC1 showing which angles contribute similarly to the PCA model.

**PCA: Loadings** Loadings describe the data structure in terms of variable correlations; variables are positively correlated if they have similar values along a given PC. The plots in Figure 5.21 show the loadings of each angle along each PC. The angles in the range over which the fibrous peak dominates scattered intensity (see Figure 5.20) are shown as black circles, while the angles where the fat peak dominates are illustrated by white circles. For both filter options, the loadings show a positive correlation between the angles within the fat and fibrous peaks and a negative correlation between these groups.

The distinction between the two groups of angles is clear for the balanced filter data, but as noted previously, a third PC is needed to fully describe the variation in the single filter data. This was further confirmed using a correlation loadings plot to test the data against the limits of 100% and 50% explained variance. For balanced filters, just a single angle (3°) was poorly described as two PCs should fully describe the data. For single filter, 10 angles are poorly described by PCs 1 and 2; a third

principal component is needed to explain the variation in these angles.

**PCA: Influence** An influence plot is used to look for any samples that are badly described by PCA and are having a significant effect on the results. It shows the residual variance of a sample plotted as a function of leverage, the distance from the projected sample (i.e. the approximation of the sample made by the PCA model) to the centre of the model (mean point).

Figure 5.22 shows that for balanced filters, all samples are well described and none have an unusually high influence on the model. For the single filter, repeat 1 and 3 of the 0% fat sample are shown to have a relatively high leverage and residual variance. Looking closely at the spectra for these repeats, there are a few points at which they deviate significantly from the average profile. Such deviations are not physically significant so are probably noise arising from either low counting statistics of the single filtration for this sample, or uncorrected noise introduced by the sensor.

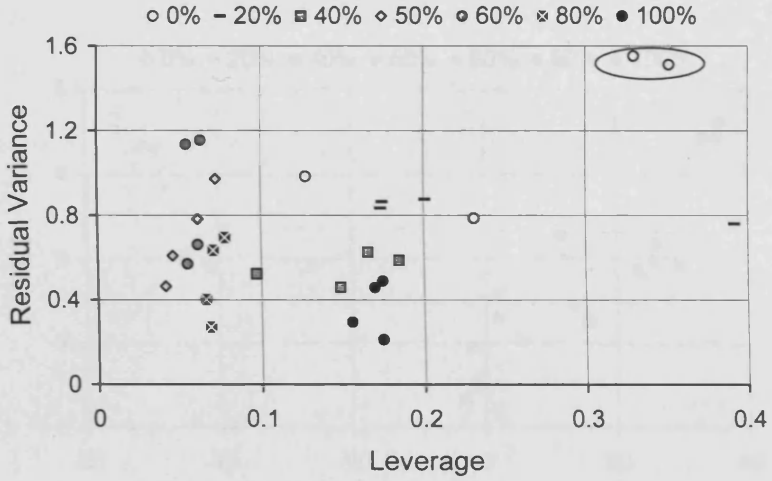


(a) Single filter

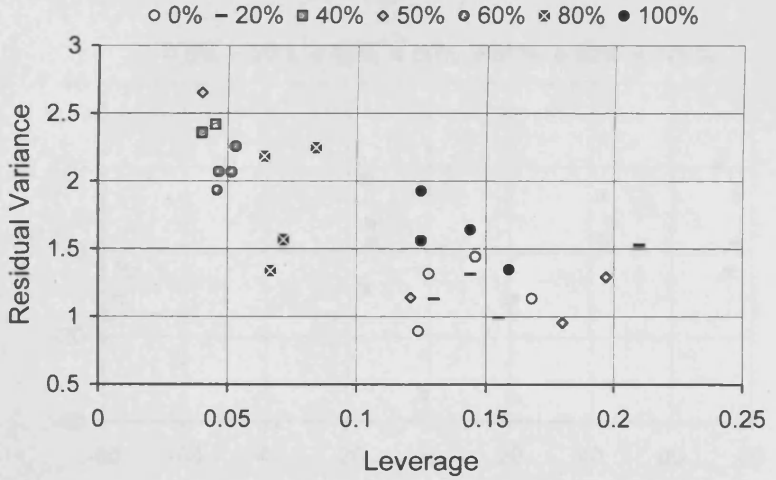


(b) Balanced filter

Figure 5.22: Residual variance vs influence, samples with high influence and residual variance are not well explained by the model and may have a significant impact on its accuracy - two of these are circled in (a)

The model describes well the actual structure in the data but cannot explain these noisy deviations leaving these two measurements with a high residual variance.

**PCA: Scores** Scores describe the data structure in terms of patterns between samples. Samples with close scores along the same PC are similar and *vice versa.* The sample scores on PC2 and PC1 are shown in Figure 5.23. Plotting a hotelling T2 ellipse on these plots showed that all samples were contained within the outlier boundary, although the two measurements identified above as having a high influence on the single filter model were closer to the boundary than the other measurements for that sample. The 'K means' clustering algorithm was used to identify 7 groups in the data. The clusters identified using the Euclidean (direct) distance between samples in the scores plot are shown as different series in Figure 5.23. Comparing the position of the samples on the scores plot to the positions of the angles on the loadings plot, we can see that PC1 clearly describes the fat content of the sample; those samples with high scores on PC1 have a higher fat content and angles with

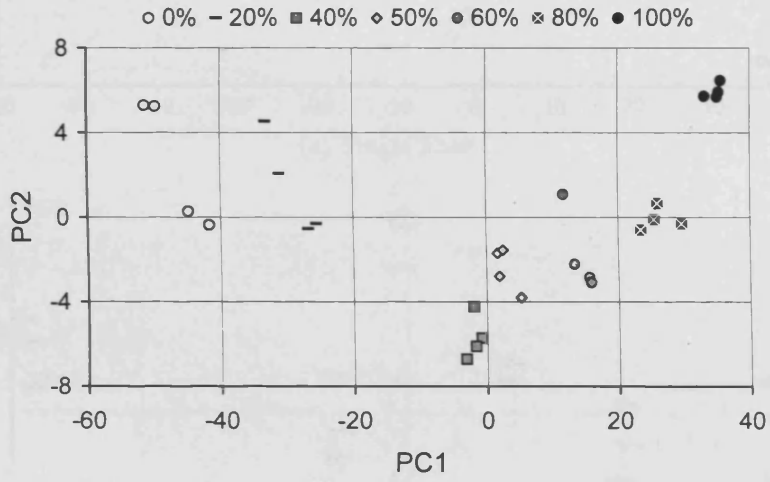


(a) Single filter

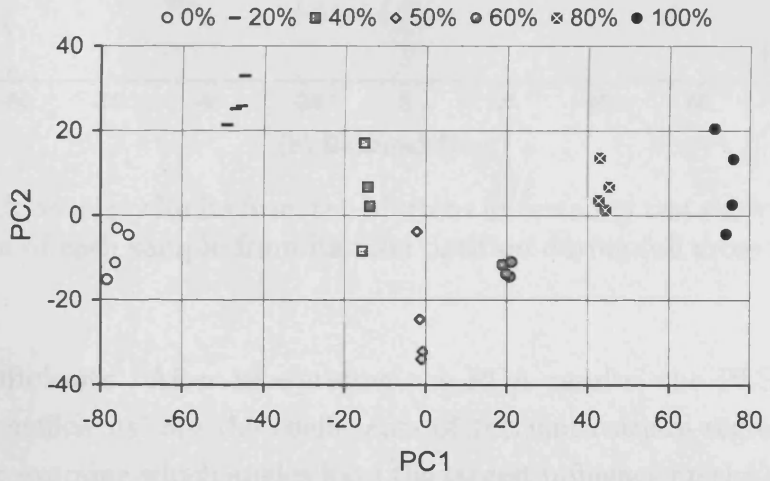


(b) Balanced filter

Figure 5.23: Scores plot result from PCA showing the separation of the samples along PC1 and PC2.

high loadings on PC1 are those found in the fat peak.

The stability of a scores plot can be examined through the Martens Uncertainty Test (see Figure 5.24). This looks at the variation of B-coefficients, scores and loadings over all sub-models in full cross validation relative to the final values in the total model. The two samples identified previously with high influence can be seen to have some instability in their scores in some of the cross validation sub-models but this is relatively small and no other significant deviations are observed, so we can conclude that the models are robust.

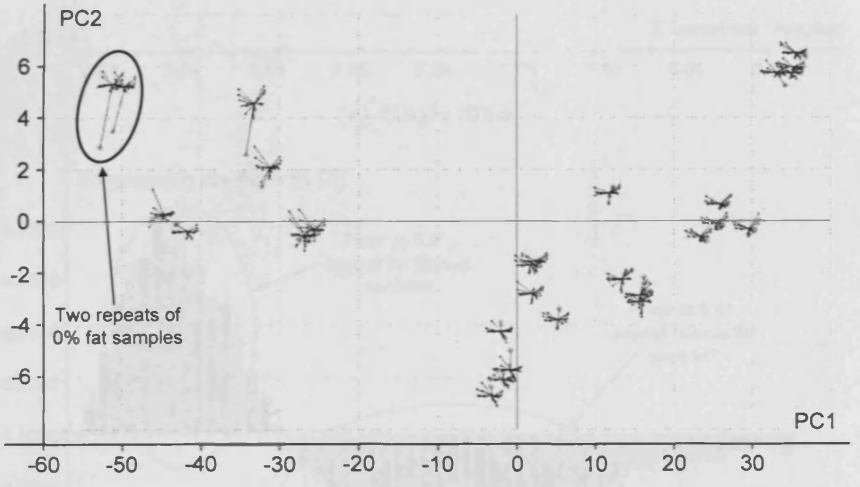


(a) Single filter

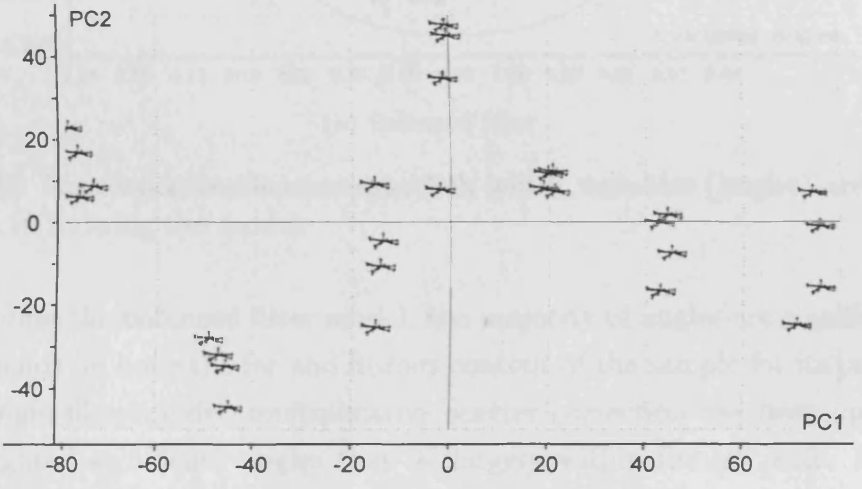


(b) Balanced filter

Figure 5.24: Uncertainty limits from the Martens uncertainty test show the deviation of the position of each sample from its final position during full cross validation

**PLS: B-coefficients** After interpreting the PCA results, the PLS1 model was finalised. 'b-coefficients' are the coefficients of the multivariate regression so they can be used to examine which angles have the largest influence on the model. Those with small values or large uncertainty limits, specifically that cross the axis, are classed as insignificant. The b-coefficients for both models are shown in Figure 5.25 with error bars illustrating the uncertainty limits.

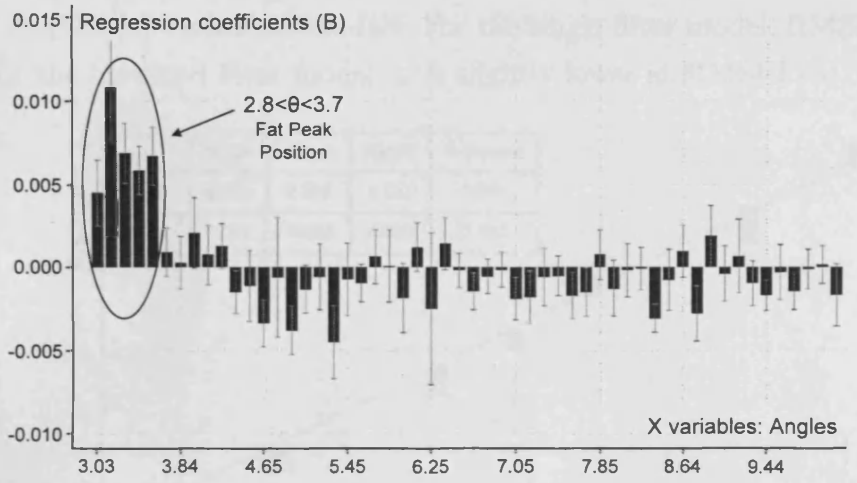


(a) Single filter

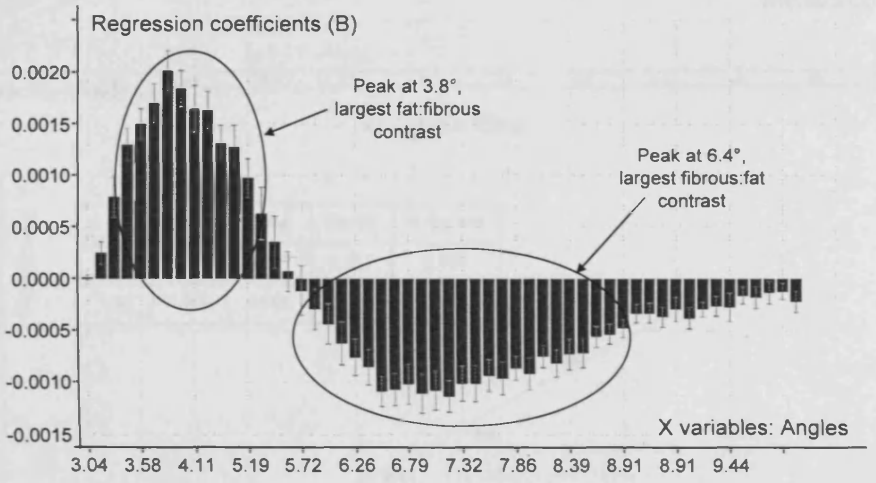


(b) Balanced filter

Figure 5.25: Regression coefficients establish which variables (angles) are the most important in forming the model.

In building the balanced filter model, the majority of angles are significant. The model depends on both the fat and fibrous content of the sample for its predictions. For the single filter model, multiplicative scatter correction has been applied and this highlighted significant angles that lie largely within the fat peak. Repeating the modelling process with only 5 angles between 3 and 3.5° achieved a model with calibration slope 0.97, validation slope 0.98, and RMSEC and RMSEP 0.04. This shows that the single filter model is almost entirely based around the changing shape and decreasing intensity of the fat peak as fat content decreases.

**PLS: Predicted vs Measured** The root mean square error (RMSE) is the average difference between the predicted and measured values of the calibration samples and should be minimised to achieve the smallest possible error on predictions. The iterative process of calibration and validation to create a model ends when the optimal RMSE has been reached. Figure 5.26 shows the predicted vs measured graphs for the optimum PC in each model. Table 5.9 summarises the calibration and validation

slopes and RMSEs for both filter models. For the single filter model, RMSEP=0.029 at PC2. For the balanced filter model, it is slightly lower at RMSEP=0.018.

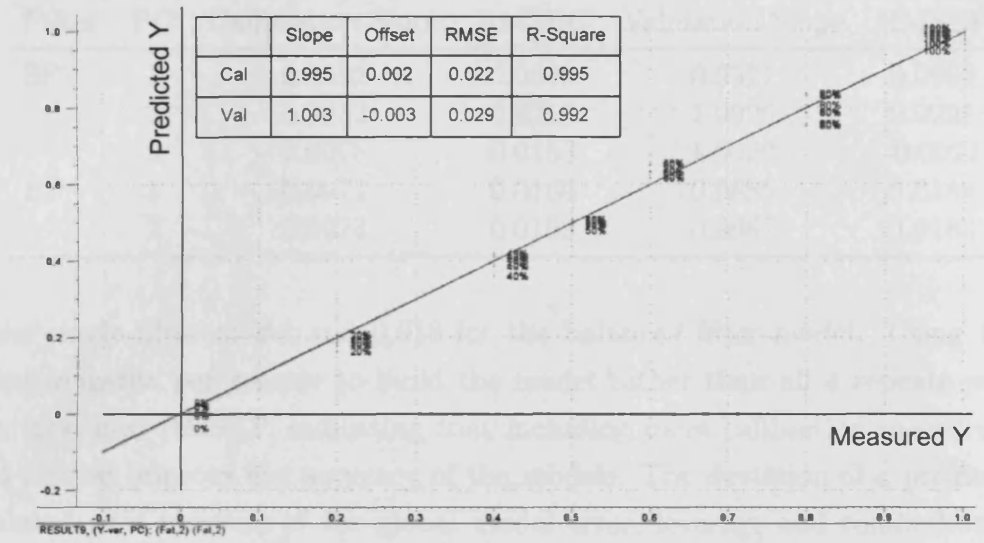


| | Slope | Offset | RMSE | R-Square |
|---|---|---|---|---|
| Cal | 0.995 | 0.002 | 0.022 | 0.995 |
| Val | 1.003 | -0.003 | 0.029 | 0.992 |

(a) Single filter

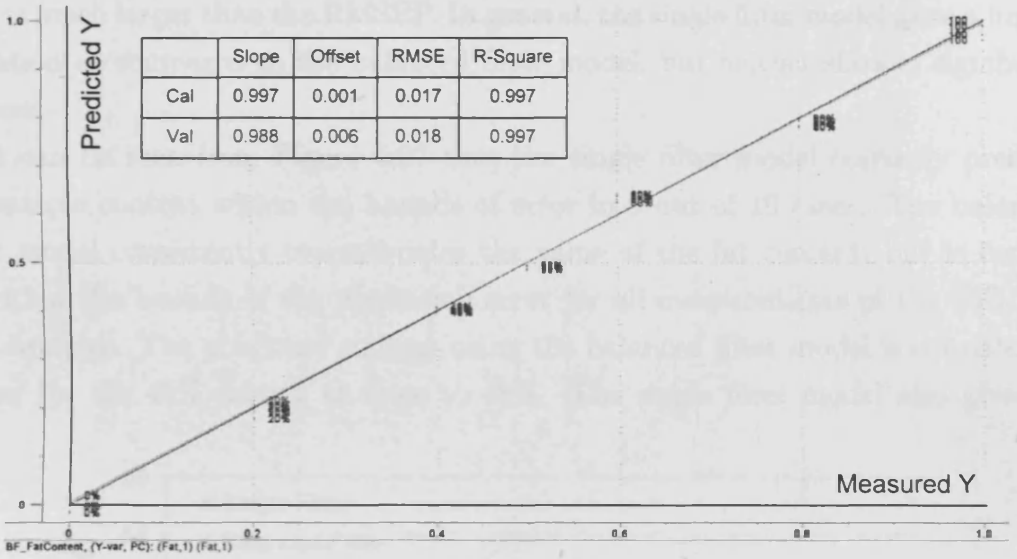


| | Slope | Offset | RMSE | R-Square |
|---|---|---|---|---|
| Cal | 0.997 | 0.001 | 0.017 | 0.997 |
| Val | 0.988 | 0.006 | 0.018 | 0.997 |

(b) Balanced filter

Figure 5.26: Predicted vs measured for the optimum prediction PC in each model (PC2 and PC1 for single and balanced filters respectively). 'Cal' refers to the calibration results, while 'Val' refers to the results predicted by the model for the calibration samples.

### 5.4.3 Predicting the composition of unknown samples

With the model refined and analysed, the next step is to test its ability to predict the content of new samples. Diffraction spectra for the 3 validation samples with compositions of 25, 35 and 45% fat were used. The resulting predictions can be seen in Figure 5.27. No predictions for the 25% set are available for the single filter model as this sample was omitted at the outlier detection stage. The error bars on the predictions illustrate the root mean square error of prediction. This was 0.029

Table 5.9: Calibration and validation slope values on each PC for single and balanced filters

| Filter | PC | Calibration Slope | RMSEC | Validation Slope | RMSEP |
|---|---|---|---|---|---|
| SF | 1 | 0.9592 | 0.0639 | 0.9527 | 0.0692 |
| | 2 | 0.9952 | 0.0219 | 1.0026 | 0.0291 |
| | 3 | 0.9978 | 0.0153 | 1.0020 | -0.0021 |
| BF | 1 | 0.9971 | 0.0169 | 0.9885 | 0.0184 |
| | 2 | 0.9973 | 0.0163 | 0.9987 | 0.0183 |

for the single filter model and 0.018 for the balanced filter model. Using 1, 2 or 3 measurements per sample to build the model rather than all 4 repeats resulted in an increased RMSEP, indicating that including more calibration measurements could further improve the accuracy of the models. The deviation of a prediction is calculated as a function of the global model error, leverage and residual variance CAMO Software AS (2008). This can be used to identify outliers if the deviation level is much larger than the RMSEP. In general, the single filter model gave a higher deviation as compared to the balanced filter model, but neither showed significant outliers.

It can be seen from Figure 5.27 that the single filter model correctly predicts the sample content within the bounds of error in 8 out of 10 cases. The balanced filter model consistently overestimates the value of the fat content, but is correct to within the bounds of the prediction error for all measurements of the 25% and 35% samples. The predicted content using the balanced filter model is consistently higher for the 45% sample at close to 48%. The single filter model also gives an

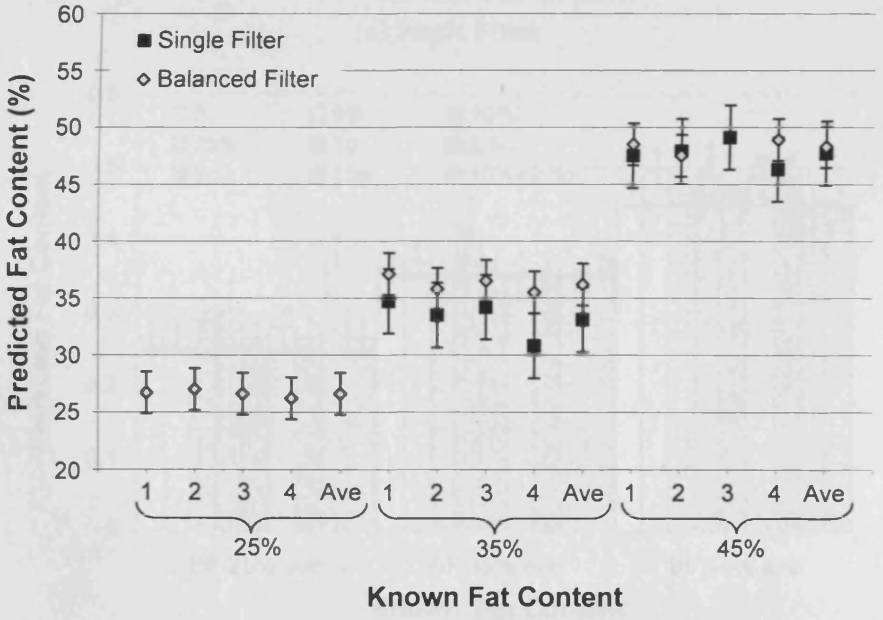


Figure 5.27: Comparison of predictions made by the PLS models of single and balanced filter data.

overestimate for this sample indicating that the 'known' fat content, as determined by the sample preparation, is probably slightly higher than expected.

One further analysis option available in The Unscrambler is a preprocessing transform that adds noise. This can be used to test the ability of the model to predict sample contents when it is presented with noisy spectra, as opposed to the optimal spectra acquired for training. Two options are available: proportional noise, which adds noise whose size depends on the level of the original data values, and additive noise, whose size is independent of the original data and the standard deviation of the added noise is the same for all data points. The models were tested with: 5, 10 and 25% proportional noise; 1, 2.5, 5 and 10$\sigma$ additive noise; and 10% proportional plus 2.5$\sigma$ added noise. The predictions resulting from these 'noisy' spectra are shown in Figure 5.28. The RMSEP for each prediction is shown in Figure 5.29.

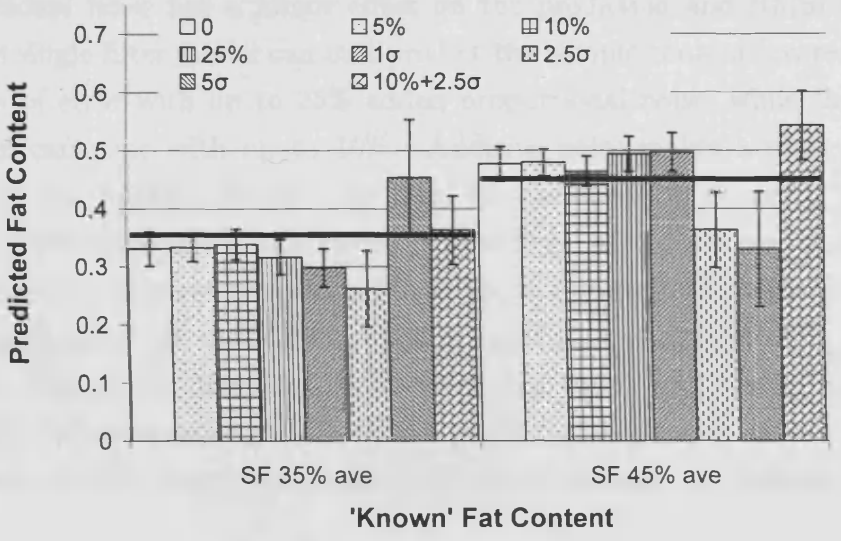


(a) Single Filter

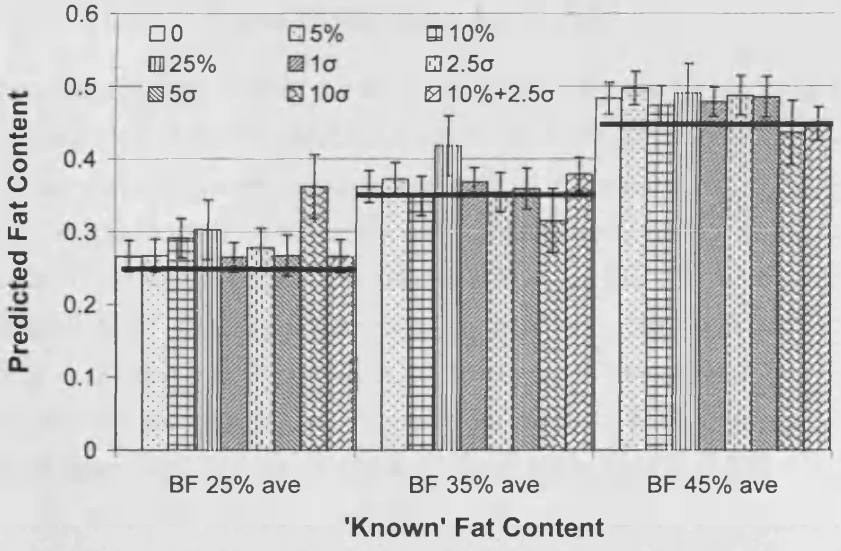


(b) Balanced Filter

Figure 5.28: Resilience of each model to added noise

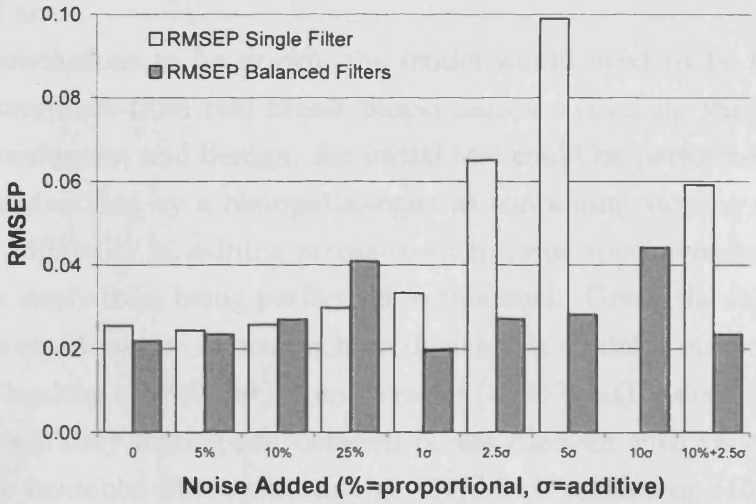


Figure 5.29: Change in RMSEP with added noise

Proportional noise has a minor effect on the prediction and RMSEP for both filters. The single filter model can still predict the sample contents correctly within the bounds of error with up to 25% added proportional noise, while the balanced filter model can cope with up to 10%. Additive noise makes a more significant difference to the RMSEP at the $2.5\sigma$ level for the single filter model and at the $5\sigma$ level for the balanced filters model. This may be due to the application of multiplicative scatter correction (MSC) to single filter data which accounts for offsets in the original data. If a different offset is present, a new MSC will need to be calculated. Future investigation would be needed to assess whether recalculation of the MSC for noisy spectra affects the prediction capability of the model. A combination of 10% proportional and $2.5\sigma$ additive noise was tolerated by both models.

### 5.4.4 Overview of multivariate analysis results

Multivariate analysis has proved to be a valuable tool for identifying the amount of fat in a variety of samples ranging from 0 to 100% fat content. Modelling on the single filter data requires preprocessing in the form of multiplicative scatter correction to be performed. However, with this preprocessing it can produce an accurate model from just 5 angular positions (those within the fat peak). Modelling on the balanced filter data produces a more robust model without the need for preprocessing. It is also less susceptible to noise, most likely because it uses all the angles in the spectra for the model. It produces more consistent predictions overall, although these may overestimate the fat content by as much as 2%.

Results from this test indicate that either filtration could be employed in future modelling, with balanced filtration being slightly preferable in terms of model robustness. The RMSEP for both models is at most 0.03 so a prediction of 25% is realistically $25 \pm 3\%$. The fat content in any sample can thus be estimated to within

this margin of error.

For final conclusions to be drawn, the model would need to be trained with a bank of measurements from real breast biopsy samples covering varying degrees of disease, both malignant and benign. An initial test could be performed using breast tissue samples identified by a histopathologist as containing varying degrees of fat. Unfortunately, difficulty in gaining access to such tissue specimens has prevented a full systematic study from being performed in this work. Given the values presented Chapter 1, the small margin of error achieved with this model is more than sufficient to distinguish healthy (> 70% fat) from diseased (< 30% fat) tissues. It also has the potential to accurately distinguish between breast diseases with varying degrees of fat content, for example, fibrocystic change (30% fat), carcinoma (15-20% fat) and fibroadenoma (almost 0% fat).

## 5.5 Feasibility study of APXRD with the Large Area Sensor

In the previous sections, the implementation and testing of the Vanilla-based APXRD system was presented. Next, results from a feasibility study using the Large Area Sensor in the APXRD system will be presented. The aim of the study was to establish the advantages that large area and wide dynamic range could bring to the system and assess the future developments that would be needed to use LAS as the APXRD detector. Details of the experimental APXRD system with LAS are given below. Scatter signatures from the six plastics included in the contrast phantom were used to compare the two systems.

### 5.5.1 Experimental setup

The experimental setup used for phantom imaging was employed for testing the LAS system and different plastics were selected by appropriate positioning of the relevant contrast phantom inserts in the X-ray beam. The LAS ADC range, reset type and conversion gain are fixed so no optimization of sensor parameters was possible. The maximum available exposure time of 2.3s (RST0) was selected to record the scattered intensity, combined with a region of reset of 250x250 pixels in the corner of the sensor with an exposure time of 0.1ms (RST1) to record the transmitted beam. LAS was placed in the top right quadrant of the scatter signature at a distance of $l_{sd}$=22.0$\pm$0.5cm from the phantom with the transmitted X-ray beam centred in the region of reset (RST1). Scatter up to 12° could be recorded in RST0.

The expected count rate was estimated using the difference in optical characterization results between the two sensors. Given that the conversion gain of LAS in DN/$e^-$ is twice that of Vanilla, the integration time is around one third

that of Vanilla, as is the quantum efficiency, it could be anticipated that the intensity of the scatter signatures recorded with LAS would be around 20% of the intensity of those recorded under the same conditions with Vanilla. The optimization of the Vanilla APXRD system showed that increasing from a 1.0mm to 1.5mm collimator affects only the peak height of the scatter signature so an aperture in collimator size could be used to partially compensate for the difference in intensity. Increasing the aperture diameter up to 1.5mm caused too great a beam divergence and the region of reset began to obscure the scatter signature so a 1.2mm pinhole was selected, yielding 0.85° angular acceptance.

For each plastic, a set of 30 data, background and dark frames were acquired for averaging. It was observed that a large, nonuniform background signal was present in the frames that did not originate from coherently scattered radiation. When Vanilla was employed in the phantom imaging setup, lead shielding was placed between the detector and the phantom to shield the detector from this background radiation. LAS has too large an area to shield effectively so instead, a second background acquisition was taken with a beam stop in front of the collimator to quantify the 'additional' radiation contributing to the images and thus correct for it.

### 5.5.2 Scatter signature calculation

Radial averaging was employed in the analysis of LAS data. The beam centre was determined using horizontal and vertical profiles through the region of reset to find the peak of the transmitted beam intensity. From this centre, data was integrated into bins of 12 pixels width and normalized to the number of pixels contributing to the bin. The corresponding scattering angle was evaluated using the distance from the sensor to the sample ($l_{sd}$=22.0 $\pm$ 0.3cm) and the distance between the radial bin and beam centres. Evaluating the scattering angle in this manner yielded an error of $\Delta\theta_p/\theta = 1.5\%$, dominated by the measurement of the distance of the sensor from the sample.

The data frame was corrected by subtracting both backgrounds from the RST0 (scatter) region. Comparing the scatter signatures from LAS to Vanilla showed a further trend was present in the data, adding a broad, shallow background peak. This was removed by calculating the average difference between the LAS and Vanilla data and subtracting this from each of the LAS profiles.

### 5.5.3 Comparison to Vanilla

Figure 5.30 shows the scatter signatures for the six plastics recorded with LAS as compared to Vanilla. The intensities are normalized to 100 so that peak position, shape and full width at half maximum can be compared. Representative error bars for the LAS data based on counting statistics are shown on a few data points, those

for the Vanilla data are contained within the data points. It was found that the peak intensity recorded by LAS for acetal was just 23% of that of Vanilla despite the increase in collimator diameter. Apart from the profile for acrylic, for which a different shape was observed compared with Vanilla, the signatures recorded with LAS generally agree with the Vanilla APXRD data within the bounds of error. This is a promising result indicating that despite the reduced sensitivity caused by the lower quantum efficiency and shorter integration time, it is still possible to correctly deduce the scatter signatures from well characterized materials.

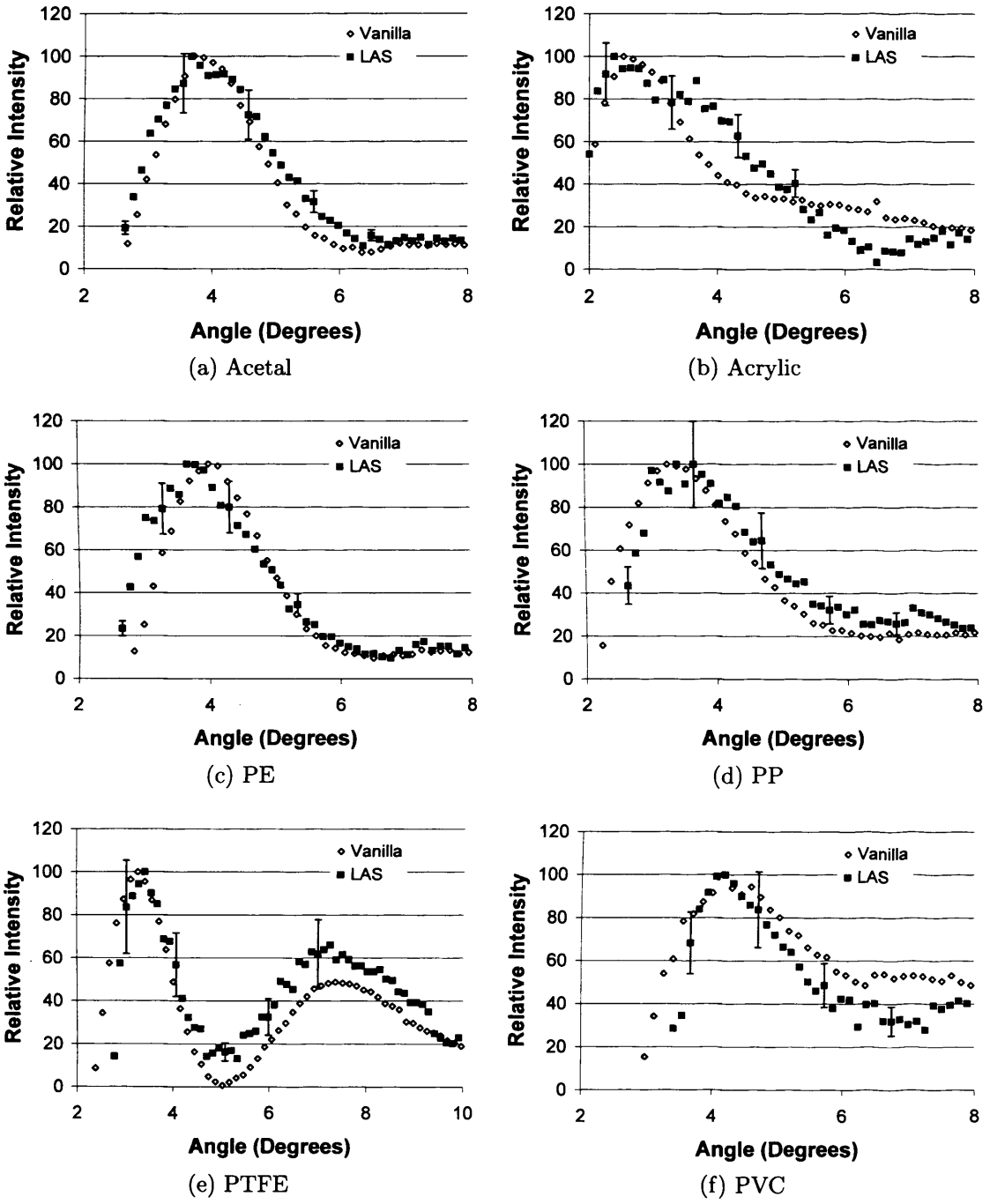


Figure 5.30: Comparison between scatter signatures recorded for the Large Area Sensor and Vanilla APXRD systems.

### 5.5.4 Transmission data

The benefit of the wide dynamic range available with LAS is the ability to simultaneously record both transmitted and scattered X-rays. For example, the beam centre was located directly within the same image frame as the scatter signature thus removing errors due to beam centre location. Knowledge of the relative transmission of different materials also provides a simple means to perform a basic attenuation correction by normalizing the scatter signatures. Figure 5.31 illustrates the dynamic range for the measurement of acetal. It shows a profile taken vertically outwards from the beam centre, the intensity of which is shown on a logarithmic scale. RST0 is operating with an integration time of 2.3s, while RST1 has an integration time of 0.1ms yielding a minimum of 87dB dynamic range. The transmitted beam is visible up to around 1.9° and the intensity falls to zero beyond this until the scatter peak begins to emerge at 2.6°. Normalizing the signal of the scatter peak and the transmitted beam to the integration time of the given ROR, the 'count rates' are $2x10^7$DN/s and 4DN/s for the transmitted and scattered X-rays respectively. The transmitted beam is thus around $10^7$ times more intense than the scatter peak, illustrating that 140dB of dynamic range has been recorded within a single image.

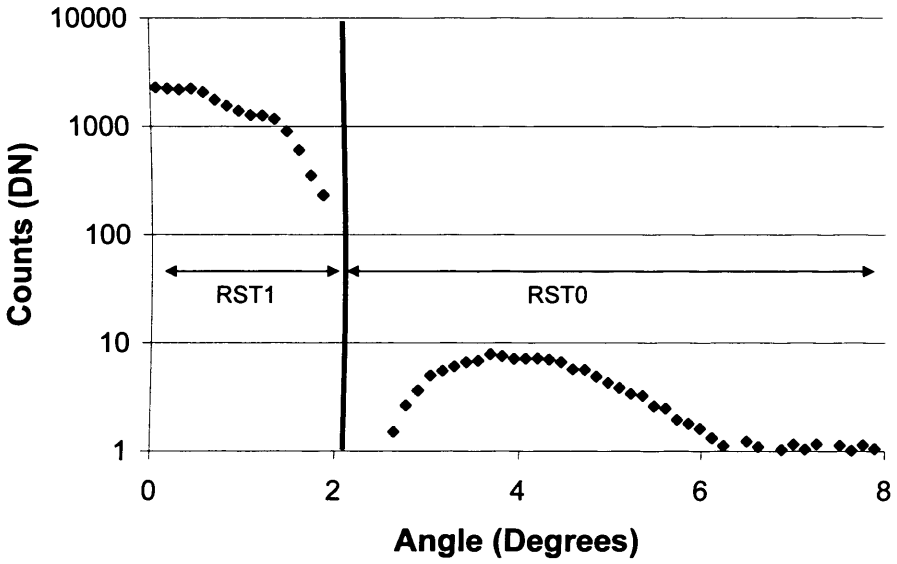


Figure 5.31: Demonstration of orders of magnitude visualized using region of reset at the beam centre for Acetal. Each point represents the radial average of a bin of 12 pixels width

The information present in the transmitted beam region can be used to perform an attenuation correction. In the RST1 (i.e. transmitted beam) region, both the data and background frames were corrected with dark field subtraction and an average of the values in a 100x100 region in the centre was calculated. A 'relative attenuation' parameter was evaluated using the ratio of the net data and background intensities $-Ln(Data - Dark/Bkgd - Dark)$, where Ln is the natural logarithm.

The values of this parameter for all six plastics are shown in Figure 5.32, which indicates that the most attenuating material in the phantom is PVC, followed by PE and Acetal, then PP, PTFE and Acrylic. An independent measurement of the energy dependent linear attenuation coefficient for each sample would be needed to verify this result.

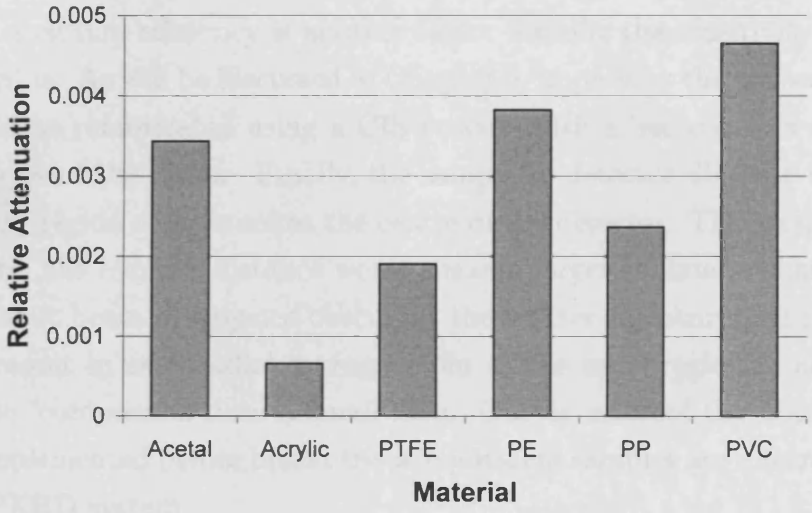


Figure 5.32: Comparison of the attenuation properties of the six plastics

### 5.5.5 Future tests required with the Large Area Sensor

While this preliminary study shows promising results from the Large Area Sensor APXRD system, a number of refinements can be identified.

Primarily, the origin of the trend observed when comparing the LAS and Vanilla scatter signatures needs to be found. The broad peaked shape may yield a clue as to its origin. This shape is similar to the dark response of Active Pixel Sensors, which is usually lower at the edges and higher in the centre, suggesting that an incomplete removal of the dark offset could responsible for the trend. In the Vanilla system, performing a dark field correction on the data and background acquisitions had no effect on the final result and it was assumed that this would also be the case for LAS. It is possible, however, that some electromagnetic interference or other time dependent effect is causing an unexpected variation in the dark level of LAS. As the sensor has not been subject to widespread use in different environments, its stability with time and temperature have yet to be fully evaluated. They could be tested by monitoring the sensor output as a function of time, both frame-to-frame, and throughout the course of a day of measurements. Further, the scatter signature measurements made with the LAS APXRD experimental setup could be taken using a different X-ray source to isolate this trend from the effect due to incomplete shielding.

The LAS APXRD system would also benefit from an increase in the number of

recorded counts. The peak intensity recorded by LAS for acetal was found to be 23% of that recorded with Vanilla, despite the increase in collimator size. The possible routes to increase the recorded intensity lie in firmware, hardware and experimental arrangement. The maximum integration time of the sensor is currently limited to 2.3s but 5s (double the count rate) would be possible with developments in the control software and firmware.

The low quantum efficiency is another factor limiting the sensitivity when compared to Vanilla. As will be discussed in Chapter 6, improving the QE would require the sensor to be refabricated using a CIS process with a less complex stack above the active layer of the sensor. Finally, the sample to detector distance could be reduced and the region of reset set at the centre of the detector. This would yield two main benefits: the reduced distance would mean a larger collimator diameter could be used without beam divergence obscuring the scatter signature and more counts would be present in each radial averaging bin as the same region of angles would effectively be 'compressed' into a small area. One or more of the above solutions should be implemented before breast tissue equivalent samples are interrogated with the LAS APXRD system.

A brief presentation of the transmission data recorded by LAS was made above. A detailed study of the best use of this data is needed to quantify what results can be obtained from this. The best method of normalizing X-ray diffraction data to the transmitted intensity should be evaluated as results from Section 5.3.2 suggested that a simple ratio of the two data sets is not appropriate. Further, the potential for producing a transmission image with this data should be studied. If a breast biopsy sample were scanned through the X-ray beam to record scatter signatures from multiple slices of the sample, a transmission radiograph of high spatial resolution could in theory be produced by 'stitching' results from the full region of reset area in each step and correcting for the nonuniformity of the beam profile. This image could potentially be combined with a material-specific X-ray diffraction image to produce an ideal 'high resolution, high contrast' image. A study of the image quality available with the X-ray spectra used in this work would be needed, as mammography is usually carried out using lower X-ray energies. Further, the direct imaging capability of LAS would need to be assessed, including evaluation of both the spatial resolution, for example through the modulation transfer function, and the detective quantum efficiency of the APFPI.

Despite the reduction in counting statistics imposed by switching from Vanilla to LAS, the shape and position of most scatter peaks remain comparable. If the Large Area Sensor can achieve longer integration times with a greater quantum efficiency in future, it will present the ideal sensor solution for the APXRD system.

## 5.6 Summary

Results obtained with the APXRD system show that a relatively simple experimental arrangement can accurately record scatter signatures from a wide variety of samples. Planar imaging of a plastic contrast test phantom illustrated that X-ray diffraction information can provide far higher contrast than is available in a standard transmission image. For amorphous materials, the effect of the spectral width of the X-ray source is sufficiently reduced by filtration so as to be almost negligible compared to the width of the scatter peaks. Scatter signatures of breast tissue equivalent materials recorded with the system are therefore highly sensitive to composition. Characteristic signatures have been used to develop a multivariate model that can predict the fat content of 'unknown' samples to within 3%, a suitable precision for categorizing different types of disease. Finally, the wide dynamic range of the Large Area Sensor has been utilized to demonstrate simultaneous X-ray transmission and diffraction measurements.

# Chapter 6

# Concluding remarks and future APXRD system potential

This work has presented the development and evaluation of an X-ray diffraction-based breast biopsy analysis system. The quantitative data available from such a system could reduce the number of unnecessary biopsies performed and provide specific information to aid histopathologists in their choice of tissue sections. In turn, the number of errors in both lesion and biopsy sampling could be reduced and ultimately, a much quicker patient diagnosis could be possible.

## 6.1 Active Pixel Sensors for X-ray Diffraction

As breast tissue structure and composition are altered by both benign and malignant disease, X-ray diffraction was identified as a quantitative technique that could potentially diagnose both the presence and type of abnormality in a breast biopsy. When the source of X-rays for diffraction has a polychromatic spectrum, energy dispersive data is usually recorded. The liquid nitrogen cooling required by high purity germanium photon counting detectors often uses a bulky cryostat, making this type of system both expensive, and challenging to install and maintain in a clinic. Instead, filtration can be employed to narrow the width of the polychromatic spectrum, allowing angle dispersive X-ray diffraction to be performed.

No area detector currently fulfils all of the requirements of an ideal X-ray diffraction detector. The specifications needed include large area, low noise, good conversion gain, high dynamic range, good linearity and high quantum efficiency. Further, for clinical application the detector needs to be portable and of low cost. A potential solution is found in the Active Pixel Sensor, which is fabricated using standard CMOS technology yielding low cost and power consumption, as well as the ability to customize on-chip functionality and performance. To satisfy the requirements of X-ray diffraction, the multitude of recent advances in Active Pixel Sensor designs need to be combined into a single device. The performance of two

Active Pixel Sensors designed for scientific imaging was assessed in this work; each development from the standard '3-T' design takes a step along the path to the ideal X-ray diffraction detector.

Characterization of the APSs found that both were indeed suitable for testing in an APXRD system. Vanilla had a high peak quantum efficiency of 70% but was of small area (1.7cm$^2$) and had only a moderate dynamic range of 62dB. The Large Area Sensor, or 'LAS', attempted to combine low noise, high speed readout and wide dynamic range into a single large area device. The LAS prototype characterized in this work had an area of over 29cm$^2$ as well as three different exposure times across the array yielding a dynamic range of over 95dB. However, evaluation revealed a low quantum efficiency of just 19% at 546nm due to the complex stack above the active layer of the pixel.

Characterization of these Active Pixel Sensors showed that the 'gold standard' methods for assessing detector performance were inappropriate because the APS suffers inherent nonlinearity from both the source follower and the variation of sense node capacitance with signal charge level. Standard detector characterization methods assume a linear camera response so an accurate evaluation of these devices demands the development of new 'nonlinear' methods. While two such methods exist, there had previously been no systematic study of their accuracy when compared to both each other and standard linear methods. A data set from Vanilla was used to make a detailed comparison of both linear and nonlinear methods. Parameters derived using two independent nonlinear methods were found to be in good agreement with each other, while linear methods were found to overestimate full well capacity and underestimate read noise by comparison. The onset of nonlinearity has been shown by other authors to be a fundamental property of the APS, beginning at signal levels of above $10^4 e^-$ and for the APSs investigated in this work was found to affect about 70% of the dynamic range. Characterization is thus needed to identify and provide a means to correct for nonlinearity.

Both Vanilla and LAS were found to be competitive with similar Active Pixel Sensors, as well as with the 'gold standard' X-ray diffraction detector, the CCD. That Vanilla is of small area means that while it can be employed for demonstration purposes, it would not be of use in a clinical system unless multiple sensors were tiled. LAS provides solutions to the size and dynamic range drawbacks of Vanilla, but has a lower quantum efficiency. Improving the QE to a level similar to that of Vanilla would satisfy all X-ray diffraction detector requirements. Future generations of the LAS design could be fabricated at a different foundry, or with a different CMOS process to achieve this.

Both Active Pixel Sensors presented in this work use a standard silicon photodiode as the detection element fabricated in a standard CMOS process. One method to improve quantum efficiency is to use customized CMOS processes, such

as the pinned photodiode (PPD) detection element or a CMOS Image Sensor (CIS) process. In the PPD, a fully depleted region of the pixel is 'pinned' below the surface using a p+ implant above the n-well. Readout is completed via a transfer gate meaning charge is transferred from a large area, high capacitance region to the small capacitance of the floating diffusion node (Lulé, 2000). While this architecture yields low dark current and increases quantum efficiency towards the shorter optical wavelengths, it can suffer from the undesirable effects of image lag (El Gamal and Eltoukhy, 2005). The CIS process, however, is tailored to exhibit lower dark current and has fewer passivation layers to reduce reflection losses in the stack. It is likely that a foundry that provides stitching technology to create large area arrays will also offer a CIS process as the two will frequently be demanded in combination so in future, LAS could be fabricated with a CIS process.

Meanwhile, developments of more advanced pixel designs have been presented in the literature. Tedde *et al.* (2007) have developed a hybrid organic Active Pixel Sensor that uses an organic photodetector layer integrated on top of amorphous silicon thin film transistor (TFT) circuitry. Organic photodiode arrays can be fabricated in large area at low cost using the printing technologies developed for production of commercial organic displays. As the electronics are embedded below the photodetector rather than included in-pixel, a near 100% fill factor and up to 60% quantum efficiency is available. Although this is the first reported active pixel style device, other organic photodetectors have already been developed for X-ray imaging (Blakesley and Speller, 2008). Further, Faramarzpour *et al.* (2008) presented a single photon avalanche photodiode system operating in Geiger mode for low light level imaging in CMOS technology. Avalanche photodiodes are the semiconductor equivalent of photomultiplier tubes and provide high quantum efficiency to visible light with gains of up to 100. An array of such devices would provide an excellent solution for detecting scatter signatures, although the performance of current CMOS APDs needs considerable development.

Future on-chip and in-pixel functionality could enable 'on-the-fly' scatter signature analysis and material identification without sacrificing sensitivity provided the challenge of maintaining performance with CMOS scaling can be met (Wong, 1996). Given the performance of the Active Pixel Sensors evaluated in this work and the developments in CMOS technology that are now available to overcome their current limitations, it is clear that Active Pixel Sensors provide a competitive option for X-ray diffraction applications. Vanilla and LAS both meet and exceed many of the demands of the ideal X-ray diffraction detector for a breast biopsy analysis system and advances on their designs have the potential to achieve complete coverage of the requirements in the near future.

## 6.2 Prospects for the APXRD system: current limitations and future developments

The requirements identified for the breast biopsy analysis system were that it should: be cost effective; be easy to install, calibrate and maintain; have high throughput; and provide accurate, reproducible estimates of sample content. In establishing that angle dispersive X-ray diffraction using Active Pixel Sensors provided an appropriate solution for analysing breast biopsy samples, the focus of this work was primarily the latter criterion, i.e., evaluating the ability of the system to accurately extract material specific information from a given sample. A summary of the results obtained and the limitations of the current system will be made in the following sections, before suggestions for how to address the remaining criteria and develop the system towards clinical implementation are made.

### 6.2.1 Progress achieved in the present study

A prototype 'Active Pixel X-ray diffraction' (APXRD) system was designed, implemented and tested using Vanilla as the angle dispersive detector. While the dynamic range and area of Vanilla were unsuitable for visualizing both the transmitted X-ray beam and the entire scatter signature from a sample, the other properties of the device made for an excellent X-ray diffraction detector. As it was available before the Large Area Sensor, Vanilla was implemented in the APXRD system and translated across the scatter signature between 2° and 15°.

The design process used a linear systems model of the Vanilla APFPI (scintillator-coupled APS) to quantify the optimum choice of spectral shaping filter to produce a 'pink' X-ray beam and model the expected scatter intensity in the final system. A data set of both energy and angle dispersion measured with an independent X-ray diffraction system was used as the input to the model, which was validated with the ICDD data bank of monoenergetic X-ray diffraction results and the measured conversion function of the APFPI. In future, this model could be used to investigate the system potential in other applications, for example, homeland security.

Based on the modelling results, a compromise between spectral width, transmitted intensity and mean energy was found. $0.28 gcm^{-2}$ Gadolinium was selected as the single filtration option, while $0.07 gcm^{-2}$ of Samarium and $0.15 gcm^{-2}$ of Tin were selected as balanced filters. These produced spectral widths of 19% and 15% respectively. Both arrangements were tested experimentally. While single filtration offered a slightly narrower full width at half maximum, balanced filtration yielded a greater peak height so each conferred different advantages. The choice of filtration in a future system will therefore depend upon the needs of the application and be one more of convenience and cost than performance.

The APXRD system was then implemented and optimization of both the experimental setup and Vanilla operational parameters was performed. Tests were made to characterize the accuracy of the system compared to previous studies and results revealed that scatter signatures of breast equivalent materials recorded with the APXRD system were in good agreement with previously published data. The system performance was seen to degrade when increasingly crystalline materials, such as kidney stone equivalent materials, were interrogated. This is because for amorphous materials, the effect of spectral width is small compared with the broad nature of their scatter peak. Crystalline materials have much sharper peaks in their scatter signatures which are broadened by the polychromatic spectrum, to the extent that the distinction of individual peaks was often lost. For this reason, the APXRD system is generally better suited to examination of amorphous materials, although if it were possible to demonstrate that sufficient information was still available in the broadened data from crystalline materials, these applications could also be considered.

The next step was to evaluate the system resolution and contrast potential. Scatter signatures recorded from the test phantoms using an angular acceptance of 0.83° (total exposure time of 61s per position at 70kV and 15mA tube current with single filtration) were shown to provide a maximum spatial resolution of 1mm. Characterization of the system resolution proved the validity of the simple geometrical calculations used to evaluate the angular acceptance of the collimator. The system resolution could be improved by reducing the collimator diameter by a known amount and compensating with increased integration time or tube current.

Investigating the depth dependence of the X-ray scatter signature showed that by carefully selecting the angle of interest with which to analyse data, it was possible to 'retrieve' signals from PTFE that had been obscured by 12mm of acrylic. However, this signal was entirely lost with the addition of 18mm of acrylic indicating that the APXRD system would not be suitable for interrogating objects of such thickness. Reduction of the 3-D data from the contrast phantom to a single 2-D material-specific image was achieved using a summation of counts between 2 and 5°. It was possible to identify 5 out of the 6 materials in the phantom individually in this image by thresholding different grayscales. The contrast of different features compared to the background with the material-specific image was an average of 7 times greater than that present in a transmission image recorded with equivalent spatial resolution.

Scatter signatures from a series of breast-equivalent mixtures of fat (lard) and fibrous (chicken meat) tissues were then studied using multivariate analysis. Principal components analysis (PCA) was able to correctly identify multiple measurements of the same sample composition, as well as distinguishing scatter signatures with different compositions. A partial least squares (PLS) regression model was trained

using a series of calibration measurements and was able to predict the percentage fat content of an unknown sample to within 3%. With such a small margin of error, the model was clearly be able to identify 'diseased' validation samples with 25, 35 and 45% fat content respectively. This is a promising outcome illustrating the potential of the APXRD system to satisfy the requirement of accurate and reproducible estimation of sample composition.

Finally, a feasibility study was made using the Large Area Sensor as the APXRD system detector. The six plastic phantom materials were interrogated and the recorded scatter signatures compared to those measured using Vanilla. It was found that despite the lower quantum efficiency of the Large Area Sensor and the reduced integration time available, it was still possible to visualize scatter signatures from these materials. It was also demonstrated that a dynamic range of 140dB could be established in a single image frame using a region of reset to set an exposure time of just 0.1ms, compared to 2.3s in the global reset region. These results are promising for future implementations of the APXRD system.

### 6.2.2 Limitations of the current APXRD system

While the APXRD arrangement has promise as a breast biopsy analysis system, a number of limitations exist that currently prevent clinical transfer of the technique. These fall into two categories: trials and instrumentation.

#### Trials

Testing limitations arise from the lack of a system trials using real breast tissues. The acquisition and storage of tissue samples is challenging and it was not possible to test the system on real breast tissues in our department. Scatter signatures obtained from breast equivalent materials with the APXRD system compare well with literature examples from real breast tissues, although the adipose equivalents exhibit a greater full width at half maximum. X-ray diffraction studies of real breast tissue in the literature indicate that low fat content could be a useful marker of breast disease. Only measurements made with real breast tissue can ultimately confirm whether the APXRD system can discern healthy and diseased tissue using fat content as a marker of disease and whether it is suitable for clinical application. Suggestions for future measurements will be made at the end of Section 6.2.3.

Studies need to be undertaken with real breast tissues to test if different types of disease can be recognised by the system. One possibility could make use of the different types of calcium microcalcification that are frequently present with malignant (calcium apatite) and benign (calcium oxalate) lesions. Figure 6.1 compares the scatter signatures recorded for the apatite and oxalate kidney stone substitute materials to the signatures from breast equivalent materials. A qualitative comparison suggests that tests should be performed to determine the common density of

microcalcification in biopsy samples and whether this is sufficiently high that the APXRD system would be sensitive to their presence.

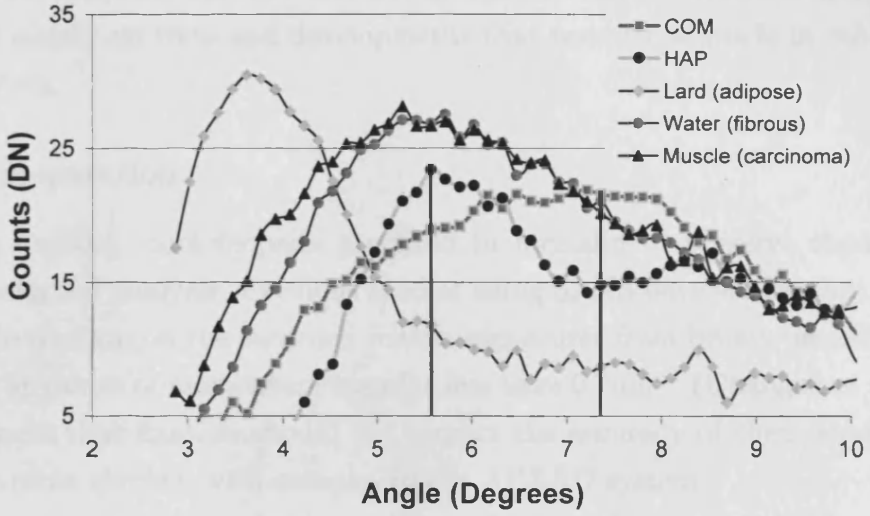


Figure 6.1: Comparison of the scatter signatures measured for calcium oxalate monohydrate and hydroxyapatite with the APXRD system to those of breast tissue equivalent materials. Angles at which the main contrast between oxalate and apatite calcium types are highlighted.

#### Instrumentation

The instrumentation limitations of the Vanilla APXRD system are the small area and dynamic range of the sensor, which are acceptable for a demonstration system but would complicate a clinical system. Further, the benefits of measuring the transmitted beam simultaneously are lost. The larger area and wider dynamic range of LAS provided an opportunity to overcome the limits of Vanilla but a number of issues were identified with the Large Area Sensor APXRD system. These include a low count rate that could inhibit its use for breast biopsy measurements and an additional background trend in the data, the cause of which needs to be established. Further, the performance of the multiple regions of reset need to be independently assessed to establish the limits of application in terms of limiting high and low X-ray exposures. If a longer exposure time can be implemented in the global reset region and the quantum efficiency of the array improved in the future generations, the Large Area Sensor could provide an ideal option for the APXRD system.

### 6.2.3 Future system developments towards clinical implementation

The system development in this work has focused on producing an X-ray diffraction system that can accurately predict the fat content of a breast biopsy and in turn, categorise it as either healthy or diseased. For the system to be widely used in a

clinical scenario, a number of other factors need to be considered including sample preparation, throughput, cost effectiveness, ease of use and packaging. It will be assumed in the following that any detector limitations can be overcome and discussion will focus largely on tests and developments that need to be made in other aspects of the system.

### Sample preparation

Following excision, core biopsies are fixed in formalin to preserve them prior to histopathological analysis. Previous studies using SAXS have shown that the effect of formalin fixation on the recorded scatter signatures from breast tissues is significant only at values of momentum transfer less than $0.7\text{nm}^{-1}$ (Changizi *et al.*, 2006). This suggests that fixation should not impact the accuracy of the system but this should be cross checked with samples in the APXRD system.

Another aspect to consider is sample packaging. Biopsy measurements should be performed with the samples in their standard containers. Subtraction of background scatter from the sample holder performed with the Vanilla APXRD system was reliable, indicating that a separate measurement of the 'background' scatter signature from current biopsy containers should be sufficient to remove their influence. Also, the effect of variations in biopsy core sizes on the scatter signatures should be assessed by making measurements of biopsy samples from all standard needle sizes and comparing the scatter signatures.

### Throughput

Throughput relates to both the number of biopsies that can be analysed with the system and the speed with which each can be assessed. The small size of biopsy samples means that many cores can currently be examined in a single radiograph to check accurate lesion sampling. These measurements are often made on a dedicated X-ray source (Ingram and Wyld, 2007) so it can be envisaged that if this were the case for the APXRD system, an automated sample loading and/or positioning system could be designed to achieve high throughput without requiring extra manpower.

The count rate recorded by the APXRD system is a trade off between the X-ray tube current, spectral filtration, collimation and the APS exposure time. Improving the count rate incident at the sample would reduce the exposure time needed to interrogate each core and in turn increase throughput. While balanced filtration recorded a higher scattered intensity than single filtration, making two exposures of each sample is not ideal. That the current spectral width barely influenced the amorphous scatter peaks indicates that it may be possible to employ a lower level of single filtration to increase the incident intensity without affecting information content. This idea could be tested using the linear systems model developed in

this work if complete data sets were acquired using the energy and angle dispersive system at a variety of X-ray tube kilovoltages for all of the calibration samples that were used to build the multivariate regression model. An iterative study of model predictions for a variety of filter materials and thicknesses would then be needed to determine the minimum filtration that could be used in the system.

### Cost effectiveness

The cost effectiveness of running an APXRD system should relate the installation and maintenance costs to improvements in both speed and accuracy of diagnosis so can only be fully assessed once the system has been implemented in a full clinical trial. The main costs of implementing the system can be briefly addressed here. Active Pixel Sensors are among the cheapest area detectors available and their price is reducing further as markets expand. The APXRD system has also been tested on a tungsten target X-ray tube operating at 70kV; these are commonly available as standard hospital equipment. Provided the collimator diameter remains below 1.5mm, changing the size influences only the recorded count rate rather than scatter peak characteristics. The collimator does not, therefore, need to be machined to high precision.

The use of a collimator does, however, imply the use of a dedicated X-ray source, which impacts upon the cost effectiveness of the system. A collimator bracket that allowed different pinhole sizes to be inserted was used in this work and large scale version of this idea could potentially be used in the clinic, allowing a pinhole to be inserted when X-ray diffraction measurements are required, or removed otherwise. Another option would be to employ an automated translation stage to move a fixed collimator in to and out of the X-ray beam. Both of these are likely to be unrealistic in practice.

Alternatively, the APXRD system could be implemented as an extension to existing dedicated specimen radiography systems. These are often microfocal X-ray sources with sub-milliampere tube current so may not provide a sufficient count rate for the APXRD system. However, the latest core biopsy units are just beginning to employ large area (5cm by 5cm) Active Pixel Sensors as their imaging receptors (Faxitron X-ray Corporation, 2008) so a straightforward implementation of the APXRD idea can be foreseen in this way. Evaluation of the scatter signatures available with different collimation and filtration options is needed to assess the potential of using a microfocal X-ray source in the existing APXRD arrangement. For example, a tungsten tube operating at 60kV with 2mm of added Aluminium filtration yields a mean beam energy of 33keV, similar to that obtained with balanced filtration, with a spectral width of 29%.

### Ease of use and information output from the system

A protocol for calibration of the APXRD system would need to be established so that regular quality assurance exercises could be performed. Angular calibration could be performed by any operator as an automated algorithm could be developed to calculate the beam centre. A record of the calibration used for each data acquisition would need to be stored with the data file. Corrections for the sample holder background scatter and APS temperature drift would need to be made. The former can be addressed by measuring the scatter signature of the sample holder and storing this locally to subtract from each data acquisition. The latter could be corrected either by monitoring the temperature of the device and normalizing results to a given temperature, or by stabilizing the temperature of the detector using a peltier. Corrected data could then be fed into an online multivariate analysis model to make predictions of biopsy composition.

Finally, a survey of histopathologists should be performed to determine the most useful way to provide them with sample data. A fiducial marker or orientation label would be needed on the sample if the X-ray diffraction analysis were to aid in the selection of tissue sections. It may be that a prediction of the sample fat content is a useful output for each sample voxel interrogated, or it may be preferred that the system be trained to provide sample classifications, for example healthy or diseased, depending on the level of detail available in the final system. A protocol would also be needed to deal with 'unidentified' samples for which predictions cannot be made.

### Summary

Without a large scale trial to prove the correlation between biopsy fat content as determined by the APXRD scatter signature and biopsy histopathology, it is not possible to draw a final conclusion on the utility of the APXRD system for breast cancer diagnosis. Such a trial would require the cooperation of both histopathologists and clinical radiologists, so a convincing small scale study would first be needed. This could be completed on a limited set of biopsy samples, perhaps as few as four within each category of disease (as used in multivariate model building).

Given the large variability in age and breast composition among women recalled after mammography, scatter signatures from a large number of biopsies covering varying degrees of disease would be needed in order to train and validate a final multivariate model. Measurements should also be repeated in multiple hospitals with different X-ray sources to ensure compatibility between different systems. Using a large number of measurements to train a model negates the effects of the system employed and the individual characteristics of the patient. A double blind trial with histopathological assessment and model results for a new set of biopsies could then be used as final confirmation of the system capability.

# Bibliography


Acosta-Serafini P M, Masaki I and Sodini C G (2004) A 1/3" VGA Linear Wide Dynamic Range CMOS Image Sensor Implementing a Predictive Multiple Sampling Algorithm With Overlapping Integration Intervals. *IEEE J Solid-State Circuits* **39** 1487–1496.

Advisory Committee on Breast Cancer Screening (2006) Screening for breast cancer in England: Past and future. NHSBSP Publication No. 61.

Afifi A (2003) *Computer-Aided Multivariate Analysis.* Chapman & Hall/CRC.

Amemiya Y (1995) Imaging plates for use with synchrotron radiation. *J Synchrotron Radiat* **2** 13–21.

Ancharov A I, Potapov S S, Moiseenko T N, Feofilov I V and Nizovskii A I (2007) Model experiment of *in vivo* synchrotron X-ray diffraction of human kidney stones. *Nucl Inst Meth A* **575** 221–224.

Arvanitis C D (2007) *Quantitative contrast enhanced mammography and evaluation of scientific CMOS active pixels sensors for medical imaging.* Ph.D. thesis, University College London.

Arvanitis C D, Bohndiek S E, Royle G J, Blue A, Liang H X, Clark A T, Prydderch M L, Turchetta R and Speller R D (2007) Empirical electro-optical and x-ray performance evaluation of CMOS active pixel sensor for low dose, high resolution x-ray medical imaging. *Med Phys* **34** 4612–4625.

Ay S U and Fossum E R (2006) A 76 x 77mm$^2$, 16.85 Million Pixel CMOS APS Image Sensor. In *Proc IEEE Symposium on VLSI Circuits.*

Ballabriga R, Campbell M, Heijne E H M, Llopart X and Tlustos L (2007) The Medipix3 Prototype, a Pixel Readout Chip Working in Single Photon Counting Model With Improved Spectrometric Performance. *IEEE Trans Nucl Sci* **54** 1824–1829.

Banks E, Reeves G, Beral V, Bull D, Crossley B, Simmonds M, Hilton E, Bailey S, Barrett N, Briers P, English R, Jackson A, Kutt E, Lavelle J, Rockall L, Wallis M G, Wilson M and Patnick J (2004) Influence of personal characteristics of

individual women on the sensitivity and specificity of mammography in the Million Women Study: cohort study. *BMJ* **329** 447–452.

Batchelar D L and Cunningham I A (2002) Material-specific analysis using coherent-scatter imaging. *Med Phys* **29** (8) 1651–1660.

Batchelar D L, Davidson M T M, Dabrowski W and Cunningham I A (2006) Bone-composition imaging using coherent-scatter computed tomography: Assessing bone health beyond bone mineral density. *Med Phys* **33** (4) 904–913.

Beecken B P and Fossum E R (1996) Determination of the conversion gain and the accuracy of its measurement for detector elements and arrays. *Applied Optics* **35** (19) 3471–3477.

Beevor S P, Sander J, Raitt I, Burrows J D and Mann K (1995) Non-invasive inspection of baggage using coherent scattering. *Proc IEEE European Convention on Security and Detection* pp. 301–305.

Bermak A and Yung Y F (2006) A DPS Array With Programmable Resolution and Reconfigurable Conversion Time. *IEEE Trans VLSI Syst* **14** 15–22.

Blakesley J C and Speller R (2008) Modeling the imaging performance of prototype organic x-ray imager. *Med Phys* **35** 225–239.

Bohndiek S E, Arvanitis C D, Royle G J, Clark A T, Crooks J P, Prydderch M L, Turchetta R, Blue A, O'Shea V and Speller R D (2007) Characterization study of two novel Active Pixel Sensors. *Opt Eng* **46** 124003 1–11.

Bohndiek S E, Blue A, Clark A T, Prydderch M L, Turchetta R, Royle G J and Speller R (2008a) Comparison of methods for estimating the conversion gain of CMOS Active Pixel Sensors. *IEEE Sensors* p. to be published.

Bohndiek S E, Cook E J, Arvanitis C D, Olivo A, Royle G J, Clark A T, Prydderch M L, Turchetta R and Speller R D (2008b) A CMOS active pixel sensor system for laboratory based x-ray diffraction studies of biological tissue. *Phys Med Biol* **53** 655–672.

Boone J M (2000) *Handbook of Medical Imaging: Volume 1. Physics and Psychophysics*, chapter 1, pp. 1–77. SPIE Press.

Boone J M and Chavez A E (1996) Comparison of X-ray cross sections for diagnostic and therapeutic medical physics. *Med Phys* **23** 1997–2005.

Boudet N, Berar J F, Blanquart L, Breugon P, Caillot B, Clemens J C, Koudobine I, Delpierre P, Mouget C, Potheau R and Valin I (2003) XPAD: a hybrid pixel detector for X-ray diffraction and diffusion. *Nucl Inst Meth A* **510** 41–44.

British Medical Journal (2008) British Medical Journal 'Best Treaments' page (http://besttreatments.bmj.com/btuk/conditions/5827.jsp).

Britton P D (1999) Fine needle aspiration or core biopsy. *The Breast* **8** 1–4.

Brügemann L and Gerndt E K E (2004) Detectors for X-ray diffraction and scattering: a user's overview. *Nucl Inst Meth A* **531** 292–301.

Brunetti A and Cesareo R (2007) A compact X-ray tomograph based on a CMOS flat panel. *Nucl Inst Meth A* **580** 782–784.

Burghartz J N, Graf H G, Harendt C, Klingler W, Richter H and Strobel M (2006) HDR CMOS imager and their applications. In *Proc IEEE ICSICT.*

CameraLink (2004) Specifications of the Camera Link Interface Standard for Digital Cameras and Frame Grabbers v1.1 (http://www.imagelabs.com/pdf/CameraLink5.pdf).

CAMO Software AS (2006) *The Unscrambler: Methods.* CAMO.

CAMO Software AS (2008) The Unscrambler v9.6 (http://www.camo.com/rt/Products/Unscrambler/unscrambler.html).

Cancer Research UK (2008) CancerStats Key Facts: Breast Cancer.

Castoldi A, Guazzoni C, Galimberti A, Hartmann R, Pani S, Royle G J and Strüder L (2007) Application of Controlled-Drift Detectors in Diffraction Enhanced Imaging of Tissues. *IEEE Trans Nucl Sci* **54** 1474–1480.

Changizi V, Oghabian M A, Speller R, Sarkar S and Kheradmand A A (2005) Application of Small Angle X-ray Scattering (SAXS) for Differentiation between Normal and Cancerous Breast Tissue. *Int J Med Sci* **2** (3) 118–121.

Changizi V, Wilkinson S, Hall C J and Grossmann G (2006) A study of the effect of formalin preservation on normal and cancerous breast tissues using small angle X-ray scattering (SAXS). *Radiat Phys Chem* **75** 932–935.

Chi Y M, Mallik U, Clapp M A, Choi E, Cauwenberghs G and Etienne-Cummings R (2007) CMOS Camera with In-Pixel Temporal Change Detection and ADC. *IEEE J Solid-State Circuits* **42** 2187–2196.

Cho H S, Jeong M H, Han B S, Kim S, Lee B S, Kim H K and Lee S C (2005) Development of a Portable Digital Radiographic System Based on FOP-Coupled CMOS Image Sensor and Its Performance Evaluation. *IEEE Trans Nucl Sci* **52** 1766–1772.

Choi J, Han S W, Kim S J, Chang S I and Yoon E (2007) A Spatial-Temporal Multiresolution CMOS Image Sensor with Adaptive Frame Rates for Tracking the Moving Objects in Region-of-Interest and Suppressing Motion Blur. *IEEE J Solid-State Circuits* **42** 2978–2989.

Cook E J (2008a) *Analysis of Energy Dispersive X-Ray Diffraction Profiles for Material Identification, Imaging and System Control.* Ph.D. thesis, University College London.

Cook E J (2008b) Private Communication.

Cullity B D (2003) *Elements of X-ray Diffraction.* Pearson Education, 3rd edition.

Cunningham I A and Shaw R (1999) Signal-to-noise optimization of medical imaging systems. *J Opt Soc Am A* **16** (3) 621–632.

Davidson M T M, Batchelar D L, Chew B H, Denstedt J D and Cunningham I A (2006) Establishing composition and structure of intact urinary calculi by x-ray coherent scatter for clinical laboratory investigations. *J Urology* **175** 2336–2340.

Davidson M T M, Batchelar D L, Velupillai S, Denstedt J D and Cunningham I A (2005) Laboratory coherent-scatter analysis of intact urinary stones with crystalline composition: a tomographic approach. *Phys Med Biol* **50** 3907–3925.

Dawson C, Horrocks J A, Kwong R, Speller R D and Whitfield H N (1996) Low-angle X-ray scattering signatures of urinary calculi. *World J Urol* **14** S43–S47.

Dixon J M (2006) Screening for breast cancer. *BMJ* **332** 499–500.

DuBois J, Ginhac D, Paindavoine M and Heyrman B (2008) A 10 000 fps CMOS Sensor With Massively Parallel Image Processing. *IEEE J Solid-State Circuits* **43** 706–717.

El Gamal A and Eltoukhy H (2005) CMOS Image Sensors. *IEEE Circuits Devices Magazine* (May/June 2005) 6–20.

El Gamal A, Fowler Bband Min H and Liu X (1998) Modeling and estimation of FPN Components in CMOS Image Sensors. In *Proc SPIE*, volume 3301, pp. 168–177.

Ellis I O, Pinder S E, Lee A H S and Elston C W (2004) *Challenges in Breast Cancer*, chapter 7: The role of cytology and needle core biopsy in nonoperative diagnosis of breast cancer, pp. 92–104. Blackwell.

Elshemey W M, Desouky O S, Mohammed M S, Elsayed A A and El-houseini M E (2003) Characterization of cirrhosis and hepatocellular carcinoma using low-angle x-ray scattering signatures of serum. *Phys Med Biol* **48** N239–N246.

European Machine Vision Association (2005) EMVA Standard 1288: Standard for Characterization and Presentation of Specification Data for Image Sensors and Cameras. Technical report, EMVA.

Evans S H, Bradley D A, Dance D R, Bateman J E and Jones C H (1991) Measurement of small-angle photon scattering for some breast tissues and tissue substitute materials. *Phys Med Biol* **36** (1) 7–18.

Faramarzpour N, Deen M J, Shirani S and Fang Q (2008) Fully integrated single photon avalance diode detector in standard 0.18$\mu$m technology. *IEEE Trans Electron Devices* **55** 760–767.

Farquharson M (2008) Private Communication.

Farquharson M J and Geraki K (2004) The use of combined trace element XRF and EDXRD data as a histopathology tool using a multivariate analysis approach in characterizing breast tissue. *X-ray Spectrom* **33** 240–245.

Faxitron X-ray Corporation (2008) Faxitron X-ray Corporation website (http://www.faxitron.com/).

Fernández M, Keyrilainen J, Karjalainen-Lindsberg M L, Leidenius M, von Smitten K, Fiedler S and Suortti P (2004) Human breast tissue characterisation with small-angle x-ray scattering. *Spectroscopy* **18** 167–176.

Fernández M, Keyrilainen J, Serimaa R, Torkkeli M, Karjalainen-Lindsberg M L, Tenhunen M, Thomlinson W, Urban V and Suortti P (2002) Small-angle x-ray scattering studies of human breast tissue samples. *Phys Med Biol* **47** 577–592.

Fossum E R (1997) CMOS Image Sensors: Electronic Camera-On-A-Chip. *IEEE Trans Electron Dev* **40** (10) 1689–1699.

Geddes D T (2007) Inside the Lactating Breast: The Latest Anatomy Research. *Journal of Midwifery and Women's Health* **52** 556–563.

Griffiths J A, Royle G J, Hanby A M, Horrocks J A, Bohndiek S E and Speller R D (2007) Correlation of energy dispersive diffraction signatures and microCT of small breast samples with pathological analysis. *Phys Med Biol* **52** 6151–6164.

Griffiths J A, Royle G J, Horrocks J A, Hanby A M, Pani S and Speller R D (2008) Angular dispersive diffraction microCT of small breast tissue samples. *Radiation Physics and Chemistry* **77** 373–380.

Griffiths J A, Royle G J, Speller R D, Horrocks J A, Olivo A, Pani S, Longo R, Spencer S H, Robbins M S, Clifford D P and Hanby A M (2003) Diffraction Enhanced Breast Imaging: assessment of realistic system requirements to improve

the diagnostic capabilities of mammography. In *Proc IEEE Nuclear Science Symposium and Medical Imaging Conference*, volume 5, pp. 3230–3234.

Gruner S M (2002) Charge-coupled device area x-ray detectors. *Rev Sci Instrum* **73** (8) 2815–2844.

Guinebretière J M, Becette V, Hagay C, Belichard C, Tardivon A and Vanel D (2005) Use of radiology for the pathologist in the management of breast lesions. *Eur Radiol* **54** 15–25.

Guo X, Qi X and Harris J G (2007) A Time-to-First-Spike CMOS Image Sensor. *IEEE Sensors* **7** 1165–1175.

Haka A S, Shafer-Peltier K E, Fitzmaurice M, Crowe J, Dasari R R and Feld M S (2005) Diagnosing breast cancer by using Raman spectroscopy. *PNAS* **102** 12371–12376.

Hamamatsu (2007) Private Communication.

Hamamatsu (2008) X-ray Flat Panel Sensors (http://www.sales.hamamatsu.com/).

Harding G, Kosanetzky J and Neitzel U (1987) X-ray Diffraction Computed Tomography. *Med Phys* **14** (4) 515–525.

Harding G and Schreiber B (1999) Coherent X-ray scatter imaging and its application in biomedical science and industry. *Radiat Phys Chem* **56** 229–245.

Hejazi S and Trauernicht D P (1997) System considerations in CCD-based x-ray imaging for digital chest radiography and digital mammography. *Med Phys* **24** (2) 287–297.

Héry C, Ferlay J, Boniol M and Autier P (2008) Quantification of changes in breast cancer incidence and mortality since 1990 in 35 countries with Caucasian-majority populations. *Annals of Oncology* **19** (6) 1187–1195.

Hillen W, Eckenbach W, Quadflieg P and Zaengel P (1991) Signal-to-noise performance in cesium iodide x-ray fluorescent screens. pp. 120–131.

Holdsworth D W, Gerson R K and Fenster A (1990) A time-delay integration charge-coupled device camera for slot-scanned digital radiography. *Med Phys* **17** (5) 876–886.

Hopkinson G R, Goodman T M and Prince S R (2004) *A Guide to the Use and Calibration of Detector Array Equipment.* SPIE Press.

Houssami N, Cuzick J and Dixon J M (2006) The prevention, detection, and management of breast cancer. *MJA* **184** 230–234.

Hukins D W L (1981) *X-ray diffraction by Ordered and Disordered Systems.* Oxford, Perganon.

Hukkinen K S, Kivisaari L M, Heikkilä P S, Von Smitten K A J and Leidenius M H K (2008) Unsuccessful preoperative biopsies, fine needle aspiration cytology or core needle biopsy, lead to increased costs in the diagnostic workup in breast cancer. *Acta Oncologica* pp. 1–9.

Ingram C E and Wyld L (2007) Imaging techniques in screening for breast cancer. *Surgery* **25** 257–260.

Ito K, Gaponov Y, Sakabe N and Amemiya Y (2007) A 3 x 6 arrayed CCD X-ray detector for continuous rotation method in macromolecular crystallography. *J Synchrotron Rad* **14** 144–150.

James V J (2006) A place for fiber diffraction in the detection of breast cancer? *Cancer Detection and Prevention* **30** 233–238.

Janesick J and Putnam G (2003) Developments and applications of high-performance CCD and CMOS imaging arrays. *Annu Rev Nucl Part S* **53** 263–300.

Janesick J R (2001) *Scientific Charge Coupled Devices.* SPIE Press.

Janesick J R (2007) *Photon Transfer* $DN \rightarrow \lambda$. SPIE Press.

Janesick J R, Andrews J T and Elliott T (2006) Fundamental performance differences between CMOS and CCD imagers; Part I. In *Proc. SPIE*, volume 6276.

Johns H E and Cunningham J R (1983) *The Physics of Radiology.* Springfield, Ill., U.S.A.

Johns P C and Wismayer M P (2004) Measurement of coherent x-ray scatter form factors for amorphous materials using diffractometers. *Phys Med Biol* **49** 5233–5250.

Johns P C and Yaffe M J (1983) Coherent scatter in diagnostic radiology. *Med Phys* **10** 40–50.

Johns P C and Yaffe M J (1987) X-ray characterisation of normal and neoplastic breast tissues. *Phys Med Biol* **32** 675–695.

Kanis J A and Glüer C C (2000) An update on the diagnosis and assessment of osteoporosis with densitometry. *Osteoporos Int* **11** 192–202.

Kidane G, Speller R D, Royle G J and Hanby A M (1999) X-ray scatter signatures for normal and neoplastic breast tissues. *Phys Med Biol* **44** 1791–1802.

Kirkpatrick P (1939) On the theory and use of Ross filters. *RSI* **10** 186–191.

Kleinfelder S, Lim S, Liu X and El Gamal A (2001) A 10000 Frames/s CMOS Digial Pixel Sensor. *IEEE J Solid-State Circuits* **36** (12) 2049–2060.

Knoll G F (2000) *Radiation Detection and Measurement*, chapter 8: Scintillation Detector Principles, pp. 219–263. John Wiley & Sons, Inc., 3rd edition.

Konstantinidis A (2008) Private Communication.

Kosanetzky J, Knoerr B, Harding G and Neitzel U (1987) X-ray diffraction measurements of some plastic materials and body tissues. *Med Phys* **14** (4) 526–532.

Kuschak P (2007) Private Communication.

Larsen W J (2002) *Anatomy: development, function, clinical correlations*, chapter 6. Saunders, London.

LeClair R J, Boileau M M and Wang Y (2006) A semianalytic model to extract differential linear scattering coefficients of breast tissue from energy dispersive x-ray diffraction measurements. *Med Phys* **33** 959–967.

Lewis R (2003) Position sensitive detectors for synchrotron radiation studies: the tortoise and the hare? *Nucl Inst Meth A* **513** 172–177.

Liberman L, Evans W P, Dershaw D D, Hann L E, Deutch B M, Abramson A F and Rosen P P (1994) Radiography of Microcalcifications in Stereotaxic Mammary Core Biopsy Specimens. *Radiology* **190** 223–225.

Lieske B, Ravichandran D and Wright D (2006) Role of fine-needle aspiration cytology and core biopsy in the preoperative diagnosis of screen-detected breast cancer. *British Journal of Cancer* **95** 62–66.

Liu X and El Gamal A (2003) Synthesis of High Dynamic Range Motion Blur Free Image from Multiple Captures. *IEEE Trans Circuits Sys I* **50** 530–539.

Livet F, Bley F, Mainville J, Caudron R, Mochrie S G J, Geissler E, Dolino G, Abernathy D, Grübel G and Sutton M (2000) Using direct illumination CCDs as high-resolution area detectors for X-ray scattering. *Nucl Inst Meth A* **451** 596–609.

Lubinsky A R, Zhao W, Ristic G and Rowlands J A (2006) Screen optics effects on detective quantum efficiency in digital radiography: Zero-frequency effects. *Med Phys* **33** 1499–1509.

Lulé T (2000) Sensitivity of CMOS based imagers and scaling perspectives. *IEEE Trans Electron Dev* **47** (11) 2110–.

Madaan S and Joyce A D (2007) Limitations of extracorporeal shock wave lithotripsy. *Current Opinion in Urology* **17** 109–113.

Malden C and Speller R D (2000) A CdZnTe array for the detection of explosives in baggage by energy-dispersive X-ray diffraction signatures at multiple scatter angles. *Nucl Inst Meth A* **449** 498–415.

Masson O, Boulle A, Guinebretière R, Lecomte A and Dauger A (2005) On the use of one-dimensional position sensitive detector for x-ray diffraction reciprocal space mapping: Data quality and limitations. *Rev Sci Instrum* **76** 063912.

Medipix (2006) The Medipix 3 consortium (http://medipix.web.cern.ch).

Meynants G, Dierickx B, Alaerts A, Uwaerts D, Cos S and Scheffer D (2003) A 35mm 13.89 Million Pixel CMOS Active Pixel Image Sensor. In *IEEE Workshop on CCD & AIS, Germany*, pp. –.

Mezouar M, Crichton W A, Bauchau S, Thurel F, Witsch H, Torrecillas F, Blattmann G, Marion P, Chavanne J, Hignette O, Morawe C and Borel C (2005) Development of a new state-of-the-art beamline optimized for monochromatic single-crystal and powder X-ray diffraction under extreme conditions at the ESRF. *J Synchrotron Rad* **12** 659–664.

Millis R R, Hanby A M and Girling A C (1994) *Diagnostic Surgical Pathology*, chapter The Breast. Raven Press.

Moe O W (2006) Kidney stones: pathophysiology and medical management. *The Lancet* **367** 333–344.

Moore K L and Dalley A F (1999) *Clinically oriented anatomy (4th Ed)*. Lippincott Williams and Wilkins.

Morin L R M and Berroir A (1983) Calculation of x-ray single scattering in diagnostic radiology. *Phys Med Biol* **28** 789–797.

Multidimensional Integrated Intelligent Imaging - M-I$^3$ (2008) (http://www.activepixels.org).

Muntz E P, Fewell T, Jennings R and Bernstein H (1983) On the significance of very small angle scattered radiation to radiographic imaging at low energies. *Med Phys* **10** 819–823.

Nagarkar V V, Singh B, Guo L, Gore D and Irving T C (2006) EMCCD-Based Detector for Time-Resolved X-Ray Diffraction and Scattering Studies of Biological Specimens. *Proc IEEE Nuclear Science Symposium and Medical Imaging Conference* **N19-6** 740–743.

National Health Service (2008) NHS Breast Screening Programme (http://www.cancerscreening.nhs.uk/breastscreen/).

Newton M, Hukins D W L and Harding G (1992) Bone composition measured by x-ray scattering. *Phys Med Biol* **37** (6) 1339–1347.

Nikl M (2006) Scintillation detectors for x-rays. *Meas Sci Technol* **17** R37–R54.

Noble P (1968) Self-Scanned Silicon Image Detector Arrays. *IEEE Trans Electron Devices* **ED-15** (4) 202–209.

Nyman J S, Reyes M and Wang X (2005) Effect of ultrastructural changes on the toughness of bone. *Micron* **36** 566–582.

Pain B and Hancock B (2003) Accurate Estimation of Conversion Gain and Quantum Efficiency in CMOS Imagers. In *Proc SPIE*, volume 5017, pp. 94–103.

Pain B, Sun C, Wrigley C and Yang G (2002) 8.4: Dynamically reconfigurable vision with high performance CMOS Active Pixel Sensors. In *Proc IEEE Sensors*, volume 1, pp. 21–26.

Pain B, Yang G, Cunningham T J, Wrigley C and Hancock B (2003) An Enhanced-Performance CMOS Imager with a Flushed Reset Photodiode Pixel. *IEEE Trans Electron Dev* **50** (1) 48–56.

Pak C Y C, Poindexter J R, Adams-Huet B and S P M (2003) Predictive value of kidney stone composition in the detection of metabolic abnormalities. *Am J Med* **115** 26–32.

Pani S, Royle G J, Speller R D, Castoldi A, Galimberti A and Guazzoni C (2007) Use of a novel controlled drift detector for diffraction enhanced breast imaging. *Nucl Inst Meth A* **573** 133–136.

Parks J H, Coward M and Coe F L (1997) Correspondence between stone composition and urine supersaturation in nephrolithiasis. *Kidney International* **51** 894–900.

Peplow D E and Verghese K (1998) Measured molecular coherent scattering form factors of animal tissues, plastics and human breast tissue. *Phys Med Biol* **43** 2431–2452.

Photron (2008) ultima APX-RS (http://www.photron.com).

Poletti M E, Goncalves O D and Mazzaro I (2002) X-ray scattering from human breast tissues and breast-equivalent materials. *Phys Med Biol* **47** 47–63.

Ponchut C (2001) Evaluation of an x-ray imaging detector based on a CMOS camera with logarithmic response. *Nucl Inst Meth A* **457** (1-2) 270–278.

Ponchut C and Zontone F (2003) Evaluation of Medipix-1 in X-ray scattering and X-ray diffraction applications. *Nucl Inst Meth A* **510** 29–34.

Ortũno Prados F, Hall C, Helsby W, Jones A, Lewis R, Parker B, Sheldon J, Bazzano A and Ubertini P (1997) A large area, 2-D, high-pressure MWPC for wide angle X-ray diffraction. *Nucl Inst Meth A* **392** 47–50.

Raab S S, Grzybicki D M, Janosky J E, Zarbo R J, Meier F A, Jensen C and Geyer S J (2005) Clinical impact and frequency of anatomic pathology errors in cancer diagnosis. *Cancer* **104** 2205–2213.

Rabbani M, Shaw R and Van Metter R (1987) Detective quantum efficiency of imaging systems with amplifying and scattering mechanisms. *J Opt Soc Am A* **4** (5) 895–901.

Rad-icon Imaging Corp (2008) RadEye (http://www.rad-icon.com/RadEye.htm).

Ramsay A D (1999) Errors in histopathology reporting: detection and avoidance. *Histopathology* **34** 481–490.

Reddy M and Given-Wilson R (2004) Screening for breast cancer. *Surgery* **22** 155–160.

Rossi G, Renzi M, Eikenberry E F, Tate M W, Bilderback D, Fontes E, Wixted R, Barna S and Gruner S M (1999) Tests of a prototype pixel array detector for microsecond time-resolved X-ray diffraction. *J Synchrotron Rad* **6** 1096–1105.

Round A R, Wilkinson S J, Hall C J, Rogers K D, Glatter O, Wess T and Ellis I O (2005) A preliminary study of breast cancer diagnosis using laboratory based small angle x-ray scattering. *Phys Med Biol* **50** 4159–4168.

Royle G J, Farquharson M, Speller R and Kidane G (1999) Applications of x-ray diffraction analysis in crystalline and amorphous body tissues. *Radiat Phys Chem* **56** 247–258.

Royle G J and Speller R D (1995) Quantitative x-ray diffraction analysis of bone and marrow volumes in excised femoral head samples. *Phys Med Biol* **40** 1487–1498.

Ryan E A and Farquharson M J (2007) Breast tissue classification using x-ray scattering measurements and multivariate data analysis. *Phys Med Biol* **52** 6679–6696.

Saito M (2004) Quasimonochromatic x-ray computed tomography by the balanced filter method using a conventional x-ray source. *Med Phys* **31** 3436–3443.

Scheffer D (2007) Wafer scale active pixels CMOS image sensor for generic x-ray radiology. In *Proc SPIE*, volume 6510, pp. 65100–O.

Schlomka J P, Harding A, van Stevendaal U, Grass M and Harding G L (2003) Coherent scatter computed tomography: a novel medical imaging technique. In *Proc SPIE*, volume 5030.

Schrey O, Huppertz J, Filimonovic G, Bussmann A, Brockherde W and Hosticka B (2002) A 1kx1k high dynamic range CMOS image sensor with on-chip programmable region-of-interest readout. *IEEE J Solid-State Circuits* **37** (7) 911–915.

Sellin P J, Rossi G, Renzi M J, Knights A P, Eikenberry E F, Tate M W, Barna S L, Wixted R L and Gruner S M (2001) Performance of semi-insulating gallium arsenide X-ray pixel detectors with current-integrating readout. *Nucl Inst Meth A* **460** 207–212.

Shcherback I, Danov T and Yadid-Pecht O (2004) A comprehensive CMOS APS crosstalk study: Photoresponse model, technology and design trends. *IEEE Trans Electron Devices* **51** (12) 2033–2041.

Shousha S (2003) Issues in the interpretation of breast core biopsies. *Int J Surg Pathol* **11** 167–176.

Siewerdsen J H, Antonuk L E, El-Mohri Y, Yorkston J, Huang W, Boudry J M and Cunningham I A (1997) Empirical and theoretical investigation of the noise performance of indirect detection, active matrix flat-panel imagers (AMFPIs) for diagnostic radiology. *Med Phys* **24** (1) 71–89.

Siewerdsen J H, Waese A M, Moseley D J, Richard S and Jaffray D A (2004) Spektr: A computational tool for x-ray spectral analysis and imaging system optimization. *Med Phys* **31** (11) 3057–3067.

Singh N and Wells C A (2001) Assessment of accuracy in breast cytology. *Cytopathology* **12** 211–218.

Speller R D and Horrocks J A (1991) Photon scattering - a 'new' source of information in medicine and biology? *Phys Med Biol* **36** 1–6.

Squires G L (1997) *Practical Physics (3rd Edition)*. Cambridge University Press.

Stark B, Nölting B, Jahn H and Andert K (1992) Method for determining the electron number in charge-coupled measurement devices. *Opt Eng* **31** 852–856.

Stoppa D, Simoni A, Gonzo L, Gottardi M and Dalla Betta G F (2002) Novel CMOS Image Sensor with a 132-dB Dynamic Range. *IEEE J Solid-State Circuits* **37** 1846–1852.

Sugiyama Y, Takumi M, Toyoda H, Mukozaka N, Ihori A, Kurashina T, Nakamura Y, Tonbe T and Mizuno S (2005) A High-Speed CMOS Image Sensor With Profile Data Acquiring Function. *IEEE J Solid-State Circuits* **40** 2816–2823.

Suryanarayanan S, Karellas A, Vedantham S and Sechopoulos I (2006) Theoretical analysis of high-resolution digital mammography. *Phys Med Biol* **51** 3041–3055.

Takeda A, Uekusa H, Kubo H, Miuchi K, Nagayoshi T, Ohashi Y, Okada Y, Orito R, Takada A and Tanimori T (2005) Development of $\mu$-PIC as a time-resolved X-ray area detector. *J Synchrotron Rad* **12** 820–825.

Tate M W, Chamberlain D and Gruner S M (2005) Area x-ray detector based on a lens-coupled charge-coupled device. *Rev Sci Instrum* **76** 081301.

Tedde S, Zaus E S, Fürst J, Henseler D and Lugli P (2007) Active Pixel Concept Combined With Organic Photodiode for Imaging Devices. *IEEE Electron Device Letters* **28** 893–895.

Theodorakou C and Farquharson M J (2008) Human soft tissue analysis using x-ray or gamma-ray techniques. *Phys Med Biol* **53** R111–R149.

Tian H, Fowler B and El Gamal A (2001) Analysis of temporal noise in CMOS photodiode active pixel sensor. *IEEE J Solid-State Circuits* **36** (1) 92–101.

Tse G M, Tan P H, Pang A L M, Tang A P Y and Cheung H S (2008) Calcification in breast lesions: pathologists' perspective. *J Clin Pathol* **61** 145–151.

Turchetta R, French M, Manolopoulos S, Tyndel M, Allport P, Bates R, O'Shea V, Hall G and Raymond M (2003) Monolithic active pixel sensors (MAPS) in a VLSI CMOS technology. *Nucl Inst Meth A* **501** 251–259.

Vedantham S, Karellas A and Suryanarayanan S (2004a) Solid-state fluoroscopic imager for high-resolution angiography: Parallel-cascaded linear systems analysis. *Med Phys* **31** (5) 1258–1268.

Vedantham S, Karellas A, Suryanarayanan S and Onishi S K (2004b) Solid-state fluoroscopic imager for high-resolution angiography: Physical characteristics of an 8cmx8cm experimental prototype. *Med Phys* **31** (6) 1462–1472.

Vision Research (2008) Phantom v12 (http://www.visionresearch.com/) .

de Vries R, Weijers S, Bethke K, Kogan V, Vasterink J, Kharchenko A, Fransen M and Bethke J (2007) Medipix 2 in X-ray diffraction. *Nucl Inst Meth A* **576** 164–168.

Wallis M, Tarvidon A, Helbich T and Schreer I (2007) Guidelines from the European Society of Breast Imaging for diagnostic interventional breast procedures. *Eur Radiol* **17** 581–588.

Weber M (2002) Inorganic Scintillators: Today and tomorrow. *J Luminescence* **100** 35–45.

Westmore M S, Fenster A and Cunningham I A (1996) Angular-dependent coherent scatter measured with a diagnostic x-ray image intensifier based imaging system. *Med Phys* **23** (5) 723–733.

Westmore M S, Fenster A and Cunningham I A (1997) Tomographic imaging of the angular-dependent coherent-scatter cross section. *Med Phys* **24** (1) 3–10.

Wong H S (1996) Technology and Device Scaling Considerations for CMOS Imagers. *IEEE Trans Electron Dev* **43** 2131–2142.

Wyld L and Ingram C E (2007) Screening of the population for breast cancer. *Surgery* **25** 254–256.

Yadid-Pecht O (1999) Wide-dynamic-range sensors. *Opt Eng* **38** (10) 1650–1660.

Yadid-Pecht O and Belenky A (2003) In-Pixel Autoexposure CMOS APS. *IEEE J Solid-State Circuits* **38** 1425–1428.

Yadid-Pecht O, Ginosar R and Diamand Y (1991) A Random Access Photodiode Array for Intelligent Image Capture. *IEEE Trans Electron Dev* **38** (8) 1772–1781.

Yadid-Pecht O, Pain B, Staller C, Clark C and Fossum E R (1997) CMOS Active Pixel Sensor Star Tracker with Regional Electronic Shutter. *IEEE J Solid-State Circuits* **32** 285–288.

Yagi N, Yamamoto M, Uesugi K and Inoue K (2004) A large-area CMOS imager as an X-ray detector for synchrotron radiation experiments. *J Synchrotron Rad* **11** 347–352.

Zaber Technologies (2008) Motorized Linear Actuator specifications (http://www.zaber.com/products/).